

# Assessment of nitryl chloride as a missing oxidant in the UK atmosphere

Thesis submitted for the degree of Doctor of Philosophy

Lloyd Daniel John Hollis (MChem)

Department of Chemistry

University of Leicester

September 2017

# Assessment of nitryl chloride as a missing oxidant in the UK atmosphere

Lloyd Daniel John Hollis

## Abstract

Nitryl chloride ( $\text{ClNO}_2$ ) is potentially an important contributor to the troposphere's oxidising capacity in the UK and European context. A lack of observational evidence means the role of  $\text{ClNO}_2$  is poorly understood, however, with only two prior publications of European  $\text{ClNO}_2$  observations - one in the UK and one in Germany. This thesis greatly extends the UK dataset with five sets of  $\text{ClNO}_2$  measurements made on Leicester University's campus and two datasets from coastal locations (Weybourne in North Norfolk and Penlee Point near Plymouth).

$\text{ClNO}_2$  forms at night from the heterogeneous reaction of dinitrogen pentoxide ( $\text{N}_2\text{O}_5$ ), derived from man-made  $\text{NO}_x$  emissions, with chloride-containing aerosol particles (sea spray).  $\text{ClNO}_2$  photolysis subsequently releases highly reactive chlorine atoms which oxidise volatile organic compounds, enhancing tropospheric ozone production and its associated effects on air quality and climate.

A chemical ionisation mass spectrometer operating with iodide reagent ions was used for work in this thesis. This instrument was calibrated for  $\text{ClNO}_2$  *via* broadband cavity-enhanced absorption spectroscopy and for  $\text{Cl}_2$  *via* reference standard. Typical sensitivities of 6-13 Hz/pptv were achieved for both  $\text{ClNO}_2$  and  $\text{Cl}_2$ .

The highest ambient  $\text{ClNO}_2$  concentration observed in this work was 1104 pptv at the Weybourne coastal site, attributed to air from the London outflow. For all sites, air mass back-trajectories showed that high  $\text{ClNO}_2$  concentrations tended to correlate with chemically-aged air masses that had spent considerable time over land. Indeed  $\text{ClNO}_2$  was observed almost every night at Leicester, and sea salt was found to be the chloride source even at this inland location.  $\text{N}_2\text{O}_5$  availability limited  $\text{ClNO}_2$  production at both coastal sites.

Nitryl chloride displayed strong seasonality. Repeat measurements at Leicester showed  $\text{ClNO}_2$  was highest in winter and lowest in summer.  $\text{ClNO}_2$  was also observed to persist throughout the day on several days in December 2014 and February 2016.

## Acknowledgements

I would like to thank Prof. Paul Monks for the opportunity to undertake this project and for providing encouragement and perspective when progress was slow. Dr. Stephen Ball has my gratitude for extensive guidance throughout the project, and for extremely detailed feedback that proved invaluable in converting a collection of thoughts, experiments and figures into a thesis. Dr. Roberto Sommariva also has my thanks for the prolonged on-the-ground assistance with work in the laboratory and field.

Thanks to the University of Leicester and the Natural Environment Research Council for respectively hosting and funding myself and my work for the last few years.

I would like to acknowledge a number of people for their contributions to work in this thesis: Tomás Sherwen and Mat Evans for work on the GEOS-Chem models; Zoe Fleming and Marios Panagi regarding the NAME models; Alex Baker for work on aerosol measurements; Rebecca Cordell for operating the AURN station instruments; the PML and ICOZA teams for hosting and assisting us in the field and making data available thereafter; the MChem students for their contributions to CIMS work; and finally to the workshop team for constructing custom laboratory equipment for us.

I am also indebted to my friends and family: Keighley for providing me with support, sanity and frequent smiles during the last few stressful months and beyond; my parents and brother for nurturing (and putting up with) me during some awkward early years; TG, who even in primary school was encouraging my curiosity; Nathan for being a long and solid friend; Matt, Ben and many others for keeping the good times rolling during my undergraduate degree.

Final thanks go to all the good folks in the office including Lewis for ensuring an interesting first year; Rik, Tom and Iain for keeping the atmosphere light with banter; Rebecca, Jono and Mike for putting up with my awful jokes and Bob for adding his own.

## Table of Contents

Abstract .....	2
Acknowledgements .....	3
Table of Contents.....	4
List of tables .....	9
List of figures.....	10
1 Introduction.....	19
1.1 Atmospheric structure & composition .....	19
1.2 Tropospheric chemistry.....	21
1.2.1 Oxidation chemistry by day .....	24
1.2.2 Oxidation chemistry by night .....	28
1.2.3 Tropospheric halogen chemistry.....	30
1.2.4 Nitryl chloride.....	33
1.3 Prior observations of nitryl chloride .....	35
1.4 Summary and motivation .....	40
2 Instruments & methods.....	43
2.1 Introduction .....	43
2.2 Chemical Ionisation Mass Spectrometry .....	43
2.2.1 Overview .....	43
2.2.2 Mass spectrometry .....	44
2.2.3 Chemical ionisation.....	46
2.2.4 CIMS hardware & application .....	49
2.3 Broadband cavity enhanced absorption spectroscopy.....	51
2.3.1 Overview .....	51
2.3.2 Absorption spectroscopy.....	52
2.3.3 Cavity enhanced absorption spectroscopy .....	53
2.3.4 Differential optical absorption spectroscopy .....	56

2.3.5	BBCEAS hardware & application .....	59
2.3.6	Data processing .....	61
2.4	Other instruments deployed .....	73
2.4.1	University of Leicester .....	73
2.4.2	Penlee Point Atmospheric Observatory .....	74
2.4.3	Weybourne Atmospheric Observatory .....	75
2.5	Data processing & analysis techniques .....	75
3	Experimental.....	77
3.1	Overview .....	77
3.2	CIMS commissioning & adjustment .....	79
3.2.1	Cl <sub>2</sub> & Br <sub>2</sub> detection trials .....	79
3.2.2	Detector mass calibration .....	83
3.2.3	CIMS optimisation.....	85
3.3	CIMS calibrations: preparation and development .....	89
3.3.1	Overview .....	89
3.3.2	Mass flow controllers.....	91
3.3.3	Nitrogen sources .....	93
3.3.4	ClNO <sub>2</sub> generation <i>via</i> N <sub>2</sub> O <sub>5</sub> + NaCl .....	94
3.3.5	ClNO <sub>2</sub> generation <i>via</i> Cl <sub>2</sub> + NaNO <sub>2</sub> .....	98
3.3.6	Reactor development .....	101
3.3.7	Humidity effects .....	102
3.3.8	Background measurement coil.....	105
3.4	CIMS calibration experiments .....	108
3.4.1	CIMS calibrations: ClNO <sub>2</sub> <i>via</i> NaCl + N <sub>2</sub> O <sub>5</sub> .....	108
3.4.2	CIMS calibrations: ClNO <sub>2</sub> <i>via</i> Cl <sub>2</sub> + NaNO <sub>2</sub> .....	110
3.4.3	CIMS calibration: Cl <sub>2</sub> .....	114
3.5	Data processing .....	115

3.5.1	Initial steps .....	115
3.5.2	Data averaging .....	116
3.5.3	Calibration plots .....	118
3.5.4	Uncertainty determination .....	119
3.5.5	Data filtering & selection.....	121
3.5.6	Linear fitting & data validation.....	124
3.6	Summary .....	127
4	Inland measurements: University of Leicester (UoL) .....	130
4.1	Site description & data overview.....	130
4.1.1	Site introduction .....	130
4.1.2	Location .....	130
4.1.3	Data overview .....	135
4.2	Diel patterns of measured species at UoL .....	144
4.3	Seasonal variability .....	146
4.3.1	Differences between winter campaigns .....	147
4.3.2	Seasonal variations .....	149
4.4	Daytime persistence of ClNO <sub>2</sub> .....	153
4.5	Radical production.....	156
4.6	Case studies .....	160
4.6.1	High ClNO <sub>2</sub> .....	161
4.6.2	Low ClNO <sub>2</sub> .....	163
4.6.3	Highest ClNO <sub>2</sub> observation at UoL.....	164
4.6.4	Change in air mass during single night .....	166
4.7	Air mass origins .....	167
4.8	Model comparison: observations vs. GEOS-Chem model .....	171
4.9	Detection of Cl <sub>2</sub> at UoL .....	175
4.10	Summary.....	177

5	Coastal measurements: Penlee Point and Weybourne Atmospheric Observatories (PPAO & WAO) .....	180
5.1	Site descriptions & data overview.....	180
5.1.1	Penlee Point Atmospheric Observatory.....	181
5.1.2	Weybourne Atmospheric Observatory .....	184
5.1.3	Data overview .....	187
5.2	Site comparisons: locations & seasons.....	195
5.3	Radical production.....	199
5.4	Case studies .....	203
5.4.1	PPAO: Low ClNO <sub>2</sub> .....	203
5.4.2	PPAO: High ClNO <sub>2</sub> .....	204
5.4.3	WAO: Low ClNO <sub>2</sub> .....	207
5.4.4	WAO: High ClNO <sub>2</sub> .....	209
5.5	Air mass origins .....	211
5.6	Emission plumes .....	214
5.6.1	PPAO .....	214
5.6.2	WAO.....	216
5.7	Limiting factors for ClNO <sub>2</sub> formation .....	218
5.7.1	Aerosol data and aerosol chloride availability.....	218
5.7.2	Gas phase precursors.....	220
5.8	Model comparison: observations vs. GEOS-Chem model .....	223
5.9	NO <sub>2</sub> measurements and intercomparison.....	230
5.10	Summary.....	236
6	Conclusions.....	240
6.1	Overview .....	240
6.2	CIMS calibration.....	240
6.3	Seasonal & geographical variability of ClNO <sub>2</sub> .....	241

6.4	Radical production <i>via</i> ClNO <sub>2</sub> photolysis.....	242
6.5	Daytime persistence of ClNO <sub>2</sub> .....	243
6.6	Conditions leading to ClNO <sub>2</sub> formation .....	244
6.7	Factors limiting ClNO <sub>2</sub> production.....	245
6.8	Observations vs. model .....	246
6.9	Future directions .....	247
	Publications .....	250
	Bibliography .....	251

## List of tables

Table 1.1 Selected atmospheric gases and sources thereof. Table reprinted from Holloway and Wayne, 2010.....	23
Table 1.2 List of ClNO <sub>2</sub> field observations including location, time of year, maximum observed concentration and published reference (by date of observation). .....	36
Table 2.1 Selected list of species detected <i>via</i> CIMS, with reagent ions used.	49
Table 3.1 Summary of principal masses investigated <i>via</i> CIMS during this thesis. ....	77
Table 3.2 Selected list of ions & clusters monitored in using the CIMS H-mode. Masses are quoted in atomic mass units (amu).....	83
Table 3.3 A comparison of the original and adjusted voltages to developed in the experiments to adjust CIMS settings (quadrupole voltages omitted). ....	86
Table 3.4 Sensitivity, precision and average flow tube pressure (FTP) for individual CIMS calibration experiments for ClNO <sub>2</sub> (top) and Cl <sub>2</sub> (bottom). .	125
Table 3.5 Table summarising campaign dates and average flow tube pressures, with corresponding calibration factors (CF) in addition to the accuracy and precision thereof. ....	126
Table 3.6 Literature values for sensitivity, accuracy, precision and LoD for literature ClNO <sub>2</sub> measurements, where reported.....	127
Table 4.1 Table summarising UoL campaigns with dates and average, maximum and interquartile ranges (IQR) for ClNO <sub>2</sub> , NO, NO <sub>2</sub> and O <sub>3</sub> (15 min averaged night-time data, 23:00 to 04:59). Aerosol chloride and nitrate (from 24-hour PM <sub>10</sub> filters) are also given for campaigns where these were measured.....	136
Table 5.1 Table summarising WAO and PPAO campaigns with comparison to UoL campaigns at similar time of year giving average, maximum and interquartile ranges (IQR) for ClNO <sub>2</sub> , NO, NO <sub>2</sub> and O <sub>3</sub> (15 min averaged night-time data, 23:00 to 04:59) in addition to aerosol chloride and nitrate (from 24-hour PM <sub>10</sub> filters (UoL) or multistage high-volume impactor (WAO)). ....	188

## List of figures

Figure 1.1 Regions of the atmosphere, defined by temperature and pressure. Figure reprinted from Finlayson-Pitts and Pitts Jr, 2000. ....	20
Figure 1.2 Simplified schematic of OH chemistry in a polluted atmosphere. .	25
Figure 1.3 Simplified schematic for nitrate radical chemistry, including ClNO <sub>2</sub> formation and photolysis. ....	29
Figure 1.4 Simplified schematic depicting atmospheric chemistry of a halogen, X (ClNO <sub>2</sub> chemistry omitted). Figure reprinted from Simpson et al., 2007. ...	31
Figure 2.1 Diagram of a quadrupole, including equation describing applied electrical potentials, where $\Phi$ = net applied electrical potential; $U$ = DC component at time $t$ ; $V$ = RF component maximum amplitude; $\nu$ = oscillation frequency. Figure reprinted from Ellis and Mayhew, 2014. ....	46
Figure 2.2 Schematic representation of the UoL-CIMS. Figure adapted from Liao et al., 2011. ....	50
Figure 2.3 Increased effective path length <i>via</i> cavity enhancement. Mirrors are aligned so that light travels exactly the same path in both directions with small amounts “leaking” through the mirrors. Figure adapted from Platt and Stutz, 2008. ....	54
Figure 2.4 Hypothetical example of DOAS principle. Figure reprinted from Ball and Jones, 2003. Descriptions of each panel are given in the text. ....	57
Figure 2.5 Schematic diagram of UoL RONOCO BBCEAS operating in red wavelengths. Figure reprinted from Daniels, 2012. ....	60
Figure 2.6 Example wavelength calibration curve for the HR2000 spectrometer used in BBCEAS instruments at blue wavelengths. ....	63
Figure 2.7 Example wavelength dependent reflectivity of cavity mirrors using field cavity data from the Weybourne Atmospheric Observatory field campaign. ....	66

Figure 2.8 Example measured and fitted NO <sub>2</sub> absorption spectra of NO <sub>2</sub> sample (top) and N <sub>2</sub> flush (bottom) measurements during a CIMS ClNO <sub>2</sub> calibration. .	69
Figure 2.9 Correlation between University of Leicester BBCEAS fitted H <sub>2</sub> O and University of Leeds humidity measurements (as mixing ratios, %vol) to calculate length factor correction. ....	71
Figure 3.1 Diagram of electroplating experimental setup (mass flow controllers not shown). ....	80
Figure 3.2 CIMS mass spectrum (average of 7 scans over 5 min) taken during the electroplating experiment showing three isotopologues of [I(Cl <sub>2</sub> )] <sup>-</sup> at 197, 199 and 201 amu. ....	81
Figure 3.3 CIMS mass spectrum (dry N <sub>2</sub> background spectrum subtracted) taken during the bromine detection experiment showing three isotopologues of [I(Br <sub>2</sub> )] <sup>-</sup> at 285, 287 and 289 amu. ....	82
Figure 3.4 Mass calibration displaying offset in mass observed by the CIMS and the equation later used to correct for this. $m =$ corrected mass; $n =$ observed mass. ....	84
Figure 3.5 Mass spectra demonstrating the effect of changes to CIMS peaks before and after adjustments to CDC voltages (note different scale on vertical axes). ....	87
Figure 3.6 Graph showing changes observed in [I(ClNO <sub>2</sub> )] <sup>-</sup> peaks at 208 and 210 amu when varying quadrupole voltages. ....	88
Figure 3.7 Picture of the calibration system in field-portable box. ....	90
Figure 3.8 Example mass flow controller calibration. The x-axis displays the voltage set on the instrument, the y-axis shows the corresponding rate measured by the flow meter. ....	92
Figure 3.9 Subtracted (cylinder - generator) 3-spectrum averages for comparison of background signals. Large peaks due to I <sup>-</sup> and [I(H <sub>2</sub> O)] <sup>-</sup> (127 and 145 amu) are omitted for clarity. ....	94

Figure 3.10 Experimental equipment for  $\text{N}_2\text{O}_5$  synthesis; (a) reaction schematic and (b) representations of the reaction chamber, left, and trap, right. Figure reprinted from Daniels, 2012. ....96

Figure 3.11 CIMS spectra with a dry nitrogen background spectrum subtracted. Elements of CIMS calibration experiments were added incrementally (in left to right order indicated on the legend) to test for interferences. ....99

Figure 3.12 Reactor designs for CIMS  $\text{ClNO}_2$  calibration in chronological order (not to scale). .... 101

Figure 3.13 Results of an experiment testing the effect of humidity upon CIMS  $\text{ClNO}_2$  sensitivity.  $\text{NO}_3$  and  $\text{H}_2\text{O}$  were measured *via* BBCEAS (data workup courtesy of Dr. T. J. Adams);  $\text{ClNO}_2$  is represented by  $[\text{I}(\text{ClNO}_2)]^-$  raw counts per second measured *via* CIMS at 207.97 amu..... 104

Figure 3.14 Time series from an experiment testing background coil effectiveness and optimal temperatures (principal calibration ions only - see section 3.5.1). .... 106

Figure 3.15 Excerpt of a time series using data from a  $\text{ClNO}_2$  calibration. The sharp rise and fall of CIMS  $\text{Cl}_2$  (197 amu) and  $\text{ClNO}_2$  (208 amu) detected exhibits fast response to changes in concentration..... 107

Figure 3.16 General experimental setup for experiments using measuring  $\text{ClNO}_2$  generated *via* R 3.1. .... 109

Figure 3.17 Schematic for the “series 1”  $\text{ClNO}_2$  calibrations. Arrows denote flow direction determined by cylinder pressure or pump draw. MFC5 was later removed and the other  $\text{N}_2$  dilutions increased to compensate. .... 112

Figure 3.18 Schematic for series 2  $\text{ClNO}_2$  calibrations. Arrows denote flow direction determined by cylinder/generator pressure or pump draw. .... 114

Figure 3.19 Excerpt of a calibration experiment time series, showing how time periods were selected for averaging. CIMS signals are normalised to  $[\text{I}(\text{H}_2\text{O})]^-$  and multiplied by  $10^6$  for ease of interpretation. .... 117

Figure 3.20 Example ClNO <sub>2</sub> calibration plot, including uncertainties as error bars (see section 3.5.4). Linear fit gradients correspond to CIMS sensitivity for a given ion. ....	119
Figure 3.21 Example isotopic and channel ratio plots from a ClNO <sub>2</sub> calibration experiment. ....	122
Figure 3.22 Time series showing how [I( <sup>35</sup> ClNO <sub>2</sub> )] <sup>-</sup> sensitivities were grouped to calibrate field data. Blue lines show each campaign's date and duration (x axis) and the calibration factor applied (y axis). Data points are coloured according to the average CIMS flow tube pressure (FTP) as shown in the legend. ....	123
Figure 4.1 Maps & satellite images.....	132
Figure 4.2 Satellite image showing location for AURN station measurements (Google Earth, 2017b) with some nearby potential influences shown. ....	134
Figure 4.3 Satellite image showing location for RAFT laboratory measurements (Google Earth, 2017b), showing enclosed area around inlet (heights estimated above ground level). ....	135
Figure 4.4 Complete time series for AURN 1 campaign (August 2014) showing concentrations of ClNO <sub>2</sub> , NO, NO <sub>2</sub> and O <sub>3</sub> (15 min averaged data).....	139
Figure 4.5 Complete time series for AURN 2 campaign (February 2016) showing concentrations of ClNO <sub>2</sub> , NO, NO <sub>2</sub> and O <sub>3</sub> (15 min averaged data).....	140
Figure 4.6 Complete time series for RAFT 1 campaign (March 2014) showing concentrations of ClNO <sub>2</sub> , NO, NO <sub>2</sub> and O <sub>3</sub> (15 min averaged data).....	141
Figure 4.7 Complete time series for RAFT 2 campaign (December 2014) showing concentrations of ClNO <sub>2</sub> , NO, NO <sub>2</sub> and O <sub>3</sub> (15 min averaged data).....	142
Figure 4.8 Complete time series for RAFT 3 campaign (September 2015) showing concentrations of ClNO <sub>2</sub> , NO, NO <sub>2</sub> and O <sub>3</sub> (15 min averaged data).....	142
Figure 4.9 Plots relating to wind conditions for all UoL campaigns (15 min averaged data). ....	143
Figure 4.10 Diel pattern of ClNO <sub>2</sub> during RAFT 2 campaign (15 min averaged data).....	145

Figure 4.11 Average diel NO, NO <sub>2</sub> and O <sub>3</sub> concentrations for RAFT 2 campaign (15 min averaged data; mean and 95% confidence intervals).....	146
Figure 4.12 Winter diel profiles of ClNO <sub>2</sub> (top), temperature (middle), NO, NO <sub>2</sub> and O <sub>3</sub> (bottom) for RAFT 2 and AURN 2 campaigns (15 min averaged data; mean and 95% confidence intervals). ....	148
Figure 4.13 Average seasonal profiles for ClNO <sub>2</sub> (top), NO, NO <sub>2</sub> and O <sub>3</sub> (bottom) for all UoL campaigns (15 min averaged data; mean and 95% confidence intervals).....	150
Figure 4.14 Time series of AURN 2 campaign showing ClNO <sub>2</sub> concentration and photolysis rate in addition to temperature (15 min averaged data; full scale (top) and low concentrations magnified (bottom)).....	154
Figure 4.15 Diel profiles of ClNO <sub>2</sub> concentration (top) and, when available, photolysis rate (s <sup>-1</sup> ; bottom) for each UoL campaign (15 min averaged data; mean and 95% confidence intervals).....	155
Figure 4.16 Time series showing comparative production rates of Cl and OH during the AURN 2 campaign in February 2016 (15 min averaged data).....	158
Figure 4.17 Time series showing comparative production rates of Cl and OH during the AURN 1 campaign in August 2014 (15 min averaged data). ....	160
Figure 4.18 Time series of AURN 2 campaign showing concentrations of ClNO <sub>2</sub> , NO, NO <sub>2</sub> and O <sub>3</sub> (top; 15 min averaged data) and NAME particle dispersion footprints at 03:00 (bottom; 5-day back), demonstrating a high-ClNO <sub>2</sub> case over 2 consecutive nights (11-12 (left) and 12-13 (right) February 2016).....	162
Figure 4.19 Time series of AURN 2 campaign showing concentrations of ClNO <sub>2</sub> , NO, NO <sub>2</sub> and O <sub>3</sub> (top; 15 min averaged data) and NAME particle dispersion footprints at 03:00 (bottom; 5-day back), demonstrating a low-ClNO <sub>2</sub> case over 2 consecutive nights (19-20 (left) and 20-21 (right) February 2016).....	163
Figure 4.20 Time series of AURN 2 campaign showing ClNO <sub>2</sub> concentration and photolysis rate during highest ClNO <sub>2</sub> observation at UoL (top; 15 min averaged data) and NAME footprint (bottom; 5-day back) in the morning of 16 February 2016. ....	164

Figure 4.21 Time series of RAFT 2 campaign showing wind speed and direction and ClNO <sub>2</sub> concentration and photolysis rate, in addition to NO, NO <sub>2</sub> and O <sub>3</sub> (top; 15 min averaged data) and NAME footprints for 18:00 (top left), 21:00 (top right), 00:00 (bottom left) and 03:00 (bottom right) on the night of 16-17 Dec 2014 (bottom; 5-day back). .....	166
Figure 4.22 Map of air mass origin divisions for UoL campaigns (Fleming, 2017). Also used in similar analysis for Penlee Point campaign (see section 5.5) ...	168
Figure 4.23 A correlation plot for the 8 days of the RAFT 2 campaign showing ClNO <sub>2</sub> concentration at 00:00 and 03:00 against percentage of air mass originating from local inland and Scandinavian sources (top; 3-hour averaged data), NAME particle dispersion footprints corresponding to the highest 4 points in the correlation plot (bottom; 5-day back). .....	170
Figure 4.24 A time series of this 12-14 Dec 2014 (RAFT 2) showing concentrations of ClNO <sub>2</sub> , NO, NO <sub>2</sub> and O <sub>3</sub> (15 min averaged data).....	171
Figure 4.25 Comparison of observed and modelled ClNO <sub>2</sub> (in ppt) average diel profiles during campaign periods for all UoL campaigns (60 min averaged data; mean and 95% confidence intervals; medium-resolution model).....	172
Figure 4.26 Time series comparing observed and modelled ClNO <sub>2</sub> concentrations for winter UoL campaigns (60 min averaged data; medium-resolution model). .....	173
Figure 4.27 Correlations between nightly (23:00-04:59) mean ClNO <sub>2</sub> with modelled accumulation mode sea salt (a) or modelled and observed NO <sub>2</sub> concentrations (b) for all UoL campaigns (60 min averaged data; medium-resolution model). .....	175
Figure 4.28 Time series of Cl <sub>2</sub> (and LoD), ClNO <sub>2</sub> , NO, NO <sub>2</sub> and O <sub>3</sub> during AURN 2 campaign (top; 15 min averaged data) and polar plots showing the wind conditions resulting in high detection of Cl <sub>2</sub> (bottom; 1 min averaged data; days defined as 00:00 to 23:59 UTC on the labelled date). .....	176
Figure 4.29 Time series of Cl <sub>2</sub> (and LoD), ClNO <sub>2</sub> , NO, NO <sub>2</sub> and O <sub>3</sub> during RAFT 2 campaign (15 min averaged data).....	177

Figure 5.1 Maps & satellite images.....	182
Figure 5.2 Housing for University of Leicester instruments during PPAO campaign.....	183
Figure 5.3 Maps & satellite images.....	185
Figure 5.4 Housing for University of Leicester instruments during WAO campaign.....	187
Figure 5.5 Complete time series for PPAO campaign (April-May 2015) showing concentrations of ClNO <sub>2</sub> , NO, NO <sub>2</sub> and O <sub>3</sub> (15 min averaged data). The off-scale ClNO <sub>2</sub> peak is shown separately (Figure 5.6). ....	190
Figure 5.6 Magnified section PPAO time series showing the large ClNO <sub>2</sub> peak, 922 ppt at 01:15 (15 min averaged data). ....	190
Figure 5.7 Complete time series for WAO campaign (July 2015) showing concentrations of ClNO <sub>2</sub> , NO, NO <sub>2</sub> and O <sub>3</sub> (15 min averaged data). Off-scale ClNO <sub>2</sub> peaks are shown separately (Figure 5.8). ....	192
Figure 5.8 Magnified sections of the WAO time series showing large ClNO <sub>2</sub> peaks (15 min averaged data; note the varying vertical axis scales). ....	193
Figure 5.9 Plots relating to wind conditions for PPAO and WAO campaigns, each paired with the closest seasonally-equivalent UoL campaign (15 min averaged data). ....	194
Figure 5.10 Average diel profiles of ClNO <sub>2</sub> , NO, NO <sub>2</sub> and O <sub>3</sub> at PPAO (left) and WAO (right) compared to UoL observations at equivalent time of year (15 min averaged data). ....	196
Figure 5.11 Satellite image of middle & southern UK with ClNO <sub>2</sub> pollution rose for each measurement location (Google Earth, 2017g). ....	198
Figure 5.12 Time series showing comparative production rates of Cl and OH during the WAO campaign in July 2015 (15 min averaged data).....	200
Figure 5.13 Time series showing comparative production rates of Cl and OH during the PPAO campaign in April/May 2015 (15 min averaged data). ....	202

Figure 5.14 Plots for low ClNO <sub>2</sub> night, 28-29 Apr 2015 during the PPAO campaign. Top: time series showing wind speed/direction, ClNO <sub>2</sub> photolysis rate and concentrations of ClNO <sub>2</sub> , NO, NO <sub>2</sub> , O <sub>3</sub> and SO <sub>2</sub> (15 min averaged data). Bottom: NAME particle dispersion footprint at 03:00 (5-day back). .....	204
Figure 5.15 Plots for PPAO campaign highest ClNO <sub>2</sub> night, 30 Apr-01 May 2015. ....	205
Figure 5.16 Plots for low ClNO <sub>2</sub> night, 24-25 July 2015 during the WAO campaign. Top: time series showing wind speed/direction, ClNO <sub>2</sub> photolysis rate and concentrations of ClNO <sub>2</sub> , NO, NO <sub>2</sub> , O <sub>3</sub> and SO <sub>2</sub> (15 min averaged data). Bottom: NAME particle dispersion footprint at 03:00 (5-day back). .....	208
Figure 5.17 Plots for WAO campaign highest ClNO <sub>2</sub> night, 10-11 Jul 2015. ..	210
Figure 5.18 Map of air mass origin divisions for WAO campaign (Fleming, 2017). PPAO used the divisions shown in Figure 4.22. ....	212
Figure 5.19 Correlation plots; top: PPAO campaign showing ClNO <sub>2</sub> and NO <sub>2</sub> concentrations against percentage of air mass originating from land-based sources; bottom: WAO campaign showing ClNO <sub>2</sub> concentration against percentage of air mass originating from local sources (3-hour averaged data, <10 ppt ClNO <sub>2</sub> filtered, 00:00-03:00 data only). ....	213
Figure 5.20 Time series for PPAO campaign showing concentrations of ClNO <sub>2</sub> , CO <sub>2</sub> , SO <sub>2</sub> and O <sub>3</sub> in addition to wind direction and speed (1 min averaged data). Note different vertical axis scales. ....	215
Figure 5.21 Time series for WAO campaign showing concentrations of ClNO <sub>2</sub> , SO <sub>2</sub> , CO <sub>2</sub> , NO <sub>2</sub> and O <sub>3</sub> in addition to wind direction and speed (2 min averaged data). ....	217
Figure 5.22 Particulate chloride and sodium data for UoL and WAO campaigns (24 hour averaged data; ClNO <sub>2</sub> data 00:00-04:00 GMT only). Figure reprinted from Sommariva et al., 2018. ....	219
Figure 5.23 Scatter plots showing concentrations of nitrogen dioxide against ozone (15 min averaged data, 23:00 to 04:59 only). Figures adapted from Sommariva et al., 2018. ....	221

Figure 5.24 Comparison of observed and modelled ClNO <sub>2</sub> average diel profiles during campaign periods for PPAO, WAO and seasonally equivalent UoL campaigns (60 min averaged data; mean and 95% confidence intervals; high-resolution model). .....	224
Figure 5.25 Time series comparing observed and modelled ClNO <sub>2</sub> concentrations for PPAO, WAO and seasonally equivalent UoL campaigns (60 min averaged data; high-resolution model). .....	226
Figure 5.26 Correlations of nightly (23:00-04:59) mean ClNO <sub>2</sub> concentrations with observed and high-resolution modelled accumulation mode sea salt aerosol and NO <sub>2</sub> . .....	228
Figure 5.27 Scatter plots showing a) observed and b) modelled concentrations of nitrogen dioxide against ozone (60 min averaged data, 23:00 to 04:59 only). .....	230
Figure 5.28 Complete time series of all NO <sub>2</sub> measurements for WAO campaign (15 min average data). .....	231
Figure 5.29 Correlations between NO <sub>2</sub> datasets at WAO.....	233
Figure 5.30 WAO NO <sub>2</sub> and ClNO <sub>2</sub> measurements for the night of 10-11 July.	235

# 1 Introduction

## 1.1 Atmospheric structure & composition

The chemistry of the atmosphere has significant effects with respect to climate and air quality, and is influenced by species present at trace concentrations. One such species is nitryl chloride ( $\text{ClNO}_2$ ), which is the focus of work presented in this thesis mostly owing to its indirect effects by increasing or decreasing levels of other species.  $\text{ClNO}_2$  was measured at ground level to assess its prevalence and influence on atmospheric composition in the UK.

The earth system can be described as a collection of sub-systems including the atmosphere, lithosphere, hydrosphere, cryosphere and biosphere - describing gas, geological, water, ice and life processes, respectively - with a complex set of interactions between them. The atmosphere is a layer of gas shrouding the planet, comprised of several regions known (in ascending order) as the troposphere, stratosphere, mesosphere and thermosphere. Nitrogen ( $\text{N}_2$ ) and oxygen ( $\text{O}_2$ ) dominate the bulk composition of the dry atmospheric composition (*i.e.* not including 0-4%  $\text{H}_2\text{O}$  (Holloway and Wayne, 2010)) at 78% and 21% respectively, with a further 0.93% represented by argon (Prinn, 2003). The remaining <0.1% of the dry atmosphere contains a wide variety of trace gases (*e.g.* nitrogen dioxide and ozone) typically present at only parts per million, billion or trillion by volume (ppmv, ppbv, pptv) mixing ratios but shaping a lot of interesting and important chemistry.

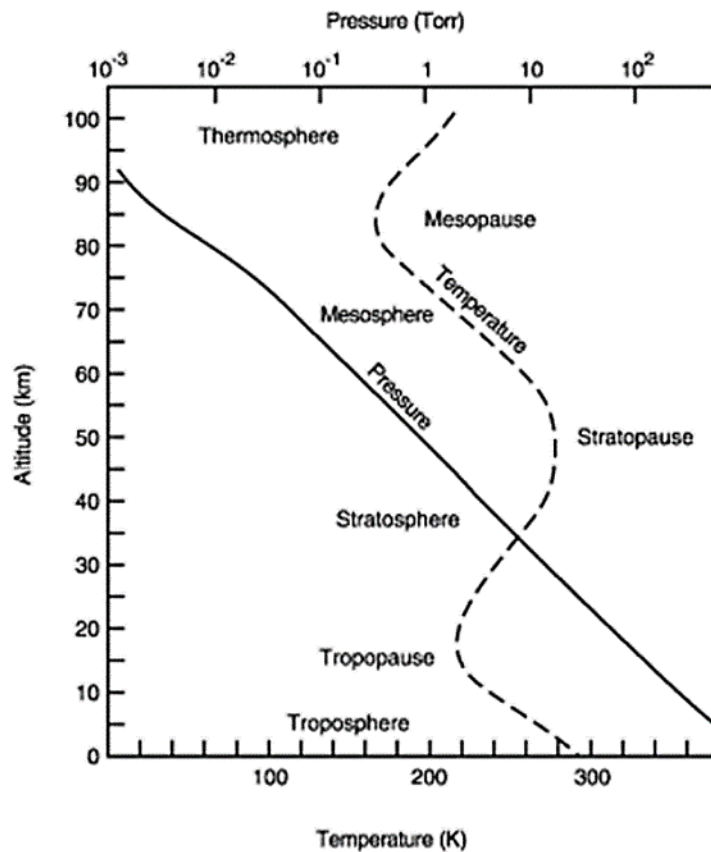


Figure 1.1 Regions of the atmosphere, defined by temperature and pressure. Figure reprinted from Finlayson-Pitts and Pitts Jr, 2000.

The regions of the atmosphere can be defined by major changes in the temperature profile, as shown in Figure 1.1. In the lowest region, the troposphere, temperature decreases with altitude, lesser temperature inversions notwithstanding (Finlayson-Pitts and Pitts Jr, 2000). The troposphere is characterised by turbulent mixing caused by convection, as air is warmed at the surface (which itself is heated mainly by absorbed solar radiation) and then travels upwards until the tropopause which traps many reactive species within this well-mixed layer. The altitude of the tropopause varies with latitude, season and time (Finlayson-Pitts and Pitts Jr, 2000) but is approx. 10 to 15 km (Monks, 2007a) at the poles and equator respectively. The troposphere is sometimes divided further into two layers, the upper of which is often known as the free troposphere. The lower “boundary layer” is adjacent to, and therefore the most influenced by, surface-based sources and sinks of trace gases. The boundary layer is confined (to a much lesser degree than the

tropopause) by a “capping inversion” which is usually 1-2 km high, and generally lower over the sea due to comparatively reduced heating (and thus convection) of air compared to the land (Holloway and Wayne, 2010).

Above the tropopause is the stratosphere, so named because it is highly stratified with little vertical mixing taking place (Holloway and Wayne, 2010). In contrast with the troposphere, temperature in the stratosphere increases with altitude owing to release of excess energy absorbed as part of ozone chemistry. Stratospheric chemistry is dominated by the Chapman cycle (Chapman, 1930) and associated chemistry in which ozone is both produced and destroyed to maintain a steady state stratospheric concentration. The reactions therein are initiated by O<sub>2</sub> photolysis *via* absorption of short-wavelength (<290 nm, *i.e.* ultraviolet (UV)) solar radiation. The abundance of molecular oxygen in combination with this photolysis reaction allows the stratosphere to shield lower altitudes from high-energy solar radiation harmful to life. The stratosphere is separated from the mesosphere above by another major temperature inversion, the stratopause (~50 km).

The mesosphere is another turbulent region where temperature decreases with height, reaching a minimum at the mesopause (~90 km). The highest region is the thermosphere which again demonstrates increasing temperature with altitude due to the absorption of solar radiation by O<sub>2</sub> and N<sub>2</sub> causing dissociation (Monks, 2007a). Pressure and density diminish quasi-exponentially as altitude increases (Warneck and Williams, 2012). As a result 99% of atmospheric mass resides below 30 km altitude (Holloway and Wayne, 2010) in the troposphere and stratosphere, where the majority of atmospheric chemistry therefore takes place.

## 1.2 Tropospheric chemistry

One of the most important aspects when considering tropospheric chemistry is interaction with the surface, especially in the boundary layer, where direct contact occurs. Factors to consider include the turbulent mixing from wind and air currents, radiation of ground heat (from both geothermal sources and, more significantly, reflected or re-emitted solar radiation) and emissions from myriad

sources, natural or man-made. Emissions are often classified as primary (directly emitted) or secondary (formed *via* chemical reactions in the atmosphere following emission of precursor(s)). Another key concept is the relationship between source, transport, reservoir and sink processes whereby a given species is introduced to the atmosphere by source(s), travels and potentially reacts (transport), possibly being temporarily stored in another form (reservoir) and is eventually removed (sink). The surface can provide the sources or sinks for many chemical species.

Emissions come from a variety of sources including radioactive decay of  $^{40}\text{K}$  yielding argon (radiogenic source; Holloway and Wayne, 2010), plant emissions of biogenic (*i.e.* originating from life processes) volatile organic compounds (VOCs) and *e.g.* carbon monoxide from industrial combustion (anthropogenic, *i.e.* instigated by human activity). Table 1.1 shows a selection of gases commonly found in the atmosphere with some natural and anthropogenic sources. Note that part or all of certain ostensibly natural (typically biogenic) emissions are classified as anthropogenic, *e.g.* methane from enteric fermentation in ruminant livestock (Holloway and Wayne, 2010), as populations (and, therefore, emissions) thereof are significantly above levels that would occur without human intervention.

Table 1.1 Selected atmospheric gases and sources thereof. Table reprinted from Holloway and Wayne, 2010.

<i>Compound</i>	<i>Natural sources</i>	<i>Man-related sources</i>
<i>Major Atmospheric Gases</i>		
Nitrogen	Present in prebiological atmosphere Microbiological	
Oxygen	Photosynthesis	
Argon	Mainly radiogenic	
Carbon dioxide	Present in prebiological atmosphere Oxidation of natural CO; destruction of forests; respiration by plants	Combustion of oil, gas, coal, and wood; limestone burning
Water	Present in prebiological atmosphere Evaporation, especially from oceans	
<i>Other relatively abundant gases not classified elsewhere</i>		
Neon	Present in prebiological atmosphere	
Helium	Mainly radiogenic	
Hydrogen	Oceans; soils; oxidation of methane, isoprene, and terpenes <i>via</i> formaldehyde	Motor-vehicle exhaust; oxidation of methane <i>via</i> formaldehyde
Ozone	Stratosphere; natural NO/NO <sub>2</sub> conversion	Man-induced NO/NO <sub>2</sub> conversion
<i>Carbon-containing gases</i>		
Methane	Enteric fermentation in wild animals; emissions from swamps, bogs, <i>etc.</i> ; natural wetland areas; oceans	Enteric fermentation in domesticated ruminants; emissions from paddies; natural-gas leakage; sewerage gas; colliery gas; combustion sources
Carbon monoxide	Oxidation of natural methane, natural C <sub>5</sub> , C <sub>10</sub> hydrocarbons; oceans; forest fires	Oxidation of Man-related hydrocarbons; incomplete combustion of wood, oil, gas, and coal, especially in motor vehicles; industrial processes; blast furnaces
Light alkanes, C <sub>2</sub> -C <sub>6</sub>	Aerobic biological source	Natural-gas leakage; motor vehicle evaporative emissions; refinery emissions
Alkenes, C <sub>2</sub> -C <sub>6</sub>		Motor-vehicle exhaust; diesel-engine exhaust
Aromatic hydrocarbons		Motor-vehicle exhaust; evaporative emissions; paints; petrol; solvents
Semiterpenes, C <sub>5</sub> H <sub>8</sub> Terpenes, C <sub>10</sub> H <sub>16</sub> Diterpenes, C <sub>20</sub> H <sub>32</sub>	Trees: broadleaves, and conifers; other plants	
<i>Nitrogen-containing gases</i>		
Nitric oxide, NO	Forest fires; anaerobic processes in soil; electric storms	High-temperature combustion (oil, gas, coal)
Nitrogen dioxide, NO <sub>2</sub>	Forest fires; electric storms	High-temperature combustion (oil, gas, coal); atmospheric transformation of NO
Nitrous oxide, N <sub>2</sub> O	Emissions from denitrifying bacteria in soil; oceans	Combustion of oil and coal
Peroxyacetyl nitrate, PAN	Degradation of isoprene	Degradation of hydrocarbons

Actinic radiation is the term given to solar radiation that initiates photochemistry. Tropospheric chemistry is dominated by oxidation processes, many of which are initiated and/or propagated *via* photolysis from actinic radiation. Oxidation is in turn the core mechanism that initiates and propagates the removal from the atmosphere of most species, notably including myriad undesirable “pollutants” which affect climate or air quality (including many of those in Table 1.1). The fairly nebulous term “oxidising capacity” refers to the rate at which the troposphere is able to remove trace species *via* oxidation, thus “cleansing” the atmosphere (Prinn, 2014). A notable class of pollutants are

VOCs, hydrocarbons whose oxidation ultimately leads to removal as CO<sub>2</sub> and water vapour (Monks, 2007a).

Three key species are responsible for the majority of tropospheric oxidation reactions: hydroxyl radicals (OH), nitrate radicals (NO<sub>3</sub>) and ozone molecules (O<sub>3</sub>). Note that ozone's chemistry (and, therefore, role) in the troposphere described in section 1.2.1 below is different than in the stratosphere (see section 1.1), as the short wavelengths required for the Chapman cycle are unavailable in the troposphere whereas a broader variety of other species with which ozone is highly reactive are abundant.

### 1.2.1 Oxidation chemistry by day

Of the three main tropospheric oxidants, OH is the most important during daylight hours. Hydroxyl radical activity is generally restricted to daylight hours as most formation is photolytically-initiated, and OH also reacts very rapidly resulting in a very short average lifetime rarely exceeding 1 second (Prinn, 2014), however it is also rapidly regenerated *via* hydroperoxy radical (HO<sub>2</sub>) reactions. Even during peak production OH concentrations at any given time are quite low in absolute terms (with estimated global average concentrations typically in the order of 10<sup>-14</sup> mixing ratio, as of the early 2000s (Prinn, 2014)) leading to rapid depletion when solar radiation becomes insufficient to support its formation. In practical terms these concentrations are actually quite high for such a reactive species, as the OH precursors O<sub>3</sub>, H<sub>2</sub>O and sunlight are abundant and ubiquitous in the troposphere therefore OH is similarly ubiquitous (Monks, 2007a) and represents the principal tropospheric oxidant.

Figure 1.2 shows a summary of OH chemistry with two of the foremost means of OH formation. The first of these is ozone photolysis by solar radiation (wavelength <340 nm) yielding an excited oxygen atom O(<sup>1</sup>D) (R 1.1). Most of these oxygen atoms are quenched and eventually re-form ozone, however approx. 10% (Monks, 2007a) subsequently react with water vapour to yield OH radicals (R 1.2). Photolysis of nitrous acid (HONO; formed from reaction of NO<sub>2</sub> with H<sub>2</sub>O on surfaces (Young et al., 2012)) is a significant source of OH, especially earlier in the day where it may even become dominant (Lee et al.,

2016) due to accumulation overnight and lower required photolysis energy, typically in polluted environments where HONO is more abundant. Other modes of OH formation also exist, such as formaldehyde or acetone photolysis and reaction of  $O(^1D)$  with methane and reactions of  $O_3$  with alkenes (Alicke et al., 2003, Monks, 2007a).

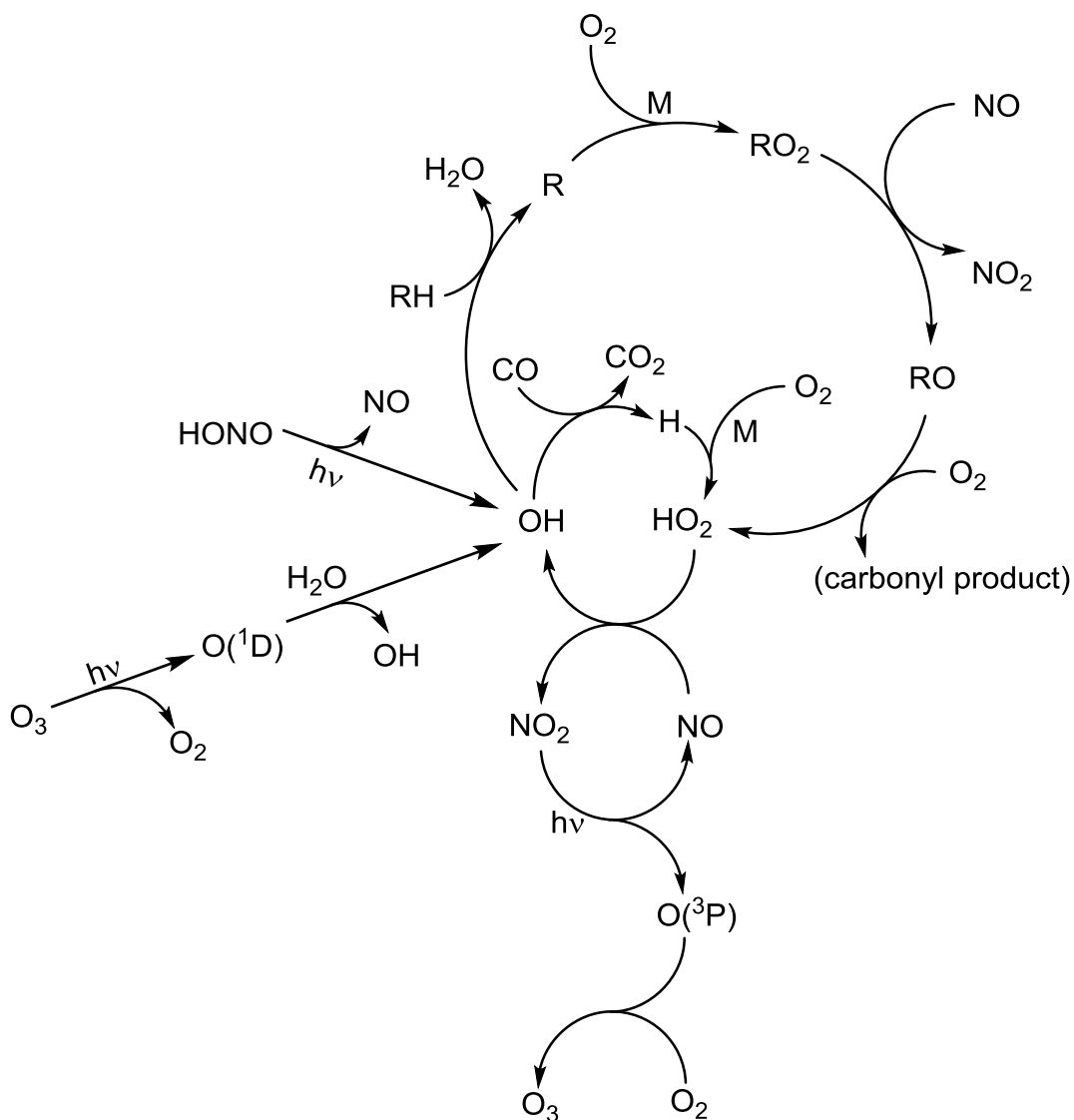


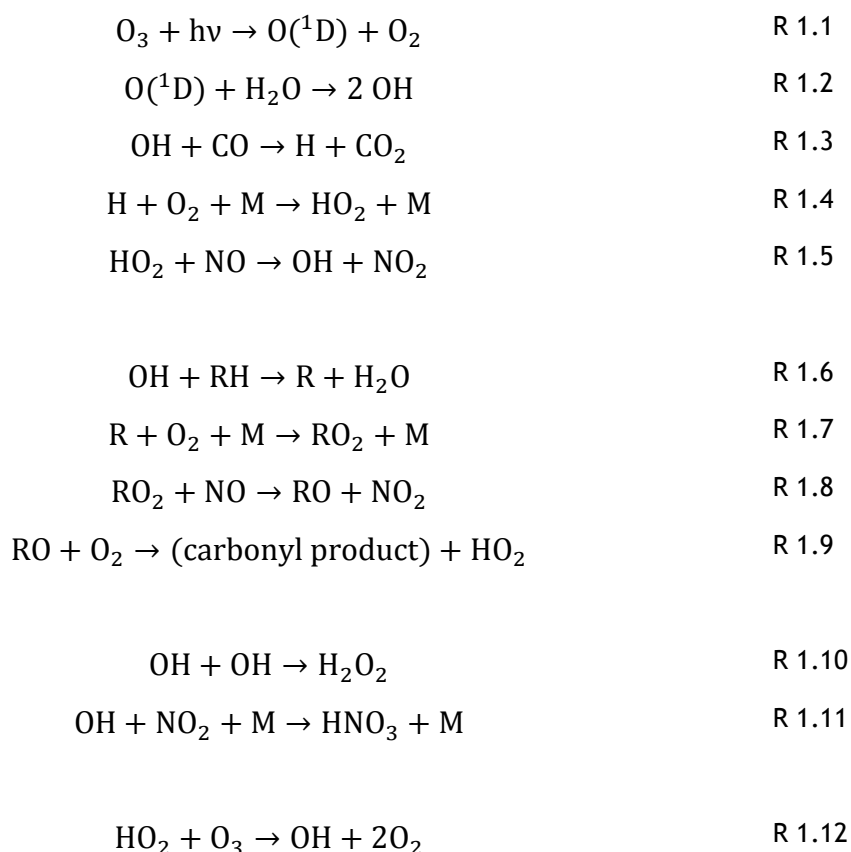
Figure 1.2 Simplified schematic of OH chemistry in a polluted atmosphere.

OH radicals are reactive with a wide range of atmospheric gases. Such reactions usually form a cycle to ultimately regenerate OH. The simplest subsequent reaction with carbon monoxide (CO) to form  $HO_2$  (R 1.3 and R 1.4) is shown in

Figure 1.2. For most examples OH reacts with RH (where R is a generic hydrocarbon), forming peroxy radicals (RO<sub>2</sub>) which re-enter the cycle as HO<sub>2</sub> after several extra steps as demonstrated in R 1.6 to R 1.9. In these reactions, M represents a third body that stabilises the association complex (Monks, 2005).

Significant concentrations of nitric oxide and nitrogen dioxide (NO and NO<sub>2</sub>; collectively “NO<sub>x</sub>”) are present in polluted air. R 1.5 shows HO<sub>2</sub> oxidising NO to regenerate OH.

Alternatively the OH/HO<sub>2</sub> (HO<sub>x</sub>) cycle can be terminated *via* radical recombination to form peroxides (R 1.10) or reaction of OH with NO<sub>2</sub> forming nitric acid (HNO<sub>3</sub>; R 1.11) which can be deposited to the surface.



Nitrogen oxides are overwhelmingly emitted by human activity (Finlayson-Pitts and Pitts Jr, 2000) chiefly *via* high-temperature combustion reactions, *e.g.* traffic fumes or power generation. A few natural processes have contributions,

however. Examples of both natural and anthropogenic NO<sub>x</sub> emissions are shown in Table 1.1.

Primary NO<sub>x</sub> emissions tend to be NO with a small fraction of NO<sub>2</sub>, however during the day these two rapidly interconvert *via* R 1.13 to R 1.15 (Jenkin and Clemitshaw, 2000), a null cycle with no net change in NO, NO<sub>2</sub> or O<sub>3</sub>. Neglecting sources and sinks, this swift interconversion represents an equilibrium often termed the photochemical steady state of NO<sub>x</sub>.



Approximately 10% of ozone exists in the troposphere, with the balance mostly in the stratosphere (Monks, 2007a). In the stratosphere, ozone has an important role protecting the biosphere from short-wavelength ultraviolet radiation, however ozone is also highly toxic to both plants and animals and is therefore viewed as a pollutant in the troposphere. Of particular interest are the adverse effects ozone has on crop yields (Krupa et al., 1998) and human health up to and including premature mortality (Halonen et al., 2010), in addition to being a greenhouse gas and a constituent of photochemical smog (Monks et al., 2015). Ozone furthermore has roles in the initiation of other oxidising species and is a major (albeit not dominant) tropospheric oxidant in its own right, and is sufficiently ubiquitous and abundant to be active throughout day and night in most locations.

The Chapman cycle is not active in this region, however some tropospheric ozone is sourced in part through (slow) exchange with the stratosphere (Finlayson-Pitts and Pitts Jr, 2000). Far more significant are R 1.14 and R 1.15 shown at the bottom of Figure 1.2, linking the chemistry of NO<sub>x</sub> and HO<sub>x</sub> leading to net ozone production and representing the main O<sub>3</sub> tropospheric formation pathway (Monks et al., 2015). The figure shows one molecule of ozone being consumed at the initiation stage (top left), however the cycling section

catalytically produces ozone at a rate of one molecule per rotation, *i.e.* net production whenever NO<sub>x</sub> is present. Note that in a clean atmosphere (*i.e.* low NO<sub>x</sub>, such as remote rural areas) the HO<sub>x</sub> cycle has the opposite effect, catalytically destroying ozone as R 1.12 replaces R 1.5. The “compensation point” is a threshold concentration of NO<sub>x</sub> below which destruction is dominant, whereas above it production is dominant - this threshold varies depending on certain conditions, but is typically in the order of 100 pptv (Monks, 2007b).

### 1.2.2 Oxidation chemistry by night

At night, HO<sub>x</sub> chemistry is minimal as OH production *via* photolysis ceases and existing OH is quickly depleted. The absence of solar radiation opens up the path to a different oxidising species in the form of the nitrate radical.



The nitrate radical is formed by the relatively slow oxidation of NO<sub>2</sub> as per R 1.16, which can in principle happen during daylight hours, however NO<sub>3</sub> is not stable at these times as formation is overwhelmed by rapid destruction processes. These daytime NO<sub>3</sub> sinks are photolysis (R 1.17 and R 1.18) or reaction with NO (R 1.19) which is also more abundant during the day - firstly because anthropogenic NO sources are also more active during these times, and secondly because without R 1.14 the NO/NO<sub>2</sub> balance at night is shifted to the latter. NO<sub>x</sub> interconversion and NO<sub>3</sub> formation are shown in the summary of nitrogen oxide and nitryl chloride chemistry represented in Figure 1.3. Note that without photolysis, the reactions shown will result in the steady consumption of ozone during the night resulting in a diel cycle for O<sub>3</sub>, rising during the day and falling at night.

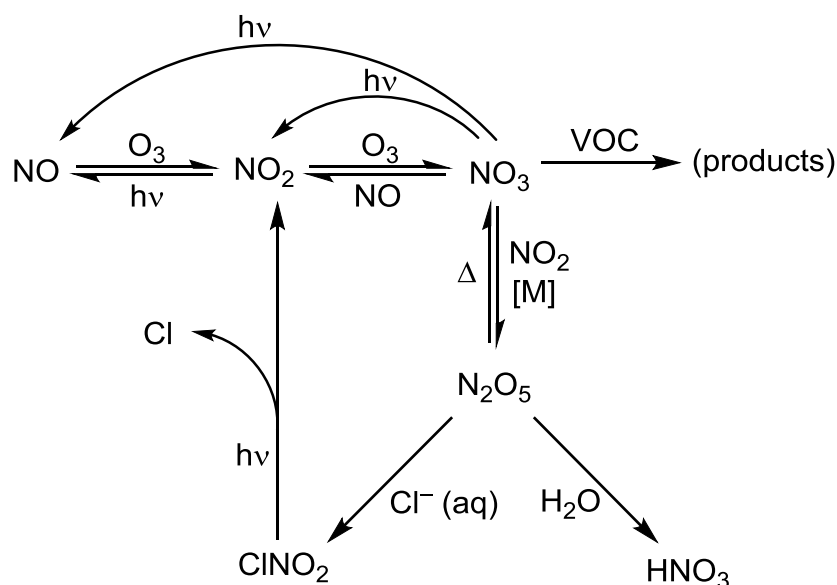


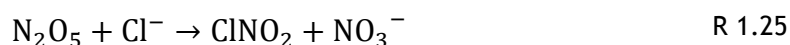
Figure 1.3 Simplified schematic for nitrate radical chemistry, including ClNO<sub>2</sub> formation and photolysis.

NO<sub>3</sub> also reacts with a wide range of species. Reactivity of NO<sub>3</sub> overlaps significantly with OH but is not identical. Oxidation reactions *via* NO<sub>3</sub> are generally slower (especially with respect to alkanes) compared to OH, however NO<sub>3</sub> is still one of the principal tropospheric oxidants as it tends to exist in much higher concentrations. The reaction of alkanes with the nitrate radical follows a similar pathway as reaction with OH (after several steps yielding HO<sub>2</sub> or RO<sub>2</sub>) with a different initial step, R 1.20, producing HNO<sub>3</sub> as a side product (rather than H<sub>2</sub>O as per R 1.6). NO<sub>3</sub> is, however, more reactive with the multiple bonds of unsaturated species such as alkenes, the initial step of which is shown in R 1.21 using the example of propene.



Alternatively, a reversible reaction between NO<sub>3</sub> and NO<sub>2</sub> produces dinitrogen pentoxide (N<sub>2</sub>O<sub>5</sub>), establishing a temperature-dependent equilibrium (R 1.22

and R 1.23).  $\text{N}_2\text{O}_5$  that has been taken up onto aerosol particles can furthermore react with water to produce  $\text{HNO}_3$  (R 1.24) which is easily deposited to the surface, acting as a sink for  $\text{NO}_y$  (total reactive nitrogen;  $\text{NO}_x$  and oxidation products thereof, e.g.  $\text{NO}_3$ ,  $\text{N}_2\text{O}_5$ ). Chloride-containing aerosols alternatively, and of particular interest in this thesis, allow the production of nitryl chloride (R 1.25), further discussion of which follows in section 1.2.4.



### 1.2.3 Tropospheric halogen chemistry

Halogens are known for efficient ozone depletion in the stratosphere (Solomon, 1999), however such reactions lose prominence in the troposphere owing to the presence of a greatly increased variety and abundance of other species. The atomic chlorine (Cl) radical is a minor oxidant compared to OH,  $\text{NO}_3$  and  $\text{O}_3$  as its abundance and sources are much smaller, however it is extremely reactive and could have significant impacts upon tropospheric chemistry. Atomic chlorine is therefore another tropospheric oxidant of note for this thesis.

Sources of reactive chlorine tend to be common with other halogens, typically originating from particulate halide salt precursors lifted into the air by wind action upon oceans (*i.e.* sea spray), though saline lakes and salt flats can contribute in a similar fashion (Simpson et al., 2015). Most atmospheric halogen sources are therefore natural (Monks et al., 2009) however some anthropogenic sources are known, such as hydrochloric acid (HCl) emission due to coal combustion (Evans et al., 2011), which may be significant especially for inland urban/industrial areas.

Halide salts ( $\text{X}^-$ ) such as those found in sea spray are “bound” within aerosol particles (von Glasow, 2008), severely limiting their influence on atmospheric

chemistry unless “activated” to a reactive form. In the case of chlorine, several main pathways of activation exist: firstly acid displacement, where HCl is released following exchange with other acids within particles; secondly reactions within particles can result in the release of photolabile halogen compounds such as  $\text{Cl}_2$  or  $\text{BrCl}$ ; thirdly reactions on particle surfaces causing the release of compounds such as  $\text{ClNO}_2$  (von Glasow, 2008). This third pathway has become the subject of increasing study as a pollution-induced halogen activation mechanism, for which  $\text{ClNO}_2$  is likely more prevalent than other nitryl halides ( $\text{XNO}_2$ ) due to lower solubility and reactivity (Simpson et al., 2015).

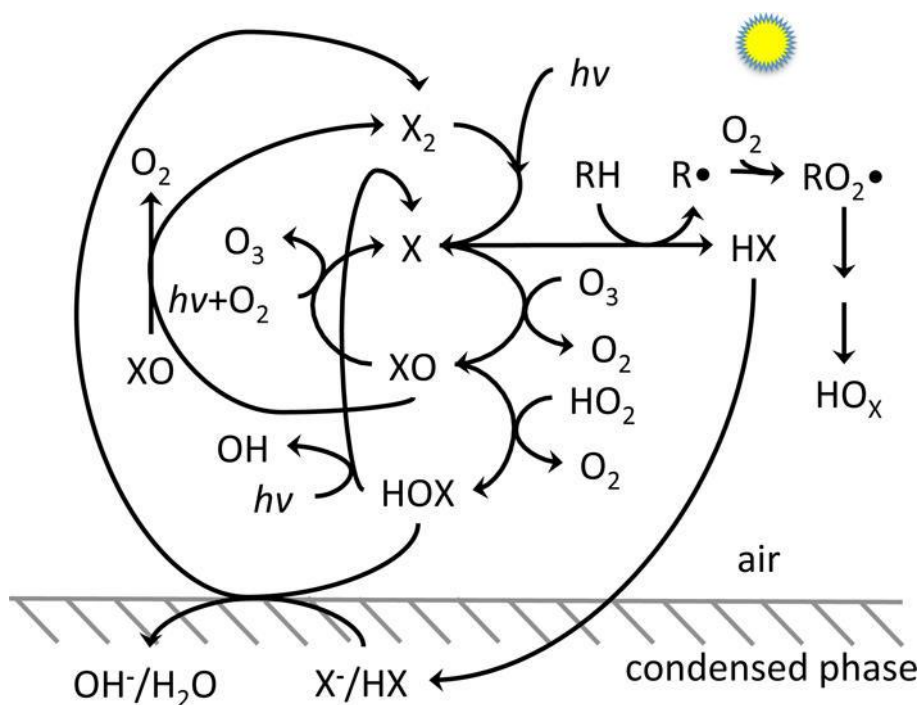


Figure 1.4 Simplified schematic depicting atmospheric chemistry of a halogen, X ( $\text{ClNO}_2$  chemistry omitted). Figure reprinted from Simpson et al., 2007.

Figure 1.4 shows a summary of tropospheric halogen (Cl, Br, I) chemistry, a notable feature of which is the catalytic destruction of ozone beginning with R 1.26 to give the halogen monoxide XO.

The first ozone destruction cycle (R 1.26, R 1.27, R 1.28) proceeds *via* self- or cross-reaction of a halogen monoxide. Another cycle (R 1.26, R 1.29, R 1.30) involves reaction with  $\text{HO}_2$  produced in the course of standard  $\text{HO}_x$  chemistry

(see Figure 1.2), and therefore affects OH/HO<sub>2</sub> partitioning. The net result of both cycles is conversion of 2 O<sub>3</sub> to 3 O<sub>2</sub> molecules. This second cycle can be interrupted by R 1.31 where HOX uptake onto a particle facilitates reaction with a halide ion to form a dihalogen molecule (X<sub>2</sub>), photodissociation of which yields 2 reactive halogen atoms from the initial investment of one (R 1.32). This autocatalytic process is sometimes known as the “bromine explosion” due to its role in arctic Br activation (Simpson et al., 2007), however the original halogen in R 1.26 does not necessarily need to be the same as the ion in R 1.31 (therefore the product of the latter reaction can be Br<sub>2</sub>, BrCl, Cl<sub>2</sub>, etc).

A third pathway (not shown) involving the reaction of XO with NO<sub>2</sub> results in a null cycle, converting photons to heat but with no net chemical change (Saiz-Lopez and von Glasow, 2012). XO can, however, affect NO/NO<sub>2</sub> partitioning via R 1.33.



Hydrochloric acid (from reaction of  $\text{HNO}_3$  with sea salt aerosols) can also produce atomic chlorine as per R 1.34 by reaction with hydroxyl radicals (Finlayson-Pitts, 2003). This could be a notable chlorine activation process like  $\text{ClNO}_2$  formation, however its influence is limited by a low rate constant (Rossi, 2003).

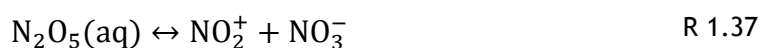
Alternatively, the halogen radical can react with unsaturated VOCs or *via* hydrogen abstraction (R 1.35) in a manner analogous to OH (R 1.6) or  $\text{NO}_3$  (R 1.20), generating  $\text{RO}_2$  and HX. Chlorine atoms in particular are highly reactive towards hydrocarbons, with which they are similarly or more reactive than even OH and notably may contribute up to 15% of the global methane sink (Saiz-Lopez and von Glasow, 2012). The increased reactivity with hydrocarbons of chlorine as compared to other halogens allows the hydrogen abstraction to outcompete the ozone destruction pathways (Simpson et al., 2015). The alkyl product resulting from this hydrogen abstraction can then feed into R 1.7, eventually producing additional  $\text{HO}_2$  to enhance  $\text{HO}_x$  chemistry. Despite the  $\text{O}_3$  destruction pathways Cl radicals therefore tend to cause a net increase of tropospheric ozone in a polluted atmosphere, especially when  $\text{ClNO}_2$  chemistry is considered (see section 1.2.4). By contrast, bromine reacts with only a few hydrocarbons (*e.g.* aldehydes) and iodine is mostly unreactive in this regard, therefore ozone destruction pathways dominate for these halogens (Saiz-Lopez and von Glasow, 2012).

A final point with regards to halogen chemistry is its reactivity with elemental mercury  $\text{Hg}^0$ . This species has a long (approx. 1 year) atmospheric lifetime, however this is greatly diminished by oxidation *via* halogens yielding the reactive  $\text{Hg}^{\text{II}}$ , which is susceptible to methylation to create highly toxic methylated mercury (Saiz-Lopez and von Glasow, 2012).

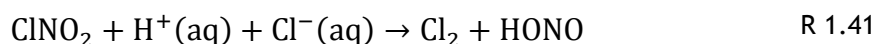
#### 1.2.4 Nitryl chloride

$\text{ClNO}_2$  formation follows uptake and subsequent dissociation of  $\text{N}_2\text{O}_5$  (formed from R 1.22; see Figure 1.3) upon aerosol particles, as per R 1.36 and R 1.37. As discussed in section 1.2.2,  $\text{N}_2\text{O}_5$  can be hydrolysed to  $\text{HNO}_3$  resulting in removal of  $\text{NO}_x$  from the atmosphere (R 1.39), however in the presence of

chloride ions R 1.38 also occurs resulting in nitryl chloride released into the gas phase (Behnke et al., 1997; Roberts et al., 2009), dependent on water and inorganic chloride concentrations. The rate limiting step for either product is thought to be R 1.37 (Roberts et al., 2009). Yields of ClNO<sub>2</sub> from the heterogeneous reaction of N<sub>2</sub>O<sub>5</sub> taken up onto aerosol particles therefore depend on the competition between R 1.38 and R 1.39. With regards to this competition, Behnke et al., 1997 demonstrated the reaction with Cl<sup>-</sup> to be dominant and Roberts et al., 2009 found that this preference was marginally (*i.e.* within uncertainties) greater at lower pH.



No significant nocturnal sinks are known for nitryl chloride (von Glasow, 2008) therefore ClNO<sub>2</sub> tends to accumulate throughout the night, representing a reservoir for nitrogen oxides until photolysis begins the following morning. ClNO<sub>2</sub> photolysis yields NO<sub>2</sub> and a chlorine radical (R 1.40), providing a significant boost to oxidation chemistry particularly in the early morning before HO<sub>x</sub> chemistry is fully established.



A reaction of ClNO<sub>2</sub> upon very acidic particles (pH<2) has been suggested as a possible source of Cl<sub>2</sub> and HONO *via* R 1.41 (Roberts et al., 2008), however concurrent measurements of Cl<sub>2</sub> and ClNO<sub>2</sub> have not found this reaction to be significant (Riedel et al., 2012; Riedel et al., 2013).

$\text{N}_2\text{O}_5$  is readily generated from  $\text{NO}_x$  and  $\text{O}_3$  (see section 1.2.2), both of which are ubiquitous in even moderately polluted atmospheres such as over urban and industrial areas and in the outflows thereof. Dinitrogen pentoxide is therefore widespread, but only at night as it photolyses rapidly (the same applies to its  $\text{NO}_3$  precursor). Chloride is the most abundant halide in the marine boundary layer (Simpson et al., 2015) owing to the large amount available in sea salt aerosols produced by turbulent action of wind at the air-sea interface (Ma et al., 2008). Primary, super-micron sea salt aerosol has a relatively short lifespan averaging 40 hours (Erickson et al., 1999) and in most cases non-sea salt sources of particulate chloride are thought to be relatively minor (Keene et al., 1999). Others have found, however, that sea salt chloride levels are likely insufficient to produce observed  $\text{ClNO}_2$  levels (Osthoff et al., 2008). In a few cases researchers have suggested non-marine (and probably mainly anthropogenic) particulate chloride sources for  $\text{ClNO}_2$ , typically in continental locations many hundreds of kilometres from the sea (e.g. Thornton et al., 2010; Mielke et al., 2011). Such sources are still surface-based, therefore  $\text{ClNO}_2$  is mainly a low-altitude tropospheric species due to its rapid photolysis and the unavailability of chloride at altitude.  $\text{ClNO}_2$  was at one point furthermore thought to be restricted to polluted marine regions such as shipping lanes and coastal cities however, as already mentioned,  $\text{ClNO}_2$  is now known to be far more prevalent as several research groups have detected the molecule in continental locations, for example Phillips et al., 2012 at a site approx. 400 km from the sea.

### 1.3 Prior observations of nitryl chloride

The formation of nitryl chloride from  $\text{N}_2\text{O}_5$  on chloride aerosol was first suggested by Finlayson-Pitts et al., 1989. Early  $\text{ClNO}_2$  observations were mostly laboratory-based, such as Behnke et al., 1997 (via FTIR) and Roberts et al., 2009 (using indirect or UV absorption measurements) investigating the formation mechanism and yield of  $\text{ClNO}_2$  from  $\text{N}_2\text{O}_5$  uptake. Field observations have since been carried out (a list of which is shown in Table 1.2) following the development of field-deployable chemical ionisation mass spectrometry using

iodide reagent ions ( $I^-$  CIMS; see section 2.2) which is capable of detecting nitryl chloride in ambient air.

Table 1.2 List of ClNO<sub>2</sub> field observations including location, time of year, maximum observed concentration and published reference (by date of observation).

Reference	Continent	Location	Type	Date	Maximum ClNO <sub>2</sub> (ppt)
Osthoff et al., 2008	North America	Houston, Texas	Coastal	2006; Aug-Sep	1200
Thornton et al., 2010	North America	Boulder, Colorado	Continental	2009; Feb	450
Mielke et al., 2011	North America	Calgary, Canada	Continental	2010; Apr	250
Riedel et al., 2012	North America	Los Angeles, California	Coastal	2010; May-Jun	2150
Mielke et al., 2013	North America	Pasadena, California	Coastal	2010; May-Jun	3600
Riedel et al., 2013	North America	Boulder, Colorado	Continental	2011; Feb-Mar	1300
Phillips et al., 2012	Europe	Frankfurt, Germany	Continental	2011; Aug-Sep	800
Bannan et al., 2015	Europe	London, UK	Coastal	2012; Jul-Aug	724
Tham et al., 2013	Asia	Hong Kong, China	Coastal	2012; Aug	1997
Faxon et al., 2015	North America	Houston, Texas	Coastal	2013; Sep	144
Wang et al., 2016	Asia	Hong Kong, China	Coastal	2013; Nov-Dec	4700
Tham et al., 2016	Asia	Tianjin, China	Continental	2014; Jun-Sep	2070

Most field observations have focused on North America but have been expanding more recently. The first field observation was made by Osthoff et al., 2008, who measured >1 ppb of ClNO<sub>2</sub> *via* CIMS on a research vessel travelling along the coastline of the Gulf of Mexico near Houston, Texas. Their highest (~1200 ppt) ClNO<sub>2</sub> measurement was calculated to represent a significant proportion (approx. 15%) of total reactive nitrogen, NO<sub>y</sub>. The high ClNO<sub>2</sub> levels were observed in polluted regions, and were attributed to shipping exhaust (notably excluding very recent plumes), however ClNO<sub>2</sub> was below the instrument's 50 ppt detection limit in clean air. Loss rates of N<sub>2</sub>O<sub>5</sub>, which was also measured, had variable but generally good correlation to ClNO<sub>2</sub> concentration (on one night R<sup>2</sup> = 0.94), adding evidence to N<sub>2</sub>O<sub>5</sub> as a precursor species.

ClNO<sub>2</sub> precursors were known to exist throughout the USA from emission inventories, therefore Thornton et al., 2010 made nitryl chloride observations at a continental site (specifically Boulder, Colorado) more than 1200 km from sea salt chloride sources. The molecule was detected in substantial concentrations (maximum ~450 ppt) notably proving that ClNO<sub>2</sub> is relatively ubiquitous, often in substantial quantities, rather than being restricted to coastal/marine locales as previously assumed. Furthermore, a model was produced that suggested that at some times chloride availability was not the limiting factor for ClNO<sub>2</sub> formation even at this continental site.

Mielke et al., 2011 observed ClNO<sub>2</sub> (maximum 450 ppt), again at an inland site (800 km from the Pacific ocean in Canada), which was calculated to represent at most 2% of NO<sub>y</sub> (much less than the polluted coastal measurements of Osthoff et al., 2008). Efforts were made to trace the aerosol chloride source, to which end 2-day back-trajectory models suggested a mainland USA origin for air masses (making sea salt sources unlikely). The chloride sources were therefore tentatively assigned as anthropogenic, possibly from municipal water treatment and road dust (containing salt spread during the winter shortly prior). The suggested mechanism for this was release and photolysis of anthropogenic Cl<sub>2</sub> - which was also observed at significant (maximum 65 ppt) concentrations - followed by reaction of Cl with hydrocarbons and partitioning of the resulting HCl to the aerosol phase.

Riedel et al., 2012 made concurrent measurements of ClNO<sub>2</sub>, Cl<sub>2</sub> and HCl just off the coast in Los Angeles, California during the CalNex 2010 campaign. These measurements were used to constrain a model comparing the importance of each of these species as a source of chlorine radicals. According to the model approx. 45% of daily Cl production is from ClNO<sub>2</sub> photolysis (dominating by a significant margin in the early morning), 45% *via* R 1.34 and the balance resulting from Cl<sub>2</sub> photolysis. Based on this model, the researchers estimate that up to 60% of daily atomic Cl production would be ClNO<sub>2</sub> in the location where the most consistent urban outflow was observed, and that up to 25% of daily alkane oxidation could be *via* atomic chlorine, thus beginning to define the potential extent of ClNO<sub>2</sub> impacts. It was furthermore concluded that Cl<sub>2</sub>

observations were more likely a result of direct emission than from ClNO<sub>2</sub> *via* R 1.41.

Also during CalNex 2010, Mielke et al., 2013 gathered data in Pasadena, California several hours downwind of the aforementioned Los Angeles site to examine the effects of more prolonged processing. This second group found that approx. 9.5% of NO<sub>3</sub> from R 1.16 was converted to ClNO<sub>2</sub>. While coarse primary sea salt aerosol contributed to ClNO<sub>2</sub> production, a far greater portion was found to have formed on much finer (sub-micron) secondary aerosols, suggesting a redistribution of sea salt chloride *via* HNO<sub>3</sub> acid displacement and NH<sub>4</sub>Cl condensation.

A vertical profile of ClNO<sub>2</sub> mixing ratios from 0-265 m above ground level was studied in Calgary, Canada by Riedel et al., 2013. The greatest ClNO<sub>2</sub> concentrations tended to be in plumes with high relative humidity (typically >45%) when the wind direction corresponded to local pollution sources. Conversely, low ClNO<sub>2</sub> concentrations tended to be evident in drier and altitudinous samples. Importantly, many of the highest ClNO<sub>2</sub> observations occurred in plumes traced back to regions containing coal-fired power plants. The researchers therefore concluded that power plant emissions are a source of ClNO<sub>2</sub> and, more tentatively, that coal combustion and water cooling processes for power generation may be sources of aerosol chloride, possibly responsible at least in part for ubiquitous ClNO<sub>2</sub> formation in continental locations such as the one in this study.

The first ambient ClNO<sub>2</sub> observations in Europe were made by Phillips et al., 2012 near Frankfurt, Germany. Significant (maximum 800 ppt) quantities of ClNO<sub>2</sub> were detected at this site ~380 km from the nearest coast. The researchers report that in this case sea salt was the most likely chloride source due to back-trajectory models showing marine origins for the sampled air masses, and furthermore a previous study observed that significant proportions (up to 75%) of super-micron particles at a nearby site (~30 km away) were composed of aged sea salt (Vester et al., 2007). These two studies again showed that sea salt chloride and, therefore, nitryl chloride is widespread even far from the sea (notably, farther than is possible within the UK) and its photolysis

products likely represent a significant contribution to oxidative capacity and ozone production.

A modelling study by Sarwar et al., 2014 assessed ClNO<sub>2</sub> production in the northern hemisphere with an attempt to quantify its impacts on atmospheric chemistry, such as reduction of total nitrate (*i.e.* HNO<sub>3</sub> + particulate NO<sub>3</sub>; a measure of NO<sub>x</sub> removal), increase in ozone concentrations and enhancement of HO<sub>x</sub> and oxidation chemistry. Findings notably include ClNO<sub>2</sub> concentrations varying substantially with time of year as in the winter N<sub>2</sub>O<sub>5</sub> levels and ClNO<sub>2</sub> yields are higher - caused, for example, by reduced photolysis due to longer nights (also allowing increased ClNO<sub>2</sub> accumulation) and lower temperatures, shifting the NO<sub>3</sub>/N<sub>2</sub>O<sub>5</sub> equilibrium towards the latter. The model often predicted ~1 ppb mean nightly ClNO<sub>2</sub> mixing ratios over areas of China and Western Europe (which were specifically mentioned as areas for greatest ClNO<sub>2</sub> impact) during winter. The authors acknowledged that true values are likely to be higher, as the model was run at 108 km grid resolution whereas tests at 12 km resolution tended to give higher concentrations.

Furthering the body of worldwide ClNO<sub>2</sub> observations, Bannan et al., 2015 reports the first measurements of nitryl chloride in the UK during the summer (July to August) of 2012 in London. The maximum observation was 724 ppt, with a nightly mean of 84 ppt over a one month period. These values are significantly higher than summertime measurements reported in this thesis at an urban background site in the much smaller city of Leicester (mean 14, max. 74 ppt; see chapter 4) and the night-time mean (65 ppt) observation at the rural Weybourne Atmospheric Observatory, but less than the maximum (1104 ppt) at the latter site (see chapter 5). The researchers report sea salt aerosol as the greatest chloride source for ClNO<sub>2</sub>. A model was used to assess the importance of Cl as an oxidant during the campaign, with an average of 4 and 7% removal of alkanes and alkynes respectively, however these increased to a far more substantial 15 and 26% following the night of highest ClNO<sub>2</sub> observation, demonstrating the importance of ClNO<sub>2</sub> chemistry for estimates of VOC processing.

Several campaigns have also measured ClNO<sub>2</sub> in China, including coastal locations near Hong Kong (Tham et al., 2013; Wang et al., 2016) and a continental site in the North China Plain (Tham et al., 2016). The highest ClNO<sub>2</sub> observation to date is ~4.7 ppb in a highly-processed air mass originating from the Pearl River Delta region combining sea salt aerosol and urban/industrial pollution (Wang et al., 2016). The continental site study (Tham et al., 2016) took place in an extremely polluted region relatively close to three megacities, and the researchers suggested crop residue incineration (*i.e.* biomass burning) may have contributed to aerosol chloride in addition to coal-based power generation.

#### 1.4 Summary and motivation

The concentrations of atmospheric oxidants (OH, NO<sub>3</sub>, O<sub>3</sub>, Cl) have substantial effects upon the oxidising capacity of the troposphere, the most direct effect of which is oxidation rate of VOCs. VOC oxidation processes significantly affect concentrations of atmospheric trace gases, having widespread and varied effects on air quality and climate. It is therefore important to obtain measurements of species such as ClNO<sub>2</sub> in order to better quantify these impacts.

Carbon dioxide and methane are both species that are directly emitted from industrial processes and are significant mostly for their properties as greenhouse gases (GHG), intercepting and absorbing infra-red radiation from Earth's surface. This absorption causes retention of heat within the Earth system for longer (as compared to being radiated from the surface directly into space), incrementally increasing the global average temperature as total GHG concentrations in the atmosphere rise. Atmospheric oxidants have a complex relationship with the greenhouse effect. For both methane and non-methane hydrocarbons (NMHC; an important subset of VOCs typically treated separately, as methane is typically far more abundant and less reactive) the end result of oxidation in the troposphere is conversion to CO<sub>2</sub>. In this way NMHC oxidation often results in an increase in the greenhouse effect whereas CH<sub>4</sub> oxidation results in reduction thereof, as methane is a much stronger greenhouse gas than

CO<sub>2</sub> (Myhre et al., 2014). Different tropospheric oxidants do not have the same reactivity towards all VOCs. Again, methane is a notable example in that it has a very long lifetime as it is unreactive with NO<sub>3</sub>, moderately reactive with OH but extremely reactive with chlorine radicals. As a result, sources of atomic chlorine such as that represented by nitryl chloride become very important with respect to climate.

As mentioned in section 1.2.3, atomic chlorine has a net enhancing effect on tropospheric ozone, which has significant effects on oxidation chemistry (directly and otherwise). Ozone is extremely important with respect to air quality due to broad toxicity to both plants and animals, and formation of photochemical smog. Ozone is also a potent greenhouse gas, however its importance in this regard is reduced by its much lower abundance and lifetime compared to CO<sub>2</sub> and CH<sub>4</sub>.

Nitrogen dioxide concentrations were also monitored during work in this thesis. NO<sub>2</sub> is a major urban pollutant integral to the principal means of tropospheric ozone production (see section 1.2.2), but is also toxic (World Health Organization, 2014) and is one of the main constituents of photochemical smog together with ozone, particulate matter and secondary organic aerosol formed from VOC oxidation products.

Nitryl chloride decreases the removal of atmospheric NO<sub>x</sub> by competing with the main sink (HNO<sub>3</sub>) and later returning NO<sub>2</sub> to the atmosphere. ClNO<sub>2</sub> more importantly represents a significant source of chlorine radicals *via* activation of aerosol chloride, marine sources of which are likely to be plentiful at most locations on an island such as the UK. ClNO<sub>2</sub>-derived chlorine radicals contribute to photochemical smog through VOC oxidation (resulting in secondary organic aerosols) and *via* enhancement of tropospheric ozone levels. Chlorine radicals may also play a significant role with regards to greenhouse gas concentrations by decreasing lifetimes of methane and producing CO<sub>2</sub> *via* NMHC oxidation.

ClNO<sub>2</sub> accumulates during the night and begins photolysing after daybreak, therefore its effects are particularly pronounced in the early morning by enhancing VOC oxidation directly due to increased Cl abundance at a time when HO<sub>x</sub> chemistry has not yet fully initiated. Indirectly, these Cl atoms interact

with and accelerate initiation of HO<sub>x</sub> cycles including O<sub>3</sub> production using NO<sub>2</sub> also released from ClNO<sub>2</sub> photolysis following night-time NO<sub>x</sub> losses *via* HNO<sub>3</sub>.

The aims of this thesis were to gather data regarding concentrations of ClNO<sub>2</sub> at several ground-level sites. ClNO<sub>2</sub> prevalence was studied in various combinations of clean/polluted and inland/coastal conditions giving rise to potentially different availability of precursor species. Nitryl chloride was also for the first time monitored in the same location in all different seasons to assess experimentally the extent of seasonal variations. This thesis represents the first methodical experimental study of nitryl chloride seasonal and geographical variations, from which an assessment of nitryl chloride ubiquity in the UK should be possible. The data thusly gathered will be useful in constraining models to extrapolate ClNO<sub>2</sub> concentrations more widely to determine the impact of its chemistry upon the concentrations of several other species directly relevant to climate and air quality at a regional level.

## 2 Instruments & methods

### 2.1 Introduction

This thesis presents measurements of atmospheric trace gases and the prior laboratory work to support these measurements. This chapter is mainly concerned with describing the operating principles behind the core instruments. A chemical ionisation mass spectrometer (CIMS) was the principal instrument for measuring the central species, nitryl chloride. Broadband cavity enhanced absorption spectroscopy (BBCEAS) was also used extensively both for CIMS calibration and for detecting  $\text{NO}_2$ ,  $\text{NO}_3$  and  $\text{N}_2\text{O}_5$  during field measurements. These techniques, explored in this chapter, are ideally suited for making atmospheric measurements because they offer high sensitivity for the target trace gas species at part per billion (ppb) concentrations or lower, good selectivity to avoid interference from the numerous other gases in ambient air and high time resolution to investigate rapid changes in atmospheric concentrations (particularly in the troposphere, where chemical lifetimes of target species are often low due to turbulent mixing and a wide variety of other species present). Some details are also given regarding other instruments that were operated during field deployments, and some of the software and techniques used in data analysis.

### 2.2 Chemical Ionisation Mass Spectrometry

#### 2.2.1 Overview

CIMS techniques, as used in atmospheric monitoring, utilise reagent ions to selectively ionise particular analyte species in the complex mixture represented by ambient air (Huey, 2007). The technique is also highly sensitive, capable of measuring  $\text{ClNO}_2$  at the very low concentrations at which it naturally occurs (typically parts per billion (ppb) or trillion (ppt) mixing ratio). Analysis of CIMS spectra is simpler than many other mass spectrometric techniques, as its selectivity and low fragmentation give a fairly clean spectrum, with a relatively small number of peaks corresponding to the analyte and other species. The CIMS instrument as used in this thesis was operated primarily in its H-mode (“hop”). In this mode, the mass filter successively dwells on several

predesignated  $m/z$  (allowing ions of these  $m/z$  ratios to pass to the detector) for a period of time in the order of milliseconds each. Depending on the dwell times and number of designated  $m/z$ , the total measurement cycle is often in the order of seconds. This enables measurements to be made in real time, and for several species to be monitored over an indefinite period. An alternative function for the CIMS is S-mode (“spectrum”), during which the mass filter sweeps across a selected range and resolution (*e.g.*  $m/z = 30-300$  amu range at 0.1 amu resolution). In either case the instrument’s output is a number of counts per second for a given  $m/z$  value, corresponding to the number of ions reaching the detector. Data acquired *via* CIMS in this project are primarily  $\text{ClNO}_2$  and  $\text{Cl}_2$  concentrations. Section 3.4 reports calibrations for these species performed in the laboratory. Several other species can be (and were) monitored *via* CIMS, notably including  $\text{N}_2\text{O}_5$ , however these are uncalibrated therefore absolute concentrations are not known. The need for calibration is one of the major drawbacks of CIMS techniques as specific techniques need to be developed for each species, and the experiments are often time- and labour-intensive.

### 2.2.2 Mass spectrometry

The core principle of mass spectrometry (MS) involves separating ions by their mass to charge ratio ( $m/z$ ) *via* deflection using an electromagnetic field, typically under vacuum to avoid collision with air molecules. In a traditional “sector” mass spectrometer, ions are sent along an initially straight path and deflected around an arc using a magnetic field - ions with high  $m/z$  are deflected less by the magnetic field and will therefore curve less than ions with lower  $m/z$ . Ions whose  $m/z$  is either too high or too low will impact the instrument’s metal walls, losing their charge and ultimately being removed by the vacuum pump. Notably any sample molecules that escaped ionisation (*i.e.* charge=0) are not deflected and are similarly removed. Surviving ions will be sorted by  $m/z$  by the time they reach a detector at the end of their path. The field strength can therefore be varied to select the  $m/z$  that reach the detector.

The Leicester CIMS instrument works on a slightly different principle, however, instead using a quadrupole mass filter which separates ions using their varying stabilities in oscillating electric fields (de Hoffmann and Stroobant, 2007). A quadrupole filter, represented in Figure 2.1, has four parallel metal rods arranged such that at a given time each rod's voltage opposes the adjacent rod and matches the oppositely-positioned rod (other "multipoles" bear similar configurations but with different numbers of rods, *e.g.* octopoles with 8 rods in 4 pairs). Each rod's potential is comprised of static (DC) and oscillating (RF) components (Ellis and Mayhew, 2014). These components are represented by  $U$  and  $V$  respectively in the equation in Figure 2.1. The oscillating component alternates each electrode pair between positive and negative net potential, causing ions to be repelled toward the centre by matching charges (stabilisation) or attracted to the electrodes by opposite charges (destabilisation). Ions with low  $m/z$  are able to change trajectory more quickly within this varying field, and the lightest will oscillate with sufficient amplitude to collide with the rods, *i.e.* high-pass filtration. The static field gives one oppositely-positioned pair of electrodes a negative offset and the other a positive one, causing the ions to be slightly more stabilised in one plane but destabilised in the other. Since the net potential on each electrode pair still alternates between positive and negative due to the RF component, ions are moved back toward the centre however ions with high  $m/z$  are less able to respond, giving lower amplitude oscillations (*i.e.* more destabilised by the static component) resulting in collision with the rods, *i.e.* low-pass filtration.

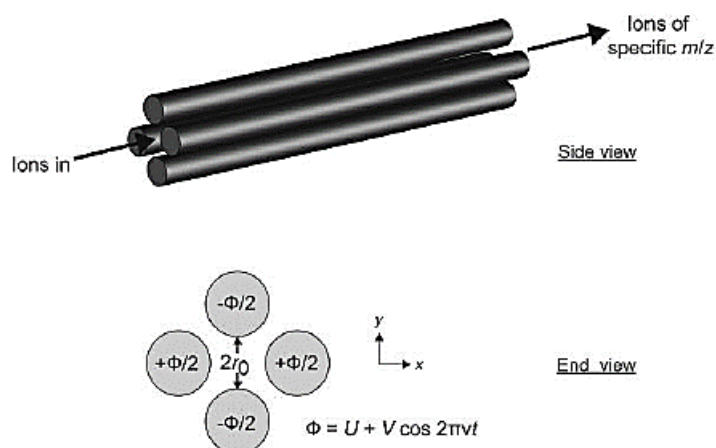


Figure 2.1 Diagram of a quadrupole, including equation describing applied electrical potentials, where  $\Phi$  = net applied electrical potential;  $U$  = DC component at time  $t$ ;  $V$  = RF component maximum amplitude;  $\nu$  = oscillation frequency. Figure reprinted from Ellis and Mayhew, 2014.

By tuning the operating parameters  $U$  and  $V$  it is therefore possible to select a narrow range of  $m/z$  that are able to reach the detector at a given time. The quadrupole will typically dwell on these settings for a fixed time period before changing to allow ions of a different  $m/z$  to be transmitted through the quadrupole. For H-mode data with the Leicester CIMS, a number of ion masses (typically around 10) were pre-selected based on work in the laboratory, and the quadrupole cycled around the appropriate configuration to monitor each mass in turn with dwell times of typically  $\sim 0.5$ - $1.0$  ms per ion. The duration of the full measurement cycle was approx. 11 s, so this was the time resolution of ambient measurements later averaged to 1 min or higher. It was informative to acquire full mass spectra periodically to check for other  $m/z$  signals in ambient air, therefore S-mode data were also obtained by scanning across a wider  $m/z$  range. This takes some time, however, depending on the selected mass range and scan resolution (typically 2-3 minutes) and interrupts any continuous monitoring.

### 2.2.3 Chemical ionisation

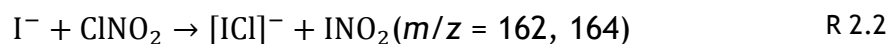
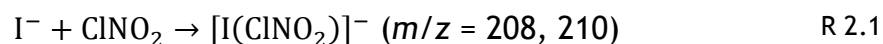
Mass filtration techniques in MS require the sample to be ionised. To achieve this many ionisation techniques are variously used for different applications.

Perhaps the most common is electron ionisation (EI) where a gaseous sample is passed through a stream of electrons with kinetic energies exceeding the analyte's ionisation energy. Collisions between the analyte molecule,  $M$ , and an electron cause another electron to be expelled and leaving a positively-charged ion (*i.e.*  $M + e^- \rightarrow M^+ + 2e^-$ ; Skoog et al., 2013). Electron ionisation causes significant fragmentation of analyte molecules (de Hoffmann and Stroobant, 2007) due to the high kinetic energy of the incident electrons, and is therefore considered a “hard” technique. Ions corresponding to these fragments also appear on a spectrum, which has benefits and drawbacks. One advantage is that the fragmentation patterns can give information regarding molecular structure making EI techniques useful for applications involving structure determination. The disadvantage for ambient measurements is that the atmosphere contains many species, and simultaneous EI of multiple species makes interpretation of mass spectra difficult. EI is furthermore not very selective and ionises the bulk components of air ( $N_2$ ,  $O_2$ , Ar, etc)

Chemical ionisation (CI) is much better suited for detecting and quantifying atmospheric species as per the work in this thesis. Ionisation is achieved *via* reaction of a pre-generated reagent ion with the sample molecules, which yields ions with little excess energy (de Hoffmann and Stroobant, 2007), resulting in minimal fragmentation of the parent ion (a “soft” technique). Ions resulting from a target molecule are therefore concentrated onto fewer  $m/z$ , simplifying the spectrum. The specific reactivity of the reagent ion makes CI very selective, which also significantly simplifies spectra by removing many signals corresponding to non-target molecules. A further advantage of CI techniques is the ability to operate using negative ions.

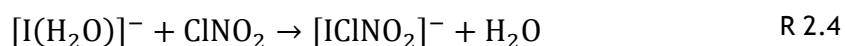
During work in this thesis iodide,  $I^-$ , was used as a reagent ion. Several  $m/z$  corresponding to nitril chloride were observable, however these are not due to fragmentation. The cluster formation reaction R 2.1 results in the  $[I(ClNO_2)]^-$  ions at approx. 208 and 210 atomic mass units (amu). However the chemical ionisation technique used in this project also resulted in  $[I(Cl)]^-$  at approx. 162 and 164 amu due to the dissociative charge transfer reaction, R 2.2 (Kercher et al., 2009). Each of these ions manifests at two  $m/z$  due to the 35 and 37 amu isotopes of chlorine, and any of these four  $m/z$  (*i.e.* 162, 164, 208, 210 amu)

can theoretically be used for detection and quantification of ClNO<sub>2</sub>. Ultimately 208 amu was chosen as the principal mass for investigation (see section 3.5.5), which was given a dwell time of 1000 ms (~9% of the duty cycle).



The reagent ion must be carefully selected as, further to being reactive with the target molecule, its stability must be sufficient to avoid reaction with abundant non-target molecules because such reactions would result in a number of interfering peaks (Slusher et al., 2001). Also, the product ion must not be reactive with other trace gases to avoid conversion to non-characteristic *m/z* via further reaction before reaching the detector (Huey, 2007). CIMS using I<sup>-</sup> is an established method for measuring ambient ClNO<sub>2</sub> (see section 1.3). I<sup>-</sup> is unreactive with respect to most atmospheric species (Huey et al., 1995), thus providing the desired chemical selectivity. For work in this thesis the reagent ion was generated *via* dissociative electron attachment by flowing methyl iodide (MeI) past a radioactive α-emitter, <sup>210</sup>Po (Burns et al., 1996).

One final element of ion chemistry is water vapour mediated cluster formation. The iodide primary reagent ion forms clusters with water vapour (R 2.3), which themselves can then act as secondary reagent ions as per R 2.4 (Kercher et al., 2009). This and other effects related to humidity are discussed in section 3.2.3.



In addition to the ClNO<sub>2</sub> studies using I<sup>-</sup> described in section 1.3, chemical ionisation techniques have been used in the past to detect a wide variety of gas-phase species. A selected list of such studies is given in Table 2.1.

Table 2.1 Selected list of species detected *via* CIMS, with reagent ions used.

Reference	Reagent ion(s)	Target species
Tanner et al., 1997	$\text{NO}_3^-$	OH (as $\text{H}_2\text{SO}_4$ )
Huey et al., 1998	$\text{SiF}_5^-$	$\text{HNO}_3$
Slusher et al., 2001	$\text{SF}_6^-$	$\text{HO}_2\text{NO}_2$
Hearn and Smith, 2004	$\text{H}^+(\text{H}_2\text{O})_2$ , $\text{H}^+(\text{CH}_3\text{OH})_2$ , $\text{NO}_2^+$ , $\text{O}_2^+$ , $\text{O}_2^-$ , $\text{F}^-$ , $\text{SF}_6^-$	Organic aerosols
Slusher et al., 2004	$\text{I}^-$	PAN (as $\text{CH}_3\text{C}(\text{O})\text{O}_2$ ) $\text{N}_2\text{O}_5$ (as $\text{NO}_3$ )
Huey, 2007	$\text{SF}_5^-$	$\text{HNO}_3$
Kercher et al., 2009	$\text{I}^-$	$\text{N}_2\text{O}_5$ $\text{ClNO}_2$
Kurten et al., 2011	$\text{NO}_3^-$	$\text{H}_2\text{SO}_4$
Liao et al., 2011 Liao et al., 2014	$\text{I}^-$	BrO $\text{Cl}_2$

#### 2.2.4 CIMS hardware & application

The CIMS instrument used in this thesis is a commercial instrument built by THS Instruments LLC (Atlanta, Georgia, USA). The instrument was operated in a negative ion mode using  $\text{I}^-$  as a reagent ion. The instrument is similar to the ones used to measure dinitrogen pentoxide and peroxyacyl nitrates in Boulder, Colorado, USA (Slusher et al., 2004) and arctic molecular chlorine and BrO in Barrow, Alaska, USA (Liao et al., 2011, Liao et al., 2014). A schematic representation of the instrument is shown in Figure 2.2.

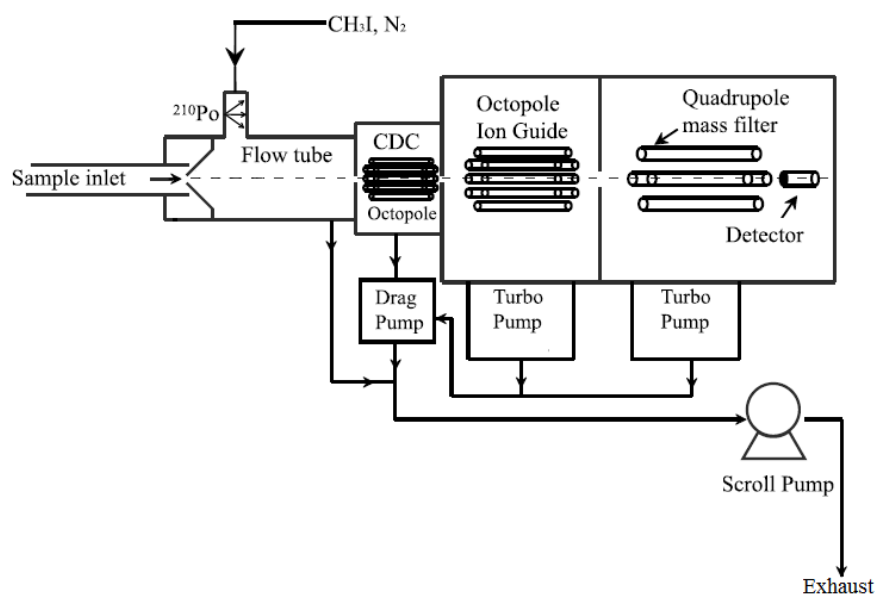


Figure 2.2 Schematic representation of the UoL-CIMS. Figure adapted from Liao et al., 2011.

The flow tube represents the ion-molecule region (IMR), where the ambient gas sample mixes and reacts with reagent ions. Sample gas is drawn into the flow tube, in which pressure is below ambient, through the inlet at approx. 1 litre per minute (slpm) using the scroll pump. Successive pressure reductions in subsequent chambers are achieved using a drag pump (for the collisional dissociation chamber, CDC) and turbomolecular pumps (for the ion guide and mass selector). Pinhole orifices are used at the interfaces between different pressure regions of the instrument (Heinritzi et al., 2016). The orifices before and after the collisional dissociation chamber (CDC) have an electric field applied to maintain flow of ions through the instrument and induce collisional dissociation.

The iodide reagent ions enter the IMR separately. Reagent ions are generated by passing methyl iodide (2005 sccm, 2.4 ppm; BOC specialist gases) through a steel tube containing a strip of  $^{210}\text{Po}$  foil attached perpendicularly to the side of the flow tube. The methyl iodide and  $\text{N}_2$  flow gas are regulated by mass flow controllers (MKS M100B series).

Some ions form clusters, often with water molecules (e.g.  $[\text{I}(\text{H}_2\text{O})_n]^-$ ). This clustering can increase instrument sensitivity to a target species as the cluster

can have a stabilising effect, however the cluster appears in the mass spectrum at a different  $m/z$  value (or several), spreading the product ion signal across multiple  $m/z$  values thus reducing sensitivity (Kercher et al., 2009). The CDC serves to break down these clusters into their constituent ions, concentrating species prone to such clustering into fewer representative  $m/z$  (Tanner and Eisele, 1995). The CDC is discussed further in section 3.2.3.

After passing through the CDC ions are focused *via* octopole ion guide through an intermediate pressure region, serving to keep the ion beam stable during this stage of vacuum. In the final chamber, ions are discriminated using the quadrupole mass selector (see section 2.2.2) before reaching an electron multiplier detector. The ion count from the detector is interpreted and recorded by a computer using specialist software provided with the instrument.

Significant work was undertaken to develop techniques using the CIMS, as this was the principal instrument for work described in this thesis. This development work is discussed in greater detail in chapter 3. Initial commissioning of the new instrument is covered in section 3.1, including optimisation of the mass selector and CDC voltages (section 3.2.3). Instrumental background signals and methods to remove interferences are discussed in sections 3.3.3 and 3.3.8 respectively. Raw CIMS output for  $\text{ClNO}_2$  and  $\text{Cl}_2$  (in counts per second) were converted into concentrations (as mixing ratios) using calibration factors. These calibration factors were determined using data from calibration experiments discussed primarily in section 3.4, which were processed as described in section 3.5.

## 2.3 Broadband cavity enhanced absorption spectroscopy

### 2.3.1 Overview

Broadband cavity-enhanced absorption spectroscopy (BBCEAS) instruments are based on the principle of absorption spectroscopy. Absorption spectroscopy enables selective, quantitative and absolute (Berden et al., 2000) quantification of compounds which absorb electromagnetic radiation using wavelengths in the visible, near UV and near IR regions of the spectrum. The technique has been employed in a wide range of applications. The use of an

optical cavity greatly enhances the path length of the absorption measurement compared to a single-pass instrument, thereby dramatically increasing the sensitivity of absorption measurements and allowing detection of absorbers at ppb or ppt mixing ratios. BBCEAS techniques as described in this thesis are therefore ideal for continuous measurement of atmospheric gases such as  $\text{NO}_2$  and  $\text{NO}_3$  (which have structured absorption spectra in the blue and red regions of the visible spectrum respectively) as, like  $\text{ClNO}_2$ , these are typically observed at ppb or lower concentrations in the troposphere and are often short-lived. It is also possible to manipulate samples prior to the cavity, for example  $\text{N}_2\text{O}_5$  (which does not absorb in visible or near UV wavelengths) can be detected as  $\text{NO}_3$  produced by thermal decomposition of  $\text{N}_2\text{O}_5$  in a heated inlet (Brown, 2003). As long as absorption cross sections of the target molecule(s) are known, BBCEAS also allows determination of absolute concentrations of the analyte, making the technique useful for calibrating other instruments. Calibrating the CIMS instrument in this way was one of the principal uses of BBCEAS instruments for work in this thesis (as detailed throughout chapter 3). This section describes how BBCEAS enables the simultaneous detection of multiple trace gas species in ambient air.

A number of studies have successfully deployed BBCEAS in the past to measure a variety of species, for example Dubé et al., 2006 ( $\text{NO}_3$  and  $\text{N}_2\text{O}_5$ ), Ball et al., 2010 ( $\text{I}_2$ ), Kennedy et al., 2011 ( $\text{NO}_2$ ,  $\text{NO}_3$  and  $\text{N}_2\text{O}_5$ ) and Min et al., 2016 (glyoxal, methylglyoxal, nitrous acid (HONO),  $\text{NO}_2$  and  $\text{H}_2\text{O}$ ).

### 2.3.2 Absorption spectroscopy

When electromagnetic radiation (EMR) passes through an absorber, photons whose energy corresponds to a specific transition between quantum states of the absorbing species can be absorbed. In the case of EMR at the visible or UV wavelengths employed in BBCEAS techniques, transitions are typically electronic excitation (whereby an electron in an absorbing species' outer shell is promoted from ground to excited state). This is the case for  $\text{NO}_2$  and  $\text{NO}_3$  as described in this thesis, however others (such as water) exhibit vibration-rotational transitions at visible wavelengths (Ball and Jones, 2003). Absorption

spectroscopy exploits this phenomenon to quantitatively identify absorbers by measuring transmittance, *i.e.* light intensity at specific wavelengths corresponding to an absorber's characteristic transitions after passing through a sample, and comparing to a similar measurement made with a non-absorbing reference (*e.g.* by excluding sample molecules from the cavity).

The Beer-Lambert law, summarised in Equation 2.1, enables absorber concentrations to be obtained from transmittance. In this equation,  $I(\lambda)$  and  $I_0(\lambda)$  are the light intensities (as functions of wavelength  $\lambda$ ) after passing through the sample and after passing through the reference with no absorbers present respectively. The ratio of  $I(\lambda)$  and  $I_0(\lambda)$  is termed transmittance. The absorption coefficient  $\alpha$  corresponds to the absorption cross section  $\sigma$  of an absorber,  $i$ , multiplied by its concentration,  $x$ .  $L$  represents the path length, *i.e.* distance travelled by the light through the sample.

$$\text{trans}(\lambda) = \frac{I(\lambda)}{I_0(\lambda)} = \exp(-\alpha(\lambda)L) = \exp\left(-\sum_i \sigma_i(\lambda)x_iL\right)$$

Equation 2.1 Beer-Lambert law.

If path length and absorption cross sections are known the concentration of a single absorber can therefore be determined relatively simply from transmittance using the Beer-Lambert law. Note that in this equation a summation is shown, indicating that it is possible to determine the concentrations of several different absorbers from the total absorption. This, however, requires separation of the terms thusly summarised which is typically achieved *via* differential optical absorption spectroscopy (DOAS; discussed in section 2.3.4).

### 2.3.3 Cavity enhanced absorption spectroscopy

One way of overcoming weak absorptions or low concentrations is by substantially increasing path length  $L$  (see Equation 2.1). Ambient

concentrations of absorbing species in the atmosphere are often so small (see section 1.1), however, such that an absorption measurement would require path lengths of several kilometres to be effective. This can be achieved in a single pass *via* long-path differential optical absorption spectroscopy (LP-DOAS; Lee et al., 2008) however this technique has a significant drawback in that it measures only an average concentration of absorbers over its extended path length, which can lose a lot of information about spatial distribution. This can be a problem for quantifying inhomogeneous and/or reactive gases, including many tropospheric species.

In contrast, cavity enhanced absorption spectroscopy (CEAS) provides similarly long path lengths (and thus sensitivity) inside a compact instrument, allowing for observations at a specific point. The cavity is a chamber through which gas is continuously flowed, with a high-reflectivity ( $R > 99.9\%$ ) concave mirror at each end. After entering, light is repeatedly reflected through the length of the cavity (continuously undergoing absorption by the sample). A small amount leaks through the output mirror to the detector for each pass of the cavity (see Figure 2.3). Multiple reflections enable effective path lengths in the order of kilometres to be achieved in an instrument whose physical length is  $< 1$  m.

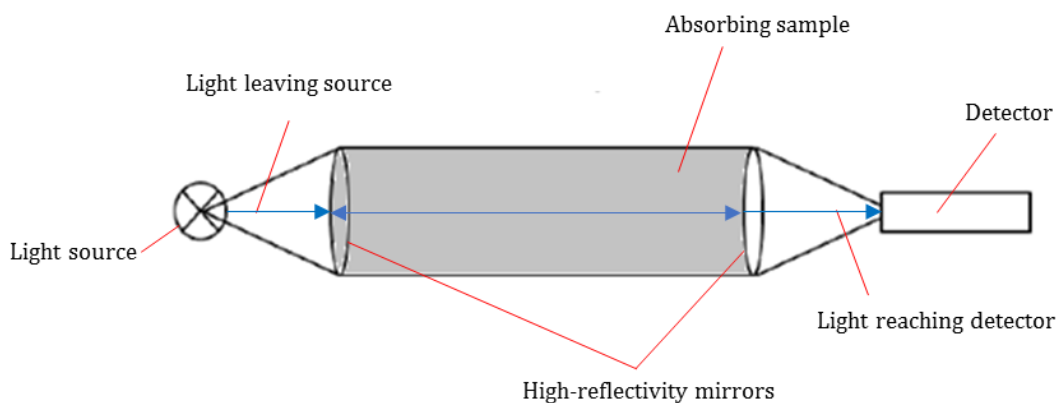


Figure 2.3 Increased effective path length *via* cavity enhancement. Mirrors are aligned so that light travels exactly the same path in both directions with small amounts “leaking” through the mirrors. Figure adapted from Platt and Stutz, 2008.

CEAS is based upon an earlier cavity-based absorption spectroscopy technique, cavity ring-down spectroscopy (CRDS), which typically uses a monochromatic pulsed laser light source. Immediately following the light pulse, the time taken for light leaking from the cavity to reach  $1/e$  of its initial intensity (“ring down time”) can be used to determine the absorption coefficient  $\alpha$  (and, therefore, absorber concentration using the Beer-Lambert law) *via* Equation 2.2. In this equation  $\tau$  represents ring down time,  $R$  and  $d$  represent the reflectivity and separation of the cavity mirrors, and  $c$  is the speed of light.

$$\tau(\lambda) = \frac{d}{c |\ln R(\lambda)| + \alpha(\lambda)}$$

Equation 2.2 Equation for calculating cavity ring down time.

Ring down time is first calculated for an “empty” cavity (filled with a non-absorbing gas such as  $N_2$ , for which  $\alpha$  will be comprised of only Rayleigh scattering). Absorption by sample molecules will result in reduced ring-down time, therefore absorber concentrations can be calculated using the ring down time for a sample-filled cavity,  $\tau'$ , related to  $\tau$  *via* Equation 2.3.

$$\frac{1}{\tau'(\lambda)} = \frac{1}{\tau(\lambda)} + c \alpha(\lambda) = \frac{1}{\tau(\lambda)} + c \sum_i \sigma_i(\lambda) x_i$$

Equation 2.3 Equation to calculate concentrations of absorbing species *via* ring down times.

The light source can be scanned across a range of wavelengths to construct an absorption spectrum, however this increases acquisition time (and monochromatic light sources typically have a limited scan range). Single-wavelength CRDS cannot be used if the wavelength-dependent losses from competing absorbing or scattering species are unknown, therefore use of DOAS and similar procedures is more difficult for CRDS when applied to mixtures (Ball and Jones, 2003) *e.g.* atmospheric measurements. These effects can, however,

be counteracted in ways such as installation of aerosol filters and careful selection of several specific wavelengths to maximise the strength of target species' absorption and minimise that for interfering species.

The key difference for CEAS compared to CRDS is the use of a continuous wave (CW) light source. Light lost due to absorption, scattering and mirror interactions is continuously replenished by the CW source, so that light intensity exiting the cavity reaches a steady state. This steady state light intensity is proportional to the ringdown time (Engeln et al., 1998). Absorbance can be calculated from steady state intensities recorded over a given integration time via Equation 2.4.

$$\text{Abs}(\lambda) = \left( \frac{I_0(\lambda)}{I(\lambda)} - 1 \right) \cdot \left( \frac{1 - R(\lambda)}{d} \right)$$

Equation 2.4 Equation to calculate absorbance per unit path length using steady state intensity.

A broadband light source further modifies the CEAS technique. The broadband light source covers a wide wavelength range simultaneously (typically ~50 nm), removing the need to scan across wavelength, potentially improving the time resolution of measurements. Being able to thusly record BBCEAS spectra also enables DOAS fitting techniques to be applied, enabling simultaneous detection of several absorbers. BBCEAS is also a very flexible technique, as various species can be detected by switching a few optical components (*i.e.* LED, cavity mirrors and spectrometer) to study a new wavelength region. The wavelength dependent reflectivity of the mirrors varies with wavelength which influences effective path length, necessitating independent determination of  $R(\lambda)$  using a reference absorber (discussed further in section 2.3.6).

#### 2.3.4 Differential optical absorption spectroscopy

The broadband light source employed in BBCEAS allows use of differential optical absorption spectroscopy, a technique often employed to counteract the influence of interfering species that are invariably present in the atmosphere.

Interferences commonly encountered while measuring atmospheric species generally fall into the categories of absorption (*i.e.* molecules with structured absorption features overlapping at the same wavelengths as the target species) or light scattering (which attenuates all wavelengths across the BBCEAS bandwidth).

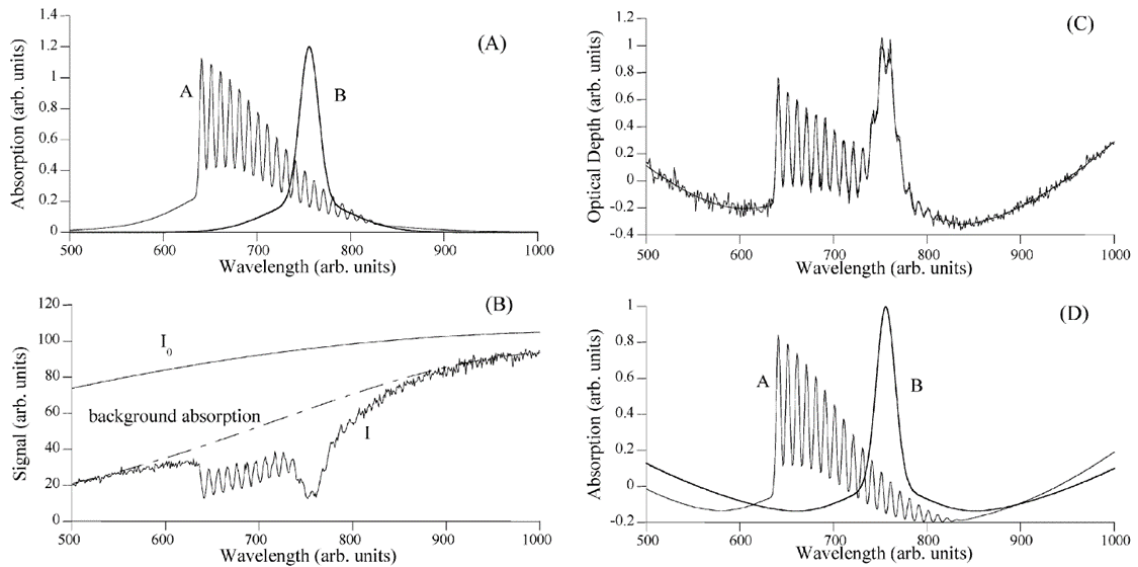


Figure 2.4 Hypothetical example of DOAS principle. Figure reprinted from Ball and Jones, 2003. Descriptions of each panel are given in the text.

In DOAS, absorbance (or in the case of BBCEAS, the wavelength-dependent absorption coefficient,  $\sigma(\lambda)$ ) is measured across a range of wavelengths much wider than any single absorption feature of the target species (often hundreds of nm; this technique is known as “spectral oversampling”). Having spectral information across a wide bandwidth allows simultaneous fitting of the structured absorption cross sections for several analyte species which can subsequently be quantified. Smoothly-varying contributions to light extinction by molecular Rayleigh and aerosol Mie scattering can also be removed using a high-pass filter (Ball and Jones, 2003). Figure 2.4 demonstrates the DOAS principle using two hypothetical absorbers A (representing a highly structured absorber, *e.g.* water vapour) and B (representing a molecule with a smoother absorption band, *e.g.* NO<sub>3</sub>). Panel (A) shows the overlapping absorption cross sections of these species. Panel (B) shows simulated measured and reference

spectra, *i.e.* with and without sample present ( $I$  and  $I_0$  respectively). These spectra include electronic noise and unstructured extinction contributions due to scattering (represented by the difference between  $I_0$  and the dot-dashed line). After  $I$  and  $I_0$  have been obtained, the optical depth (OD; defined in Equation 2.5a) is calculated; this necessarily includes contributions from both absorption and scattering. The broadband extinction due to scattering can be removed using a high-pass filter, usually a polynomial function  $P$  of order  $n$  which is fitted to and subtracted from the measured optical depth to give the differential optical depth,  $\Delta OD$  (Equation 2.5b).

$$\text{OD} = -\ln\left(\frac{I(\lambda)}{I_0(\lambda)}\right) = \alpha(\lambda)L = \sum_i \sigma_i(\lambda)x_iL \quad \text{a}$$

$$\Delta\text{OD} = \sum_i \sigma_i(\lambda)x_iL - P(\lambda, n) \quad \text{b}$$

Equation 2.5 Equations defining optical depth (a) and differential optical depth (b).

This process gives the molecular spectrum in panel (C). In this figure, a polynomial of order  $n=2$  was used however for work in this thesis  $n=6$  was typically used. Higher order polynomials are better able to account for (and therefore remove) the broadband continuum due to aerosol and any instrument instabilities, but risk reducing the size of the target molecules' differential absorption cross sections. Differential absorption cross sections,  $\Delta\sigma$ , are determined by applying the same polynomial filtering method as for the differential optical depth to molecular cross sections for all absorbers present as per Equation 2.6, as shown in panel (D).

$$\Delta\sigma_i(\lambda) = \sigma_i(\lambda) - P_i(\lambda, n)$$

Equation 2.6 Equation to calculate differential absorption cross sections.

The molecular cross sections applied in this thesis have been extensively studied by other research groups and are reported in the literature; recommended cross sections are therefore available in spectral databases (*e.g.* Keller-Rudek et al., 2013). Finally, the concentrations of absorbers can be calculated *via* simultaneous fitting of the differential cross sections to the measured differential optical depth using a minimisation method, *e.g.* nonlinear least-squares (Ball and Jones, 2003), resulting in a fitted spectrum shown in panel (C). As a final step, fitted molecular absorptions are subtracted from the original measured spectrum to leave the underlying broadband continuum which, for the highly stable BBCEAS instruments used in this work, provides a measurement of aerosol extinction.

### 2.3.5 BBCEAS hardware & application

Two BBCEAS instruments were deployed by the University of Leicester (UoL) team in the course of this project (see chapters 4 and 5). The “RONOCO cavity” instrument was named after the campaign for which it was built, to measure  $\text{NO}_3$  and  $\text{N}_2\text{O}_5$  (Kennedy et al., 2011). The “field cavity” instrument has previously been used for measurements of  $\text{I}_2$  from seaweed (Ball et al., 2010) and for  $\text{NO}_2$ , glyoxal and methyl glyoxal measurements at the EUPHORE atmospheric simulation chamber (Thalman et al., 2015). Both instruments operate in the same way but have physical cavity lengths (*i.e.* mirror separation) of 59 and 110 cm respectively. Different optics (*i.e.* light source, cavity mirrors and spectrometer) are installed depending on target species, whose absorption band(s) determine the required wavelength range. Sets of optics are therefore referred to in this thesis by the colour of light from the source. “Blue” optics were used to detect  $\text{NO}_2$  at 430-485 nm, and “red” optics for  $\text{NO}_3+\text{N}_2\text{O}_5$  at 639-680 nm wavelength, which includes the 662 nm band of  $\text{NO}_3$  ( $\text{NO}_3$  and  $\text{N}_2\text{O}_5$  were later separated using a steady state equation - see

section 2.3.6). A schematic diagram of the UoL RONOCO BBCEAS instrument is shown in Figure 2.5.

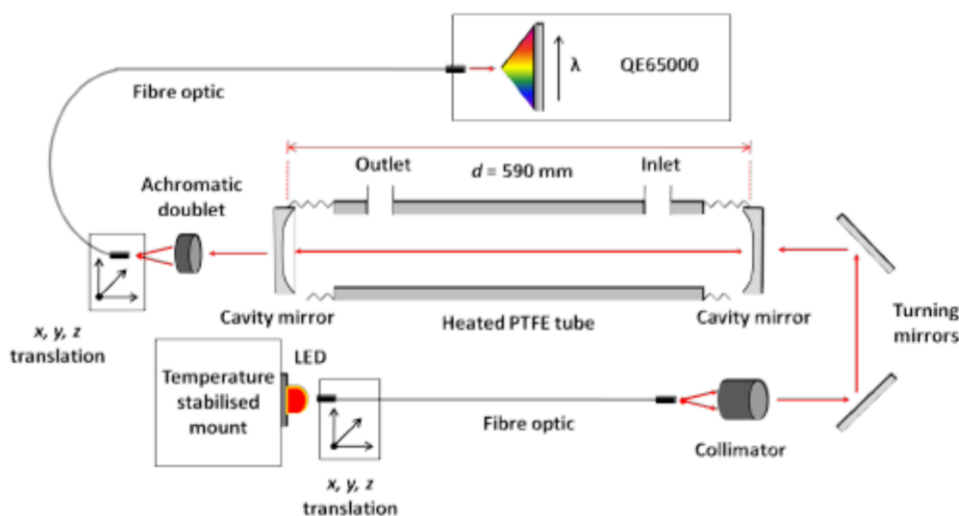


Figure 2.5 Schematic diagram of UoL RONOCO BBCEAS operating in red wavelengths. Figure reprinted from Daniels, 2012.

High power light emitting diodes (LED) were chosen as the broadband, CW light sources for BBCEAS work described in this thesis, as these represent compact and energy-efficient broadband light sources with highly stable output. LED Engin LZ1-00R200 was used for work in red wavelengths (for  $\text{NO}_3 + \text{N}_2\text{O}_5$ ) or LED Engin LZ1-10B205 for work in the blue wavelength region (for  $\text{NO}_2$ ). The LED was supplied with a steady current, using a regulated power supply (Thurlby EL302). Additionally, the LED was temperature-stabilised by mounting on Peltier thermoelectric cooled (TEC) mounts (Newport Corporation) which is necessary because LED output typically decreases with increasing temperature, and shifts to longer wavelengths. An optic fibre (Ocean Optics QP400; 400  $\mu\text{m}$  fibre core diameter, 0.22 numerical aperture, 2 m length) carried the light from the LED to an infinity corrected microscope objective lens (Leica) to collimate the light. The resultant light beam was directed into the cavity *via* two turning mirrors.

A diaphragm pump (KNF Neuberger) attached to the outlet pulled sample gas through the cavity. Calibration gas inputs, in addition to the output *via* the pump, were controlled *via* mass flow controller (MFC; Alicat MC series). The optical cavity itself was a thick-walled PTFE tube (25.4mm internal diameter).

Cavity mirrors (Layertec 104355 (red) or 108621 (blue); 1" diameter, 1000 mm curvature radius) were held by bellows mounts enabling alignment optimisation to maximise light intensity throughput. An optional MFC-controlled mirror purge (not shown) allowed a small flow of nitrogen to be passed over each mirror continuously to protect against contaminants such as dust or sea salt that may affect reflectivity (this was only used during Weybourne field measurements). The use of mirror purge flows reduces the portion of the cavity filled with absorbing sample, necessitating a length factor correction (see section 2.3.6). The RONOCO instrument was also fitted with heated inlet and cavity heater which, during work in red wavelengths, were set to 100 and 70 °C respectively to instigate and maintain dissociation of  $\text{N}_2\text{O}_5$  to  $\text{NO}_3$  (see section 2.3.1). Heating of the cavity was not necessary for work in blue wavelengths, therefore both heaters were deactivated.

The light leaking from the cavity was collected by an achromatic doublet lens (Thorlabs; 25.4 mm diameter, 40 mm focal length) for focusing onto a second similar optic fibre. The fibre conveyed the light into a USB spectrometer (Ocean Optics QE65000 (red) or Ocean Optics HR2000 (blue)). Data were logged using Ocean Optics SpectraSuite software (provided with the USB spectrometers) and stored on a laptop computer. For work in red wavelengths, 10 scans of 1 s were averaged to give a 10 second integration time per data point whereas for blue wavelengths 50 scans of 0.1 s were averaged (5 second integration time).

### 2.3.6 Data processing

Raw BBCEAS output takes the form of a spectrum *via* the intensity of light observed by an array of pixels within the spectrometer, each of which corresponds to a specific wavelength of light. This subchapter describes the processing of spectrometer outputs (*i.e.* BBCEAS data) to give the concentration of target absorbing species as a mixing ratio.

BBCEAS spectra were processed using a series of analysis routines using the PTC Mathcad Prime 3.1 software package. These routines were developed and previously reported by Hollingsworth, 2010, Daniels, 2012 and Adams, 2015. Before the DOAS fitting procedure can be applied to determine absorber

concentrations, several other techniques must first be applied. First, the wavelength scale reported by the spectrometer is corrected. Line shapes for the spectrometer are then established to adapt absorption cross sections from the literature to the resolution of the spectrometer used. Electronic noise (dark currents) are removed and the wavelength dependent mirror reflectivity determined. After absorber concentrations are established, a length factor correction must be applied for cases where a mirror purge was used.

#### a) Detector line shapes & wavelength calibration

The first step in processing raw data is to determine the detector line shapes and calibrate the wavelength scale to ensure correct fitting of absorption cross sections. This was experimentally determined by successively positioning argon and krypton lamps (Pen-ray) in front of the collection optic fibre and measuring the lamps' emission spectra. Atomic emission lines occur at a number of well-defined wavelengths across the spectrometer's wavelength range. A modified Gaussian function was fitted to the measured emission lines using the intensities, centre wavelengths, half width at half maximum height (HWHM) and an asymmetry parameter. The centre wavelengths of fitted peaks were then compared with those of reference peaks from the NIST Atomic Spectra Database (Kramida et al., 2016) in which well-known, precise wavelengths of the Ar and Kr lines can be found (typically to 0.0001 nm accuracy). The difference between reference and measured values was fitted with a third order polynomial function to determine the accurate wavelength for each pixel. An example of differences between measured and reference wavelengths for Ar and Kr lines is shown in Figure 2.6, with the fit through the data points (a second order polynomial in this case) used to shift spectra's reported wavelength scale onto the absolute wavelength scale. The HWHM and asymmetry parameter similarly showed significant wavelength dependency and were also fitted with third order polynomial functions to interpolate across the range of the detector to apply to reference cross sections used in the DOAS fitting procedure.

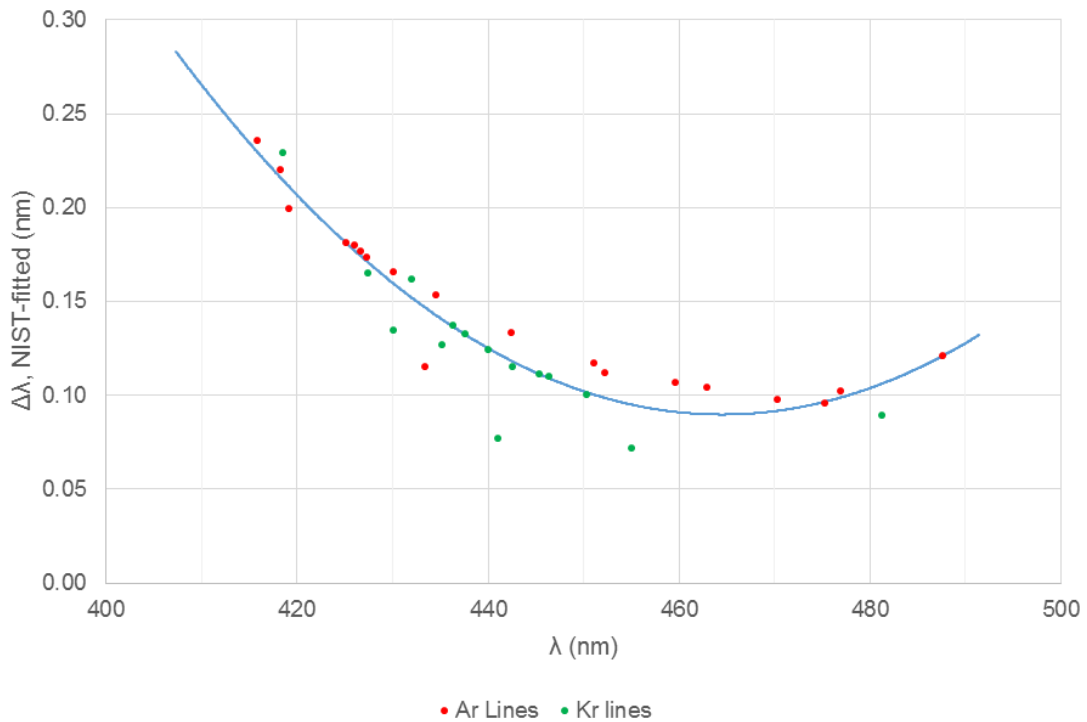


Figure 2.6 Example wavelength calibration curve for the HR2000 spectrometer used in BBCEAS instruments at blue wavelengths.

#### b) Dark currents

The spectrometers record a non-zero spectrum even when no light is present, known as a dark current spectrum, which it is necessary to subtract from measured sample spectra before calculating absorption. The dark current is a manifestation of electronic noise within the spectrometers' charged couple device (CCD) detectors, and is heavily dependent on temperature. Spectrometer temperatures were therefore controlled.

The HR2000 (blue) spectrometer functioned adequately in the air-conditioned laboratory for ClNO<sub>2</sub> calibration experiments detailed in section 3.4, but was placed inside a TEC-regulated refrigerator during field measurements at Weybourne (see section 5.1.2). The QR65000 (red) spectrometer has an integrated TEC system on the CCD detector to minimise dark current, however this became overwhelmed by excessive temperatures in the observatory room space during the Penlee Point deployment (see section 5.10). The QR65000 spectrometer was therefore placed inside a modified camping refrigerator

(Halfords) partway through this campaign and throughout the subsequent Weybourne deployment. Refrigerators were purged with a small flow of nitrogen (~200 sccm) to prevent water condensation.

Dark spectra were acquired periodically throughout campaigns (typically twice daily) covering a range of room temperatures. To do this several dark spectra were recorded (at the same integration time as general measurements) with the light beam blocked, and averaged over 2 minutes. Several dark pixels exist on each spectrometer. Dark pixels are never illuminated even with the light source present, however the intensity detected by these pixels scale linearly with temperature, for which they can therefore be used as a proxy. The mean intensity of the full dark spectrum also scales linearly with temperature. For each measured spectrum, a synthetic dark spectrum was therefore generated using the observed intensity of dark pixels, which could then be subtracted to account for dark currents.

### c) Mirror reflectivity

The reflectivity of the cavity mirrors varies with wavelength, giving different effective path lengths across the spectrum. Reflectivity of the mirrors can furthermore be affected by factors such as cleanliness and alignment. The wavelength dependent reflectivity therefore had to be determined frequently *via* Equation 2.7. This equation is a rearrangement of Equation 2.4, where the absorption coefficient  $\alpha$  is the known absorption coefficient of a reference sample ( $\alpha_{ref}$ ). In Equation 2.7,  $LF$  represents the length factor (described below), however the mirror purge flows were disabled for the purposes of this procedure therefore  $LF=1$ .

$$R(\lambda) = 1 - \frac{\alpha_{ref}(\lambda)d}{LF} \cdot \left( \frac{I_0(\lambda)}{I_{ref}(\lambda)} - 1 \right)^{-1}$$

Equation 2.7 Equation to determine wavelength dependent reflectivity of cavity mirrors.

Mirror reflectivity could in principle be measured using a sample containing a target absorber of known concentration, for which standard cylinders may be available. In practice, however, cylinder concentrations can degrade over time (particularly for reactive gases, e.g. NO<sub>2</sub>) therefore an alternative method using Rayleigh scattering is used.

Extinction due to Rayleigh scattering varies slowly with wavelength, allowing mirror reflectivity to be determined from the difference in scattering between two non-absorbing species that have different Rayleigh cross sections (Washenfelder et al., 2008). For a cavity purged with 100% pure, non-absorbing gas (e.g. N<sub>2</sub> or He), Rayleigh scattering and mirror interactions will be the only light losses. Therefore as part of standard calibration procedures used throughout work in this thesis nitrogen and helium were successively flowed through the cavity for 10 minutes each, as their Rayleigh cross sections are significantly different and well-known (N<sub>2</sub>, Snee and Ubachs, 2005; He, Jack and Alois, 2004).

The reference absorption coefficient ( $\alpha_{ref}$ ) is calculated *via* Equation 2.8 using the measured extinction due to Rayleigh scattering ( $\epsilon_{Rayleigh}$ ) and the molecular concentrations of the calibration gases ([He] and [N<sub>2</sub>]) at cavity operating temperature and pressure. The known  $\alpha_{ref}$  can then be used with the  $I(\lambda)$  and  $I_0(\lambda)$  from measured spectra to determine mirror reflectivity *via* Equation 2.7.

$$\alpha_{ref} = [\text{He}] \cdot \epsilon_{Rayleigh(\text{He})} - [\text{N}_2] \cdot \epsilon_{Rayleigh(\text{N}_2)}$$

Equation 2.8 Equation to calculate reference absorption coefficient using Rayleigh scattering of N<sub>2</sub> and He.

An example of wavelength dependent mirror reflectivity determined from the difference in Rayleigh scattering measured in N<sub>2</sub> and He are shown in Figure 2.7a. Since the mirror reflectivity is expected to vary smoothly with wavelength, the reflectivity curve is smoothed by applying a cubic spline between selected points at ~5 nm separations (Figure 2.7b). This curve is

applied to calculate  $\alpha_{sample}$ , which is then fitted *via* DOAS to retrieve absorber concentrations.

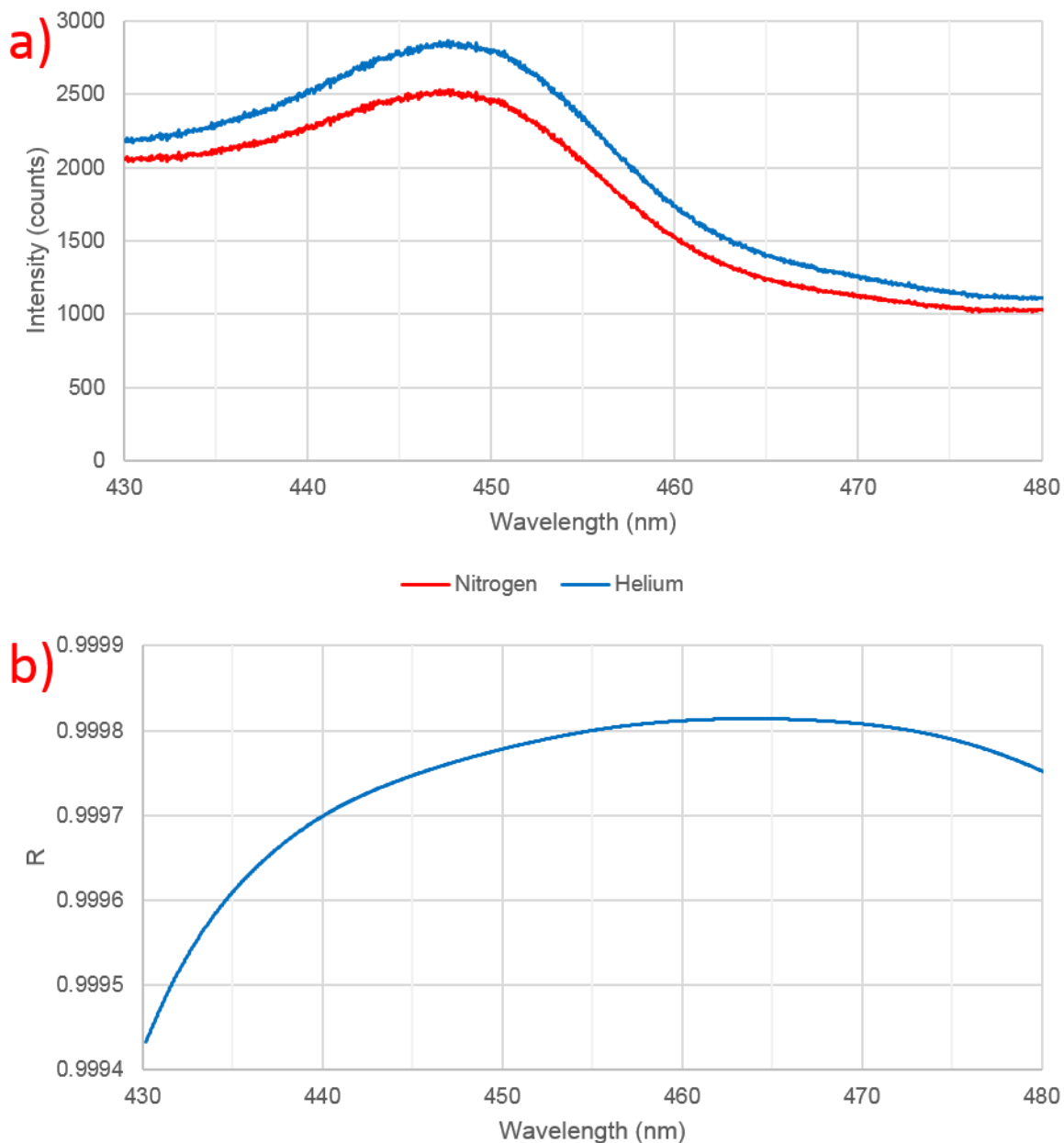


Figure 2.7 Example wavelength dependent reflectivity of cavity mirrors using field cavity data from the Weybourne Atmospheric Observatory field campaign.

- a) Light intensity observed by HR2000 spectrometer during nitrogen and helium flushes.
- b) Mirror reflectivity curve.

The cavity was similarly filled with pure oxygen for 10 minutes to check and tweak mirror reflectivity using DOAS fitting of the structured absorption of the O<sub>2</sub>-O<sub>2</sub> collision complex as a reference absorber, which is not susceptible to instrument instability (unlike unstructured extinction due to Rayleigh scattering).

#### d) Fitting procedure

In brief, the reference ( $I_0$ ; with N<sub>2</sub>-flushed cavity) and observed ( $I$ ; from sample-filled cavity) spectra were corrected for dark currents to give optical depth and used in Equation 2.4 to calculate the wavelength-dependent absorption coefficient of the sample,  $\alpha_{sample}$ . The DOAS fitting procedure for absorbers was applied to  $\alpha_{sample}$  as detailed in section 2.3.4. Smoothly-varying contributions to the absorption coefficient by non-molecular absorbers (e.g. aerosol extinction) were removed *via* fitting of a polynomial function to give the differential optical depth. Reference absorption cross sections were taken from literature sources (H<sub>2</sub>O, Rothman et al., 2009; NO<sub>2</sub>, Vandaele et al., 2002; glyoxal, Volkamer et al., 2005; NO<sub>3</sub>, Yokelson et al., 1994) and convolved with the spectrometer line width and asymmetry functions (measured in section 2.3.6a). Differential absorption cross sections were then obtained by fitting the instrument-adapted molecular cross-sections with polynomial functions of the same ( $n=6$ ) order applied to observed spectra. Finally, absorber concentrations were determined by fitting the differential cross sections to the differential optical depth using a singular value decomposition method. The continuum absorption was calculated *via* subtraction of all fitted molecular spectra from measured spectra. The continuum measurement represents extinction contributions from unstructured absorbers and any broadband Mie scattering by aerosol particles. The continuum also contains variations in the  $I_0$  spectrum due to changes in light source or mirror reflectivity (notably dust contamination). To account for changes in  $I_0$  spectrum, calibrations were performed at both the start and end of experiments (or daily, during campaigns).

Figure 2.8 shows examples of the final resulting fitted spectrum using sample (top) and blank (bottom) data from a CIMS calibration experiment (see section

3.4) using blue optics to detect NO<sub>2</sub>. The retrieved NO<sub>2</sub> concentrations are shown, along with measured spectra for comparison. Note that, based on these individual measurements, the uncertainty in the 6.1 ppb NO<sub>2</sub> measurement is 0.092 ppb (~1.5%), and the 1 $\sigma$  limit of detection (*i.e.* mean + 1 standard deviation of blank measurements) is 0.11 ppb, demonstrating the high precision and sensitivity of the technique.

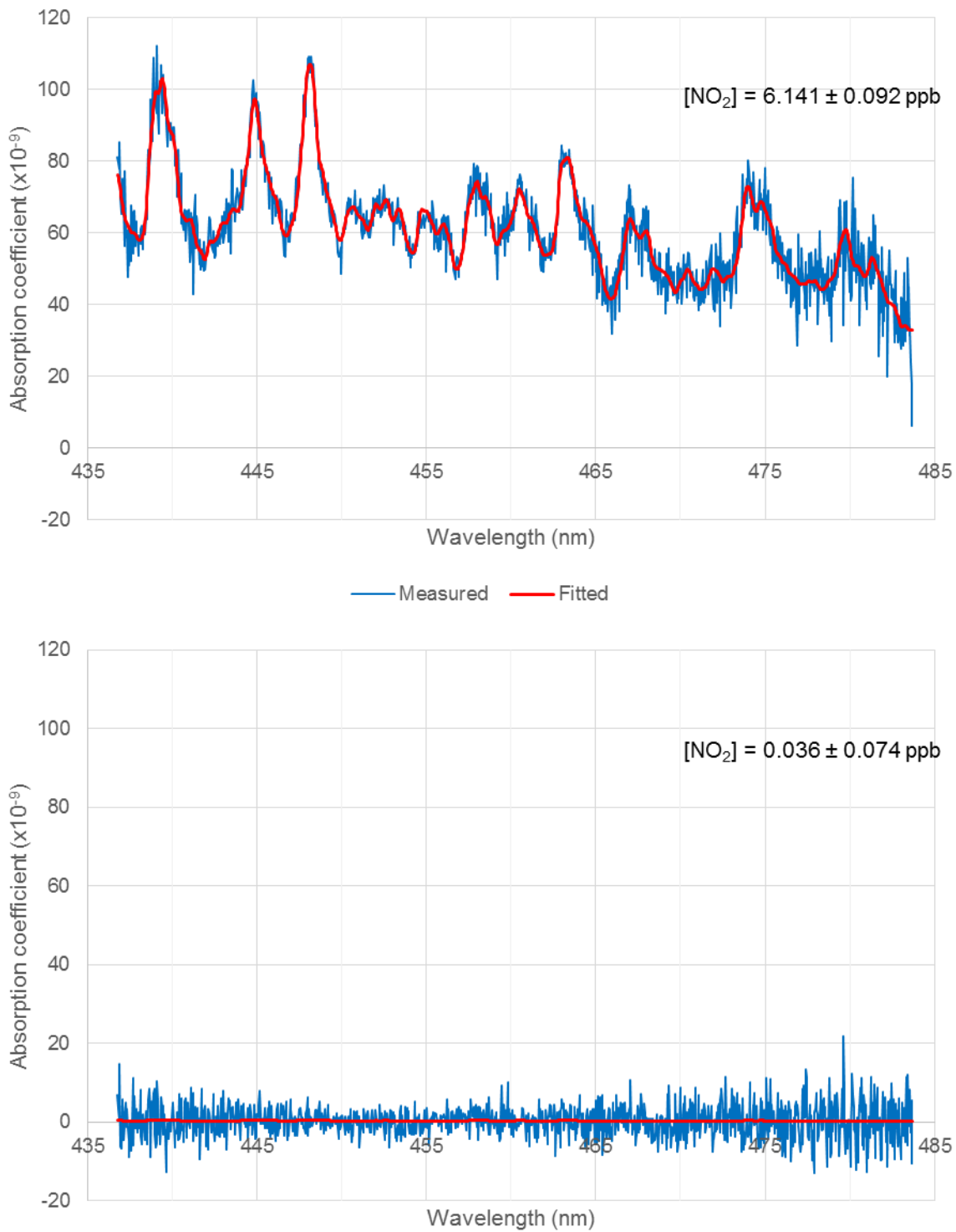


Figure 2.8 Example measured and fitted NO<sub>2</sub> absorption spectra of NO<sub>2</sub> sample (top) and N<sub>2</sub> flush (bottom) measurements during a CIMS ClNO<sub>2</sub> calibration.

#### e) Length factor correction

The final step in data processing is the application of a length factor correction (where applicable). This correction must be applied in situations where N<sub>2</sub> was flowed over the mirrors, thus reducing the fraction of the cavity occupied by samples (for data in this thesis, only during the Weybourne Atmospheric Observatory campaign). When the mirror purges are enabled, a small flow of nitrogen is passed over the cavity mirrors to protect from contaminants, however the cavity is then not completely filled with the absorber sample. The resultant under-measurement of absorber concentration in the central (sample) part of the cavity therefore applies equally to all species in the sample.

Two simple methods can be used to calculate length factors, represented in Equation 2.9. Both of these methods are flawed, however, as the dilution length factor assumes full mixing between the N<sub>2</sub>-purged mirror mounts and the sample gas, whereas the geometric length factor assumes no mixing. In practice, there is partial mixing between the mirror mount and sample gas sections of the cavity.

$$LF = \frac{F_s + F_p}{F_s} \quad \text{a}$$

$$LF = \frac{d_m}{d_s} \quad \text{b}$$

Equation 2.9 Simple equations for calculating length factor.

- a) *Via* dilution, using flow rates of the sample ( $F_s$ ) and combined N<sub>2</sub> mirror purges ( $F_p$ ).
- b) *Via* geometry, using separation distances between the mirrors ( $d_m$ ) and between sample inlet & outlet ports ( $d_s$ ).

A more sophisticated and accurate method was applied to data gathered in this thesis. BBCEAS data are worked up as outlined above, and the retrieved concentration of water (or another absorbing species) is correlated to an independent measurement.

For the example of Weybourne NO<sub>2</sub> measurements, the H<sub>2</sub>O concentration retrieved by the UoL BBCEAS (using its 444 nm absorption band) were converted to a mixing ratio. University of Leeds relative humidity measurements were also converted to a mixing ratio and correlated with the UoL retrieved H<sub>2</sub>O (Leeds measurements were selected for their proximity to the UoL BBCEAS inlet). The resulting correlation plot is shown in Figure 2.9, from which the length factor was determined as the inverse of the gradient (in this case  $LF=1.61$ ). All concentrations retrieved from fitting BBCEAS spectra were then multiplied by the length factor (*i.e.*  $\alpha(\lambda)_{true} = \alpha(\lambda)_{retrieved} \times LF$ ).

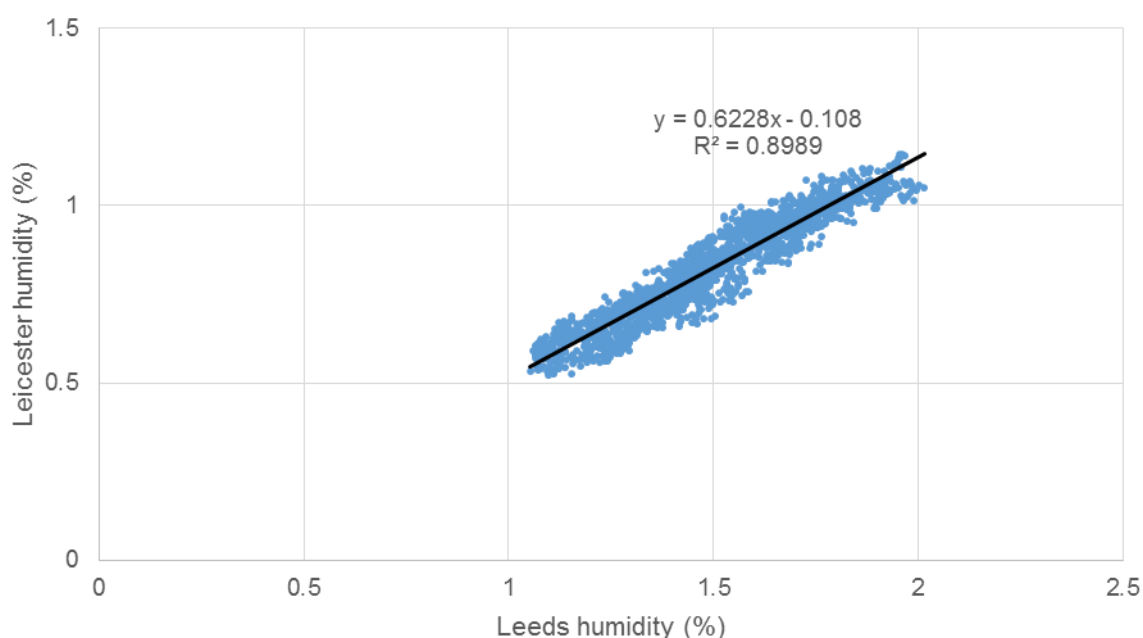


Figure 2.9 Correlation between University of Leicester BBCEAS fitted H<sub>2</sub>O and University of Leeds humidity measurements (as mixing ratios, %vol) to calculate length factor correction.

#### f) Additional processing of NO<sub>3</sub> and N<sub>2</sub>O<sub>5</sub> data

N<sub>2</sub>O<sub>5</sub> does not have any absorption bands at visible wavelengths. BBCEAS measurements of this species were therefore done by drawing gas into the instrument *via* heated inlet (100 °C), dissociating N<sub>2</sub>O<sub>5</sub> to be measured as NO<sub>3</sub>. While laboratory measurements of N<sub>2</sub>O<sub>5</sub> (see section 3.3.4) did not contain NO<sub>3</sub> from other sources, it was necessary for field measurements to separate signal

due to dissociated N<sub>2</sub>O<sub>5</sub> from NO<sub>3</sub> present in the ambient atmosphere. This separation was done by calculating the partitioning of NO<sub>3</sub> and N<sub>2</sub>O<sub>5</sub> via Equation 2.10a (Benton et al., 2010), from which Equation 2.10b and c (Ball, 2017) are derived.

$$\frac{[\text{NO}_3]}{[\text{N}_2\text{O}_5]} = \frac{1}{K_{\text{eq}}[\text{NO}_2]} \quad \text{a}$$

$$[\text{NO}_3] = \frac{[\text{NO}_3 + \text{N}_2\text{O}_5]}{1 + K_{\text{eq}}[\text{NO}_2]} \quad \text{b}$$

$$[\text{N}_2\text{O}_5] = [\text{NO}_3 + \text{N}_2\text{O}_5] \cdot \left(1 + \frac{1}{K_{\text{eq}}[\text{NO}_2]}\right)^{-1} \quad \text{c}$$

Equation 2.10 Equations to determine NO<sub>3</sub> and N<sub>2</sub>O<sub>5</sub> from BBCEAS measurements.  $K_{\text{eq}} = 5.5 \times 10^{-27} \exp\left(\frac{10724}{T}\right)$  (Brown and Stutz, 2012).

This partitioning assumes equilibrium conditions - *i.e.* production, loss and transport processes are slow compared to chemical interconversion of NO<sub>3</sub> and N<sub>2</sub>O<sub>5</sub> via the temperature-dependent equilibrium formed by R 2.5 and R 2.6.



NO<sub>3</sub> and N<sub>2</sub>O<sub>5</sub> data inferred from such steady state analysis should be used with caution as Brown et al., 2003 showed that the equilibrium assumption fails in conditions of low NO<sub>2</sub> concentration (*i.e.* exceptionally clean air masses) or temperature. A near-equilibrium assumption should be adequate for WAO observations, however, as NO<sub>2</sub> concentrations were rarely under 0.5 ppb and temperature typically varied between 15 and 25 °C.

It was assumed that not all ambient N<sub>2</sub>O<sub>5</sub> was transmitted into the cavity to be detected as NO<sub>3</sub> (the rest being lost to NO<sub>3</sub> + wall reactions), therefore a correction factor was applied to NO<sub>3</sub>+N<sub>2</sub>O<sub>5</sub> data. Transmission efficiency was

determined through a variable flow experiment to be 76% during previous work using the same instrument and similar flow rates as were used in this work, and is not believed to change significantly over time (Daniels, 2012).

## 2.4 Other instruments deployed

In addition to the CIMS and BBCEAS, several supporting instruments were also deployed during the field campaigns at the University of Leicester, Penlee Point and Weybourne Atmospheric Observatories (UoL, PPAO and WAO respectively), described in chapters 4 (UoL) and 5 (PPAO, WAO).

### 2.4.1 University of Leicester

The UoL campaigns took place at 2 slightly different sites on the University campus. These were, for the purposes of reference, named for the location of the CIMS however all supporting instruments were at the AURN station for all UoL campaigns (see section 4.1.2 for details). The AURN station instruments described in this section (2.4.1) were operated by Dr. R. L. Cordell except where otherwise stated.

Ozone concentrations were measured using a commercial Teledyne Model T400 photometric ozone analyser with a detection limit of 0.6 ppb (Cordell, 2017). Ozone absorbs strongly at the 254 nm wavelength of a mercury vapour UV lamp, and is quantified by light absorption relative to ambient air samples drawn through a scrubber to remove O<sub>3</sub>. Possible interferences include mercury vapour and, in sufficient concentrations, aromatic hydrocarbons (Teledyne Inc., 2014). There is no reason to believe these are a significant issue at the University of Leicester urban background AURN station, however.

NO and NO<sub>2</sub> measurements at UoL were taken using a Teledyne T200 NO<sub>x</sub> chemiluminescence analyser with 0.4 ppb detection limit (Cordell, 2017). NO is exposed to ozone generated within the instrument. The NO + O<sub>3</sub> reaction produces NO<sub>2</sub> molecules in an electronically excited state (NO<sub>2</sub><sup>\*</sup>) which emit photons as they return to ground state. Photons are detected at wavelength 645 nm using a photomultiplier tube. The instrument then switches to a second

channel, flowing the sample over a molybdenum catalyst at 315 °C (Teledyne Inc., 2015). The catalyst converts ambient NO<sub>2</sub> to NO, which is then detected in the same way. The initial NO concentration is subtracted from this measurement to determine the NO<sub>2</sub> concentration. Chemiluminescence instruments experience several sources of interference. One is “third-body quenching” where NO<sub>2</sub>\* is deactivated before it can fluoresce by collision with another molecule, primarily N<sub>2</sub>, O<sub>2</sub>, H<sub>2</sub>O or CO<sub>2</sub> (Teledyne Inc., 2015). Quenching due to N<sub>2</sub> and O<sub>2</sub> can be accounted for *via* frequent calibration, whereas an optional dryer on the sample inlet can counteract quenching due to H<sub>2</sub>O. Exceedances of the 0.5% CO<sub>2</sub> concentration threshold to cause interference are not expected at this location. Another source of interference is catalytic reaction of NO<sub>y</sub> species (other than NO<sub>2</sub>) to NO frequently acting as a false positive NO<sub>2</sub> signal, which is discussed more in section 5.9.

Aerosol data for the UoL AURN station (section 5.7.1) were gathered *via* 24-hour PM<sub>10</sub> filters using a Leckel SEQ47/50 sequential standard reference sampler (Cordell, 2017) as detailed in Mooibroek et al., 2016. Filters were then analysed using ion chromatography by Dr. A. R. Baker.

A spectral radiometer (operated by Dr. T. J. Adams) was used to collect actinic flux data, which were converted into photolysis rates by Prof. R. J. Leigh. Instrument details are described in Edwards and Monks, 2003.

#### 2.4.2 Penlee Point Atmospheric Observatory

At PPAO the University of Leicester team operated the CIMS and RONOCO BBCEAS (using red optics for NO<sub>3</sub>+N<sub>2</sub>O<sub>5</sub>) instruments. The spectral radiometer and Teledyne T200 chemiluminescence NO<sub>x</sub> analyser described in section 2.4.1 were also deployed here. Additionally, carbon monoxide measurements were also made using a Teledyne T300U analyser. The CO analyser detects infrared absorption by CO at 4.7 µm wavelength, employing high-reflectivity mirrors at either end of the sample chamber to increase effective path length (similarly to the BBCEAS). Interferences due to other absorbers at the same wavelength (most notably water) are counteracted using a “gas filter correlation (GFC)

wheel” which allows rapid alternation between a sample and reference cell (Teledyne Inc., 2012).

### 2.4.3 Weybourne Atmospheric Observatory

For the WAO campaign the University of Leicester team deployed the I<sup>-</sup> CIMS, two BBCEAS (operating in red and blue wavelengths), a spectral radiometer (see section 2.4.1) and a proton transfer reaction time of flight mass spectrometer (PTR-ToF-MS) for use with comparative reactivity measurement (CRM) determination of OH reactivity. The CRM research project (Panchal, 2016) was mostly unrelated to ClNO<sub>2</sub> however, therefore PTR-ToF-MS measurements will not be discussed further in this thesis. A multistage high-volume impactor (Baker et al., 2007) was used to gather size-resolved aerosol composition data at this site and subsequently analysed by Dr. A. R. Baker *via* ion chromatography.

## 2.5 Data processing & analysis techniques

Air mass histories for each of the measurement campaigns described in chapters 4 and 5 were modelled by Dr. Z. L. Fleming using the UK Met Office’s Numerical Atmospheric dispersion Modelling Environment (NAME) in a fashion similar to that reported in Bannan et al., 2015. The model simulates the paths of a number of inert particles using meteorological data, tracing backwards from a measurement site over 5 days. 3-hourly averaged air mass footprints were generated from these particle concentrations, indicating where particles are likely to have travelled, where a given air mass is likely to have spent time and therefore which regions have influenced it. More details about the NAME model are available in Jones et al., 2007.

Plots shown in this thesis were produced using a variety of software packages. Time series and correlation plots were produced using Microsoft Excel or WaveMetrics Igor Pro. Most other plots, including wind/pollution roses, polar plots and average diel profiles were produced using R *via* the Openair software package (Carslaw and Ropkins, 2012).

Project collaborators (Dr. T. Sherwen and Dr. M. J. Evans; University of York) ran version 10-01 of the GEOS-Chem model modified to include Cl, Br and I halogen chemistry as detailed in Sherwen et al., 2016 and references therein (in brief, included are O<sub>x</sub>, HO<sub>x</sub>, NO<sub>x</sub>, VOC, Cl, Br, I chemistry and aerosol). Some of the model outputs are discussed briefly in this thesis (sections 4.8 and 5.8) however a more detailed analysis, including attempts to evaluate ClNO<sub>2</sub> impact on regional ozone concentrations, can be found in Sherwen et al., 2017.

## 3 Experimental

### 3.1 Overview

In order to assess the ubiquity and formation conditions of nitryl chloride in the UK, atmospheric ClNO<sub>2</sub> concentrations were measured using the I<sup>-</sup> CIMS instrument described in section 2.2. This technique has substantial history in the measurement of ClNO<sub>2</sub> over the last decade (see section 1.3), as it is highly sensitive and selective, as discussed in section 2.2.1. The same section also mentions the major drawback of CIMS, *i.e.* the need for calibration. This chapter therefore describes experiments carried out in the commissioning of a new CIMS instrument, in addition to the development of equipment and techniques for calibrating the instrument for ClNO<sub>2</sub> and Cl<sub>2</sub>.

Raw CIMS outputs are given as the signal at a given mass in counts per second (CpS), corresponding to the number of ions of a given  $m/z$  reaching the detector per unit time (see section 2.2.1). Ions investigated in the course of this thesis were singly-charged (*i.e.*  $m/z = m$ ), therefore in this thesis  $m/z$  and mass are used interchangeably in this context. In most cases the monitored mass corresponds to the analyte's cluster with the iodide ion, appearing on mass spectra at  $m + 127$  amu.

ClNO<sub>2</sub> and Cl<sub>2</sub> each have several corresponding masses detectable by I<sup>-</sup> CIMS, all of which were studied and are summarised in Table 3.1. Several of these masses originate from the two isotopes of chlorine, <sup>35</sup>Cl and <sup>37</sup>Cl, which occur naturally in approx. 3:1 ratio.

Table 3.1 Summary of principal masses investigated *via* CIMS during this thesis.

Target species	Ion	Mass (amu)	Ionisation
ClNO <sub>2</sub>	[ <sup>35</sup> Cl] <sup>-</sup>	162	I <sup>-</sup> + ClNO <sub>2</sub> → [ICl] <sup>-</sup> + INO <sub>2</sub>
ClNO <sub>2</sub>	[ <sup>37</sup> Cl] <sup>-</sup>	164	I <sup>-</sup> + ClNO <sub>2</sub> → [ICl] <sup>-</sup> + INO <sub>2</sub>
ClNO <sub>2</sub>	[I( <sup>35</sup> ClNO <sub>2</sub> )] <sup>-</sup>	208	I <sup>-</sup> + ClNO <sub>2</sub> → [I(ClNO <sub>2</sub> )] <sup>-</sup>
ClNO <sub>2</sub>	[I( <sup>37</sup> ClNO <sub>2</sub> )] <sup>-</sup>	210	I <sup>-</sup> + ClNO <sub>2</sub> → [I(ClNO <sub>2</sub> )] <sup>-</sup>
Cl <sub>2</sub>	[ <sup>35</sup> Cl <sub>2</sub> ] <sup>-</sup>	197	I <sup>-</sup> + Cl <sub>2</sub> → [I(Cl <sub>2</sub> )] <sup>-</sup>
Cl <sub>2</sub>	[I( <sup>35</sup> Cl <sup>37</sup> Cl)] <sup>-</sup>	199	I <sup>-</sup> + Cl <sub>2</sub> → [I(Cl <sub>2</sub> )] <sup>-</sup>
Cl <sub>2</sub>	[ <sup>37</sup> Cl <sub>2</sub> ] <sup>-</sup>	201	I <sup>-</sup> + Cl <sub>2</sub> → [I(Cl <sub>2</sub> )] <sup>-</sup>

ClNO<sub>2</sub> has 4 masses detectable *via* I<sup>-</sup> CIMS corresponding to [I(<sup>35</sup>ClNO<sub>2</sub>)]<sup>-</sup> at 208 amu (ionisation *via* cluster formation) and [I<sup>35</sup>Cl]<sup>-</sup> at 162 amu (ionisation *via* dissociative charge transfer), each with a <sup>37</sup>Cl isotopomer at +2 amu. Branching between *via* cluster formation and dissociative charge transfer ionisation channels (the ion chemistry of which is discussed in section 2.2.3) is dependent upon humidity, CDC field strength and pressure (Kercher et al., 2009).

The signals due to Cl<sub>2</sub> correspond to the [I(Cl<sub>2</sub>)]<sup>-</sup> ion with three different isotopomers at 197, 199 and 201 amu, arising from the combination of <sup>35</sup>Cl and <sup>37</sup>Cl (see section 3.2.1). The ideal ratio for these masses is 10:6:1, as the natural abundance of <sup>35</sup>Cl and <sup>37</sup>Cl is 3:1.

While a subjective CpS measurement for a given mass (in Hz) can be occasionally useful, such as for testing and diagnostics, the principal focus of this project involved quantification of ambient ClNO<sub>2</sub>. Data acquired *via* CIMS therefore required conversion into absolute terms, *i.e.* calibration. Atmospheric trace gases are typically quoted in terms of mixing ratio (usually parts per trillion in the case of ClNO<sub>2</sub>), therefore calibration/sensitivity factors were determined experimentally under similar conditions as ambient measurements (*e.g.* temperature, flow tube pressure) in order to translate the CIMS output into a mixing ratio.

Calibration procedures require an independent measurement that can be equated to a given species. For Cl<sub>2</sub> this independent measurement was obtained by calculating successive dilution factors starting from a source of known concentration. For ClNO<sub>2</sub> the independent measurement was slightly different according to the method used to generate ClNO<sub>2</sub>, however both utilised a BBCEAS instrument to quantify ClNO<sub>2</sub> by proxy; in one case as NO<sub>3</sub> with red optics and in the other as NO<sub>2</sub> with blue optics.

The BBCEAS red optics measurement actually detected NO<sub>3</sub> *via* the absorption band around 662 nm wavelength following thermal dissociation of N<sub>2</sub>O<sub>5</sub> to NO<sub>3</sub> using a heater integrated into the BBCEAS. No other NO<sub>3</sub> sources were expected, therefore the detected NO<sub>3</sub> concentration was equated to the ClNO<sub>2</sub> concentration (*i.e.* [NO<sub>3</sub>] = [N<sub>2</sub>O<sub>5</sub>] = [ClNO<sub>2</sub>] under laboratory conditions). As this methodology assumed the concentration of ClNO<sub>2</sub> observed *via* CIMS is

equal to the concentration of  $\text{N}_2\text{O}_5$  observed *via* BBCEAS, unit conversion of  $\text{N}_2\text{O}_5$  to  $\text{ClNO}_2$  and zero wall losses of either species after the reactor were therefore also assumed. Experiments using the BBCEAS in this way are discussed further in sections 3.3.4 and 3.4.1.

BBCEAS instruments using blue optics are extremely effective at measuring  $\text{NO}_2$  using the absorption at 450 nm wavelength. In later calibrations, quantitative thermal dissociation of  $\text{ClNO}_2$  was induced, which was then measured as  $\text{NO}_2$ . Calibration using the BBCEAS in this way is discussed further in section 3.4.2.

This chapter describes laboratory-based work to prepare for field deployment of the CIMS, which can be divided into several main stages forming the coming subsections of this chapter. The first section discusses experiments to set up and test the CIMS instrument. The second part is concerned with development of the calibration system, along with other related equipment and techniques. The CIMS calibration experimental procedures are outlined in the third section. Finally, the methods for processing calibration data to obtain suitable calibration factors for application to field data are detailed, along with data selection/validation and error analysis.

## 3.2 CIMS commissioning & adjustment

### 3.2.1 $\text{Cl}_2$ & $\text{Br}_2$ detection trials

The UoL-CIMS used in this project was a new instrument, therefore several experiments were designed to commission the instrument and test its ability to detect species of potential interest. These experiments also served the purpose of testing the instrument using methyl iodide reagent gas as all work in this project used this reagent gas, whereas initial instrument function testing used  $\text{SF}_6$ .

## Cl<sub>2</sub> (electroplating experiment)

An early experiment was designed to test CIMS operation with MeI reagent gas (experimental setup shown in Figure 3.1). Cl<sub>2</sub> was chosen as this molecule is relatively easy to generate, is of interest for ambient campaigns and has been detected *via* I<sup>-</sup> CIMS previously (e.g. Spicer et al., 1998; Finley and Saltzman, 2006; Liao et al., 2014; Faxon et al., 2015).

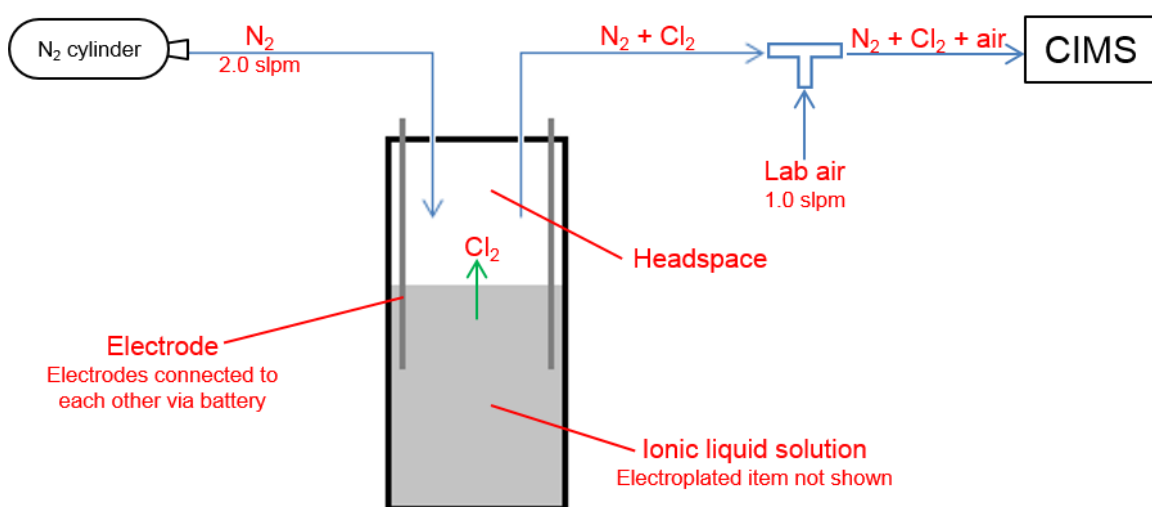


Figure 3.1 Diagram of electroplating experimental setup (mass flow controllers not shown).

Nitrogen (2 slpm *via* mass flow controller) was flowed through the headspace of a reaction vessel containing chlorine gas (released in the process of an experimental chrome electroplating technique) and diluted with laboratory air before entering the CIMS. Figure 3.2 is a mass spectrum representing the results of this experiment.

Peaks corresponding to Cl<sub>2</sub> were observed, at a ratio of approximately 7:5:1. This ratio is slightly different to the theoretical 9:6:1, possibly due mainly to saturation of the 197 amu peak. The presence of three peaks at the correct *m/z* in approximately the expected (if not quite the ideal) isotope ratio allows the conclusion that Cl<sub>2</sub> was successfully detected by the instrument.

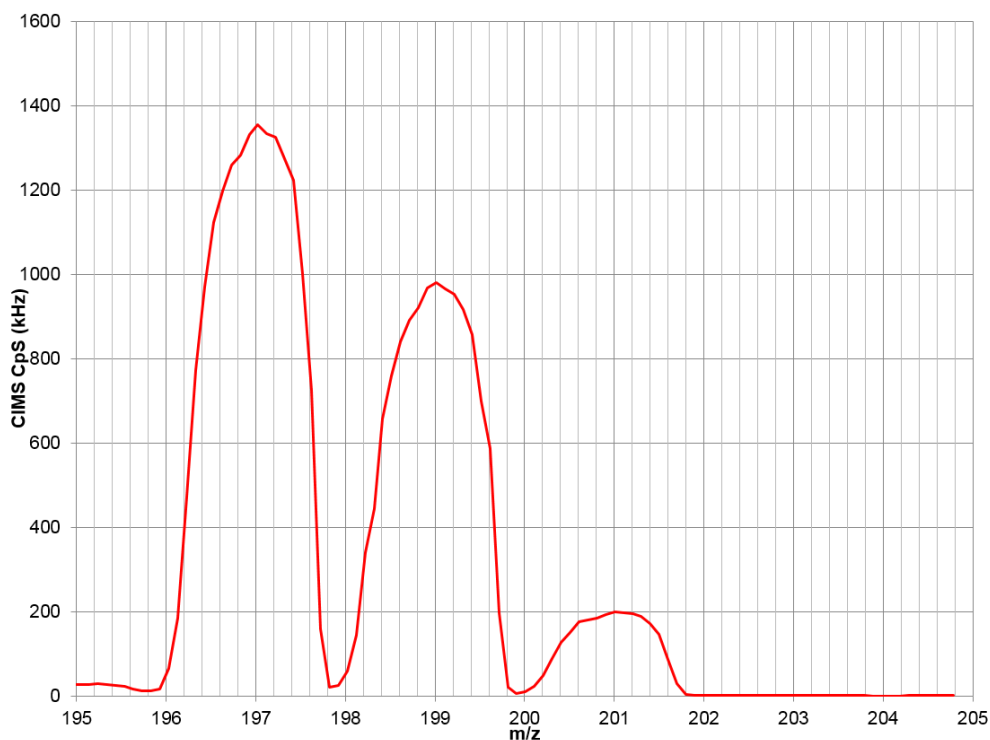


Figure 3.2 CIMS mass spectrum (average of 7 scans over 5 min) taken during the electroplating experiment showing three isotopologues of  $[I(Cl_2)]^-$  at 197, 199 and 201 amu.

### Br<sub>2</sub> (bottle headspace)

A second experiment with the same objective was carried out to detect Br<sub>2</sub>. A 10 µl syringe filled with gas from the headspace of a bottle of bromine was injected near to the inlet otherwise sampling a mixture of N<sub>2</sub>/laboratory air (the needle was inserted *via* T-connector serving as the laboratory air inlet until the tip was level with the inlet, taking care not to fully block the overflow), and a scan of a selected mass window was taken a few seconds later.

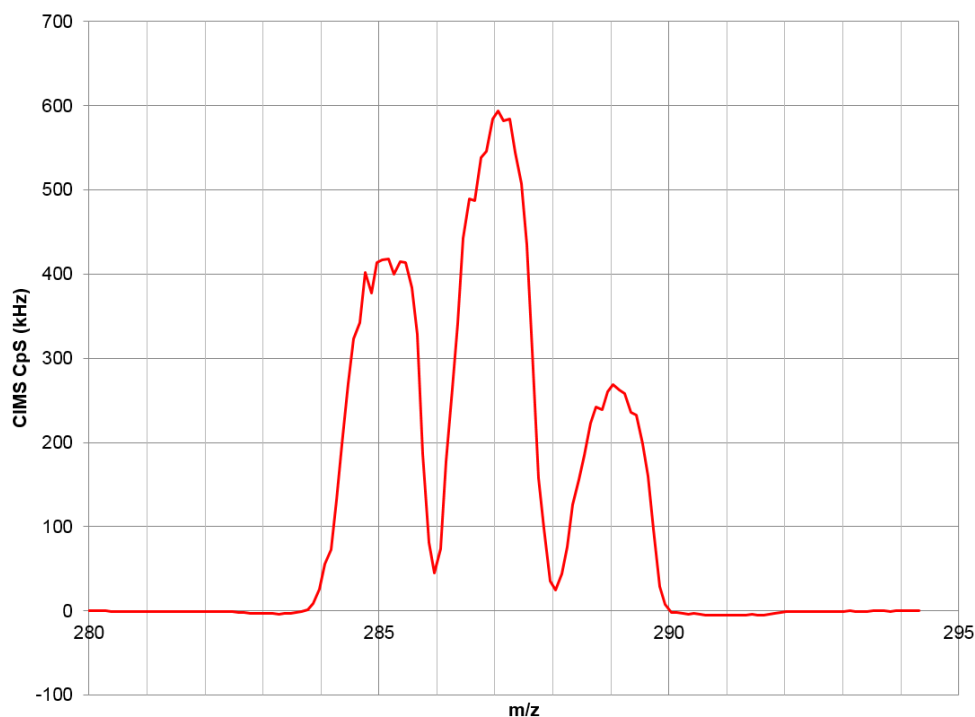


Figure 3.3 CIMS mass spectrum (dry N<sub>2</sub> background spectrum subtracted) taken during the bromine detection experiment showing three isotopologues of [I(Br<sub>2</sub>)]<sup>-</sup> at 285, 287 and 289 amu.

A similar observation was expected here - a trio of peaks representing the isotopologues of [I(Br<sub>2</sub>)]<sup>-</sup> at approximately 285 amu (for <sup>79</sup>Br<sup>79</sup>Br), 287 (<sup>79</sup>Br<sup>81</sup>Br) and 289 (<sup>81</sup>Br<sup>81</sup>Br).

The three expected peaks were observed at the correct *m/z* (Figure 3.3), indicating that Br<sub>2</sub> was successfully detected. The observed isotope ratio (approx. 8:12:5) was again a close but not exact match to ideal values (1:2:1). Assuming the other two peaks are roughly correct, the leftmost peak was too large. It is possible that another unidentified species may have been enhancing the peak at 285 amu. It should also be noted that in S-mode the detector does not perceive the spectrum instantaneously due to the time taken to scan across a defined range, during which the analyte concentration may change subtly. Injection of the Br<sub>2</sub> by hand was also non-instantaneous, which may have had a similar effect.

### 3.2.2 Detector mass calibration

A degree of offset exists between actual  $m/z$  of an ion in the mass spectrum compared to that perceived by the CIMS data logging software. The magnitude of this offset varies across the standard mass spectral range typically studied for this project CIMS (30-300 amu). For example, the three isotopologues of  $[\text{I}(\text{Cl}_2)]^-$  observed during the electroplating experiment (section 3.2.1) should display peaks in the mass spectrum at 196.8, 198.8 and 200.8 amu (for clarity, these precise masses are rounded to integers elsewhere in this thesis) but in fact were detected at approximately 0.4 amu higher than expected at 197.2, 199.2 and 201.2 amu respectively. Lower masses displayed a negative bias, with an inflexion point at approx. 165 amu. The offset was generally small and did not drastically affect the operation of the instrument but required calibration in order to analyse data as accurately as possible, for example to measure the centre (and, therefore, full height) of a given mass spectral peak during ambient measurements when the CIMS is operating primarily in H-mode (*i.e.* monitoring predefined masses, accurate to 0.1 amu).

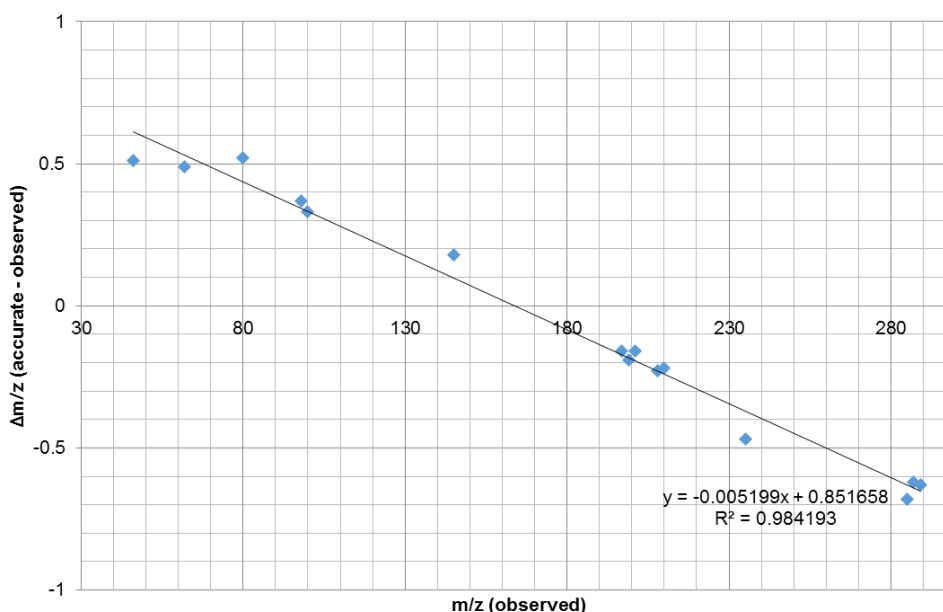
Table 3.2 Selected list of ions & clusters monitored in using the CIMS H-mode. Masses are quoted in atomic mass units (amu).

Ion	Mass (accurate)	Mass (observed)	Comments
$\text{I}^-$	126.90	126.81	Reagent ion
$[\text{I}(\text{H}_2\text{O})]^-$	144.92	144.90	Secondary reagent ion
$[\text{I}^{35}\text{Cl}]^-$	161.87	161.99	Secondary $\text{ClNO}_2$ ion (major isotope)
$[\text{I}^{37}\text{Cl}]^-$	163.87	164.00	Secondary $\text{ClNO}_2$ ion (minor isotope)
$[\text{I}^{35}\text{Cl}_2]^-$	196.84	197.18	Observed in electroplating experiment
$[\text{I}^{35}\text{Cl}^{37}\text{Cl}]^-$	198.84	199.19	Observed in electroplating experiment
$[\text{I}^{37}\text{Cl}_2]^-$	200.84	201.20	Observed in electroplating experiment
$[\text{I}^{35}\text{ClNO}_2]^-$	207.87	208.23	Primary monitored $\text{ClNO}_2$ ion (major isotope)
$[\text{I}^{37}\text{ClNO}_2]^-$	209.86	210.24	Primary monitored $\text{ClNO}_2$ ion (minor isotope)
$[\text{I}(\text{N}_2\text{O}_5)]^-$	234.89	235.37	$\text{ClNO}_2$ precursor
$[\text{I}^{79}\text{Br}_2]^-$	284.74	285.64	Observed in bromine isotopologue experiment
$[\text{I}^{79}\text{Br}^{81}\text{Br}]^-$	286.74	287.65	Observed in bromine isotopologue experiment
$[\text{I}^{81}\text{Br}_2]^-$	288.74	289.66	Observed in bromine isotopologue experiment

## Offset correction

For the first step in the mass calibration, mass spectra were collected from various prior experiments. Fifteen different masses from 46 to 289 amu were selected for confidence in their identities. Table 3.2 is a selected list of ions observed by the CIMS, many of which were used in this mass calibration, with accurate mass values and where each was observed on a mass spectrum.

The full width at half maximum height (FWHM) for these peaks were determined by hand. These peak widths were checked to ensure each represented 1 amu (*i.e.* no merged peaks). The accurate location of each observed peak, defined as the centre point of the FWHM, was compared against the ideal mass of that ion. The equation made from a plot of accurate mass values against these masses observed *via* CIMS (Figure 3.4) was then used to compensate for CIMS detector offset, and adjust masses monitored in H-mode for subsequent experiments.



$$m = -0.005199 n + 0.8516 + n$$

Figure 3.4 Mass calibration displaying offset in mass observed by the CIMS and the equation later used to correct for this.  $m$  = corrected mass;  $n$  = observed mass.

## Drift correction

The detector experiences a slow drift over time (on the timescale of months). This means that the full peak height for a given ion was not necessarily being represented at masses monitored in H-mode in subsequent data (e.g. during field observations) therefore a correction factor had to be devised for retroactive application. Numerous mass spectra had been acquired over the prior 18 months of experiments and field data, which were analysed to determine the average heights of a given peak at 1) the exact mass monitored in H-mode, and 2) the maximum height of that ion's peak in spectrum mode (Brown, 2016). The relative heights were therefore translated into a set of correction factors at key dates. As the drift is slow, the correction factor at the nearest key date was applied to field and laboratory measurements.

### 3.2.3 CIMS optimisation

A set of experiments was devised to optimise sensitivity for peaks of interest. An explanation of the components mentioned in this section (and the functions thereof) is included in section 2.2.

During these experiments a sample gas containing a steady concentration of ClNO<sub>2</sub> was flowed into the CIMS, the signal for which was monitored while changing instrument settings. The reaction and experimental setup was similar to that used in ClNO<sub>2</sub> calibration detailed later in section 3.4.2.

## Collisional dissociation chamber

The detection sensitivity for ClNO<sub>2</sub> (and potentially other analytes) via I<sup>-</sup> CIMS is in one regard increased due to cluster formation, as the [I(H<sub>2</sub>O)]<sup>-</sup> cluster acts as an additional reagent ion (see section 2.2.3) but, as mentioned in section 2.2.4, clustering can also reduce sensitivity by distributing a given analyte over different clusters of various  $m/z$ . The CDC is designed to counteract this effect by inducing collisions between ions.

Potentials are applied to the pinhole orifices at the entrance and exit of the CDC, the difference between which determines the net electric field strength. Higher net field strengths result in greater collision energy and thus more declustering, but if too high this can lead to dissociation of the reagent ion/analyte cluster (e.g.  $[I(\text{ClNO}_2)]^-$ ). In practice a balance must therefore be struck between maximum water/analyte cluster dissociation and minimum reagent ion/analyte cluster dissociation (Kercher et al., 2009). In this experiment, the CDC net field strength was therefore adjusted by changing entrance and exit orifice voltages (and the CDC octopole voltages to compensate).

Table 3.3 shows the initial and final CDC voltage settings. Ultimately the CDC net field strength was increased significantly (15.4 to 31.7 V). The  $[I(\text{H}_2\text{O})]^-$  water cluster peak at 145 amu was dramatically reduced (Figure 3.5a) so that it was no longer saturated. Desaturation of this peak therefore gives an accurate measure of  $[I(\text{H}_2\text{O})]^-$ , which was a prerequisite for using this signal to normalise others during data processing to account for humidity-related sensitivity variations (see section 3.5.1).

Additionally, the increased field strength improved sensitivity of  $[I(\text{Cl}_2)]^-$  via the principal mass for ambient  $\text{Cl}_2$  measurements at 197 amu, enhancing its signal:noise ratio (S/N; Figure 3.5b). Sensitivity of the  $[I(\text{Cl}_2)]^-$  isotopologue at 199 amu was also improved. The sensitivity of masses corresponding to  $\text{ClNO}_2$  at 208 and 210 amu were mostly unaffected, while those of several unidentified interferences were diminished (Figure 3.5c).

Table 3.3 A comparison of the original and adjusted voltages to developed in the experiments to adjust CIMS settings (quadrupole voltages omitted).

Component	Original	Adjusted
Entrance orifice	-10.00	-25.00
Exit orifice	5.400	6.700
CDC RF	1.480	1.850
CDC DC	-4.600	-4.600

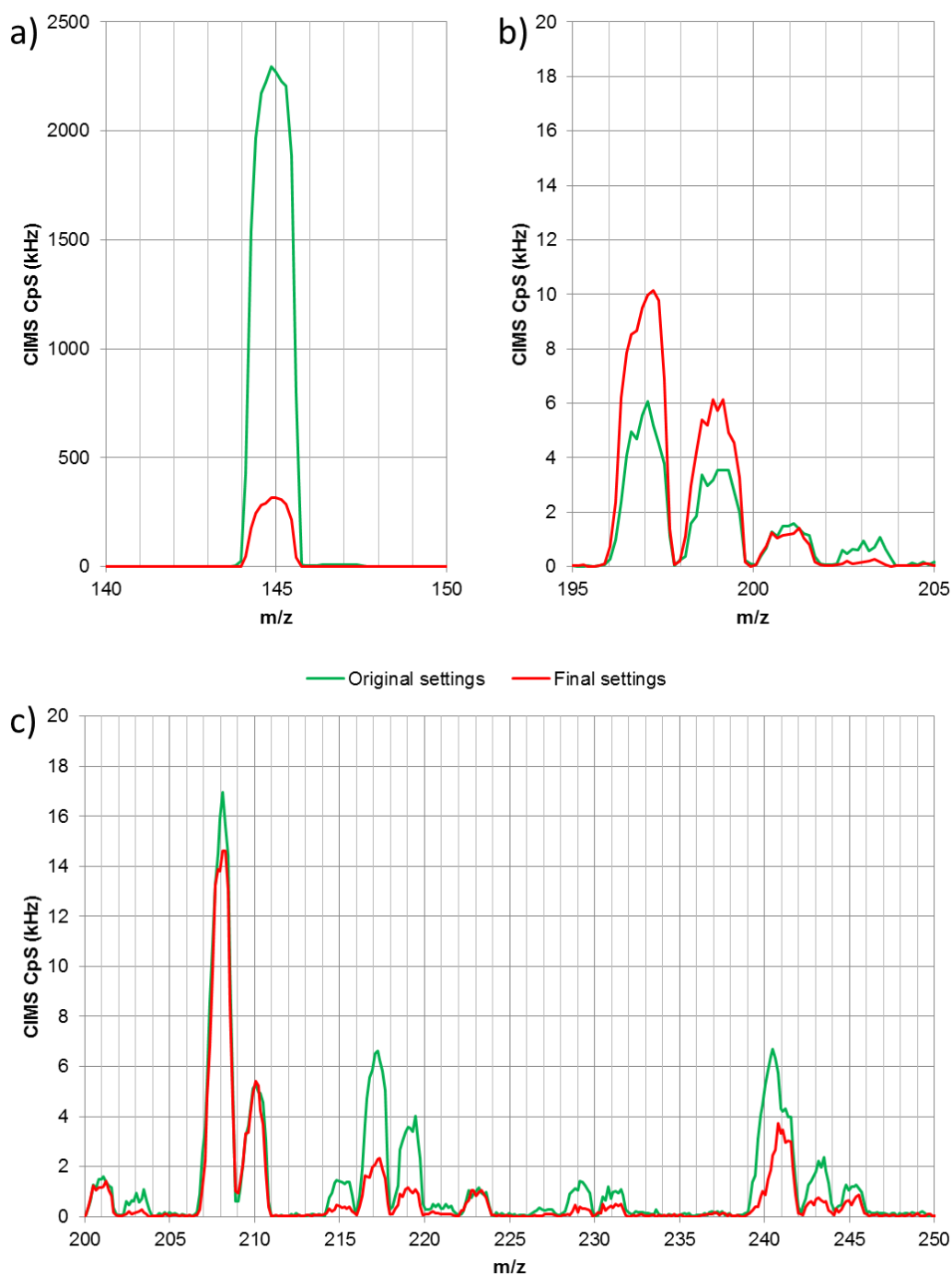


Figure 3.5 Mass spectra demonstrating the effect of changes to CIMS peaks before and after adjustments to CDC voltages (note different scale on vertical axes).

- Around the  $[I(H_2O)]^-$  cluster at 145 amu, which loses saturation.
- Enhanced peaks for  $[I(Cl_2)]^-$  at 197, 199 and 201 amu.
- At 200-250 amu, demonstrating the reduction of several “noise” peaks compared to relatively minimal impact upon  $[I(ClNO_2)]^-$  at 208 and 210 amu.

## Mass filter

Some peaks in the mass spectrum were very broad, in some cases merging together. To correct this, resolution was improved by tuning the quadrupole mass selector voltage. In this case, increasing voltage enhances peak separation but causes a loss of sensitivity as a greater proportion of ions are filtered out. For the UoL-CIMS, adjusting quadrupole settings changes two coupled variables (corresponding to DC and RF voltages - see section 2.2.2).

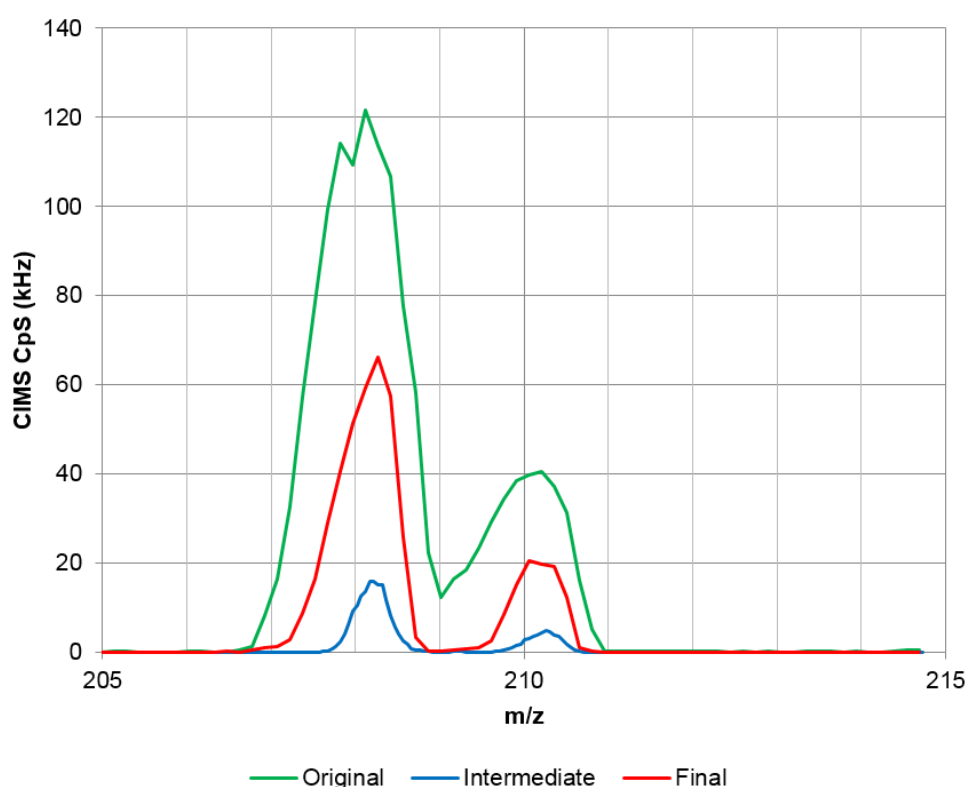


Figure 3.6 Graph showing changes observed in  $[I(\text{ClNO}_2)]^-$  peaks at 208 and 210 amu when varying quadrupole voltages.

Figure 3.6 shows a non-zero reading present at 209 amu under the original settings (green line), seemingly due not to a peak at this  $m/z$  but from incomplete separation of the two  $[I(\text{ClNO}_2)]^-$  isotopomers peaks at 208 and 210 amu. The blue line shows the effects of increasing voltage too far resulting in a severe drop in sensitivity with more peak separation than necessary, however

the final settings (red) demonstrate complete separation while retaining significant sensitivity.

The new settings therefore improved clarity by removing some peak merging in the mass range of main interest (150-250 amu) with only a modest loss of sensitivity. Furthermore, use of data for the  $[^{35}\text{Cl}]^-$  and  $[^{37}\text{Cl}]^-$  isotopologues (which also correspond to  $\text{ClNO}_2$  - see section 2.2.3) was made possible, as their respective peaks at 162 and 164 amu now had better separation from a signal at 163 amu (possibly a water cluster,  $[(\text{H}_2\text{O})_2]^-$ ) which previously overlapped with both.

### 3.3 CIMS calibrations: preparation and development

#### 3.3.1 Overview

The CIMS instrument was calibrated during this project to detect  $\text{Cl}_2$  and  $\text{ClNO}_2$ . This subchapter describes various equipment and experiments supporting calibration procedures which themselves are discussed in section 3.4. Most of the equipment beyond the CIMS and BBCEAS instruments was eventually assembled within a portable case (the “calibration box”) designed to facilitate  $\text{ClNO}_2$  and  $\text{Cl}_2$  calibrations in the field.



Figure 3.7 Picture of the calibration system in field-portable box.

The experimental setup for calibration experiments was designed to be compact, and the final iteration was fixed into a portable case with removable sides, as shown in Figure 3.7. The calibration box was approx. 40x40x50 cm (external dimensions) with a built-in control panel to regulate flow controllers (see section 3.3.2). Components of the calibration system were connected using PFA tubing (Swagelok). Connections between tubing and metal components were made using Swagelok stainless steel fittings and ferrules, whereas tubing-to-tubing or -glassware connections (for example T-connectors or 3-way valves) used Galtek integral-ferrule PFA fittings except to a glass dissociator coil (see section 3.4.2). The dissociator became extremely hot, therefore connections were made using a Swagelok stainless steel Ultra-Torr tube fitting union. Nitrogen was humidified by passing the flow through a custom-made glass

bubbler containing deionised water (18.2 mΩ) followed by a filter or trap to reduce aerosol being carried into the lines.

Schematics showing how equipment was connected for CIMS calibration experiments are discussed in section 3.4. Many of the following experiments were designed to test aspects of calibrations and therefore utilised a similar setup, so discussion of these experiments refer the reader to the appropriate schematic in section 3.4 as necessary.

### 3.3.2 Mass flow controllers

Flow rates of the various gases used throughout experiments in this project were regulated by mass flow controllers (MFCs). The CIMS and BBCEAS instruments each use a number of integrated MFCs (detailed in their respective sections in chapter 2), which were calibrated using the same techniques as described for those in the calibration box (Tylan 260 series or MKS GE50A series).

#### MFC Calibration

The flow controllers operate using a mechanical iris which opens or closes depending on a voltage supplied to the device (0 V being fully closed, 5 V fully open). The actual flow allowed through a fully open flow controller does not necessarily correspond exactly to the manufacturer-specified maximum of its operational range, however (i.e. an individual 0-500 sccm flow controller might give a flow rate of, for example, 537 sccm at 5.00 V). To ensure stable flows of gas, and thus consistent reactions and results, the flow controllers therefore required calibration which was executed using Gilian “Giliberator 2” or TSI 4100 series primary flow calibrators (flow meters). Dry nitrogen was flowed through the MFC which was set in turn to several non-sequential flow rates spanning the controller’s dynamic range. Flow rates were measured either using the Giliberator as an average of at least 10 point readings, or with the TSI 4100 series flow meter by simply waiting for a stable reading.

A calibration graph was produced for each flow controller by plotting measured flow rates against setpoint voltages (Figure 3.8), the equation of which was subsequently used to determine the requisite setpoint to give a desired flow rate. This procedure was carried out periodically to ensure stability.

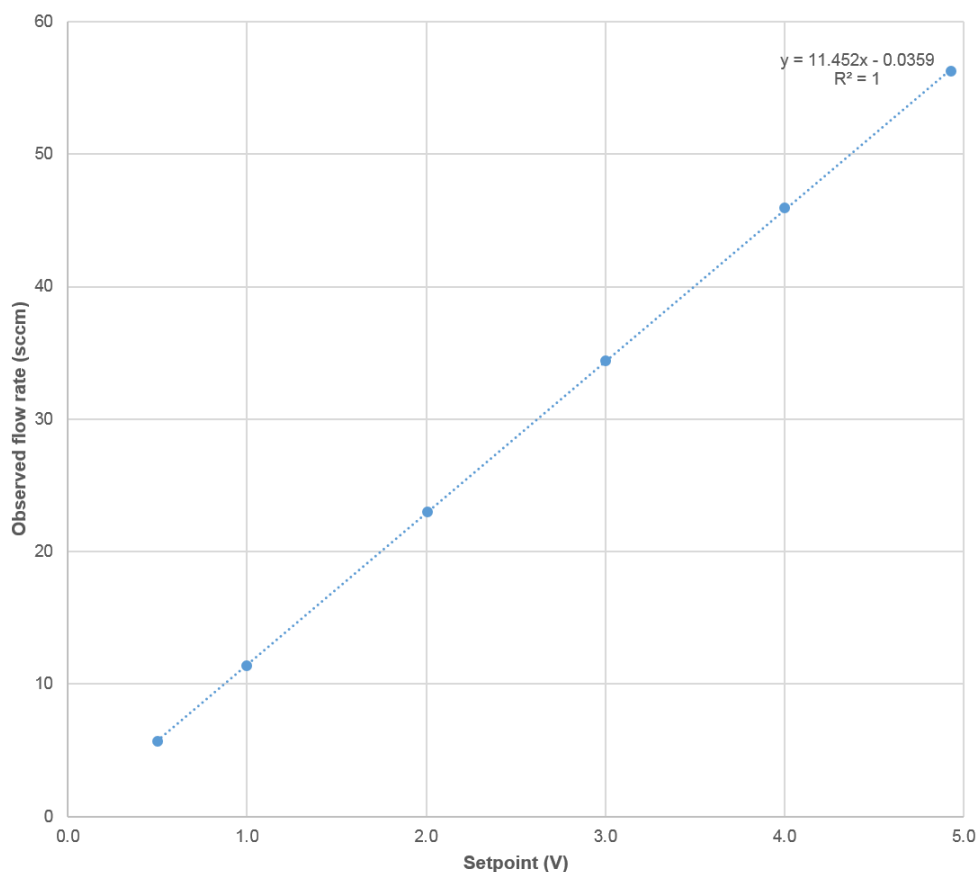


Figure 3.8 Example mass flow controller calibration. The x-axis displays the voltage set on the instrument, the y-axis shows the corresponding rate measured by the flow meter.

### Gas correction factor

The mass flow controllers are calibrated to regulate pure N<sub>2</sub>, therefore early in the project a gas correction factor (GCF) was also calculated (Equation 3.1a to c) to account for the different density and heat capacity of methyl iodide in the CIMS reagent ion precursor gas.

$$\text{GCF}_{\text{MeI}, \text{N}_2 (1000 \text{ ppm})} = \frac{0.3106((a_{\text{N}_2} s_{\text{N}_2}) + (a_{\text{MeI}} s_{\text{MeI}}))}{(a_{\text{N}_2} \rho_{\text{N}_2} c_{\text{pN}_2}) + (a_{\text{MeI}} \rho_{\text{MeI}} c_{\text{pMeI}})} \quad \text{a}$$

$$\text{TC} = \frac{P_l T_s V_l}{P_s T_l} \quad \text{b}$$

$$V_s = V_l \cdot \text{GCF} \cdot \text{TC} \quad \text{c}$$

Equation 3.1 Equations for calculating mass flow controller gas correction factor (Mykrolis Corporation).

- Gas correction factor equation.  $S_x$  = molecular structure correction; 1.000 ( $\text{N}_2$ ) or 0.880 (MeI);  $\rho_x$  = density at standard temperature and pressure;  $c_{p_x}$  = specific heat;  $a_x$  = fractional flow.
- Temperature correction for GCF.  $T_s$ ,  $P_s$  = standard temperature, pressure;  $V_l$  = measured flow;  $T_l$ ,  $P_l$  = laboratory temperature, pressure.
- Equation to find actual flow ( $V_s$ ) of gas mixture from measured flow calibrated to pure  $\text{N}_2$ .

Even with 1000 ppm of methyl iodide in nitrogen the overall correction factor was well within the MFCs' uncertainty range (detailed in section 3.5.4) and thus could be neglected. All other gases were used at lower concentrations (e.g. 5 ppb  $\text{Cl}_2$ ) so this analysis was not repeated.

### 3.3.3 Nitrogen sources

All experiments (and instruments) described in this chapter use nitrogen in some capacity - for this, cylinders supplied by BOC gases were predominantly used. In January 2016 a nitrogen generator (Peak Scientific NG5000A) was installed, which took over as the source of nitrogen for the CIMS instrument.

To check for changes in background signals, the two sources of nitrogen were compared by flowing 2 slpm through mass flow controllers (half *via* dry tubing, half *via* bubbler filled with deionised water (18.2 mΩ)) then to the CIMS. Three mass spectra (30-300 amu) were taken with each source, and the average of the 3 cylinder spectra were subtracted from the average of the 3 generator spectra as shown in Figure 3.9.

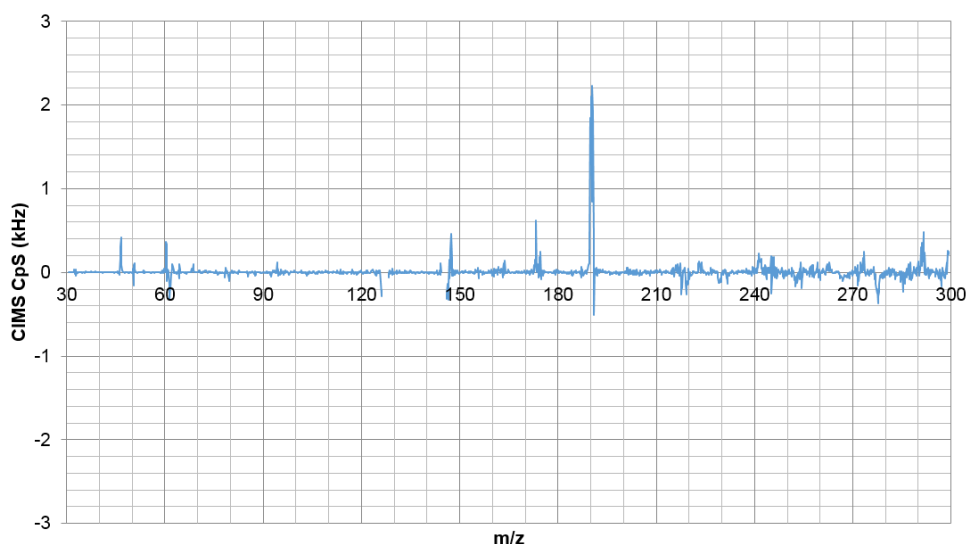
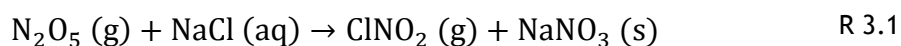


Figure 3.9 Subtracted (cylinder - generator) 3-spectrum averages for comparison of background signals. Large peaks due to  $I^-$  and  $[I(H_2O)]^-$  (127 and 145 amu) are omitted for clarity.

This comparison revealed that the two sources of nitrogen generally showed minimal differences, and the main areas of interest (162-164, 197-199, 208-210 amu) were clear (<0.2 kHz difference, where even low concentration measurements of species of interest are typically >2 kHz signal) so the two sources were subsequently treated as equivalent.

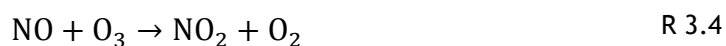
#### 3.3.4 $ClNO_2$ generation via $N_2O_5 + NaCl$

$Cl_2$  for calibration procedures was commercially available from specialist suppliers however this was not the case for nitryl chloride, which therefore had to be generated in situ. This was done within custom glass vessels, the development of which is detailed in section 3.3.6.



One established method for generating  $ClNO_2$  utilises R 3.1, which was initially used by the UoL group to calibrate the CIMS as detailed in section 3.4.1. This method of producing  $ClNO_2$  for CIMS calibration is well established (Osthoff et al., 2008; Kercher et al., 2009; Riedel et al., 2012; Riedel et al., 2013; Bannan

et al., 2015; Tham et al., 2016; Wang et al., 2016). Selecting this method also simplifies equipment requirements for calibrations during fieldwork, as a BBCEAS instrument with the requisite red optics would already be present during fieldwork to measure  $\text{NO}_3 + \text{N}_2\text{O}_5$ . It would therefore be relatively simple to temporarily rearrange connections and inlets for calibration experiments during daylight hours (when  $\text{N}_2\text{O}_5$  is absent), thus incurring no loss of useful data for either instrument.



$\text{N}_2\text{O}_5$  was synthesised *via* R 3.2 to R 3.6 (Davidson et al., 1978; Daniels, 2012) similar to the natural formation process of  $\text{N}_2\text{O}_5$  (see section 1.2.2), using equipment shown in Figure 3.10. Alternative syntheses often start with  $\text{NO}_2$  rather than  $\text{NO}$  (both of which are commercially available), the methodology of which is much the same but omitting R 3.4 (Huey et al., 1995; Bannan et al., 2015).

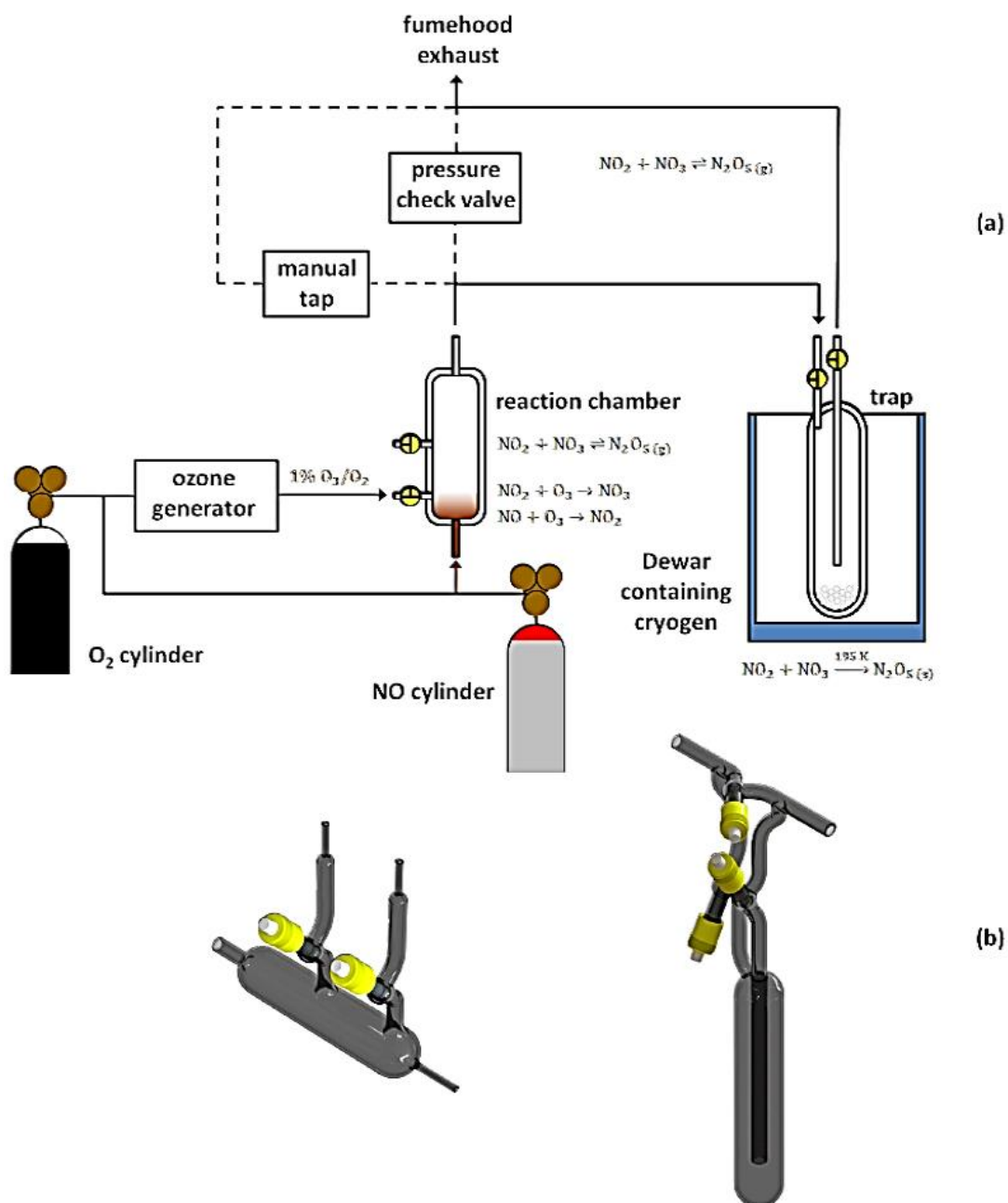
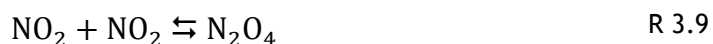


Figure 3.10 Experimental equipment for  $\text{N}_2\text{O}_5$  synthesis; (a) reaction schematic and (b) representations of the reaction chamber, left, and trap, right. Figure reprinted from Daniels, 2012.

Oxygen from a cylinder (BOC gases) was fed through a corona discharge ozone generator (Fischer Technologies ozone generator 500M; 1.2 mA) converting approx. 1% to ozone as per R 3.2 and R 3.3. This flow was used to purge the glassware and tubing for 30 min. Nitrogen monoxide (BOC special gases, 99% purity) was introduced to the reaction chamber and left to equilibrate for 10 min, opening the way for  $\text{N}_2\text{O}_5$  formation following oxidation of NO and  $\text{NO}_2$  (R

3.4, R 3.5 and R 3.6). Finally the bypass valve on the glass finger trap was closed, directing the flow into the main section cooled using a vacuum flask of cryogen (methanol and dry ice;  $\sim 196$  K) which pushes the R 3.6 equilibrium towards  $\text{N}_2\text{O}_5$  and allows white crystals thereof to deposit on the walls of the trap over several hours. Gases were controlled using stainless steel needle valves in addition to the PTFE taps on glassware (indicated in yellow on the figure). The stainless steel manual tap and pressure check valves were present to allow gas to be vented directly to exhaust after the reaction chamber, the latter to protect against over-pressurisation (automatically opening if internal pressure exceeds approx. 60 mbar above ambient).

Following  $\text{N}_2\text{O}_5$  synthesis, the glass trap was isolated using the integrated PTFE taps and separated from the rest of the experimental equipment (maintained in the vacuum flask of cryogen) for use as an  $\text{N}_2\text{O}_5$  source (as it is henceforth called) for subsequent experiments.



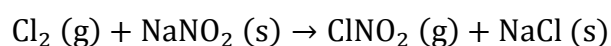
Several further reactions are relevant to this synthesis. Firstly, some  $\text{O}_2$  was directed to join the  $\text{NO}$  entering the reaction chamber to take advantage of R 3.7. Additional  $\text{NO}_2$  formed this way reduces the amount of required ozone to complete the reaction to  $\text{N}_2\text{O}_5$  and speeds the overall reaction, as without this the rate-limiting step is R 3.5 (Daniels, 2012). Secondly, the glassware was oven-dried after cleaning to ensure complete removal of water and prevent  $\text{HNO}_3$  formation (R 3.8). The  $\text{O}_2/\text{O}_3$  purge served as additional cleaning by oxidising away any residues, passivating the tubing and flushing out any remaining water vapour. Finally, a side reaction (R 3.9) also occurred whereby  $\text{NO}_2$  dimerises to produce and deposit an impurity in the form of  $\text{N}_2\text{O}_4$  in addition to  $\text{N}_2\text{O}_5$  (which are similar in form and appearance), necessitating a final purification step.

Purification was achieved *via* distillation, as N<sub>2</sub>O<sub>4</sub> has a higher vapour pressure at room temperature than N<sub>2</sub>O<sub>5</sub> and therefore sublimates more readily (Daniels, 2012). To this end O<sub>2</sub>/O<sub>3</sub> were left purging the system (with the NO source closed off) and the trap was gently warmed by lifting out of the cryogen. The N<sub>2</sub>O<sub>4</sub> would sublime and begin to dissociate back to visible brown NO<sub>2</sub> which was removed by the O<sub>2</sub>/O<sub>3</sub> flow. To avoid excessive loss of N<sub>2</sub>O<sub>5</sub> the trap was not allowed to warm too far, and was cooled again. This process repeated several times until the brown colouration due to NO<sub>2</sub> was no longer observed. The N<sub>2</sub>O<sub>5</sub> was preserved for ~8 weeks in the glass finger trap. The long-term stability of N<sub>2</sub>O<sub>5</sub> kept in this way is uncertain, and while no specific purity issues were detected the distillation procedure reported in the synthesis was repeated after several weeks as a precaution to counteract decomposition of N<sub>2</sub>O<sub>5</sub> to O<sub>2</sub> + NO<sub>2</sub> and the associated formation of N<sub>2</sub>O<sub>4</sub>.

The effectiveness of the CIMS calibration to ClNO<sub>2</sub> based on R 3.1 was tested using the N<sub>2</sub>O<sub>5</sub> generated as described above. The equipment involved a setup similar to the one shown later in Figure 3.16. Initially the system was tested by incrementally adding components to check for background signals and ensure both instruments effectively detect their species of interest. For example, no change was expected to be observed *via* BBCEAS or CIMS after adding an empty ClNO<sub>2</sub> reactor with the N<sub>2</sub>O<sub>5</sub> source closed; N<sub>2</sub>O<sub>5</sub> was detected *via* BBCEAS after opening the N<sub>2</sub>O<sub>5</sub> source, and finally ClNO<sub>2</sub> was observed *via* CIMS after adding a slurry of NaCl to the reactor.

### 3.3.5 ClNO<sub>2</sub> generation *via* Cl<sub>2</sub> + NaNO<sub>2</sub>

Later on, ClNO<sub>2</sub> for CIMS calibrations was generated *via* R 3.10, based upon the work of Thaler et al., 2011. Reasons for changing to this reaction are discussed later in section 3.4.1. This method has also been used in the past to calibrate CIMS field data for ClNO<sub>2</sub> (Mielke et al., 2011; Mielke et al., 2013).



R 3.10

For these experiments the independent measure of concentration was again achieved using BBCEAS, this time using blue optics measuring  $\text{NO}_2$  produced from thermal dissociation of  $\text{ClNO}_2$ . The thermal dissociator used to achieve this is essentially a glass tube fashioned into a coil, insulated and housed in a thermostatically-controlled metallic sleeve capable of maintaining temperatures up to  $400\text{ }^\circ\text{C}$ .

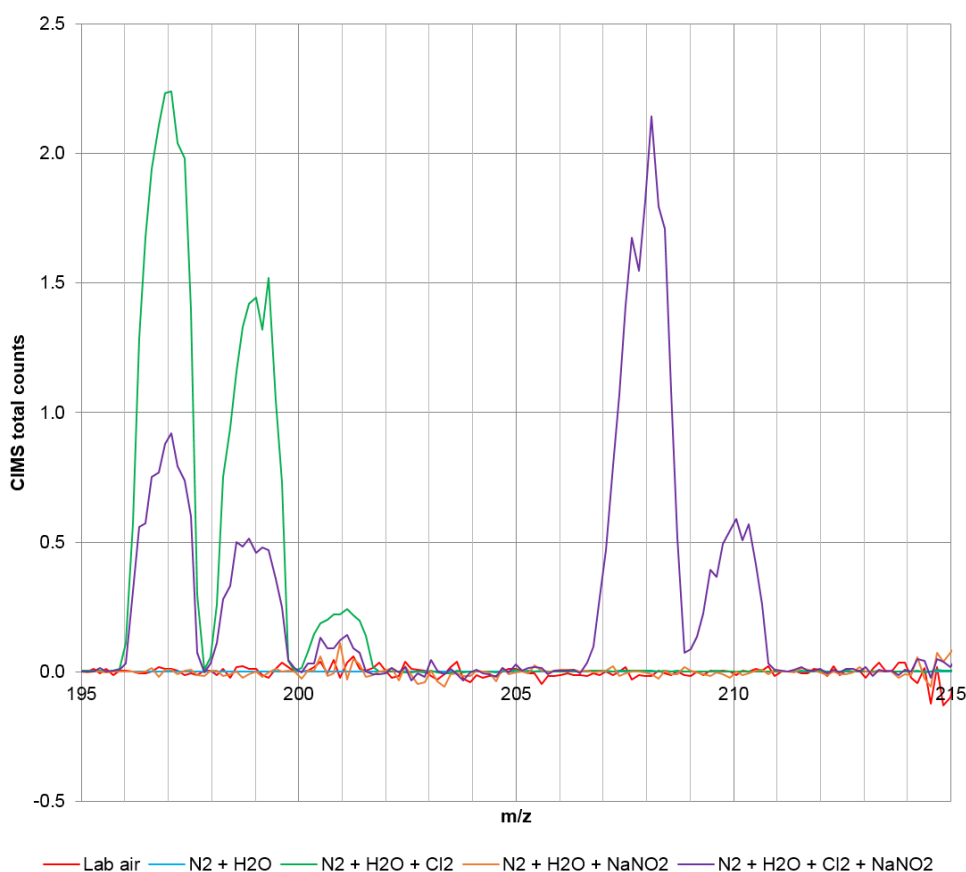


Figure 3.11 CIMS spectra with a dry nitrogen background spectrum subtracted. Elements of CIMS calibration experiments were added incrementally (in left to right order indicated on the legend) to test for interferences.

Figure 3.11 demonstrates the successful production and detection of  $\text{ClNO}_2$  via R 3.10 following an early experiment wherein equipment and reagents were added incrementally to test calibration system effectiveness and check for the presence of background signals. No peaks were observed in the range of interest with just laboratory air or humidified nitrogen, both of which were used as a

dilutant at some point.  $[I(\text{Cl}_2)]^-$  peaks were easily detectable at 197, 299 and 201 amu when  $\text{Cl}_2$  was inserted. The chlorine flow was stopped and  $\text{NaNO}_2$  salt added, resulting in a clean spectrum again. When chlorine was reintroduced (so both  $\text{Cl}_2$  and  $\text{NaNO}_2$  were present simultaneously)  $[I(\text{ClNO}_2)]^-$  (208, 210 amu) was observed, as was residual  $\text{Cl}_2$ . Residual  $\text{Cl}_2$  signals could not be eliminated as loss of  $\text{ClNO}_2$  to the side reaction discussed in section 3.3.6 necessitated very low reactor residence times, preventing quantitative reaction of chlorine. CIMS  $\text{ClNO}_2$  (and BBCEAS  $\text{NO}_2$ ) detection was responsive and proportional to  $\text{Cl}_2$  added, however, in agreement with Thaler et al., 2011 and proving the efficacy of this method.

Literature indicates that  $\text{ClNO}_2$  begins dissociating at approx. 150 °C (Zhu and Lin, 2004; Kercher et al., 2009), however optimum temperatures to ensure complete dissociation were tested. A constant concentration of  $\text{Cl}_2$  was flowed over  $\text{NaNO}_2$  in the reactor then through the dissociator and to the CIMS, while increasing the dissociator temperature in steps. Residual CIMS  $\text{ClNO}_2$  signals disappeared (indicating complete dissociation) at 300 °C, however the dissociator was set slightly higher than this at 350 °C for calibration experiments to allow flexibility for higher concentrations.

At first the source of  $\text{Cl}_2$  was a permeation tube (Kin-Tek). The tube was placed in a glass vessel encased inside a thermostatically-controlled oven maintained at 40 °C with a constant flow (25 sccm) of nitrogen flowing through to provide a constant rate of  $\text{Cl}_2$  release. The permeation tube's mass was measured weekly to calculate how much  $\text{Cl}_2$  had been released, after which the tube was left under the aforementioned conditions at least overnight to equilibrate prior to experiments, ensuring the constant rate of  $\text{Cl}_2$  emission. The permeation tube was later replaced by a cylinder of  $\text{Cl}_2$  (5 ppm in  $\text{N}_2$ ; BOC specialist gases). The cylinder allowed greater flexibility and, as it contained a certified concentration of chlorine, facilitated calibration of the CIMS to  $\text{Cl}_2$  as detailed in section 3.4.3.

Salt in the reactor was replaced weekly as it was found that the calibration system's responses became non-linear (suggesting poisoning of the salt) if the  $\text{NaNO}_2$  was not frequently changed.

### 3.3.6 Reactor development

The reaction vessel used to produce nitryl chloride was subject to some development, undergoing three iterations shown in Figure 3.12.

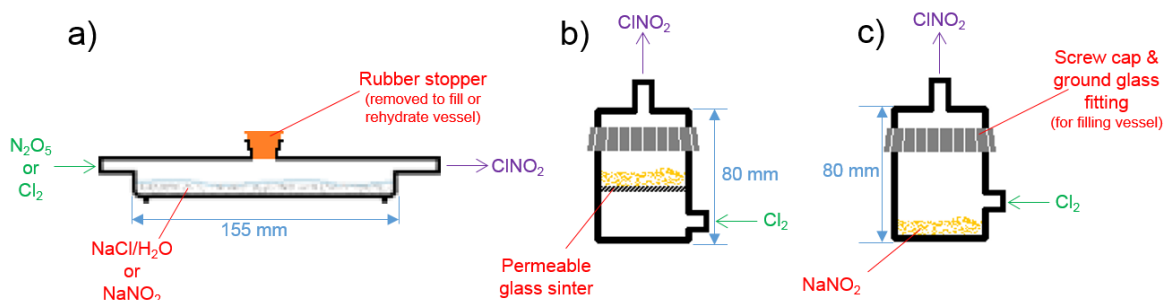
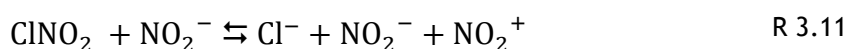


Figure 3.12 Reactor designs for CIMS ClNO<sub>2</sub> calibration in chronological order (not to scale).

The first “salt bed” reactor (Figure 3.12a) was a long, flat design intended for use with R 3.1, for which it was filled with an aqueous slurry of sodium chloride while dilute N<sub>2</sub>O<sub>5</sub> was flowed across its length. One of the issues that arose with this method was rapid drying of the salt, requiring frequent interruptions to the experiment in which the top was opened to replenish the water (discussed further in section 3.3.7).

Eventually the UoL team moved to R 3.10 using dry NaNO<sub>2</sub> for ClNO<sub>2</sub> generation (see sections 3.3.5 and 3.4). The decision to update the reactor design was made because it was initially found that very little ClNO<sub>2</sub> was observed by the CIMS despite substantial quantities of NO<sub>2</sub> being detected *via* BBCEAS (whether the dissociator was inline or not), an effect which became less pronounced if flow rate was increased. Thaler et al., 2011 found that greater residence time in the reactor resulted in increasing co-production of NO<sub>2</sub> *via* R 3.11, R 3.12 and R 3.13.



The second iteration of the reactor (Figure 3.12b) was therefore much smaller to decrease the reactor residence time and thus minimise opportunity for ClNO<sub>2</sub> conversion to NO<sub>2</sub> in this way. NaNO<sub>2</sub> was placed on a permeable platform inside the reactor so that Cl<sub>2</sub> would flow in the bottom and through the salt crystals to form ClNO<sub>2</sub>. The bottom to top flow introduced turbulence and was intended to give a high degree of mixing over a short time period where in the previous, larger reactor Cl<sub>2</sub> flowed a greater distance but over the top of the salt resulting in less mixing but over a longer period of time. The stoppered opening was also removed and a screw fitting with ground glass connection was added to enable salt replacement, as the NaNO<sub>2</sub> salt component is used dry therefore the reactor no longer to be opened during experiments for rehydration. The reactor was tested by completely filling the reactor (approx. 2 g NaNO<sub>2</sub>) in which case almost no ClNO<sub>2</sub> reached the CIMS (indicating near-quantitative conversion to NO<sub>2</sub>), whereas ClNO<sub>2</sub> detection increased dramatically after the reactor was emptied and only a thin layer of salt was distributed on the glass sinter. This was caused by deliquescence of the salt, which then blocked the pores in the platform.

The reactor was therefore altered again to remove the sinter and raise the inlet (Figure 3.12c). NaNO<sub>2</sub> could then be placed on the base and Cl<sub>2</sub> flowed over the salt again, rather than through it.

This third reactor design produced adequate ClNO<sub>2</sub> under experimental conditions. While NO<sub>2</sub> co-production was dramatically reduced it could not be eliminated therefore ClNO<sub>2</sub> was measured as the difference between BBCEAS NO<sub>2</sub> measurements with the dissociator bypassed and inline (see section 3.5).

### 3.3.7 Humidity effects

Another preparatory experiment set about altering conditions and flow rates to test for the system's sensitivity to water vapour and dilution. Ambient humidity is known to influence CIMS sensitivity (Slusher et al., 2004; Bannan et al., 2015).

Sensitivity can be increased *via* formation of iodide-water clusters which can act as secondary reagent ions (see sections 2.2.3 and 3.2.3), or by dispersing excess collisional energy to stabilise analyte clusters (Lee et al., 2014).

Contrariwise, sensitivity can be diminished by additional humidity as the primary reagent ion can experience decreased reactivity. Another mechanism is where one or more water molecules form clusters with analyte ions dispersing them over several masses, an effect which the CDC is intended to counteract (see section 3.2.3). Alternatively increasing humidity can lead to increased deposition on surfaces as Thornton et al., 2003 found with  $\text{N}_2\text{O}_5$  however the low solubility of  $\text{ClNO}_2$  (Simpson et al., 2015) means this unlikely to be a factor in these experiments.

An experiment to investigate the effects of humidity was set up as per the  $\text{ClNO}_2$  calibrations detailed in section 3.4.1. Humidified nitrogen was introduced by dividing the dilution line into one direct (dry) flow and a second route that passes through a deionised water (18.2 m $\Omega$ ) filled bubbler (and an aerosol filter) then re-joining the dry flow before the dilution merged with the  $\text{N}_2\text{O}_5$ -enriched nitrogen. Humidity was adjusted by changing the MFCs governing the balance of flows between dry and humidified routes while maintaining the same combined flow.

Figure 3.13 shows the results of this experiment. The ratio of  $\text{NO}_3$  detected *via* BBCEAS (in ppt) compared to  $\text{ClNO}_2$  measured *via* CIMS (in CpS) is quite high (generally  $\text{NO}_3/\text{ClNO}_2 > 3$ ) when the sample gas is extremely dry (approx. 0 %vol  $\text{H}_2\text{O}$ ). The  $\text{NO}_3/\text{ClNO}_2$  ratio seems to fall quickly as humidity rises, however, and does not appear to be entirely linear. Notably there is much less scatter in data points corresponding to  $\text{NO}_3/\text{ClNO}_2$  ratio at higher humidity. Previous studies (Kercher et al., 2009; Mielke et al., 2011) found that the impact of humidity diminishes above approx. 0.6 % absolute humidity (approx. 30% RH under typical UoL laboratory conditions) in the ion-molecule region of the CIMS, which is below typical inlet humidity during calibration experiments and fieldwork described in this thesis.

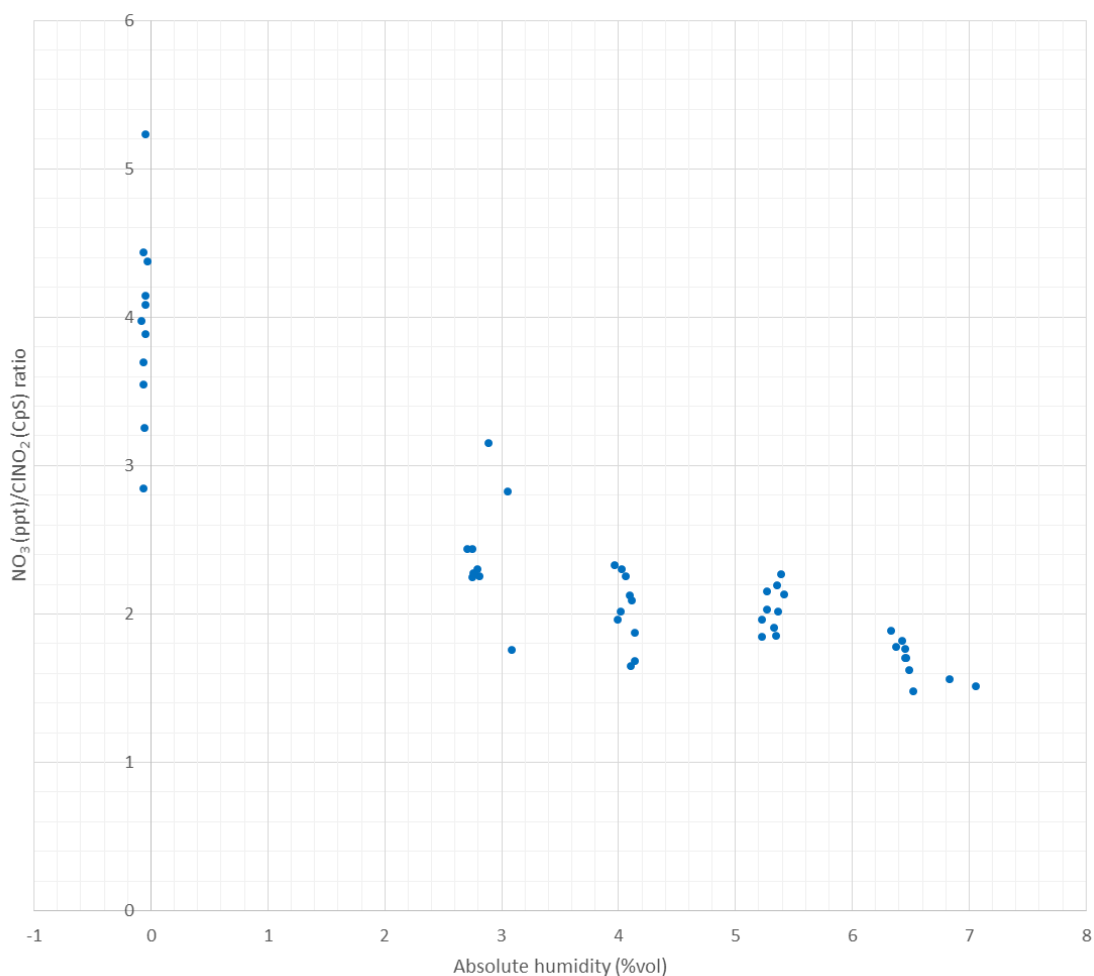


Figure 3.13 Results of an experiment testing the effect of humidity upon CIMS ClNO<sub>2</sub> sensitivity. NO<sub>3</sub> and H<sub>2</sub>O were measured *via* BBCEAS (data workup courtesy of Dr. T. J. Adams); ClNO<sub>2</sub> is represented by [I(ClNO<sub>2</sub>)]<sup>-</sup> raw counts per second measured *via* CIMS at 207.97 amu.

The amount of liquid water in the reaction vessel (Figure 3.12a) was also studied - the quantity of sodium chloride was noted and the hydration closely monitored, adding measured amounts of water. There was, however, little difference in ClNO<sub>2</sub> concentration observed *via* CIMS (at 208 amu) until the salt became extremely dry, at which point ClNO<sub>2</sub> detection fell sharply. During normal operation the reactor was therefore watched closely and replenished when necessary *via* the opening ordinarily sealed by a rubber stopper, following which the system would need a few minutes for flows (and, therefore, analyte concentrations) to stabilise. The resulting breaks in measurements were approximately 15 minutes in total.

### 3.3.8 Background measurement coil

A heated stainless steel coil ( $\frac{1}{4}$  inch OD; approx. 140 cm path length) was designed to encourage reactions on the metal surface, stripping out a wide range of potential analytes to allow CIMS background measurement (Huey, 2007).

A pair of 3-way solenoid valves, controllable *via* manual switches or automatically by computer, were mounted onto the CIMS frame and connected before the inlet. The valves guided sample flow either directly to the inlet using a short length of PFA tubing or through the coil.

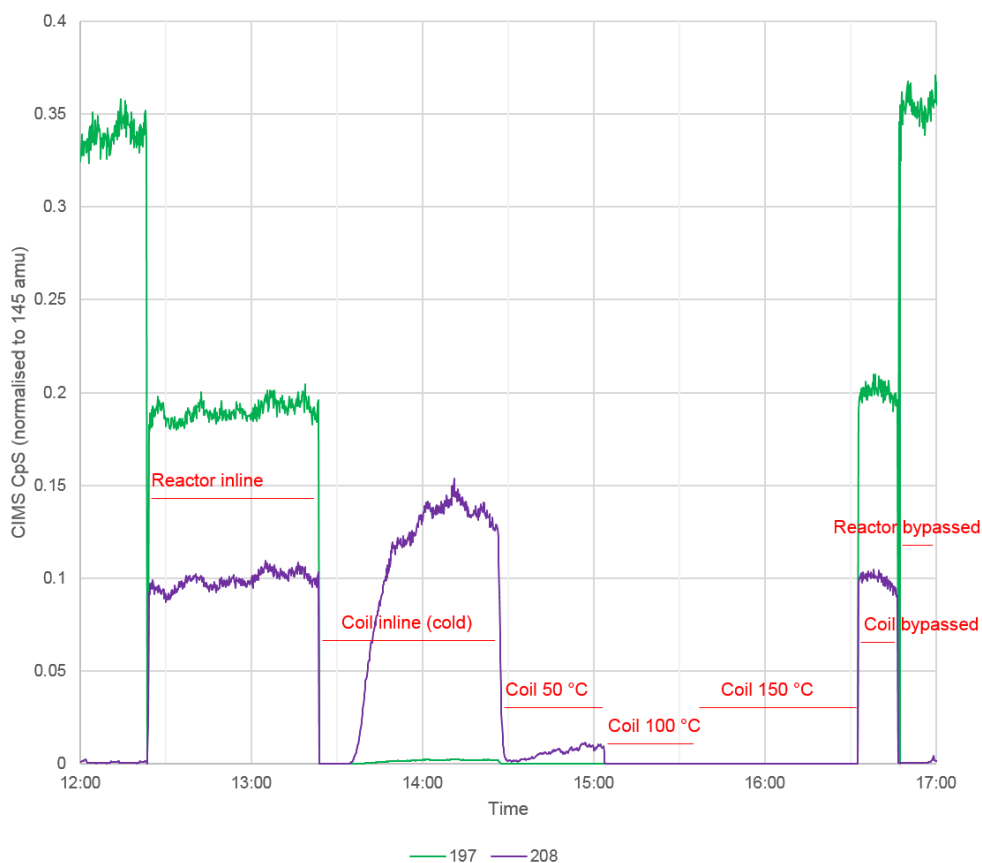


Figure 3.14 Time series from an experiment testing background coil effectiveness and optimal temperatures (principal calibration ions only - see section 3.5.1).

$\text{ClNO}_2$  was generated as per “series 2” CIMS calibrations (section 3.4.2) and passed through the inlet coil at various temperatures (including ambient) in an experiment to test its effectiveness at removing  $\text{Cl}_2$  and  $\text{ClNO}_2$  (Diec, 2015). Figure 3.14 shows the impact of the coil on  $\text{Cl}_2$  and  $\text{ClNO}_2$  (via 197 and 208 amu, respectively). Detection of each species was near-zero when the coil was above 100 °C, however 150 °C was chosen as the standard operating temperature as this was still well within the operational range of the coil and allowed greater flexibility in the event of larger analyte concentrations.

The background measurement coil was also used to test stability and response time of CIMS signals, to ensure readings are consistent and responsive to quick changes. Figure 3.15 shows  $\text{Cl}_2$  and  $\text{ClNO}_2$  CIMS signals in a time series taken during a CIMS calibration experiment. The solenoid valves redirect the flow very quickly therefore signals due to  $\text{Cl}_2$  and  $\text{ClNO}_2$  are expected to drop

instantaneously as they are destroyed in the coil and return similarly quickly when the coil is bypassed.

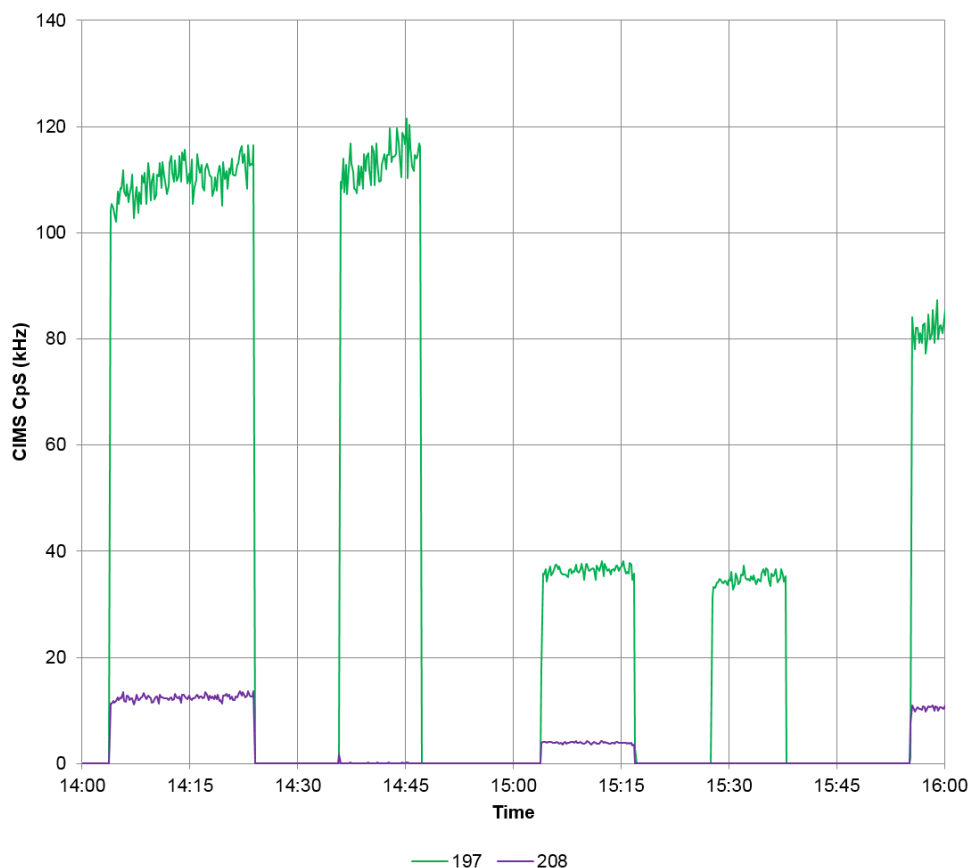


Figure 3.15 Excerpt of a time series using data from a ClNO<sub>2</sub> calibration. The sharp rise and fall of CIMS Cl<sub>2</sub> (197 amu) and ClNO<sub>2</sub> (208 amu) detected exhibits fast response to changes in concentration.

CIMS signals responded promptly to changes in concentration levels well beyond those usually expected in ambient air, *i.e.* up to 15 ppb (Cl<sub>2</sub>) or 2 ppb (ClNO<sub>2</sub>), compared to typical atmospheric concentrations of <1 ppb. This response time was essentially the measurement cycle (approx. 11 seconds), determined by the sum of dwell times for masses monitored by the CIMS in H-mode. The instrument was therefore shown to be suitable for measuring Cl<sub>2</sub> and ClNO<sub>2</sub> in the field at the selected time resolution.

### 3.4 CIMS calibration experiments

Following the commissioning of the CIMS and other preparatory experiments, development of a consistent and reliable technique for calibrating the CIMS to ClNO<sub>2</sub> and Cl<sub>2</sub> could begin. This subchapter includes discussion of method development and basic equipment for CIMS calibration experiments themselves.

#### 3.4.1 CIMS calibrations: ClNO<sub>2</sub> *via* NaCl + N<sub>2</sub>O<sub>5</sub>

Early experiments used R 3.1 to generate ClNO<sub>2</sub> for CIMS calibration. A number of preparatory experiments described in previous sections were based upon this technique however it was not ultimately used to calibrate field data, for reasons discussed below.

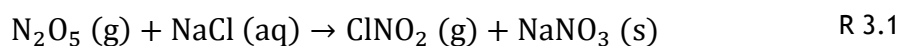


Figure 3.16 shows a schematic for CIMS calibration equipment at this stage. A small (250 sccm) amount of dry nitrogen was flowed through the N<sub>2</sub>O<sub>5</sub> source then diluted with a larger (10 slpm total) stream of partially-humidified nitrogen, both of which were regulated using mass flow controllers (see section 3.3.2). Following dilution the flow was separated using a T-connector - one branch was directed to the BBCEAS, the other to the CIMS *via* the reaction vessel (an overflow was also present directly before the CIMS to prevent overpressurisation) allowing both instruments to be inline simultaneously. The reaction vessel was filled at the start of the experiment with an aqueous slurry of NaCl and deionised water (18.2 mΩ), over which the dilute N<sub>2</sub>O<sub>5</sub> was flowed.

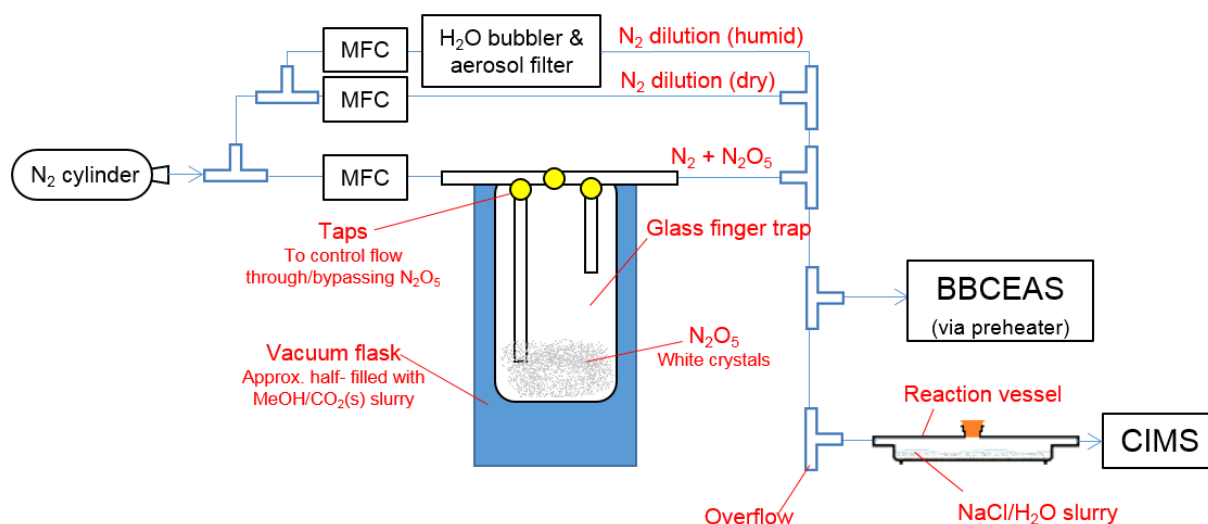


Figure 3.16 General experimental setup for experiments using measuring  $\text{ClNO}_2$  generated via R 3.1.

The BBCEAS was set up using red optics with a cavity heater set to  $100\text{ }^\circ\text{C}$  to thermally dissociate  $\text{N}_2\text{O}_5$  and detect the  $\text{NO}_3$  product. A preheater ( $70\text{ }^\circ\text{C}$ ) was also installed to warm the sample flow and prevent a dramatic temperature gradient from occurring within the cavity, potentially leading to effects such as variations in refractive index (*i.e.* mirages) or condensation of water vapour. The main CIMS masses of interest were  $[\text{I}(\text{N}_2\text{O}_5)]^-$  (*i.e.* unreacted  $\text{N}_2\text{O}_5$ ) at 235 amu, in addition to two isotopologues of  $[\text{I}(\text{ClNO}_2)]^-$  at 208 and 210 amu and the equivalent secondary  $\text{ClNO}_2$  ions  $[\text{ICl}]^-$  at 162 and 164 amu (see section 2.2.3). A scan was taken using the CIMS spectrum mode whenever a significant adjustment to the system was made, to monitor changes in signals and check for interferences.

While  $\text{ClNO}_2$  was successfully produced and detected using this method a number of issues arose with this method of calibration. The first problem was that the experiment relied upon the assumption of unit conversion of  $\text{N}_2\text{O}_5$  to  $\text{ClNO}_2$  (Finlayson-Pitts et al., 1989; Behnke et al., 1997), as the  $\text{N}_2\text{O}_5$  concentrations detected *via* BBCEAS were treated as equivalent to  $\text{ClNO}_2$  detected *via* CIMS. Some methods using this reaction involve flowing a known quantity of  $\text{N}_2\text{O}_5$  over NaCl and assuming complete conversion (Kercher et al., 2009; Bannan et al., 2015). The UoL method (measuring  $\text{N}_2\text{O}_5$  concentration *via* BBCEAS) is more robust regarding this assumption (and with respect to  $\text{N}_2\text{O}_5$

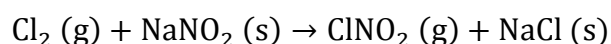
source degradation) as  $\text{N}_2\text{O}_5$  concentration is determined experimentally after passing through the system rather than using a “known” concentration entering it, however a major issue with the unit conversion assumption still exists. This was highlighted by McNeill et al., 2006, who observed a sub-100%  $\text{ClNO}_2$  yield from  $\text{N}_2\text{O}_5 + \text{NaCl}$  aerosol, though the authors also hypothesize that the yield from sea salt aerosol is likely greater than the 80% they observed. Furthermore, CIMS spectra from these experiments at UoL showed a species at 190 amu, presumed to correspond to  $\text{HNO}_3$  resulting from reaction of  $\text{H}_2\text{O}$  with  $\text{N}_2\text{O}_5$  (*i.e.* the competition for  $\text{N}_2\text{O}_5$  between  $\text{Cl}^-$  and  $\text{H}_2\text{O}$  mentioned in section 1.2.4), also indicating that  $\text{N}_2\text{O}_5$  conversion was probably less than quantitative.

The second issue was that negligible  $\text{N}_2\text{O}_5$  wall losses and post-reactor decomposition also had to be assumed. A fast total flow rate (~10 slpm) was intended to ensure such losses were minimal, but also caused the salt bed to swiftly dry out, resulting in frequent breaks in measurements (see section 3.3.7). The extent of  $\text{N}_2\text{O}_5$  wall losses were not investigated in the course of these experiments, but are known to be an issue for  $\text{N}_2\text{O}_5$  measurements (Kennedy et al., 2011).

Finally, the  $\text{N}_2\text{O}_5$  source was time- and resource-intensive. Synthesis of  $\text{N}_2\text{O}_5$  on-site would be impractical, therefore safe transport of the source under the cold conditions would be essential. Furthermore a consistent supply of dry ice was necessary to maintain the cryogen, adding to logistical requirements. Both of these requirements detract from the objective of developing a portable calibration system for fieldwork.

#### 3.4.2 CIMS calibrations: $\text{ClNO}_2$ via $\text{Cl}_2 + \text{NaNO}_2$

Owing to the issues described in section 3.4.1 above,  $\text{ClNO}_2$  was generated *via* R 3.10 for CIMS calibration experiments used to determine instrument sensitivities for field data.



R 3.10

Total flow rates for these experiments (1-3 slpm) were not as fast as during  $\text{N}_2\text{O}_5 + \text{NaCl}$  methods (~10 slpm). The chlorine furthermore had a tendency to stick to the lines, resulting in delayed responses to changes in the concentration. Following changes in flow regime the system was therefore left until CIMS signals due to both  $\text{Cl}_2$  and  $\text{ClNO}_2$  flattened out completely, indicating the lines were sufficiently conditioned (*i.e.* analyte adsorption and desorption upon tubing approximately at equilibrium). This ensured concentrations of these species were stable and allowed negligible wall losses to be assumed. Approximately 10 minutes of this stable data, representing a calibration step, was acquired for each flow regime (*i.e.* analyte concentration) before moving on to the next.

#### Series 1 $\text{ClNO}_2$ calibrations

For the sake of distinguishing experiments with common methodology, the initial  $\text{ClNO}_2$  calibration experiments using R 3.10 were dubbed “series 1”, a general scheme for which is shown in Figure 3.17.

50 sccm of chlorine from the cylinder entered the system *via* mass flow controller (MFC) 1. It was found that this flow controller performed poorly at the very bottom of its range, and a much greater degree of control could be exercised by setting this MFC to maximum and installing a pump, regulated by a second flow controller (MFC2), to remove most of the  $\text{Cl}_2$  again.

$\text{Cl}_2$  was then diluted with dry nitrogen to make up the balance of 100 sccm using MFC3. A second dilution of humid nitrogen (200 sccm) was added *via* MFC4 giving approx. 30% relative humidity entering the reaction vessel. Later experiments increased the dry and humid flows to 500 and 1000 sccm respectively to achieve lower  $\text{ClNO}_2$  concentrations but similar humidity.

The reactor contained approx. 1 g dry  $\text{NaNO}_2$ , following which a three-way valve controlled whether the flow bypassed or entered the dissociator to measure  $\text{ClNO}_2$  *via* CIMS or decompose  $\text{ClNO}_2$  to  $\text{NO}_2$  for measurement *via* BBCEAS, respectively.

Sample flow was diluted again using dry nitrogen (900 sccm) from MFC5 then separated to the BBCEAS or to CIMS *via* T-connector. The CIMS and BBCEAS instruments drew approximately 1000 sccm each, and the total flows of reagent and dilution gases were lower than the combined instrument draw of 2 slpm. A T-connector open to the laboratory was positioned just before the CIMS allowing air to be drawn in, serving as a final dilution.

Flow rates were measured at several points (including before the CIMS inlet, after the BBCEAS branch and at the laboratory air intake) using *Gilian “Giliberator 2”* or *TSI 4100 series* flow meters in order to later calculate dilution factors. Later the flow rate through the reactor was increased, therefore MFC5 was removed and MFC3-4 increased (to 500 and 1000 sccm respectively).

The procedure for these experiments involved generating different concentrations of ClNO<sub>2</sub> by adjusting the amount of Cl<sub>2</sub> pumped out of the system (*i.e.* how much reaches the reactor). Data were gathered for a few minutes of stable signal with the dissociator bypassed (*i.e.* detecting ClNO<sub>2</sub> *via* CIMS) before the valve was switched to flow through the dissociator (*i.e.* to detect NO<sub>2</sub> *via* BBCEAS) and several more minutes of stable data acquired. The flows were then changed, the dissociator bypassed and the process was repeated. 3-6 non-sequential concentrations of ClNO<sub>2</sub> were measured in this way per experiment.

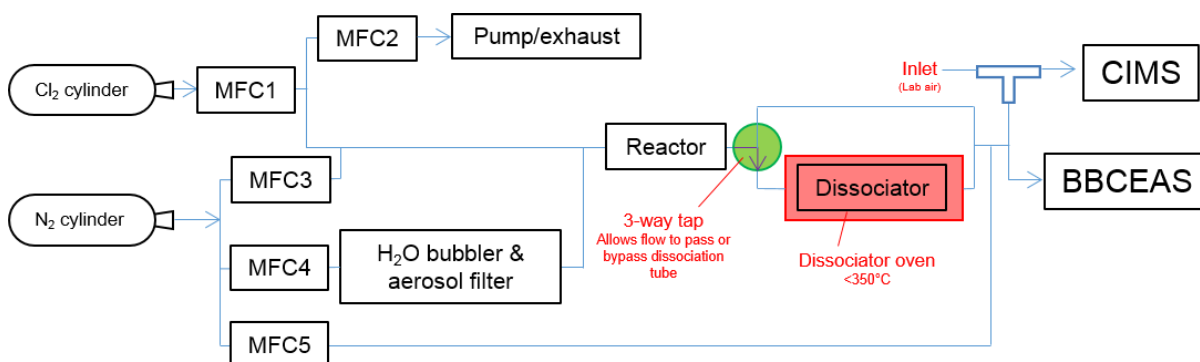


Figure 3.17 Schematic for the “series 1” ClNO<sub>2</sub> calibrations. Arrows denote flow direction determined by cylinder pressure or pump draw. MFC5 was later removed and the other N<sub>2</sub> dilutions increased to compensate.

## Series 2 ClNO<sub>2</sub> calibrations

The first major change in series 2 experiments (Figure 3.18) was to increase the flows in the calibration system to exceed the combined instrument inlet flow of 2 slpm, converting the final T-connector before the CIMS into an overflow. This change simplified data analysis by removing a dilution correction between CIMS and BBCEAS measurements. Furthermore, humidity in the CIMS ion-molecule region was now controllable, as laboratory air (of variable humidity) was no longer used in the system. This set of calibrations also focused on smaller concentrations (much closer to realistic atmospheric levels) with dilutions at only 2 points.

As before, MFC1-2 controlled Cl<sub>2</sub> entering then removed from the system, and MFC3 made up the balance of 100 sccm using dry nitrogen. Before the reactor a much larger dilution was added totalling 2000-2400 sccm comprised of humid and dry nitrogen *via* MFC 4-5 respectively.

Humidity was controlled by changing the balance of the large dilution components, and was monitored by a temperature & humidity probe (*Vaisala HMP60*) prior to joining the Cl<sub>2</sub>-enriched flow. General practice was to keep the MFC4-5 ratio equal (resulting in 45-50% relative humidity at the probe).

The increased total flow rate further reduced reactor residence time and thus co-production of NO<sub>2</sub>. To the same end the composition of salt in the reactor was changed in series 2 calibrations to approx. 0.5 g NaNO<sub>2</sub> and 0.5 g NaCl, with the intention of introducing Cl<sup>-</sup> to push the R 3.11 equilibrium toward ClNO<sub>2</sub> (Thaler et al., 2011).

While several changes were made in the equipment between series 1 and 2, the experimental procedure remained largely the same.

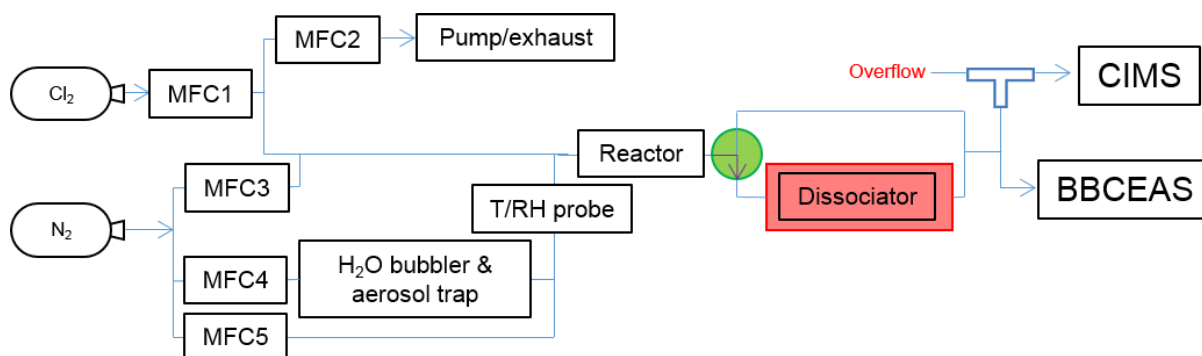


Figure 3.18 Schematic for series 2 ClNO<sub>2</sub> calibrations. Arrows denote flow direction determined by cylinder/generator pressure or pump draw.

### Series 2-3 ClNO<sub>2</sub> calibrations

Series 3 was largely the same as series 2, however the heated steel coil detailed in see section 3.3.8 was installed just before the CIMS inlet to allow for background measurement. The procedure also changed very slightly so that there were now three measurement periods per ClNO<sub>2</sub> concentration: 1) both dissociator and inlet coil bypassed; 2) dissociator bypassed but coil inline; and 3) dissociator inline.

While the CIMS calibration technique was developed over time to reach the final series 3 methodology, experiments from all three of the major iterations used with R 3.10 were variously used in calibrating field data as described in section 3.5.5.

#### 3.4.3 CIMS calibration: Cl<sub>2</sub>

Molecular chlorine (Cl<sub>2</sub>) is also eminently detectable *via* CIMS and has previously been studied simultaneously with ClNO<sub>2</sub> (*e.g.* Riedel et al., 2012). This species similarly represents a source of chlorine radicals, therefore the University of Leicester instrument was also calibrated to measure this molecule.

After the Cl<sub>2</sub> source for ClNO<sub>2</sub> calibration was changed from permeation tube to a cylinder of known concentration, it became relatively simple to also calibrate the CIMS to Cl<sub>2</sub>. The equipment and procedure for these experiments was almost exactly the same as for ClNO<sub>2</sub> calibrations based on R 3.10 and

therefore development proceeded in parallel (*i.e.* series 1-3). Differences were as follows: 1) the reactor was empty; 2) the dissociator was bypassed throughout; and 3) as of series 2 (*i.e.* when the laboratory air dilution was converted to an overflow) the BBCEAS tubing was instead capped (the flow normally leading to the cavity therefore went to overflow instead). Instead of relying on a second instrument, independent determination of concentration was achieved mathematically, using the initial certified cylinder concentration and calculating forward through the consecutive dilution factors. These methods were similarly successful in allowing quantification of Cl<sub>2</sub> in ambient measurements.

## 3.5 Data processing

### 3.5.1 Initial steps

ClNO<sub>2</sub> and Cl<sub>2</sub> each have several corresponding masses detectable by CIMS, all of which were studied. The signals due to Cl<sub>2</sub> correspond to the [I(Cl<sub>2</sub>)]<sup>-</sup> ion with three different isotopomers at 197, 199 and 201 amu, arising from the combination of <sup>35</sup>Cl and <sup>37</sup>Cl (see section 3.2.1). ClNO<sub>2</sub> has 4 masses detectable *via* I<sup>-</sup> CIMS corresponding to [I(<sup>35</sup>ClNO<sub>2</sub>)]<sup>-</sup> and [I<sup>35</sup>Cl]<sup>-</sup> at 208 and 162 amu, each with a <sup>37</sup>Cl isotopomer at *n*+2 amu. The two channels (ions) due to ClNO<sub>2</sub> occur as a result of ion chemistry discussed in section 2.2.3, the branching between which is dependent upon humidity, CDC field strength and pressure (Kercher et al., 2009).

For Cl<sub>2</sub>, the major isotopomeric ion at 197 amu was selected to calibrate field data, as significant interferences have previously been observed at the other two isotopomer masses (Riedel et al., 2012; Riedel et al., 2013). Furthermore this isotopomer is the most abundant, therefore providing the best signal:noise ratio.

For ClNO<sub>2</sub> the [I(<sup>35</sup>ClNO<sub>2</sub>)]<sup>-</sup> ion (208 amu) was selected over its <sup>37</sup>Cl counterpart for similar reasons. While the [ICl]<sup>-</sup> (162, 164 amu) ion was more abundant, it also displayed a more complex response to humidity variations and is in a more crowded region of the mass spectrum. Furthermore Kercher et al., 2009 reported distorted isotopic ratio (biasing 164 amu over 162) during field

measurements, and some early UoL ambient data occasionally detected a discrepancy in channel ratio (biasing 162 amu over 208) suggesting the presence of unidentified interferences at  $[\text{ICl}]^-$  masses. The choice of  $[\text{I}^{35}\text{ClNO}_2]^-$  for calibration of field data is in accord with previous studies due to its high specificity (Osthoff et al., 2008; Thornton et al., 2010; Mielke et al., 2011; Phillips et al., 2012; Mielke et al., 2013; Bannan et al., 2015; Tham et al., 2016; Wang et al., 2016).

Both the  $\text{Cl}_2$  and  $\text{ClNO}_2$  CIMS calibration experiments primarily used H-mode data, therefore signals due to a number of discrete masses were monitored continuously over the period of the experiment. These masses are discussed in sections 2.2.3 ( $\text{ClNO}_2$ ) and 3.2.1 ( $\text{Cl}_2$ ).

The first step of the data processing method was to multiply the raw counts per second (Hz) for a given mass by a correction factor to compensate for a drift in the detector over time (see section 3.2.2).

The  $\text{I}^-$  reagent ion signal at 127 amu was saturated, and not presumed to affect sensitivity. Sensitivity variations due to water vapour mediated cluster formation have been observed in the past, however (Kercher et al., 2009), due to  $[\text{I}(\text{H}_2\text{O})]^-$  also acting as a reagent ion (see section 2.2.3). As  $[\text{I}(\text{H}_2\text{O})]^-$  formation is dependent on humidity (Slusher et al., 2004), which is highly variable in ambient measurements, this effect had to be accounted for in the calibration factors applied to field data. This was achieved by normalising data to the  $[\text{I}(\text{H}_2\text{O})]^-$  ion. In practice, the normalisation procedure was to divide the counts per second for each mass (after detector drift correction) by the counterpart for the water cluster at 145 amu (the resulting number was then multiplied by  $10^6$  for ease of interpretation).

### 3.5.2 Data averaging

CIMS data were gathered at a time resolution of approx. 11 s for several minutes at each calibration step. For each experiment, normalised CIMS data were plotted as a continuous time series alongside a similar time series of  $\text{NO}_2$  data from the BBCEAS or calculated  $\text{Cl}_2$  concentrations. A time period where the

relevant signals were stable was sought out for each step and trimmed by eye, as exemplified by the flat green line in Figure 3.19. Data for each mass of interest were then averaged across the duration of the stable period to give a single value during that calibration step.

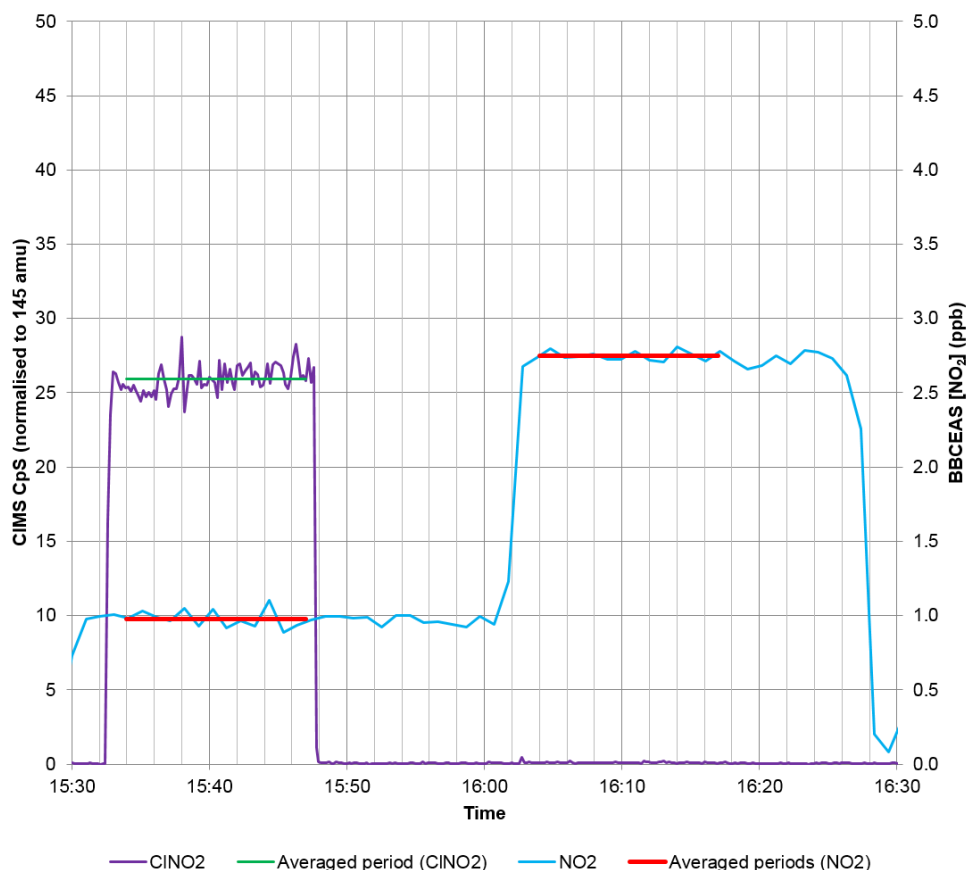


Figure 3.19 Excerpt of a calibration experiment time series, showing how time periods were selected for averaging. CIMS signals are normalised to  $[I(\text{H}_2\text{O})]^-$  and multiplied by  $10^6$  for ease of interpretation.

Each of these average values was subjected to background subtraction. The background value for each mass of interest was determined as a similar stable interval average, corresponding to a step when no  $\text{Cl}_2$  was entering the system (thereby preventing  $\text{ClNO}_2$  formation). The additional condition of the background measurement coil (see section 3.3.8) being inline was also applied after this was installed (*i.e.* series 2 and onwards). During calibration it was not

expected that significant interferences were present, but this method also accounts for instrumental electronic noise.

ClNO<sub>2</sub> concentrations were independently determined *via* BBCEAS as NO<sub>2</sub>, and point values were calculated in a similar way as for the CIMS, *i.e.* using a time series to obtain the average concentration for each flow regime. For BBCEAS data it was necessary to subtract NO<sub>2</sub> co-produced during ClNO<sub>2</sub> synthesis (see section 3.3.6). This was achieved using a process akin to CIMS background subtraction mentioned above. For each Cl<sub>2</sub> (and thus ClNO<sub>2</sub>) concentration, average NO<sub>2</sub> from a step with the dissociator bypassed was subtracted from the average NO<sub>2</sub> from a step wherein the dissociator was inline (in Figure 3.19 the lower and upper red lines, respectively).

Independent determination of Cl<sub>2</sub> concentrations was achieved by calculation of successive dilutions, starting at the certified concentration within the cylinder and working through the successive dilution factors between there and the CIMS inlet.

### 3.5.3 Calibration plots

At this point calibration plots could finally be produced using the background-subtracted average values for a given analyte concentration detected *via* CIMS and the corresponding independently-determined concentration (Figure 3.20).

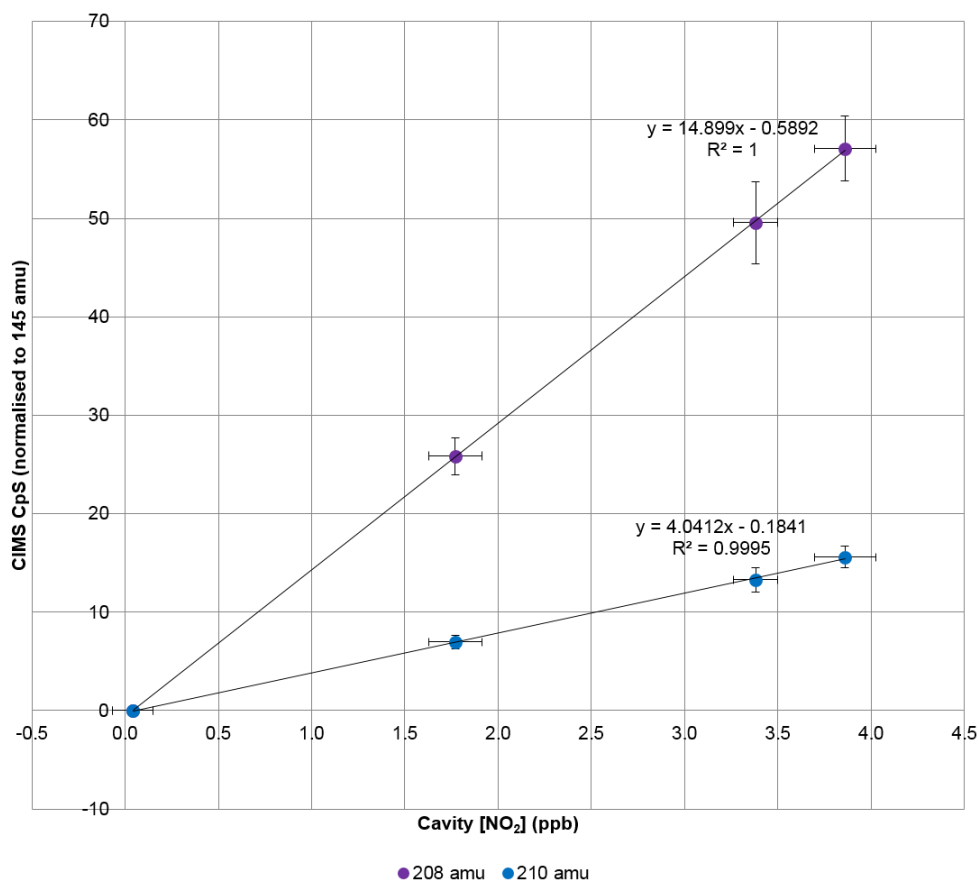


Figure 3.20 Example ClNO<sub>2</sub> calibration plot, including uncertainties as error bars (see section 3.5.4). Linear fit gradients correspond to CIMS sensitivity for a given ion.

The linear fits on these plots represent the sensitivity for a given ion. Additional work remained, however, as uncertainties still needed to be calculated (see section 3.5.4). Furthermore, the simple linear fits shown in the figure were provisional, as a more robust method for fitting the line was performed later for application to field data (see section 3.5.6).

### 3.5.4 Uncertainty determination

Uncertainty of each CIMS data point in the calibration plot (*i.e.* flow regime) was defined as 2 standard deviations ( $2\sigma$ ) of data from the averaged period. As each value had undergone background subtraction which itself had a similar  $2\sigma$  uncertainty, error was therefore propagated as per Equation 3.2a. In this equation the two components  $x$  and  $y$  of combined value  $C$  represent  $2\sigma$  of the

measured and background periods respectively to determine uncertainty of the combined value (*i.e.*  $\delta C$ ).

$$\partial C_a = \sqrt{\partial x^2 + \partial y^2 \dots} \quad \text{a}$$

$$\partial C_m = C \cdot \sqrt{\left(\frac{\partial x}{x}\right)^2 + \left(\frac{\partial y}{y}\right)^2 \dots} \quad \text{b}$$

Equation 3.2 (Skoog et al., 2013) Equations to calculate propagated uncertainty ( $\delta$ ) of several components  $x$ ,  $y$  [*etc*] for numbers combined:

- a) *Via* addition or subtraction ( $C_a$ ).
- b) *Via* multiplication or division ( $C_m$ ).

The uncertainty in NO<sub>2</sub> measurements is based on error associated with spectral fitting of NO<sub>2</sub> (see section 2.3.6) from error in retrieving the NO<sub>2</sub> concentration from the differential absorption spectrum (“statistical”) in addition to errors in the reference cross section and mirror reflectivity (“systematic”). Systematic and statistical errors are combined *via* Equation 3.2a. This overall uncertainty was determined for each NO<sub>2</sub> data point and averaged across the respective stable period. The calculation used to remove co-produced NO<sub>2</sub> from BBCEAS measurements was similar to that for CIMS background subtraction, therefore Equation 3.2a was used again to combine errors in the two measurements.

Uncertainties in Cl<sub>2</sub> concentrations were more complicated as these were based on a mixture of sources: the first source was uncertainty in the cylinder concentration determined by the manufacturer, and the second was uncertainty in the flows (*i.e.* dilutions). For most experiments, flows were measured *via* flow meter, however some were set according to the most recent flow controller calibration. Flow uncertainties were calculated according to relevant calibration certificates or operation manuals. Uncertainty was 0.5% of the reading for the *Gilian “Giliberator 2”* or the greater of 5 sccm or 2% of the reading for the *TSI 4100 series*. Where flows were set using MFC calibrated values, uncertainty was 1% of the controller’s full scale (*Tylan 260 series*), 1%

of setpoint (MKS M100B series operating at >20% of full scale) or 0.2% of full scale (MKS M100B series, <20% of full scale). Propagated uncertainties for individual dilution factors were again calculated via Equation 3.2a using the propagated uncertainties in the relevant MFCs. The dilution factors were subsequently multiplied by each other and the cylinder concentration, however, therefore uncertainty in the overall dilution factor was determined using Equation 3.2b.

### 3.5.5 Data filtering & selection

In each experiment, isotope ratios were plotted as a diagnostic measure to check for the presence of interfering species and confirm identity, as these ratios should fall close to the ratio corresponding to natural chlorine abundance (Kercher et al., 2009), *i.e.* 3:1 for ClNO<sub>2</sub>, and 9:6:1 for Cl<sub>2</sub>. For ClNO<sub>2</sub> calibrations channel ratios were also plotted with a similar objective, whereby channel ratios for the major and minor isotopomers were checked to ensure they match (Figure 3.21). Several calibrations were discarded as outliers where the isotope ratio deviated too far from theoretical values, and/or channel ratios were too different to each other, either of which is suggestive of interferences.

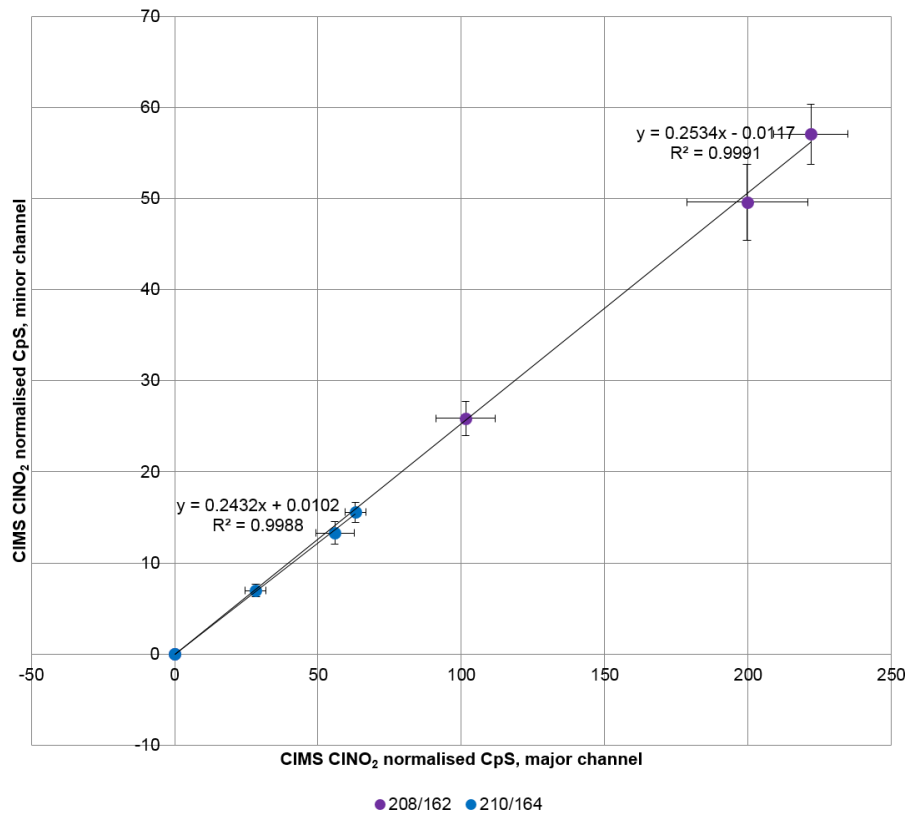
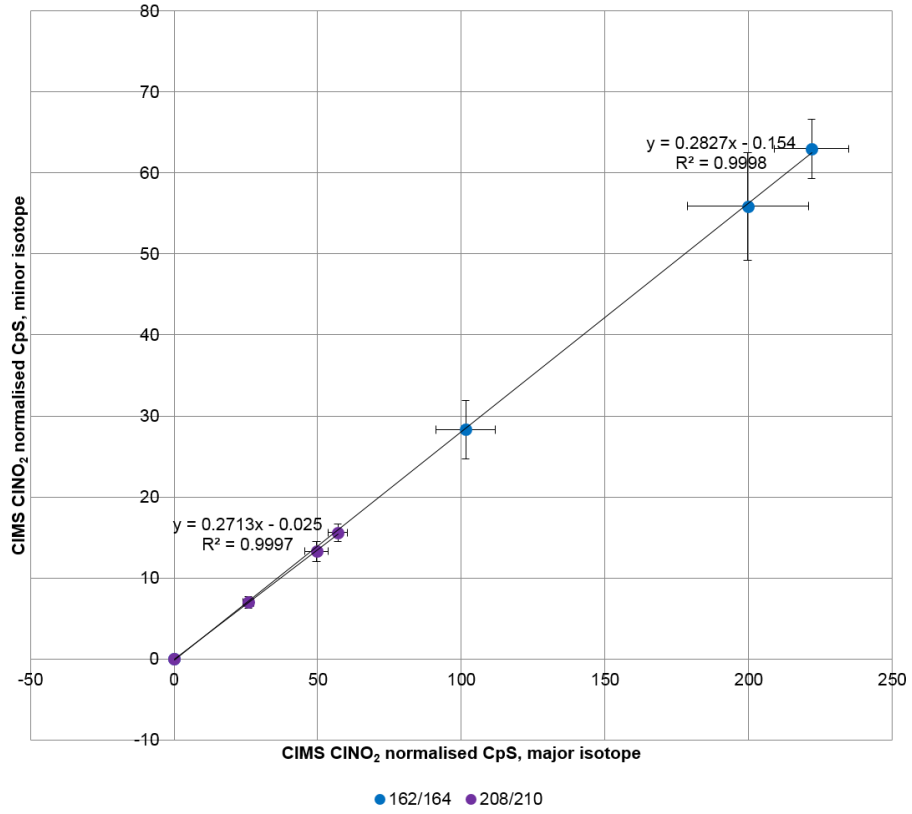


Figure 3.21 Example isotopic and channel ratio plots from a  $\text{ClNO}_2$  calibration experiment.

After sensitivities were filtered for outliers as explained above they still displayed some degree of variation over time. This variation was found to result mainly from a gradual decline in flow tube pressure and detector performance, both of which seemed to reduce sensitivity. Taking these factors into account, sensitivities were grouped together chronologically. Sensitivities calculated while using the background coil (see section 3.3.8) were also segregated from those calculated without. All sensitivities within each group were averaged to obtain several overall calibration factors for application to campaign data as summarised in Figure 3.22.

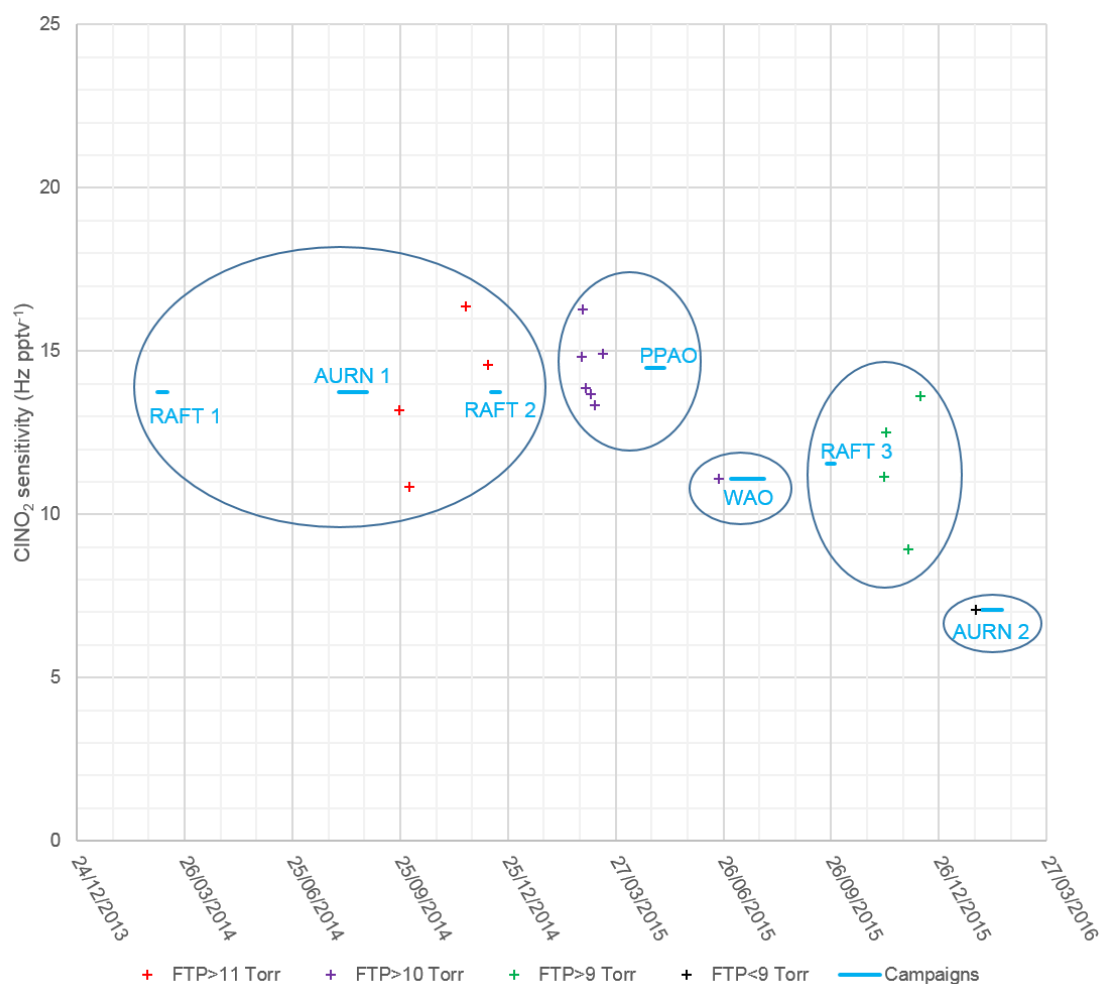


Figure 3.22 Time series showing how  $[I(^{35}\text{ClNO}_2)]^-$  sensitivities were grouped to calibrate field data. Blue lines show each campaign's date and duration (x axis) and the calibration factor applied (y axis). Data points are coloured according to the average CIMS flow tube pressure (FTP) as shown in the legend.

### 3.5.6 Linear fitting & data validation

In these experiments, calibration plots were formed from the concentration of  $\text{Cl}_2$  or  $\text{ClNO}_2$  (x axis) and the CIMS ion counts (y axis), both of which are subject to some degree of uncertainty, however most simple plotting software fails to take into account uncertainty in x axis variables. The “Williamson-York method” of linear least-squares fitting (Cantrell, 2008) was therefore used to determine a bivariate linear fit for each calibration experiment, representing a more accurate sensitivity. Uncertainty values for both CIMS and BBCEAS/calculated concentrations detailed above were used to weight data points (*i.e.* fitting weight= $1/\delta C$ ) in determining the bivariate fit for each experiment. The relative standard error was also calculated for each linear fit, giving a measure of precision. Table 3.4 shows sensitivities determined in each experiment and their precision. The overall average precision for any given sensitivity was  $\pm 6.19\%$  ( $\text{ClNO}_2$ ) and  $\pm 4.83\%$  ( $\text{Cl}_2$ ).

Table 3.4 Sensitivity, precision and average flow tube pressure (FTP) for individual CIMS calibration experiments for  $\text{ClNO}_2$  (top) and  $\text{Cl}_2$  (bottom).

Date	$[(^{35}\text{ClNO}_2)]$ sensitivity (normalised CpS pptv <sup>-1</sup> )	Precision (+/-)	Average FTP (Torr)
24/09/2014	13.2	6.52%	11.8
03/10/2014	10.8	3.62%	11.9
20/11/2014	16.4	3.50%	11.8
09/12/2014	14.6	4.93%	11.7
26/02/2015	14.8	4.21%	11.0
27/02/2015	16.3	3.59%	10.9
02/03/2015	13.9	3.96%	10.8
06/03/2015	13.7	5.47%	10.8
09/03/2015	13.3	2.04%	10.7
16/03/2015	14.9	0.27%	10.3
23/06/2015	11.1	2.03%	10.9
10/11/2015	11.1	5.54%	9.91
12/11/2015	12.5	18.9%	9.80
01/12/2015	8.92	9.48%	9.56
11/12/2015	13.6	21.6%	9.20
27/01/2016	7.07	3.42%	8.96

Date	$[(^{35}\text{Cl}_2)]$ sensitivity (normalised CpS pptv <sup>-1</sup> )	Precision (+/-)	Average FTP (Torr)
11/09/2014	8.07	2.94%	11.8
25/09/2014	5.89	3.10%	11.8
26/09/2014	5.63	5.05%	11.9
23/10/2014	8.94	1.87%	11.9
27/10/2014	7.43	1.09%	11.9
13/11/2014	6.89	0.70%	11.8
19/11/2014	7.77	3.66%	11.8
08/12/2014	8.35	8.18%	11.7
13/01/2015	8.60	8.17%	11.5
11/02/2015	9.00	2.07%	11.4
12/02/2015	9.49	2.16%	11.3
23/02/2015	9.22	6.60%	11.0
10/03/2015	12.7	2.83%	10.6
17/03/2015	13.5	11.7%	10.3
25/03/2015	10.8	1.83%	10.2
14/10/2015	6.83	6.15%	10.1
15/10/2015	6.82	8.29%	10.2
19/10/2015	7.01	8.02%	10.1
20/10/2015	6.50	9.38%	10.1
21/10/2015	6.79	8.00%	10.0
22/10/2015	6.14	3.34%	10.0
02/11/2015	5.95	3.48%	9.95
03/11/2015	6.31	4.88%	9.92
28/01/2016	5.31	4.23%	8.80
24/03/2016	6.35	3.08%	7.35

As mentioned in section 3.5.5, several sensitivities were averaged together to create calibration factors for each campaign. The relative standard deviation of the averaged sensitivities gives an estimate of the calibration factor

accuracy. Table 3.5 shows information regarding calibration factors applied to data for each campaign.

Table 3.5 Table summarising campaign dates and average flow tube pressures, with corresponding calibration factors (CF) in addition to the accuracy and precision thereof.

Campaign	Start/end dates	I <sup>[35]ClNO<sub>2</sub>]</sup>			I <sup>[35]Cl<sub>2</sub>]</sup>			Average FTP (Torr)
		CF (normalised CpS pptv <sup>-1</sup> )	Accuracy (+/-)	Average precision (+/-)	CF (normalised CpS pptv <sup>-1</sup> )	Accuracy (+/-)	Average precision (+/-)	
RAFT 1	03/03/2014 11/03/2014	13.7	16.9%	4.64%	7.94	16.0%	3.80%	11.2
AURN 1	04/08/2014 28/08/2014	13.7	16.9%	4.64%	7.94	16.0%	3.80%	11.5
RAFT 2	11/12/2014 19/12/2014	13.7	16.9%	4.64%	7.94	16.0%	3.80%	11.6
PPO	22/04/2015 07/05/2015	14.4	7.46%	3.26%	12.3	11.4%	5.45%	11.0
WAO	03/07/2015 31/07/2015	11.1	N/A	2.03%	12.3	11.4%	5.45%	10.8
RAFT 3	22/09/2015 29/09/2015	11.5	17.6%	13.9%	6.54	5.80%	6.45%	10.5
AURN 2	01/02/2016 18/02/2016	7.07	N/A	3.42%	5.83	12.6%	3.66%	8.66

Limits of detection (LoD) were determined per experiment as mean+2 $\sigma$  of a blank measurement, for which a 1-minute section from the same period used for background subtraction was employed. The detection limits for field measurements was determined as the average LoD over all calibration experiments. 2 $\sigma$ , 1 min detection limits were therefore 4.20 ppt (ClNO<sub>2</sub>) and 7.14 ppt (Cl<sub>2</sub>).

Table 3.6 summarises the sensitivity, accuracy, precision and LoD for ClNO<sub>2</sub> measurements reported in the literature. Sensitivities are included in this table, as they are often quoted in the literature, but these tend to be very instrument-specific and are therefore not a sensible comparison. The accuracies of calibration factors used in this thesis (approx. 7-18%) compare favourably to literature values (18-30%). Average precision for the UoL ClNO<sub>2</sub>

calibration factors ranges between 4-14%, which is similar to literature values (3-10%). It should be noted, however, that the higher end of this range is given by the RAFT 3 calibration factor, whereas the others are <5%.

Table 3.6 Literature values for sensitivity, accuracy, precision and LoD for literature ClNO<sub>2</sub> measurements, where reported.

Reference	Sensitivity (Hz/pptv)	Accuracy (%)	Precision (%)	LoD (pptv)
Osthoff et al., 2008	-	18	-	50
Kercher et al., 2009	1	20	10	5 (S/N>2)
Mielke et al., 2011	0.31	30	5	5
Mielke et al., 2013	-	30	3	-
Bannan et al., 2015	0.093	30	-	11 (3σ)
Wang et al., 2016	1.2	20	10	2 (1σ)
Tham et al., 2016	1.4	25	3	14 (3σ)
[This work]	7-13	7-18	2-14	4 (2σ)

The early measurements by Osthoff et al., 2008 had a relatively high (50 ppt) LoD, however all others report much lower values (<15 ppt). Only Wang et al., 2016 reported a limit of detection lower than the current UoL work (1σ LoD are 2 and 3.36 ppt respectively).

### 3.6 Summary

The principal masses that were monitored and calibrated *via* CIMS over the course of this thesis were 208 amu for [I(ClNO<sub>2</sub>)]<sup>-</sup> and 197 amu for [I(Cl<sub>2</sub>)]<sup>-</sup>, however other masses were also studied resulting from the two isotopes of chlorine and ion chemistry of ClNO<sub>2</sub>.

During commissioning, the new CIMS instrument was tested by successfully measuring molecular chlorine and bromine. CDC and mass selector voltages were adjusted to optimise the CIMS instrument, improving the sensitivity and resolution to improve detection of species of interest.

The CIMS instrument was operated mainly in H-mode, monitoring specific masses over time. The specific mass observed did not always represent the full height (and thus, intensity) of the corresponding species' peak. Correction factors were determined to correct for this effect, which varied over time.

The equipment used in the calibration system was designed to be portable to facilitate calibrations during field work, and was therefore built into a compact case. A variety of experiments were carried out to test and develop individual components or aspects of the calibration experiments. This started with basics such as mass flow controllers, which were tested to ensure that the gas flows used during all experiments were quantifiable and consistent. Nitrogen was used as a dilutant and flow gas, the source of which was changed requiring a test to ensure no additional background signals were added.

Two different reactions were used to generate ClNO<sub>2</sub> for calibration of the CIMS. The first of these involved N<sub>2</sub>O<sub>5</sub> which was itself synthesised from the base reagents NO and O<sub>2</sub> and purified by distillation. ClNO<sub>2</sub> was quantified by detecting N<sub>2</sub>O<sub>5</sub> (thermally dissociated to NO<sub>3</sub>) *via* BBCEAS before the reactor, in which quantitative conversion to ClNO<sub>2</sub> was assumed. Several issues were apparent with calibrations using N<sub>2</sub>O<sub>5</sub>, prompting development of methods using the second reaction to form ClNO<sub>2</sub>.

Calibrations using Cl<sub>2</sub> and NaNO<sub>2</sub> (both of which are commercially available) to generate ClNO<sub>2</sub> required the nitryl chloride to be thermally dissociated to NO<sub>2</sub>, therefore the BBCEAS optics were changed. A thermal dissociator was developed and tested to ensure quantitative dissociation. The reaction vessel also underwent some development to compensate for issues related to loss of ClNO<sub>2</sub> after formation.

The effects of variable humidity were investigated, as this can affect CIMS detection sensitivities through the [I(H<sub>2</sub>O)]<sup>-</sup> ion acting as a reagent ion. Detection of ClNO<sub>2</sub> was found to be affected by humidity, however this effect was minimal except at extremely low humidity, well below typical levels in the laboratory or expected in the field. As a precaution, ions detected *via* CIMS corresponding to Cl<sub>2</sub> and ClNO<sub>2</sub> were normalised to the [I(H<sub>2</sub>O)]<sup>-</sup> ion to neutralise this effect.

A steel coil was designed to facilitate CIMS background determination by stripping out all species of interest, which it was shown to do effectively. This coil was set up to gather background data automatically at timed intervals

during fieldwork. The coil was also used to show the responsiveness of the CIMS, demonstrating its suitability for gathering data at the chosen time resolution.

The equipment used in experiments to determine CIMS calibration factors for fieldwork was developed over several distinct iterations, all of which used the core principle of changing the concentration of chlorine entering the system through several dilutions and to the CIMS either directly (to calibrate Cl<sub>2</sub>) or *via* reactor and dissociator (for ClNO<sub>2</sub>). Independent measures of the calibrated species were obtained simultaneously, *via* BBCEAS (for ClNO<sub>2</sub>) or mathematically (for Cl<sub>2</sub>).

CIMS data were corrected for detector drift then Cl<sub>2</sub> and ClNO<sub>2</sub> ion signals were normalised to the [I(H<sub>2</sub>O)]<sup>-</sup> ion. Several minutes of stable CIMS data were averaged together to ascertain a single value for each concentration of the analyte. BBCEAS data underwent the same process, whereas Cl<sub>2</sub> concentrations were calculated by tracing the known concentration in the cylinder through successive dilutions.

Uncertainty in each sensitivity value was calculated as 2 standard deviations of the averaged value (CIMS ClNO<sub>2</sub> and Cl<sub>2</sub>), *via* spectral fitting error (BBCEAS NO<sub>2</sub>) or through the dilutions due to flow rate measurements (Cl<sub>2</sub>). The uncertainties of each measurement were used to weight points on the calibration plot during a bivariate fitting procedure to determine the sensitivity in a given experiment.

Data from some experiments were filtered due to irregularities in isotope or channel ratios indicating potential interferences (*i.e.* reduced confidence in the identity of masses corresponding to the analyte).

Sensitivity was observed to change over time, therefore remaining calibration factors were grouped along lines of methodology, chronology and flow tube pressure. Calibration factors within each group were averaged and applied to corresponding field data. The accuracy, precision and detection limits determined for UoL calibration factors were compared with literature values, and were generally similar to (and often better than) these previous studies.

## 4 Inland measurements: University of Leicester (UoL)

### 4.1 Site description & data overview

#### 4.1.1 Site introduction

Ambient concentrations of nitryl chloride and several related species were measured to examine the conditions leading to ClNO<sub>2</sub> formation at an inland location in the UK. Data were gathered at two locations on the suburban University of Leicester (UoL) campus over five distinct campaigns from March 2014 to February 2016. The measurement periods are referred to as “RAFT n” for campaigns where the CIMS was based in the Real-Time Air Fingerprinting (RAFT) laboratory and “AURN n” for those based in the Automatic Urban and Rural Network (AURN) station as per the dates given in Table 4.1, which can be found in section 4.1.3. This chapter gives an overview of these results and places them in a climatological context. The campaigns carried out at UoL were spread across different times of year, enabling exploration of seasonal effects upon ClNO<sub>2</sub>. The city of Leicester with population ~348 000 in 2016 (Office for National Statistics, 2017) provides chemical conditions typical of urban environments (in terms of NO<sub>x</sub> and VOC) for a medium-sized UK city. Moreover, Leicester is located in the centre of England, potentially limiting the availability of sea salt chloride also necessary for ClNO<sub>2</sub> formation (see section 1.2.4).

#### 4.1.2 Location

Leicester is an interesting location to investigate ClNO<sub>2</sub> chemistry in a UK context as it is an urban location in the centre of England (52° 37' 21" N, 01° 7' 27" W - Figure 4.1a) approximately 200 km from the open sea. The marine influence is therefore limited but nitrogen oxides are typically in plentiful supply, allowing an indication to be given of the prevalence of ClNO<sub>2</sub> throughout the UK when the main aerosol chloride source, sea salt, is as low as is likely to occur within the UK.

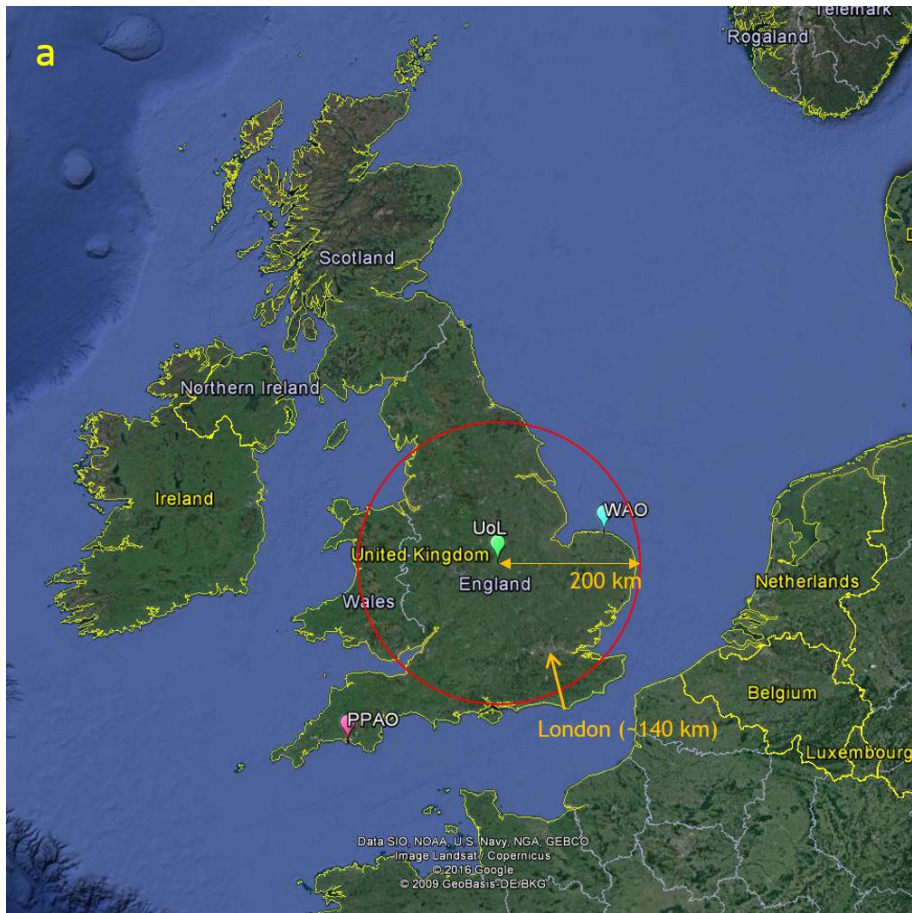




Figure 4.1 Maps & satellite images.

- a) Measurement sites for campaigns discussed in this thesis in a UK context (Google Earth, 2017a).
- b) University of Leicester location relative to urban centre (Google Earth, 2017b).
- c) University of Leicester and immediate surroundings (Google Earth, 2017b).

Figure 4.1b shows the university within the context of the city. The university is within the city limits but approximately 1.6 km south/southeast of the city centre. Several roads are marked on this figure, the largest of which are two major roads into the city, London Road and Welford Road, positioned either side of the university (to the northeast and southwest, respectively) with Tigers Way connecting them to the northwest. University Road and Victoria Park Road are both smaller but very close to the university (northwest and southeast respectively) and are therefore also likely to influence measurements at UoL. Numerous open and/or green areas are nearby, such as Victoria Park, Welford Road Cemetery and the Queens College playing field (indicated on Figure 4.1c).

The Automatic Urban and Rural Network (AURN) is a network of monitoring stations operated by the Department for Environment, Food and Rural Affairs (Defra) and distributed nationwide to observe the UK's compliance with air quality legislation (Defra, 2011a). The AURN station located on the University of Leicester campus is categorised as an urban “background” station, meaning that it is placed to get a general indication of the pollution level from all combined sources in an area representative of a few square kilometres rather than monitoring pollution from a specific source or street as do “industrial” or “traffic” stations (Defra, 2011b). AURN measurements used in this thesis are the chemical parameters NO, NO<sub>2</sub>, O<sub>3</sub> (see section 2.4.1 for instrument details) and meteorological parameters temperature, humidity, wind speed and wind direction. For some UoL campaigns photolysis data are also available, gathered *via* spectral radiometer also positioned at the AURN station. For AURN campaigns, the CIMS instrument was co-located with supporting instruments inside an air-conditioned building with an inlet line (¼ inch OD PFA tubing, approx. 4 m length) passing through a hole in the southeast wall and attached to the wall at approx. 3 m height. The inlet was affixed facing downwards and sheltered using an upturned plastic funnel to prevent entry of rainwater. The station is, as shown in Figure 4.2, located on the southwest corner of the University of Leicester campus adjacent to the university's sports centre. Some interference in terms of Cl<sub>2</sub> was anticipated as the exhaust vents for the sports centre, which includes a swimming pool, are positioned approximately 40 m northeast of the inlet. Other notable features include Welford Road (~120 m southwest), one of the major routes into the city centre, and the smaller University Road (~25 m northwest) and Victoria Park Road (~340 m southeast). The area immediately around the measurement site is flat and open due to the college playing field (and to a lesser extent the cemetery, as this contains some trees) allowing air to flow relatively freely around this site.

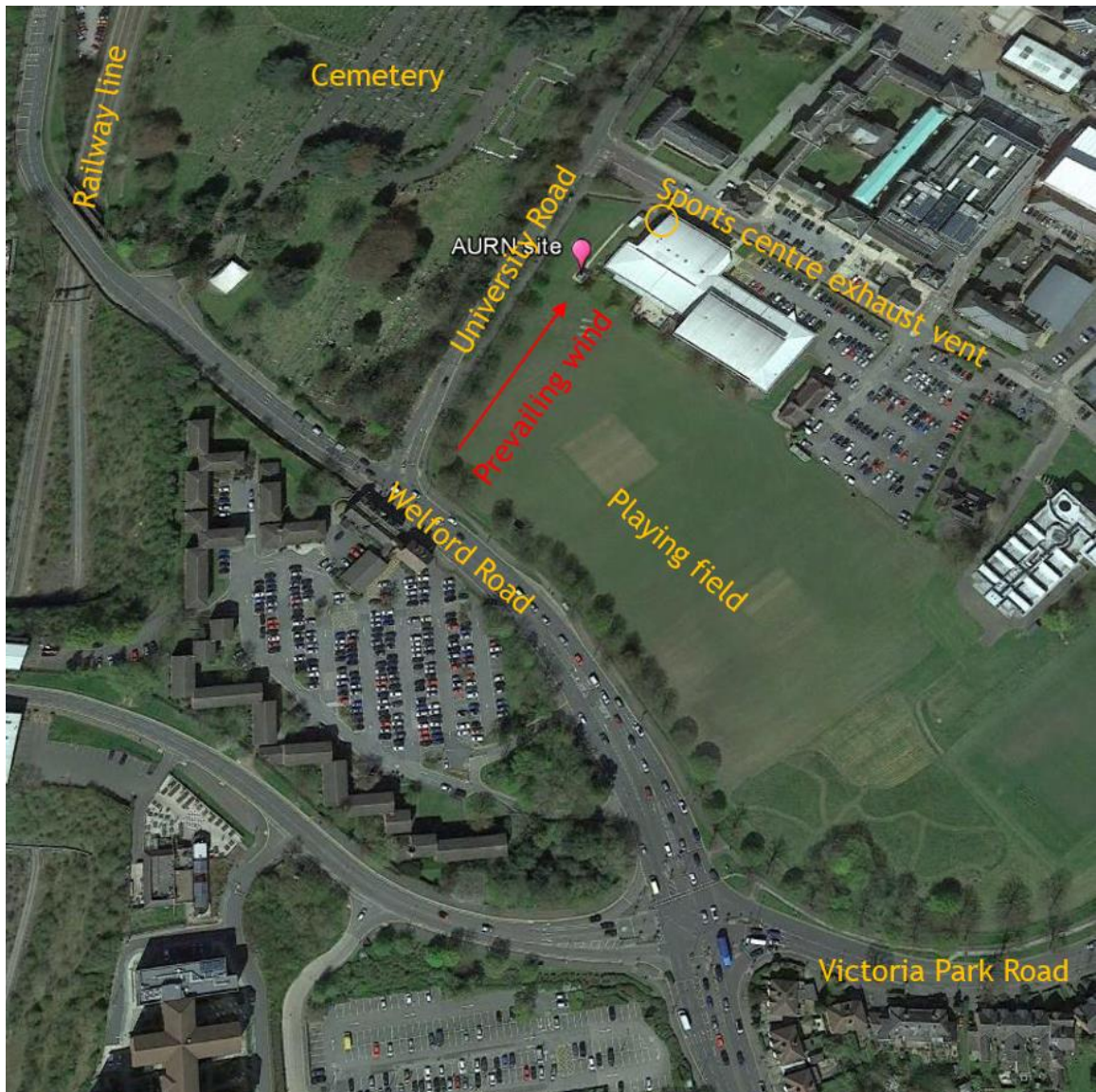


Figure 4.2 Satellite image showing location for AURN station measurements (Google Earth, 2017b) with some nearby potential influences shown.

The University of Leicester RAFT (Real-Time Air Fingerprinting) laboratory is located in the George Porter building. For RAFT campaigns the CIMS instrument was inside the air conditioned laboratory with a long inlet line ( $\frac{1}{4}$  inch OD PFA tubing, approx. 5 m length) reaching outside through a hole in the northeastern wall at the position indicated on Figure 4.3. The inlet line was fixed to the wall at  $\sim 3$  m height, with similar shielding from rainwater as for AURN measurements. The same AURN station instruments (located approx. 400 m away) were used for supporting measurements (e.g.  $\text{NO}$ ,  $\text{NO}_2$ ,  $\text{O}_3$ ) for these campaigns. Air flow in the vicinity of the inlet is likely to have been somewhat

hindered by a wall (~4 m height) and the Rattray, George Porter and Adrian buildings (approx. 8, 15 and 15 m respectively) which enclose the courtyard, in addition to the mature tree in the centre (~10 m). The most likely source of pollution at this location is University Road (~80 m northwest of inlet). Positioning the CIMS at this location also allowed comparison of observations to the AURN station to assess what, if any, interference was present in  $\text{Cl}_2$  and  $\text{ClNO}_2$  due to any chlorine species that may have been emitted from the leisure centre exhaust system while still being close enough to the AURN station to retain the relevance of supporting measurements collected there.

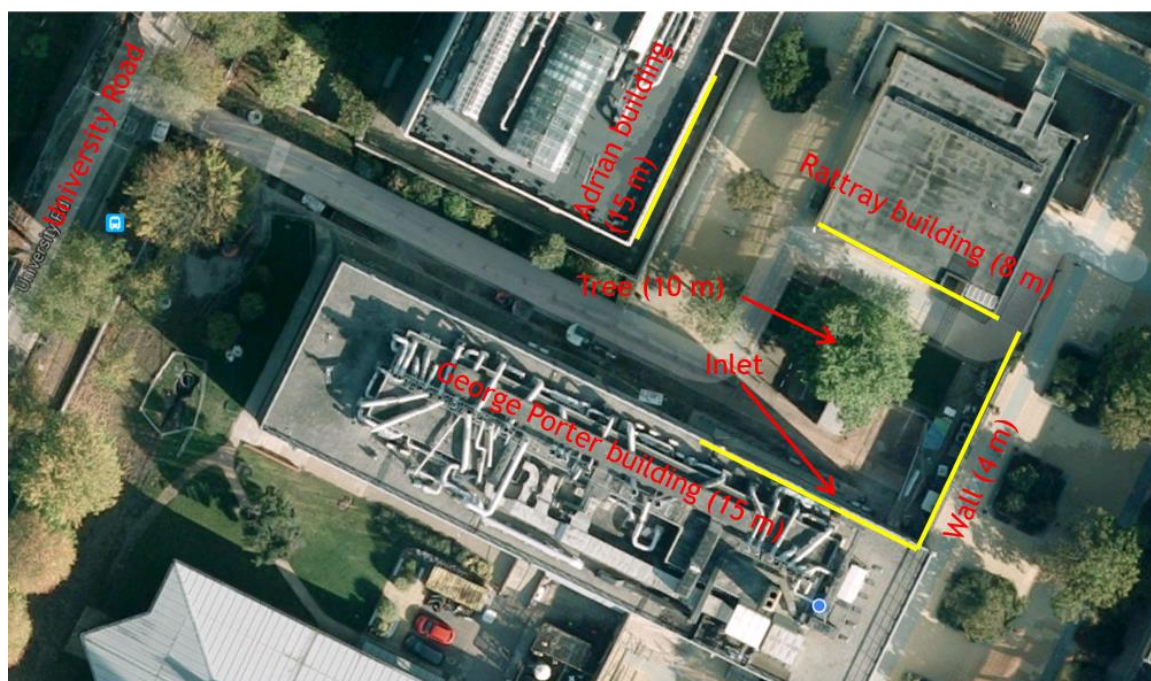


Figure 4.3 Satellite image showing location for RAFT laboratory measurements (Google Earth, 2017b), showing enclosed area around inlet (heights estimated above ground level).

#### 4.1.3 Data overview

The dates of each campaign are shown in Table 4.1 (note that only night time data, 23:00 to 04:59 are used). Figure 4.4 to Figure 4.8 are complete time series showing concentrations of  $\text{ClNO}_2$  and several related pollutants throughout each of the Leicester campaigns. Note that the y axis for  $\text{ClNO}_2$  is scaled differently for each campaign due to the wide range in  $\text{ClNO}_2$  concentrations observed over different seasons (see section 4.3).

Table 4.1 Table summarising UoL campaigns with dates and average, maximum and interquartile ranges (IQR) for ClNO<sub>2</sub>, NO, NO<sub>2</sub> and O<sub>3</sub> (15 min averaged night-time data, 23:00 to 04:59). Aerosol chloride and nitrate (from 24-hour PM<sub>10</sub> filters) are also given for campaigns where these were measured.

		RAFT 1 03-11 Mar 2014 (Spring)	AURN 1 04-28 Aug 2014 (Summer)	RAFT 2 11-19 Dec 2014 (Winter)	RAFT 3 22-29 Sep 2015 (Autumn)	AURN 2 01-18 Feb 2016 (Winter)
ClNO <sub>2</sub> (ppt)	Mean	72	14	52	24	117
	IQR	4.7 - 130	1.3 - 23	5.1 - 71	2.8 - 37	1.1 - 205
	Max	274	74	248	90	733
NO (ppb)	Mean	9.7	4.1	6.4	10.0	6.9
	IQR	0.8 - 4.2	0.6 - 5.6	2.0 - 4.7	1.0 - 7.3	0.7 - 3.3
	Max	81	23	86	90	106
NO <sub>2</sub> (ppb)	Mean	14	10	12	13	14
	IQR	5.9 - 25	4.5 - 14	5.5 - 16	6.4 - 19	5.2 - 21
	Max	38	27	41	36	47
O <sub>3</sub> (ppb)	Mean	20	16	20	11	20
	IQR	13 - 28	11 - 22	16 - 27	3.3 - 16	12 - 29
	Max	36	30	35	27	40
Cl <sup>-</sup> (µg m <sup>-3</sup> )	Mean	4.6	3.1	5.0	-	-
	IQR	2.1 - 5.4	1.1 - 4.2	4.4 - 5.9	-	-
	Max	10.5	7.8	6.2	-	-
NO <sub>3</sub> <sup>-</sup> (µg m <sup>-3</sup> )	Mean	21.6	3.6	4.8	-	-
	IQR	8.8 - 33.2	2.5 - 3.8	2.8 - 5.7	-	-
	Max	49.9	10.0	10.2	-	-

Nitryl chloride observations exhibit strong seasonality (discussed later in section 4.3), therefore comparisons with the literature must be selective. While mean nightly maximum would likely be the best measure for comparison, overall maximum observations were chosen for the following comparisons as these are more commonly reported in the literature. Prior observations of ClNO<sub>2</sub>, including the literature campaigns used for comparison here, are discussed in section 1.3.

The maximum observation in spring at UoL was 274 ppt. This is similar to the 250 ppt observed by Mielke et al., 2011 (continental Canada, April 2010) but much lower than the 1300 ppt observed by Riedel et al., 2013 in a plume above the nocturnal surface layer (continental USA, February/March 2011).

Summertime measurements at UoL were very low, with a maximum observation of 74 ppt. Summertime maximum measurements in the literature typically dwarf this, including the 1200 ppt observed by Osthoff et al., 2008 (coastal USA, August/September 2006), 800 ppt by Phillips et al., 2012 (continental Germany, August/September 2011), 1997 ppt by Tham et al., 2013 (coastal China, August 2013) and 2070 ppt by Tham et al., 2016 (continental China, June to September 2014). Of special note the UoL maximum is lower than the only other UK measurement reported in the literature, 724 ppt reported by Bannan et al., 2015 in London (July/August 2012). It may, however, be comparable with the 144 ppt reported by Faxon et al., 2015 (coastal USA, September 2013).

The highest autumn measurement at UoL was 90 ppt. This may also be comparable to the 144 ppt from Faxon et al., 2015 (coastal USA, September 2013), but is again much lower than the 800 ppt reported by Phillips et al., 2012 (continental Germany, August/September 2011) and 1200 ppt by Osthoff et al., 2008 (coastal USA; August/September 2006).

Winter measurements at UoL were significantly higher than other seasons. The maximum shown in the table is 733 ppt in February 2016, however this only takes into account night-time data (23:00 to 04:59). The actual maximum  $\text{ClNO}_2$  measurement at UoL is 911 ppt (09:15 on 16/02/16). This is somewhat lower than many literature values such as 1300 ppt reported by Riedel et al., 2013 (continental USA, February/March 2011) and much lower than the 4700 ppt observed by Wang et al., 2016 (coastal China, November/December 2013). It is, however, higher than the 450 ppt reported by Thornton et al., 2010 (continental USA, February 2009).

Overall the maxima observed during UoL campaigns tend to be significantly lower than those reported in the literature. It should be noted, however, that most of the literature studies took place in or near cities much larger than Leicester, with populations at least an order of magnitude greater. For example the Bannan et al., 2015 and Riedel et al., 2012 studies took place in London and Los Angeles respectively, both of which are megacities with population two orders of magnitude greater than Leicester. Of all the studies compared here only Boulder, Colorado has a population (~100 000) smaller than Leicester (~350

000), the studies near which (Thornton et al., 2010; Riedel et al., 2013) gave relatively similar ClNO<sub>2</sub> concentrations (see comparison of winter measurements above). The study near Frankfurt, Germany (Phillips et al., 2012; population ~700 000) is also relatively similar to Leicester, however measurements at this location were also significantly larger (see the comparison of autumn measurements above). This is likely due to the relative magnitude of pollution emitted (which increases with city size and density) will significantly affect formation of N<sub>2</sub>O<sub>5</sub> and, therefore, ClNO<sub>2</sub>.

The AURN 1 (August 2014; approx. 3 weeks) campaign time series is shown in Figure 4.4. CIMS (ClNO<sub>2</sub> and Cl<sub>2</sub>) data are available throughout most of the campaign except during full spectrum scans, background measurements and ~2 days from 13<sup>th</sup> to 15<sup>th</sup> August. A much larger gap was present in the NO, NO<sub>2</sub> and O<sub>3</sub> data (08-19 August). Figure 4.5 shows the time series for the AURN 2 campaign in February 2016 (approx. 3.5 weeks). Some CIMS data were again removed (17-18<sup>th</sup> and 23-24<sup>th</sup> February) however NO, NO<sub>2</sub> and O<sub>3</sub> are almost entirely continuous. Photolysis data are available for both AURN campaigns.

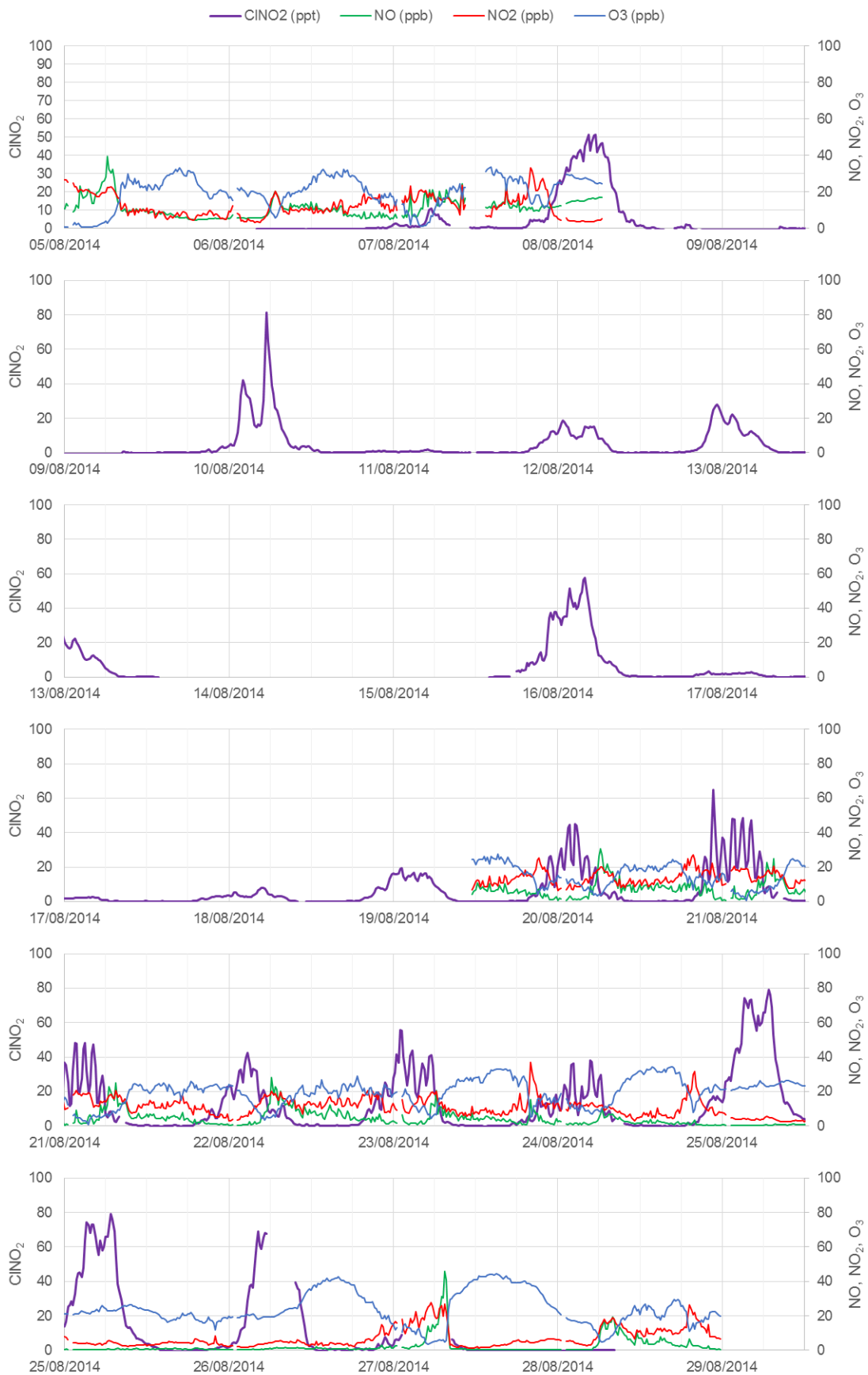


Figure 4.4 Complete time series for AURN 1 campaign (August 2014) showing concentrations of ClNO<sub>2</sub>, NO, NO<sub>2</sub> and O<sub>3</sub> (15 min averaged data).

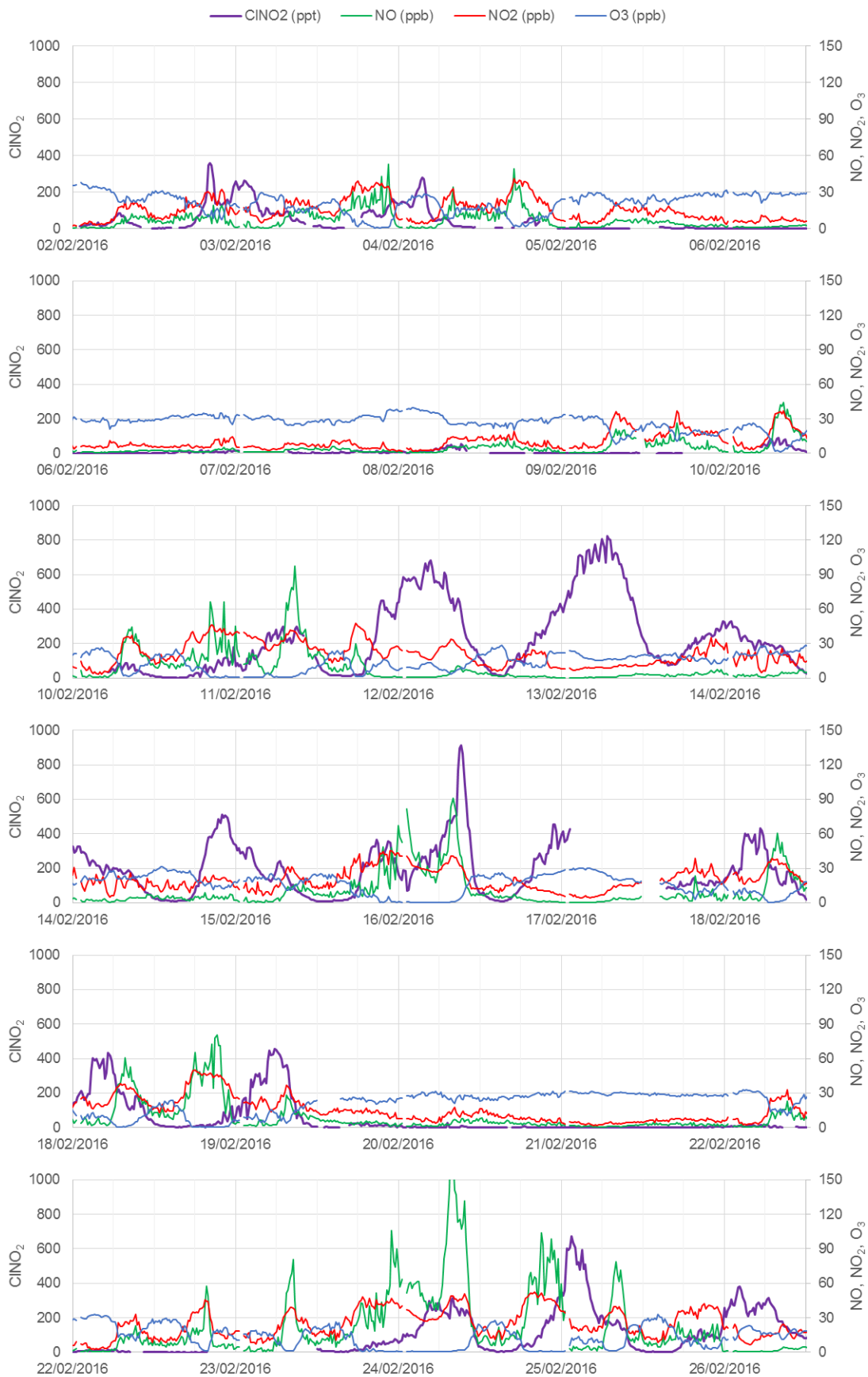


Figure 4.5 Complete time series for AURN 2 campaign (February 2016) showing concentrations of ClNO<sub>2</sub>, NO, NO<sub>2</sub> and O<sub>3</sub> (15 min averaged data).

The time series in Figure 4.6 shows the RAFT 1 campaign in March 2014. ClNO<sub>2</sub>, NO, NO<sub>2</sub> and O<sub>3</sub> data are almost entirely continuous for approx. 1 week. The same applies to the RAFT 2 campaign in Figure 4.7 (December 2014; ~1 week). Figure 4.8 shows a time series of the RAFT 3 campaign (September 2015; ~1 week) with near-continuous CIMS data but NO, NO<sub>2</sub> and O<sub>3</sub> missing for 24-25<sup>th</sup> September. Photolysis rates are also available for RAFT 2.

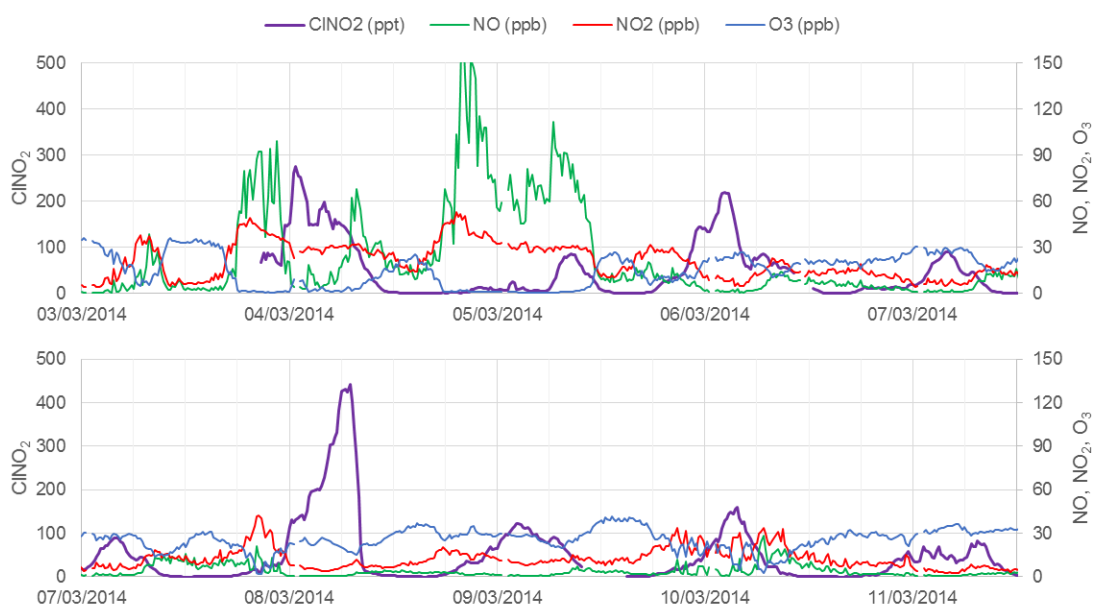


Figure 4.6 Complete time series for RAFT 1 campaign (March 2014) showing concentrations of ClNO<sub>2</sub>, NO, NO<sub>2</sub> and O<sub>3</sub> (15 min averaged data).

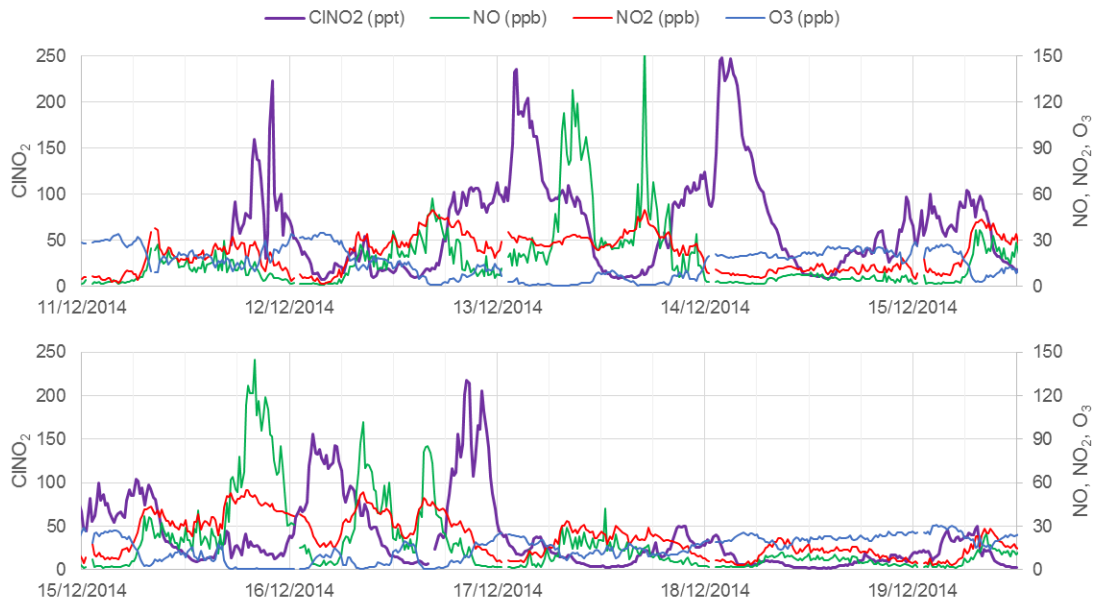


Figure 4.7 Complete time series for RAFT 2 campaign (December 2014) showing concentrations of  $\text{ClNO}_2$ ,  $\text{NO}$ ,  $\text{NO}_2$  and  $\text{O}_3$  (15 min averaged data).

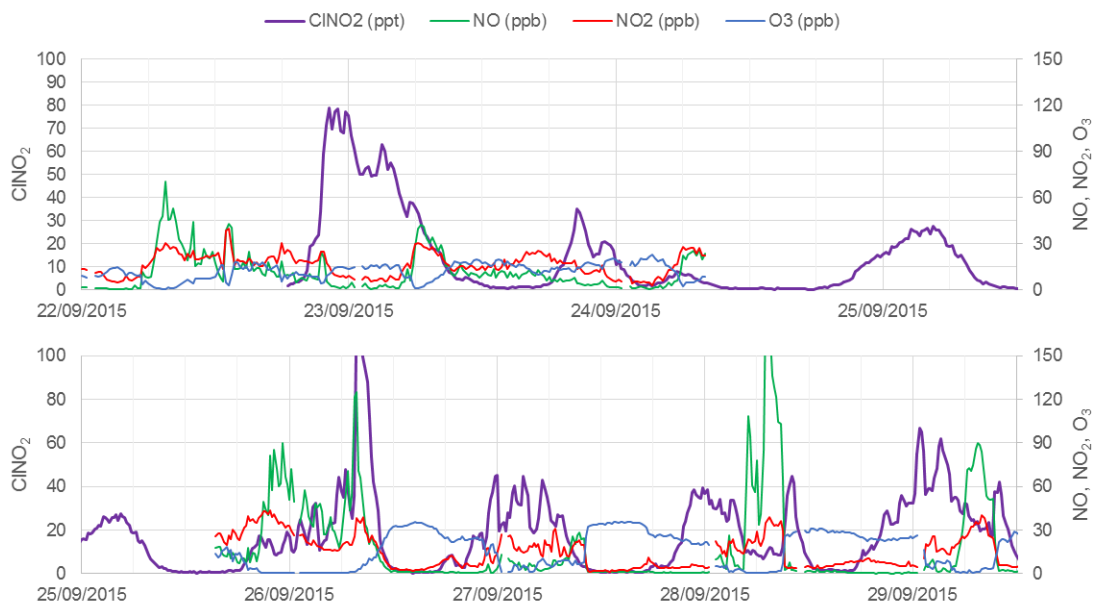


Figure 4.8 Complete time series for RAFT 3 campaign (September 2015) showing concentrations of  $\text{ClNO}_2$ ,  $\text{NO}$ ,  $\text{NO}_2$  and  $\text{O}_3$  (15 min averaged data).

Figure 4.9 shows wind roses (a) and pollution roses (b) for all campaigns giving data regarding wind direction combined with wind speed or observed  $\text{ClNO}_2$  concentrations respectively. These are placed here to facilitate comparisons with the time series, but are mostly discussed in section 4.3.

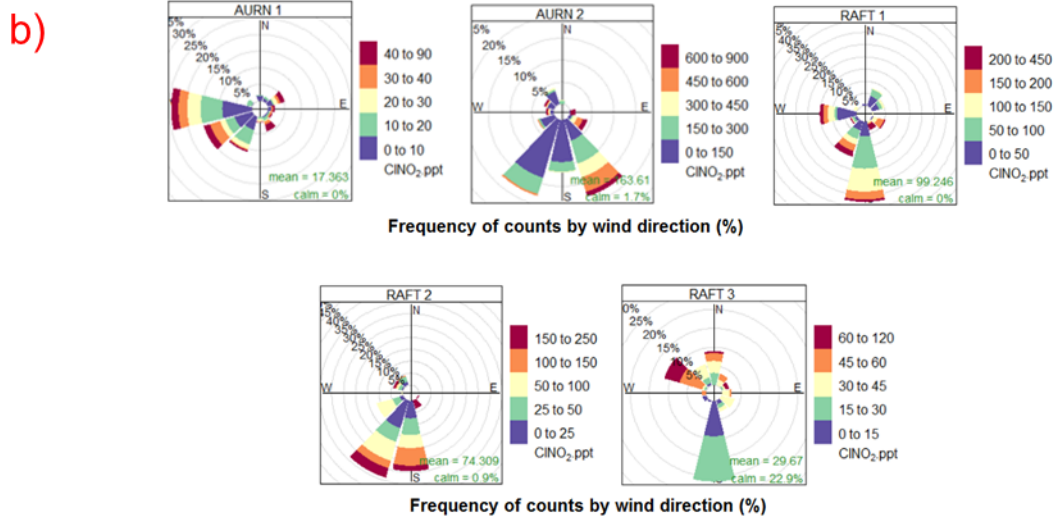
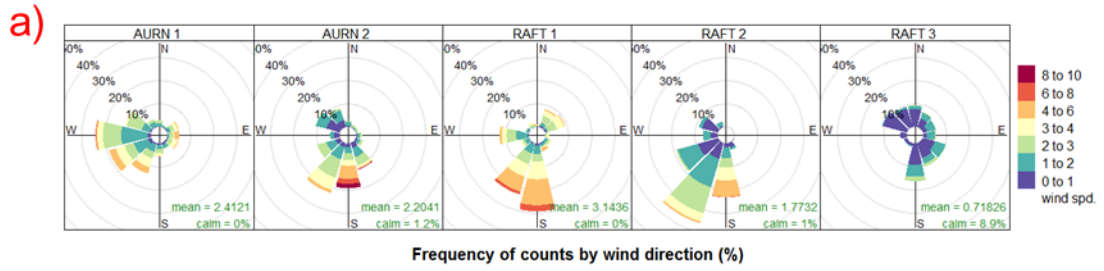


Figure 4.9 Plots relating to wind conditions for all UoL campaigns (15 min averaged data).

- a) Wind roses (wind speed in  $\text{ms}^{-1}$ ).
- b)  $\text{CINO}_2$  pollution roses (night-time data only, 23:00 to 04:59 UTC).

## 4.2 Diel patterns of measured species at UoL

ClNO<sub>2</sub> is formed at night from the reaction of N<sub>2</sub>O<sub>5</sub> (another night-time species) with aerosol chloride, and is photolysed during the day. This pattern is demonstrated clearly in Figure 4.10 by the patterns of ClNO<sub>2</sub> photolysis rate ( $j_{\text{ClNO}_2}$ ) and concentration. The figure shows these patterns are consistent both for individual days (a) and as an average diel profile (b).

In this figure, ClNO<sub>2</sub> concentrations can be seen to rise during the night, typically peaking at 03:00 (~100 ppt) and falling sharply at dawn, usually reaching a minimum shortly after midday. The nitryl chloride photolysis rate is approximately in opposition with ClNO<sub>2</sub> concentration, reaching a peak at 11:00 ( $\sim 4.1 \times 10^{-5} \text{ s}^{-1}$ ), a few hours before the ClNO<sub>2</sub> minimum. This general diel profile agrees with other studies (*e.g.* Bannan et al., 2015) and was fairly consistent for ClNO<sub>2</sub> observations in all locations and seasons over the course of this project, with ClNO<sub>2</sub> being observed on most nights.

Both the magnitude and time of arrival of the maximum ClNO<sub>2</sub> concentrations varied from night to night. Large differences in peak magnitude and arrival time were also observed between seasons and locations (these variations are discussed further in sections 4.3 and 5.2 respectively).

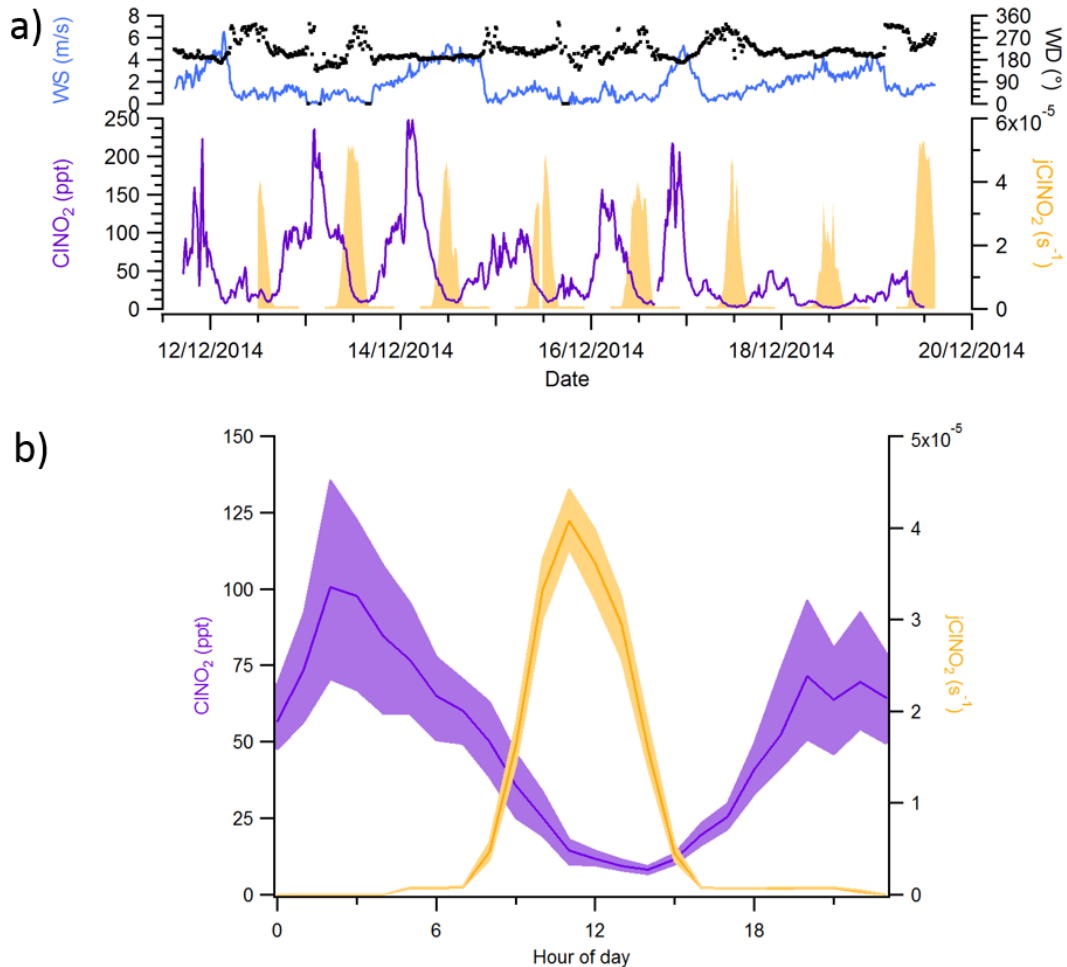


Figure 4.10 Diel pattern of ClNO<sub>2</sub> during RAFT 2 campaign (15 min averaged data).

- a) Time series showing wind speed and direction (top) in addition to ClNO<sub>2</sub> concentration and photolysis rate (bottom).
- b) Average diel ClNO<sub>2</sub> concentration and photolysis rate (mean and 95% confidence intervals).

As one might expect, the NO, NO<sub>2</sub> and O<sub>3</sub> also measured during all campaigns at UoL similarly demonstrated their own diel variations, shown in Figure 4.11. Noticeable peaks are present in NO and NO<sub>2</sub> during the morning (07:00-09:00) and evening (17:00-21:00) rush hour. The morning rush hour seems to be characterised by a sharp peak slightly richer in NO than NO<sub>2</sub> (approx. 38 and 30 ppb), whereas the evening peak is much broader with almost equal NO and NO<sub>2</sub> (~33 ppb). Ozone is quite depleted around rush hours, reaching a minimum of ~10 ppb at approx. 07:00 and 17:00 as it becomes titrated by influxes of freshly-emitted NO. After morning rush hour photolytic ozone production has had a

chance to fully initialise, rising again to an afternoon peak (~16 ppb) at approx. 13:00 before the next rush hour depletion. The difference in NO/NO<sub>2</sub> ratio between the two rush hours is likely due to the fresh emissions are spread out over a greater time period during evening rush hour, putting less instantaneous strain on O<sub>3</sub> concentration.

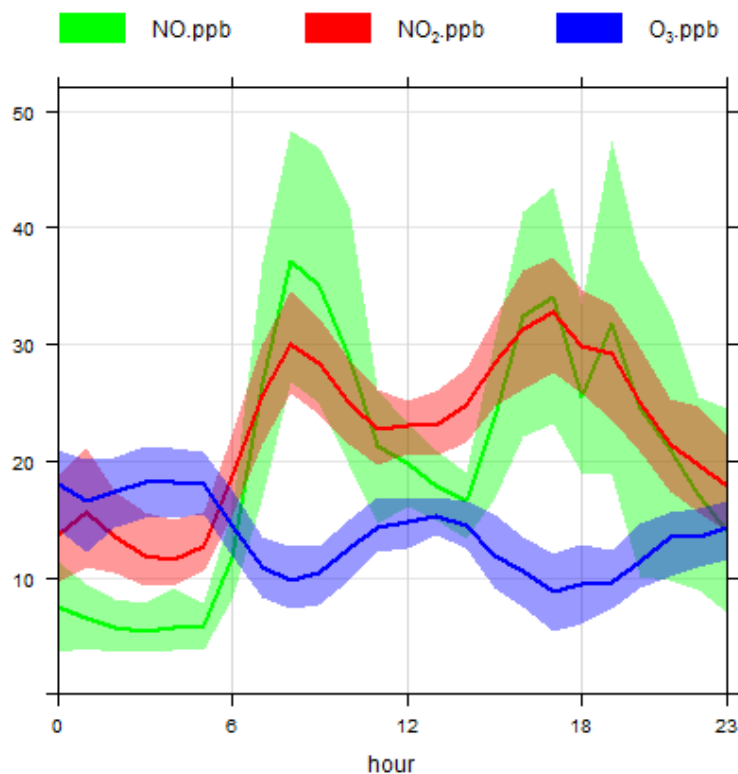


Figure 4.11 Average diel NO, NO<sub>2</sub> and O<sub>3</sub> concentrations for RAFT 2 campaign (15 min averaged data; mean and 95% confidence intervals).

### 4.3 Seasonal variability

The five periods during which the CIMS was deployed at the University of Leicester covered all 4 seasons, with data available for spring (RAFT 1, March 2014), summer (AURN 1, August 2014), autumn (RAFT 3, September 2015) and winter (RAFT 2, December 2014; AURN 2, February 2016).

#### 4.3.1 Differences between winter campaigns

Figure 4.12 shows the separate average diel profiles for the two UoL winter campaigns. The average campaign ClNO<sub>2</sub> maximum for AURN 2 (~175 ppt at 03:00) is much higher than for RAFT 2 (90 ppt at 02:00). Average ClNO<sub>2</sub> daytime minima are notably above zero, ~10 ppt at around 14:00 for both campaigns (this is discussed further in section 4.4). Temperature was quite similar for both campaigns and was therefore unlikely to be responsible for the difference in ClNO<sub>2</sub> maxima.

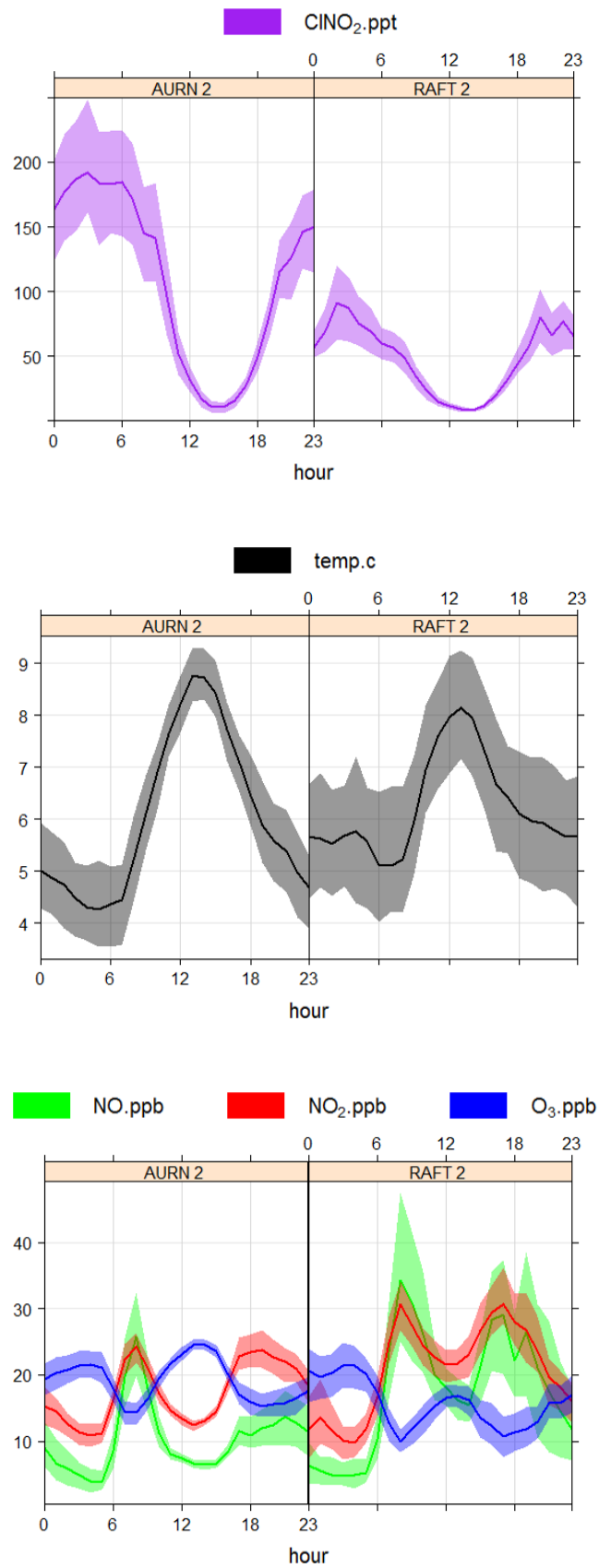


Figure 4.12 Winter diel profiles of  $\text{ClNO}_2$  (top), temperature (middle), NO, NO<sub>2</sub> and O<sub>3</sub> (bottom) for RAFT 2 and AURN 2 campaigns (15 min averaged data; mean and 95% confidence intervals).

Ozone measurements are largely the same between both campaigns but have a slightly wider range for RAFT 2, however this campaign's wider 95% confidence intervals indicates that the smaller number of data points may contribute to this effect.  $\text{NO}_2$  is distinctively higher during the RAFT 2 campaign but there was an even greater increase in  $\text{NO}$ , such that its concentration matches that of  $\text{NO}_2$  much of the time. This is generally indicative of a less mature air mass (*i.e.* air that has not had time to undergo significant chemical processing) and may explain the lower  $\text{ClNO}_2$  concentration exhibited in this campaign by  $\text{NO}$  inhibiting  $\text{ClNO}_2$  formation *via* the reaction of  $\text{NO}_3$  with  $\text{NO}$ , reducing the amount of available  $\text{N}_2\text{O}_5$ .

Wind conditions bore some similarity between both campaigns. Prevailing winter winds were from the south and southwest (see Figure 4.9a). Pollution roses (Figure 4.9b) show that air bearing significant  $\text{ClNO}_2$  concentrations (up to 300 ppt) was received from these directions in both campaigns. The main difference in wind conditions is that the largest concentrations of  $\text{ClNO}_2$  (300-900 ppt) observed at UoL originated almost entirely from the southeast, during the AURN 2 campaign. Tellingly, no significant quantity of wind was intercepted from this direction during the RAFT 2 campaign, suggesting a different source is responsible for these >300 ppt concentrations. These large  $\text{ClNO}_2$  concentrations from the southeast possibly originated from London (~145 km).

#### 4.3.2 Seasonal variations

Figure 4.13 shows average diel profiles of  $\text{ClNO}_2$ ,  $\text{NO}$ ,  $\text{NO}_2$  and  $\text{O}_3$  for all campaigns, separated by season. Winter panels therefore represent aggregated RAFT 2 and AURN 2 data.

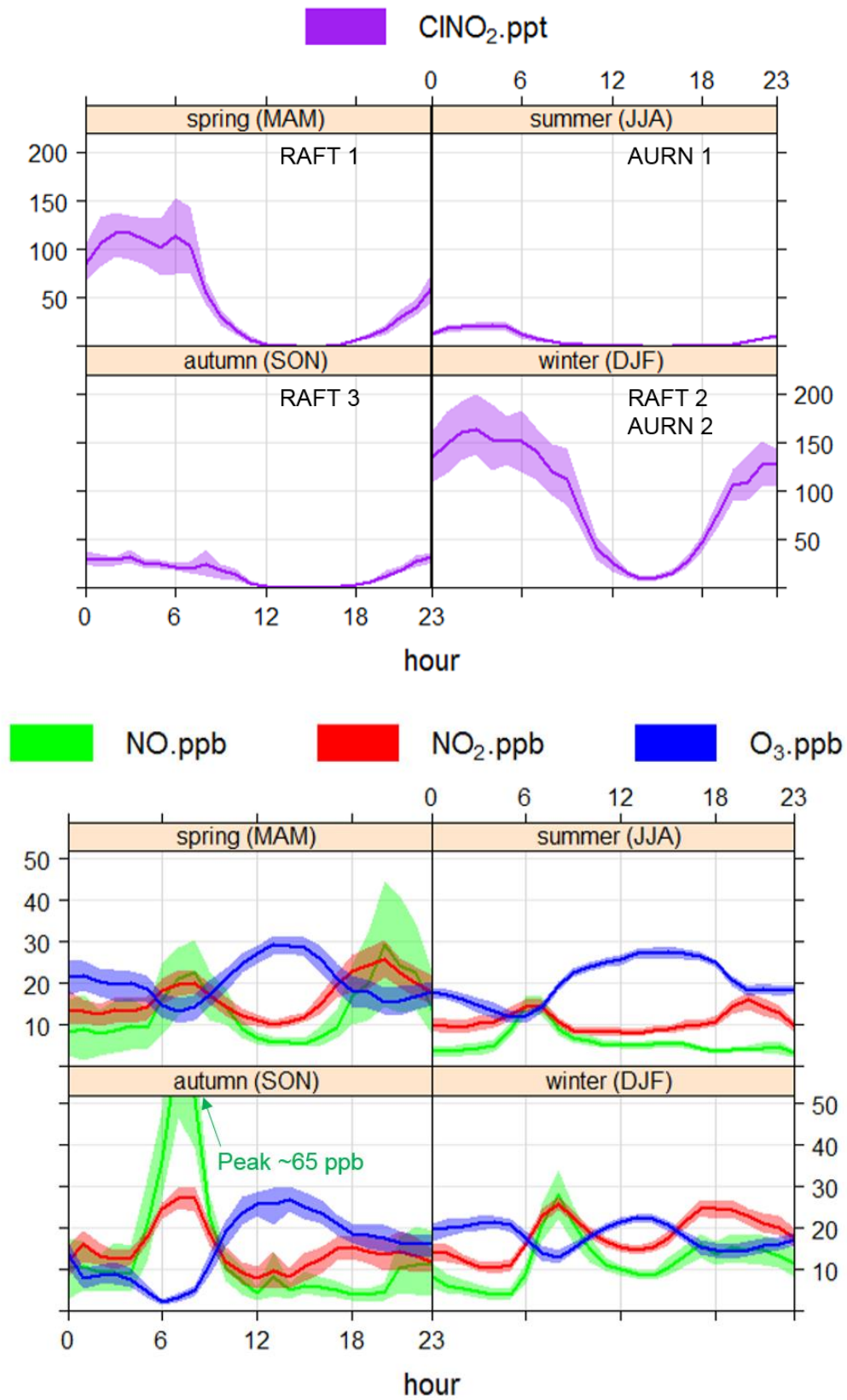


Figure 4.13 Average seasonal profiles for  $\text{ClNO}_2$  (top),  $\text{NO}$ ,  $\text{NO}_2$  and  $\text{O}_3$  (bottom) for all UoL campaigns (15 min averaged data; mean and 95% confidence intervals).

Ozone and NO<sub>2</sub> profiles have some similarities throughout all of the seasons. Ozone minima are usually 12-14 ppb, occurring in the early morning (~07:00). This matches up to the morning rush hour as indicated by the coinciding NO maxima (usually 20-30 ppb), as this is emitted in large quantities and titrates ozone to form NO<sub>2</sub>. As a result one of two NO<sub>2</sub> maxima (20-30 ppb) also occur at this time.

The morning rush hour effect is particularly pronounced in the autumn profile of Figure 4.13, seeming to result from an unusually high NO maximum (~65 ppb), with cascading effects upon the corresponding O<sub>3</sub> minimum (~3 ppb) and NO<sub>2</sub> maximum (~28 ppb). This may be related to the short measurement period (7 nights) of the RAFT 3 campaign solely represented by this section of figure, however, as only one or two unusual days can easily distort the graph. This scenario is possible, as the shape of this profile is less smooth than for other seasons but unlikely because the 95% confidence intervals (shaded area around the mean) are not much wider than for other seasons, indicating that all of the days within that campaign were somewhat consistent with each other.

Ozone maxima occur during the afternoon (~14:00) at 25-30 ppb. The shape of the O<sub>3</sub> diel profile is noticeably flatter in winter with a slightly lower maximum (~23 ppb). The weaker winter sunlight results in a slowdown of O<sub>3</sub> production via photolytically-initiated VOC and NO<sub>x</sub> chemistry (see section 1.2.1).

Nitrogen dioxide diel profiles (also shown in Figure 4.13) are quite consistent in concentration across the spring, autumn and winter campaigns (approx. 10-25 ppb with peaks around morning and evening rush hour). The summer measurements (AURN 1 campaign) show much lower levels of NO<sub>2</sub> (approx. 9-16 ppb). This effect is unlikely to be a result of higher photolysis altering the partitioning between NO and NO<sub>2</sub>, however, as the NO concentrations are similarly low during this campaign. A more likely explanation is a difference in sources, as indicated by the difference in prevailing wind direction (primarily west and southwest, where the AURN 2, RAFT 1 and RAFT 2 campaigns were mainly south and southwest) shown earlier in Figure 4.9). An alternative explanation is linked to students representing a significant fraction of the Leicester population (having 2 universities in a medium-sized city), further to

which the UoL measurement sites are positioned next to University Road. The population and traffic are therefore reduced both locally and city-wide during undergraduate students' holidays (including August, as in the case of AURN 1 campaign). This hypothesis still fits with the elevated autumn  $\text{NO}_2$  levels observed in the RAFT 3 campaign which took place in late September (as term begins again) but is difficult to confirm without traffic data.

In all seasons the evening rush hour  $\text{NO}_2$  maxima tend to be broader than the morning equivalent, but other than this the shapes of the  $\text{NO}_2$  diel profiles show more variability than  $\text{NO}$  and  $\text{O}_3$ . The spring campaign (RAFT 1) shows a larger peak for the evening rush hour than for the morning, and vice versa for autumn (RAFT 3). These are, however, short campaigns (8 and 7 days respectively). The summer and winter seasons are represented by much more data - AURN 1 (22 nights) for summer and AURN 2 and RAFT 2 (25 and 8 nights) for winter - which is reflected by these profiles having much narrower 95% confidence intervals (notably, the morning and evening rush hour  $\text{NO}_2$  maxima for these two plots also match in height).

In contrast,  $\text{ClNO}_2$  diel profiles show dramatic differences between the seasons. Winter has the highest average  $\text{ClNO}_2$  maximum of approx. 150 ppt around 03:30. Increased precipitation associated with colder months will increase the availability of aerosol surfaces upon which  $\text{ClNO}_2$  can form. Lower temperatures may also contribute, as these stabilise the precursor  $\text{N}_2\text{O}_5$  in its equilibrium with  $\text{NO}_2 + \text{NO}_3$ , thus enhancing  $\text{ClNO}_2$  formation where ample aerosol chloride is available. This effect will be more pronounced if  $\text{ClNO}_2$  formation is limited by  $\text{NO}_x$  rather than  $\text{O}_3$ , however the latter may more often be the case in Leicester (this is explored later, in section 5.7). An additional effect, explored later in section 4.4, was observed during the course of this thesis whereby  $\text{ClNO}_2$  is not always completely photolysed during the day and thus might contribute to the following night's peak. The average winter minimum shown in Figure 4.13 is in fact around 10 ppt - approx. 6.7% of the average winter maximum, and on a level with the average summertime maximum - suggesting a potentially substantial contribution of surviving  $\text{ClNO}_2$  to the following night's maximum concentration.

During spring, summer and autumn ClNO<sub>2</sub> reaches zero at 12:00-13:00 and remains there until 17:00-18:00. While not as high as winter, the average ClNO<sub>2</sub> maximum in spring is also quite high, reaching ~130 ppt at approx. 02:00. Significantly, autumn and summer average maxima are an order of magnitude lower (approx. 15 and 10 ppt respectively). Pollution roses for each campaign (Figure 4.9b) show the largest ClNO<sub>2</sub> observations during AURN 1 and RAFT 3 campaigns (summer and autumn, respectively) coming from westerly directions, whereas the highest ClNO<sub>2</sub> concentrations during winter and spring campaigns (with much greater ClNO<sub>2</sub> maxima) were borne by more southerly winds. The overall wind directions indicated by the wind roses (Figure 4.9a) also show a general bias towards the south and southwest in winter and spring, which suggests a difference in ClNO<sub>2</sub> source.

#### 4.4 Daytime persistence of ClNO<sub>2</sub>

Past studies of nitryl chloride have observed ClNO<sub>2</sub> maxima occurring after dawn (e.g. Tham et al., 2016), however during the course of work described in this thesis nitryl chloride was observed several times surviving throughout the day. Figure 4.14 shows a time series of 11-15<sup>th</sup> February 2016 (AURN 2), centred on the night of 12-13<sup>th</sup> February 2016 which had the campaign's highest nightly average ClNO<sub>2</sub> concentration (also in Figure 4.18). A very clear diel profile is visible in this figure with the temperature and ClNO<sub>2</sub> photolysis rates peaking during the days and ClNO<sub>2</sub> concentrations during the nights. The AURN 2 campaign took place during winter, with the increased aerosol and low temperature assisting ClNO<sub>2</sub> formation during the nights (see section 4.3).

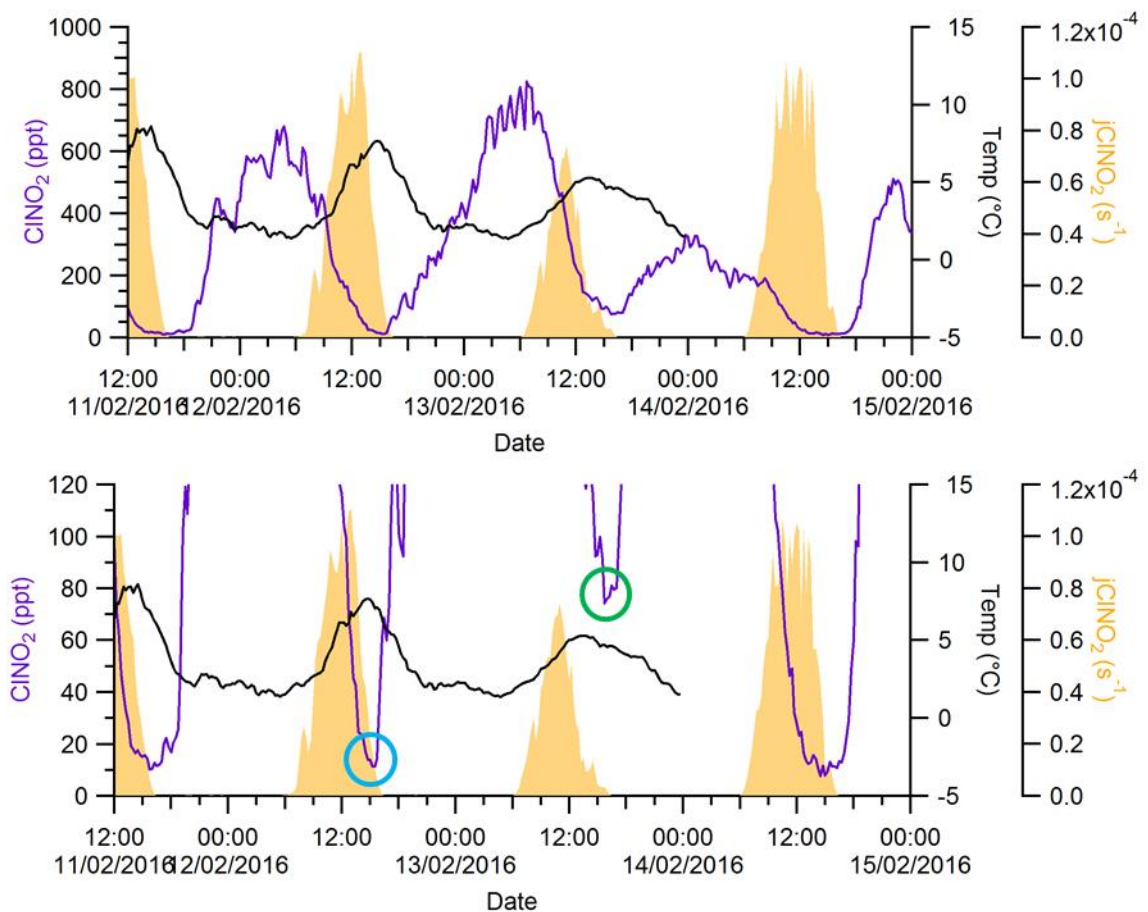


Figure 4.14 Time series of AURN 2 campaign showing ClNO<sub>2</sub> concentration and photolysis rate in addition to temperature (15 min averaged data; full scale (top) and low concentrations magnified (bottom)).

The photolysis rate during the day of February 13<sup>th</sup> is abnormally low even for winter, peaking at approx.  $7.5 \times 10^{-5} \text{ s}^{-1}$  (equivalent to a ClNO<sub>2</sub> lifetime of  $\sim 3.70$  hours). This, combined with the prior night's high ClNO<sub>2</sub> concentration (12/02/16 23:00 to 13/02/16 04:59 average 558 ppt), resulted in ClNO<sub>2</sub> surviving throughout the day. The ClNO<sub>2</sub> concentration on 13/02/16 reaches a minimum of 74 ppt (green circle) at 15:45, shortly before sunset ( $\sim 16:15$ ). This ClNO<sub>2</sub> minimum significantly exceeds the instrumental limit of detection (4.20 ppt). It is also well above the nightly average ClNO<sub>2</sub> observed during the summer ( $\sim 14$  ppt) and autumn ( $\sim 24$  ppt) campaigns and, as mentioned in section 4.3.2, may contribute significantly to ClNO<sub>2</sub> concentrations on the following night.

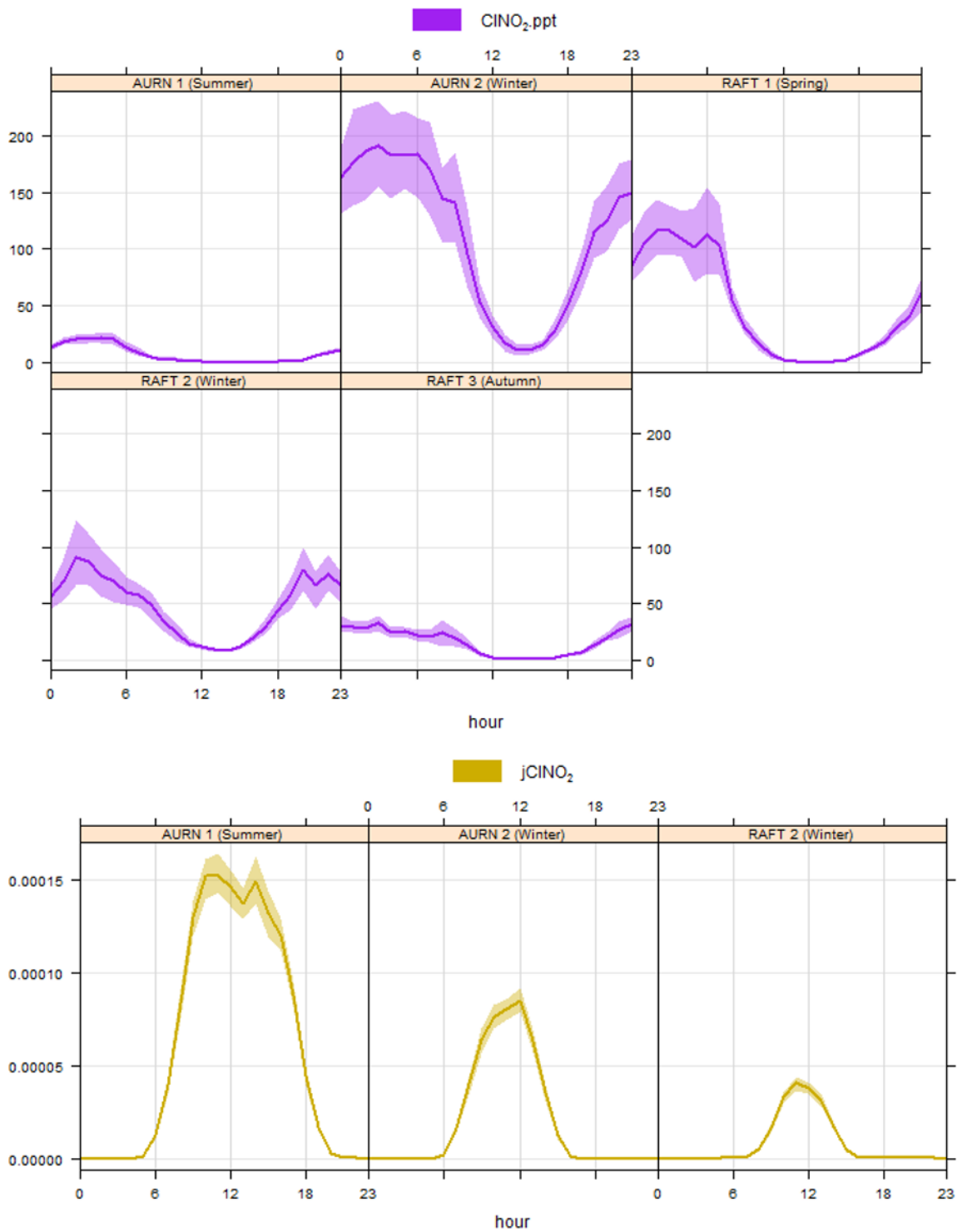


Figure 4.15 Diel profiles of  $\text{ClNO}_2$  concentration (top) and, when available, photolysis rate ( $\text{s}^{-1}$ ; bottom) for each UoL campaign (15 min averaged data; mean and 95% confidence intervals).

While the daytime concentration of  $\text{ClNO}_2$  is unusually high in this specific case, the phenomenon of  $\text{ClNO}_2$  surviving throughout the day was not confined to this single day. Also shown in Figure 4.14 is 12/02/16, following a night of similarly

high ClNO<sub>2</sub> (11/02/16 23:00 to 12/02/16 04:59 average 541 ppt). On this day the photolysis rate peaked at  $\sim 1.1 \times 10^{-4} \text{ s}^{-1}$  (equivalent to a ClNO<sub>2</sub> lifetime of  $\sim 2.52$  hours) which was much more typical for the campaign, however the daytime minimum ClNO<sub>2</sub> (blue circle; 11 ppt at 15:30, again just before sunset) is still well above the CIMS LoD. The other two days shown in the same figure exhibit ClNO<sub>2</sub> surviving throughout the day (despite lower ClNO<sub>2</sub> maxima on their respective previous nights), as did several nights during the RAFT 2 campaign indicating this is not an unusual occurrence.

ClNO<sub>2</sub> drops to zero for most of the 12:00-17:00 period outside of winter, as shown by the ClNO<sub>2</sub> minima in average diel profiles for spring, summer and autumn campaigns (Figure 4.15 top). The winter campaigns (RAFT 2 and AURN 2) instead reach non-zero minima in the afternoon due to the much reduced photolysis rate (Figure 4.15 bottom).

#### 4.5 Radical production

To assess the impact of ClNO<sub>2</sub> photolysis upon oxidation chemistry in the early morning, the primary production of Cl and OH radicals were calculated and compared for both AURN campaigns.

The production of atomic chlorine from ClNO<sub>2</sub> was calculated *via* Equation 4.1 using the observed nitryl chloride concentrations and photolysis rates.

$$P_{\text{Cl}} = [\text{ClNO}_2] \cdot j(\text{ClNO}_2)$$

Equation 4.1 Equation for calculating atomic chlorine production,  $P_{\text{Cl}}$ , using observed ClNO<sub>2</sub> concentration and photolysis rate.

The calculation of OH radical production is shown in Equation 4.2, which includes a similar calculation but also a branching ratio to account for non-reactive quenching of O(<sup>1</sup>D), which does not produce OH (see section 1.2.1).

$$P_{\text{OH}} = 2f \cdot [\text{O}_3] \cdot j(\text{O}({}^1\text{D})) \quad \text{a}$$

$$f = \frac{k_1 \cdot [\text{H}_2\text{O}]}{k_1 \cdot [\text{H}_2\text{O}] + k_2 \cdot [\text{N}_2] + k_3 \cdot [\text{O}_2]} \quad \text{b}$$

Equation 4.2 Equations for calculating photolytic production of OH radicals (Stone et al., 2014).

- a) Equation for calculating  $P_{\text{OH}}$  from the branching ratio  $f$  for the fate of  $\text{O}({}^1\text{D})$  and observed ozone concentration and photolysis rate.
- b) Equation for calculating the branching ratio  $f$ . Rate constants  $k_1$ ,  $k_2$  and  $k_3$  (Atkinson et al., 2004) correspond to the rates of reactive (*via*  $\text{H}_2\text{O}$ ) and quenching (*via*  $\text{N}_2$  and  $\text{O}_2$ ) removal of  $\text{O}({}^1\text{D})$ , respectively.

Figure 4.16a shows a complete time series of the AURN 2 campaign, with  $\text{ClNO}_2$  concentration and the instantaneous production rates of Cl and OH radicals.

The section shown in Figure 4.16b was selected as an “average” winter day, as  $\text{ClNO}_2$  on the night of 23-24 February matches well both the magnitude and shape of the campaign’s average diel profile (shown earlier in Figure 4.15). This period demonstrates that Cl production initiates immediately after first light at ~06:00, whereas OH production only begins to pick up well after dawn at ~10:00. Furthermore, overall Cl production throughout the day is much higher than OH from ozone (maximum  $1.4 \times 10^{-9}$  and  $2.4 \times 10^{-10}$  molecules  $\text{cm}^{-3} \text{s}^{-1}$  respectively), potentially adding significantly to the overall tropospheric oxidising capacity in winter. Note, however, that the contribution of Cl appears amplified in these plots as only initial production of OH *via*  $\text{O}_3$  is considered in this basic model, whereas the recycling processes that support the majority of oxidation due to OH is neglected, as is production *via* HONO (see section 1.2.1). Any contribution of  $\text{Cl}_2$  photolysis to Cl was also neglected (see section 4.9).

In Figure 4.16c a slightly longer period from the same campaign is selected. During these few nights unusually high  $\text{ClNO}_2$  concentrations were observed, with accordingly elevated Cl production during each day. Note that this section includes February 13<sup>th</sup>, during which an exceptional quantity of  $\text{ClNO}_2$  survived throughout the day (as discussed in section 4.4). On this day the photolysis rate was unusually low, and  $\text{ClNO}_2$  photolysis provides a steady release of atomic chlorine throughout the day, peak production of which exceeds OH by an order of magnitude ( $1.4 \times 10^{-9}$  vs.  $1.3 \times 10^{-10}$  molecules  $\text{cm}^{-3} \text{s}^{-1}$  maxima respectively).

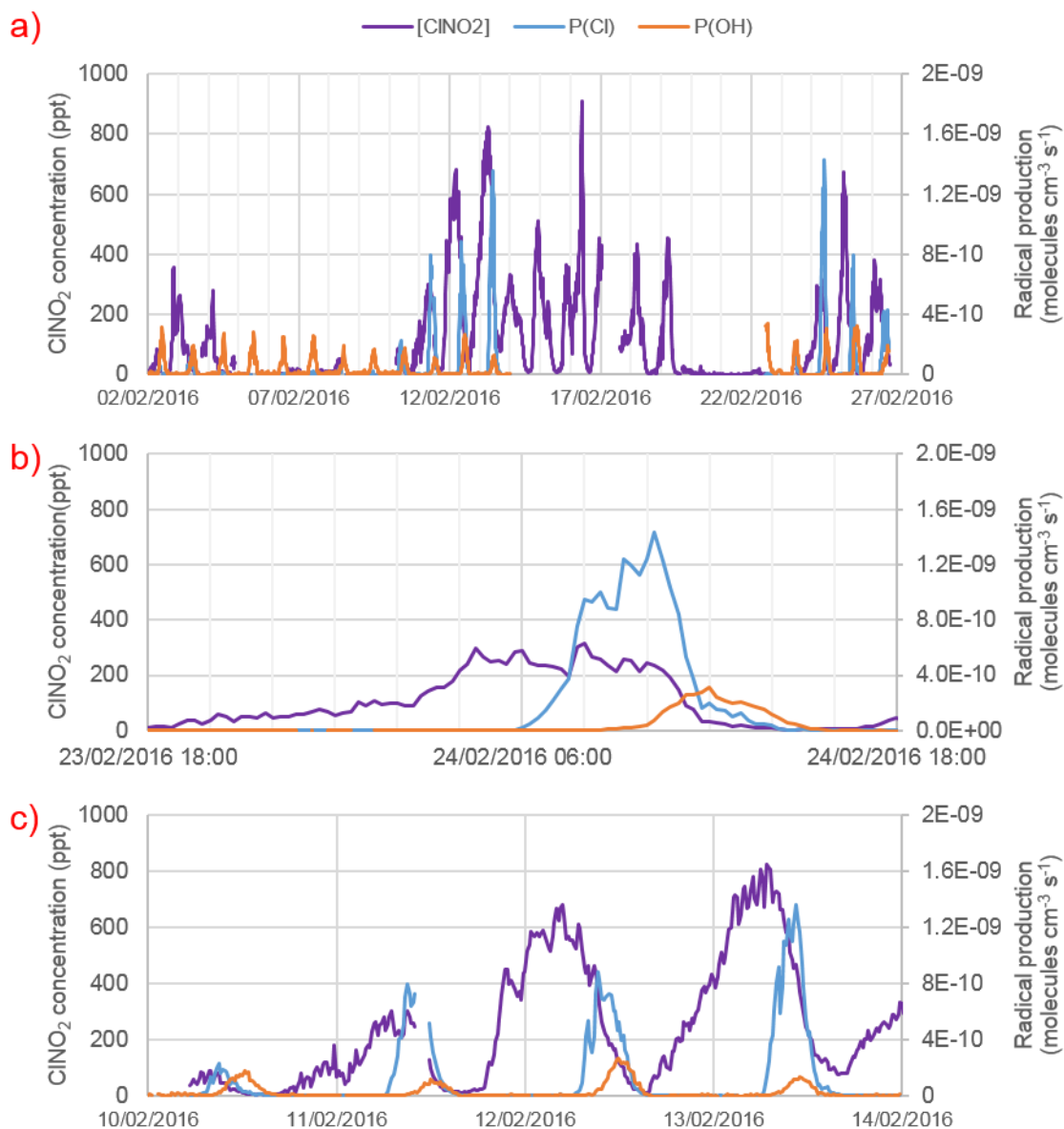


Figure 4.16 Time series showing comparative production rates of Cl and OH during the AURN 2 campaign in February 2016 (15 min averaged data).

- Full campaign time series (19-22 Feb gap in radical production due to spectral radiometer maintenance).
- Partial time series centred upon 23/02/16, showing night-time accumulation and subsequent photolysis of ClNO<sub>2</sub> resulting in extensive Cl production.
- Selected partial time series of 10-14<sup>th</sup> February. This section includes 13/02/16, during which an exceptionally high amount of ClNO<sub>2</sub> survived throughout the day (see Figure 4.14).

Figure 4.17a shows a similar complete time series of the AURN 1 campaign. This figure allows comparison between winter and autumn, and demonstrates significantly increased OH production in the summer (note that the vertical axes are scaled differently to Figure 4.16).

The section shown in Figure 4.17b displays several days during the campaign period with varying amounts of ClNO<sub>2</sub> production. Regardless of the ClNO<sub>2</sub> concentration on the previous night, Cl production remains minimal, with a campaign maximum of  $5.4 \times 10^{-11}$  molecules cm<sup>-3</sup> s<sup>-1</sup> (which occurs during this period), two orders of magnitude less than the AURN 2 campaign maximum. Meanwhile, OH production maxima vary from  $1.0 \times 10^{-9}$  to  $5.3 \times 10^{-9}$  molecules cm<sup>-3</sup> s<sup>-1</sup>, compared to the AURN 2 campaign maximum of  $3.4 \times 10^{-10}$  molecules cm<sup>-3</sup> s<sup>-1</sup>.

As Cl production is very low in this campaign, Figure 4.17c shows the production rates of Cl and OH plotted on separate vertical axes. This shows that the profile of Cl production is similar following nights where significant ClNO<sub>2</sub> was observed but on some nights in this campaign Cl production is minimal, often negligible.

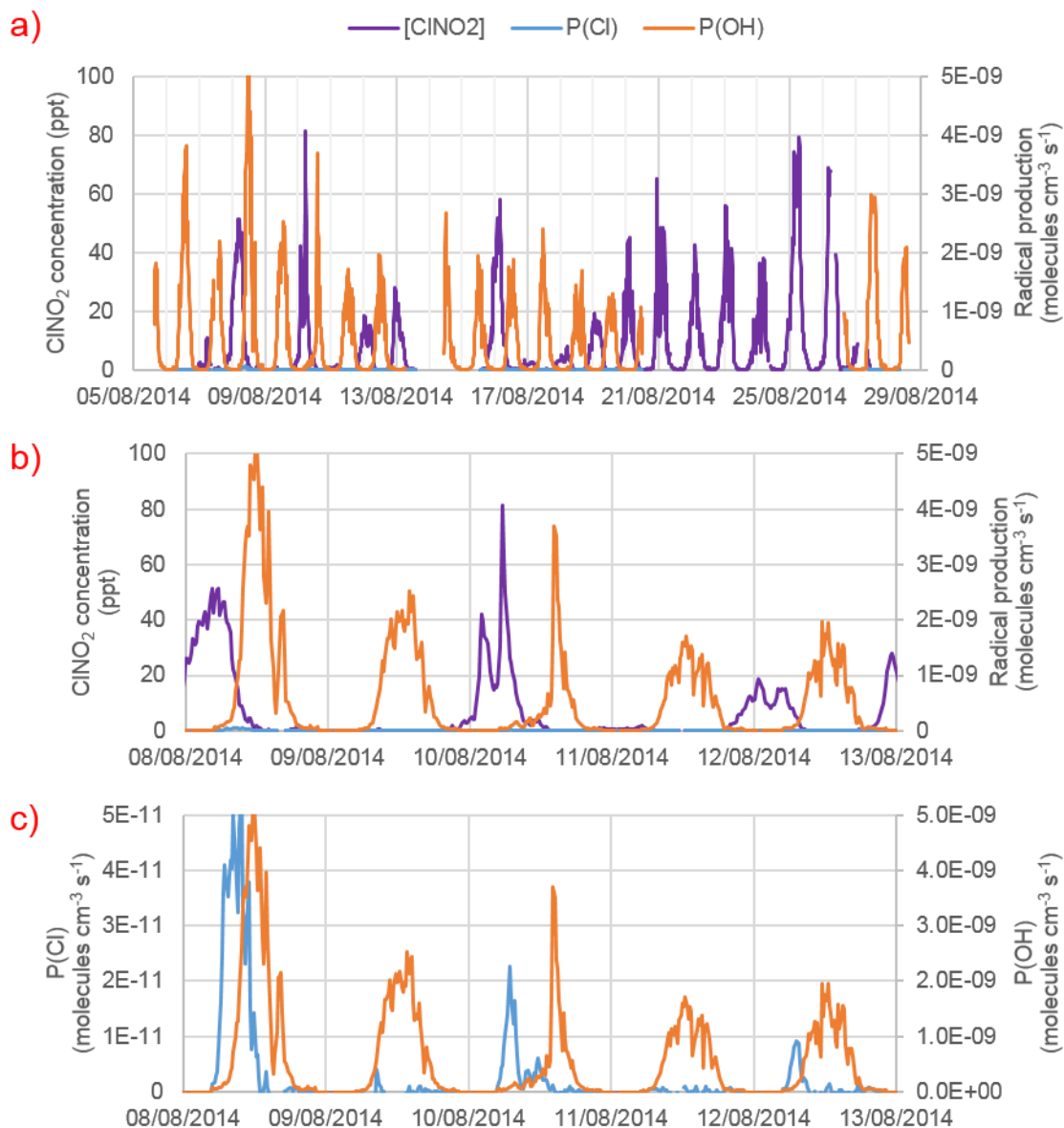


Figure 4.17 Time series showing comparative production rates of Cl and OH during the AURN 1 campaign in August 2014 (15 min averaged data).

- a) Full campaign time series.
- b) Selected partial time series showing 08-13 August.
- c) Partial time series also showing 08-13 August, with P(Cl) and P(OH) on separate scales.

#### 4.6 Case studies

A number of nights were selected to explore the conditions leading to both high and low ClNO<sub>2</sub> concentrations on given night(s) at UoL. The first case study was selected because notably high ClNO<sub>2</sub> concentrations were consistently observed, and the nights shown therein have the highest nightly average

concentrations observed at UoL. The second case demonstrates very low ClNO<sub>2</sub> concentrations and was selected to contrast with the first. As seasonal effects were shown to be significant (see section 4.3.2), two nights were selected from the same campaign as the first case study, *i.e.* AURN 2 in February 2016. The third study contains the highest ClNO<sub>2</sub> concentration observed at UoL however the concentration profile over time was different compared to the first case, with the peak concentration occurring after daybreak. The fourth case study also corresponds to a night which showed a concentration profile that differed from “normal”, this time with ClNO<sub>2</sub> falling before dawn.

Air mass footprints (based upon the NAME model; see section 2.5) were examined in conjunction with meteorological data and chemical tracers to assess the conditions that produced night to night variations in ClNO<sub>2</sub> concentrations observed in Leicester. In brief, the NAME footprints resemble maps showing the 5-day history of air intercepted at the measurement site (marked as “X”) at a given time. On these plots “hot” colours (*e.g.* red/yellow) represent the air mass having spent time in that location, whereas “cold” colours (*e.g.* green/blue) are more indicative of briefly passing over that location.

#### 4.6.1 High ClNO<sub>2</sub>

The time series in Figure 4.18 shows ClNO<sub>2</sub> concentrations that were not only high but consistently so, displaying the highest nightly (23:00-04:59) averages observed at UoL; 558 ppt on the night of 12-13<sup>th</sup> February and 541 ppt on the night of 11-12<sup>th</sup> February.

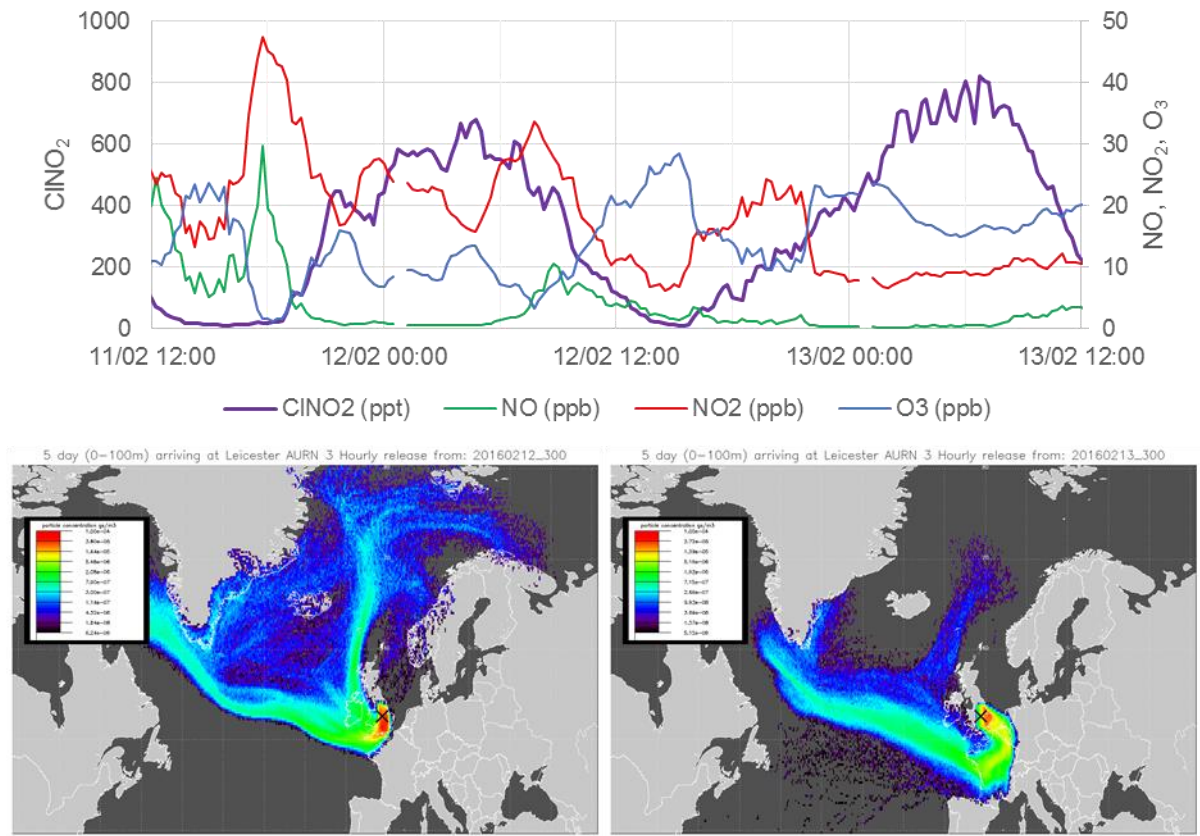


Figure 4.18 Time series of AURN 2 campaign showing concentrations of ClNO<sub>2</sub>, NO, NO<sub>2</sub> and O<sub>3</sub> (top; 15 min averaged data) and NAME particle dispersion footprints at 03:00 (bottom; 5-day back), demonstrating a high-ClNO<sub>2</sub> case over 2 consecutive nights (11-12 (left) and 12-13 (right) February 2016).

Significant levels of NO<sub>2</sub> also were also available, rarely dropping below 10 ppb during this period, indicating a supply of NO<sub>2</sub> and O<sub>3</sub> necessary for N<sub>2</sub>O<sub>5</sub> production. Additionally, the concentration of NO<sub>2</sub> is quite high relative to the primary pollutant NO, suggestive of a mature air mass. The low NO concentration allows formation of N<sub>2</sub>O<sub>5</sub> without too much NO<sub>3</sub> becoming titrated back to NO<sub>2</sub>. The major feature common to the majority of high ClNO<sub>2</sub> cases is where an air mass has spent considerable time over land. For example the red and yellow area in the NAME footprint for 13/02/16 (Figure 4.18, bottom right) suggests that the air mass arriving in Leicester at 03:00 had initially come from the Atlantic into northwest France, then spent time in the highly polluted London area prior to reaching the measurement site.

#### 4.6.2 Low ClNO<sub>2</sub>

In comparison to the high-ClNO<sub>2</sub> case study above, Figure 4.19 shows exceptionally low ClNO<sub>2</sub> levels (23:00-04:59 averages of <5 ppt) on the nights of 19-20 and 20-21<sup>st</sup> Feb 2016. It is important to note these data were obtained during the same campaign as the last case study (*i.e.* AURN 2).

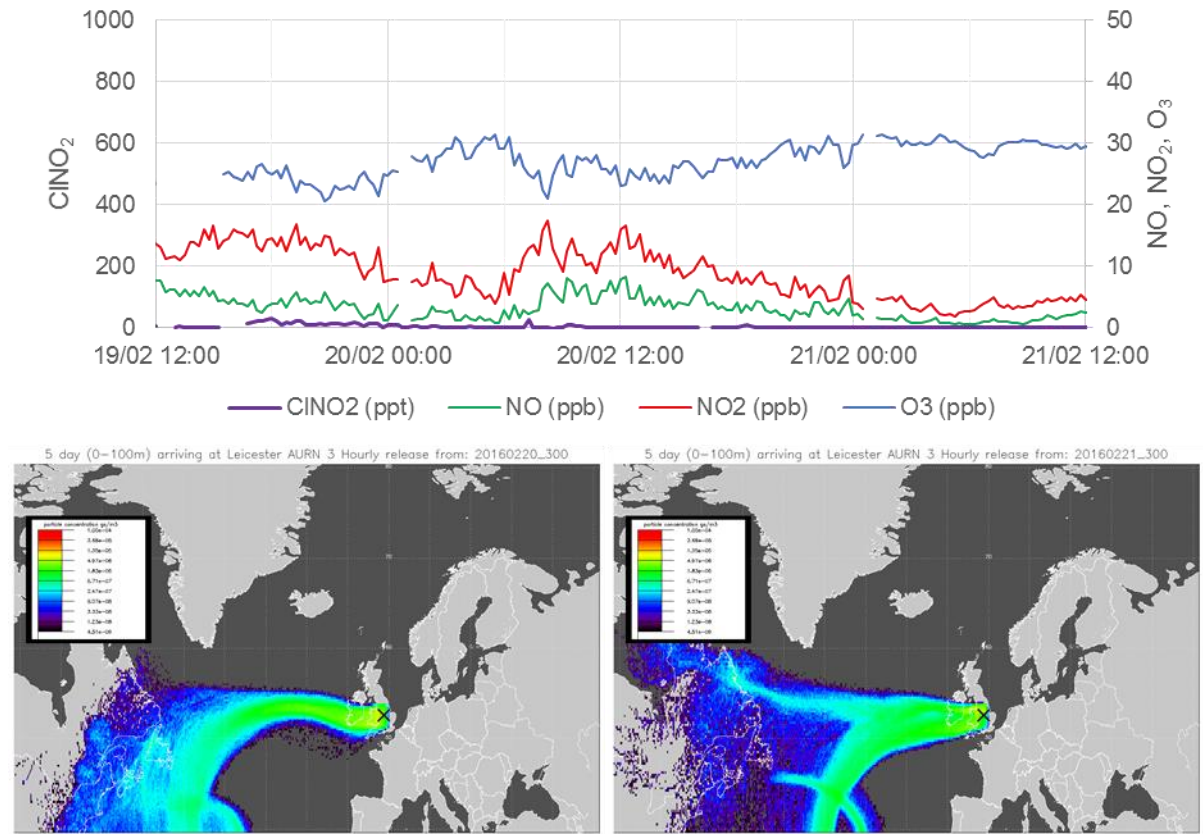


Figure 4.19 Time series of AURN 2 campaign showing concentrations of ClNO<sub>2</sub>, NO, NO<sub>2</sub> and O<sub>3</sub> (top; 15 min averaged data) and NAME particle dispersion footprints at 03:00 (bottom; 5-day back), demonstrating a low-ClNO<sub>2</sub> case over 2 consecutive nights (19-20 (left) and 20-21 (right) February 2016).

The time series in this figure shows much higher concentrations of O<sub>3</sub> (20-30 ppb) and lower levels of NO and NO<sub>2</sub> (rarely exceeding approx. 9 and 15 ppb respectively) than are visible in Figure 4.18. Furthermore NO, NO<sub>2</sub> and O<sub>3</sub> all show much less variation over this period of time suggesting a much fresher, cleaner air mass. This is borne out by NAME footprints showing the air mass coming straight across the Atlantic to the measurement site without appearing to dwell much in any one location and spending relatively little time over land.

### 4.6.3 Highest ClNO<sub>2</sub> observation at UoL

The highest 15 min averaged ClNO<sub>2</sub> concentration observed across all UoL campaigns was 911 ppt detected during the AURN 2 campaign at 09:15 on 16/02/16, shown in Figure 4.20.

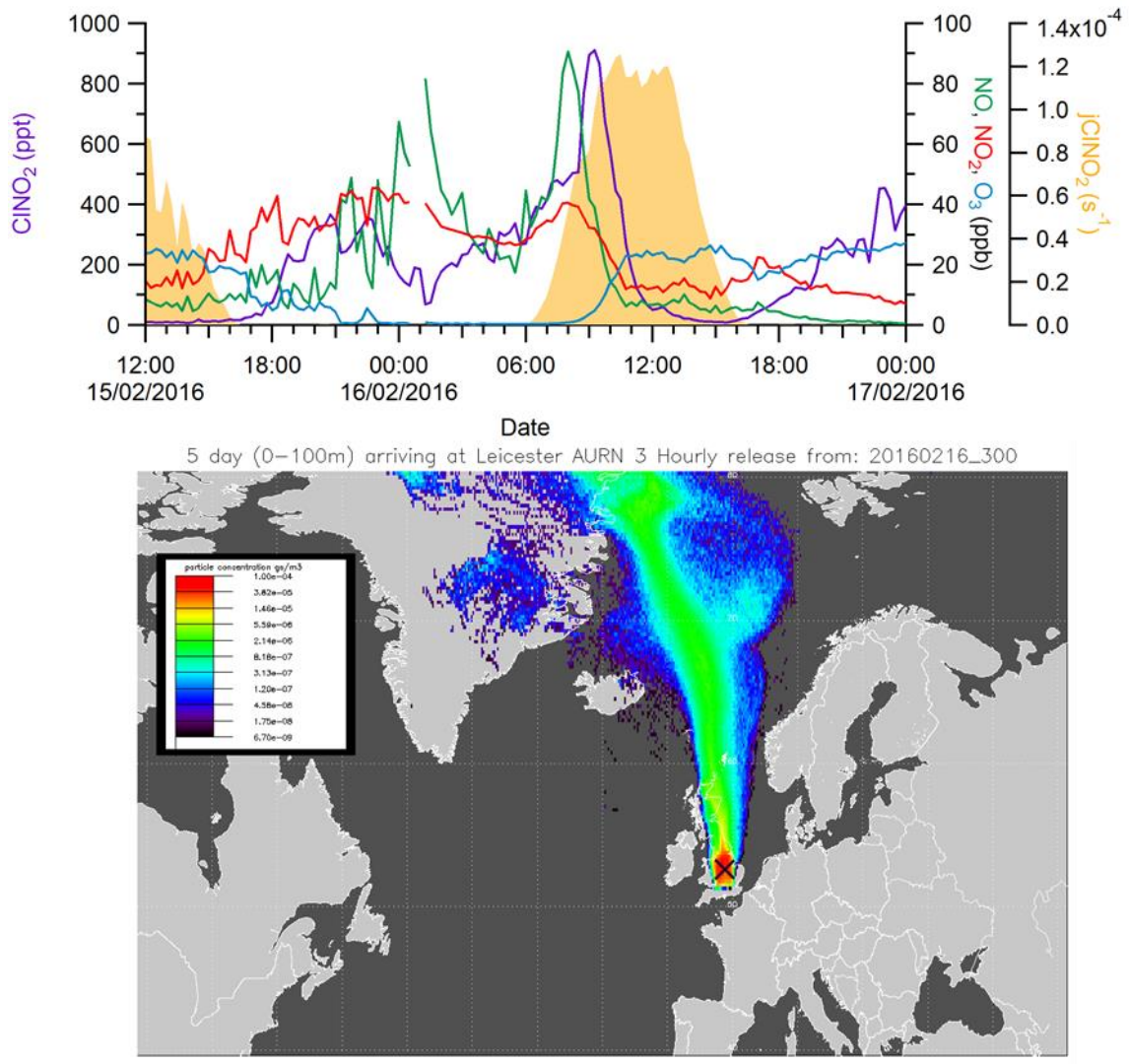


Figure 4.20 Time series of AURN 2 campaign showing ClNO<sub>2</sub> concentration and photolysis rate during highest ClNO<sub>2</sub> observation at UoL (top; 15 min averaged data) and NAME footprint (bottom; 5-day back) in the morning of 16 February 2016.

A typical nightly ClNO<sub>2</sub> concentration profile such as those shown in the first case study (see Figure 4.18) tends to show a relatively steady rise throughout the night, peaking around dawn and falling over the course of the morning.

The profile in Figure 4.20 is different, however. While concentrations remain well above the instrumental detection limit throughout the night, ClNO<sub>2</sub> levels

on this night were not as consistently high as other nights with high maximum ClNO<sub>2</sub>, with a night-time average of 201 ppt.

ClNO<sub>2</sub> concentration actually falls at one point during the night (approx. 01:00). This drop coincides with an increase in NO concentration likely due to the O<sub>3</sub> having been titrated to zero, preventing oxidation of fresh NO emissions. Otherwise the conditions were relatively similar to the high ClNO<sub>2</sub> case (11-13 Feb 2016) described in section 4.6.1, specifically that the high ClNO<sub>2</sub> concentrations here appear to correspond to a highly processed air mass judging by high NO<sub>2</sub> and low O<sub>3</sub> (>35 and ~0 ppb respectively, through most of the night) and the NAME footprint shows the air mass again having spent significant time over the UK since arriving from the Arctic ocean.

A significant rise in ClNO<sub>2</sub> concentration begins fairly abruptly at approx. 08:15, reaching the 911 ppt apex at ~09:15 before dropping similarly quickly. This major peak occurs more than 3 hours after local dawn (approx. 06:00) when N<sub>2</sub>O<sub>5</sub> (and NO<sub>3</sub>) will have been photolysed, precluding the formation of fresh ClNO<sub>2</sub> at this time and suggesting that this peak concentration represents a plume that was formed elsewhere and transported to the site. This hypothesis is supported by the short-lived nature of the peak (whose rise and fall are both steeper than one would expect of normal formation and photolysis), and the variable wind conditions observed earlier in the night.

A simple extrapolation of the 911 ppt concentration backwards to dawn using photolysis rates measured at the UoL site suggests that the peak value of ClNO<sub>2</sub> in this plume may have been up to 1509 ppt when photolytic losses began. This extrapolation assumes firstly that photolysis rates measured at UoL were representative of all points along the plume's path. The smooth rise of jClNO<sub>2</sub> in Figure 4.20 suggests minimal cloud cover at these times therefore the photolysis rates used are an upper boundary. The second assumption is that ClNO<sub>2</sub> exchange, production and non-photolytic losses since dawn were zero. N<sub>2</sub>O<sub>5</sub> would also be photolysed quickly, and no significant sinks are known for ClNO<sub>2</sub> other than photolysis (as mentioned in section 1.2.4), therefore ClNO<sub>2</sub> production and losses should be minimal.

#### 4.6.4 Change in air mass during single night

Figure 4.21 shows a time series and several consecutive NAME footprints at 3-hour intervals for the night of 16-17 December 2014 during the RAFT 2 campaign.

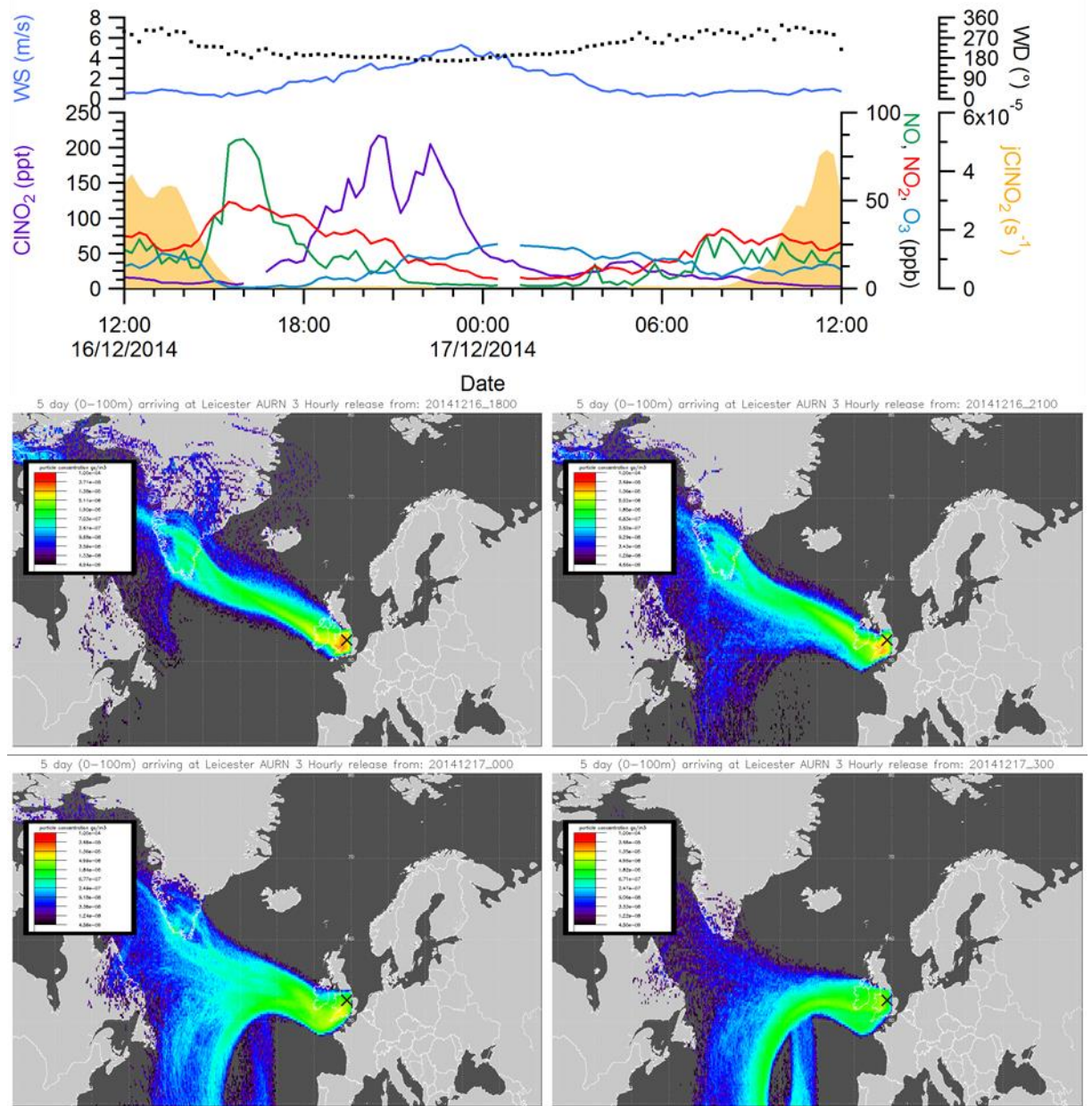


Figure 4.21 Time series of RAFT 2 campaign showing wind speed and direction and ClNO<sub>2</sub> concentration and photolysis rate, in addition to NO, NO<sub>2</sub> and O<sub>3</sub> (top; 15 min averaged data) and NAME footprints for 18:00 (top left), 21:00 (top right), 00:00 (bottom left) and 03:00 (bottom right) on the night of 16-17 Dec 2014 (bottom; 5-day back).

ClNO<sub>2</sub> began the expected rise after sunset (approx. 16:00) and reached significant levels (maximum 214 ppt, compared to campaign maximum 248 ppt) but dropped quickly to low concentrations (<50 ppt) shortly after midnight.

NAME footprints indicate that during the night of 16-17<sup>th</sup> December the air mass intercepted at UoL came mainly from the northern Atlantic Ocean and Greenland, with significant residence time over the western UK and Ireland. Consistent with most high ClNO<sub>2</sub> cases, significant NO<sub>2</sub> concentrations exceeding NO and relatively depleted O<sub>3</sub> (approx. 40, 25 and 3 ppb respectively at 18:00) were apparent when ClNO<sub>2</sub> was on the rise, indicative a mature air mass with readily available NO<sub>x</sub>. By 03:00, NO + NO<sub>2</sub> dropped to <10 ppb while O<sub>3</sub> has risen to >20 ppb conditions suggesting a different, cleaner air mass beginning to arrive at the site despite relatively constant local wind. This is supported by the NAME footprints at 00:00 and 03:00 showing the shift of the air mass origins to a predominantly middle/southern Atlantic direction with very little residence over land.

#### 4.7 Air mass origins

The origins of air masses were determined using the NAME particle dispersion model (see section 2.5). A number of zones were defined as per Figure 4.22, and the influence of each zone upon an air mass was defined as its percentage contribution to each 3-hourly probability footprint (Dr. Z. L. Fleming; University of Leicester). Each zone's influence was then used to determine air mass origins.

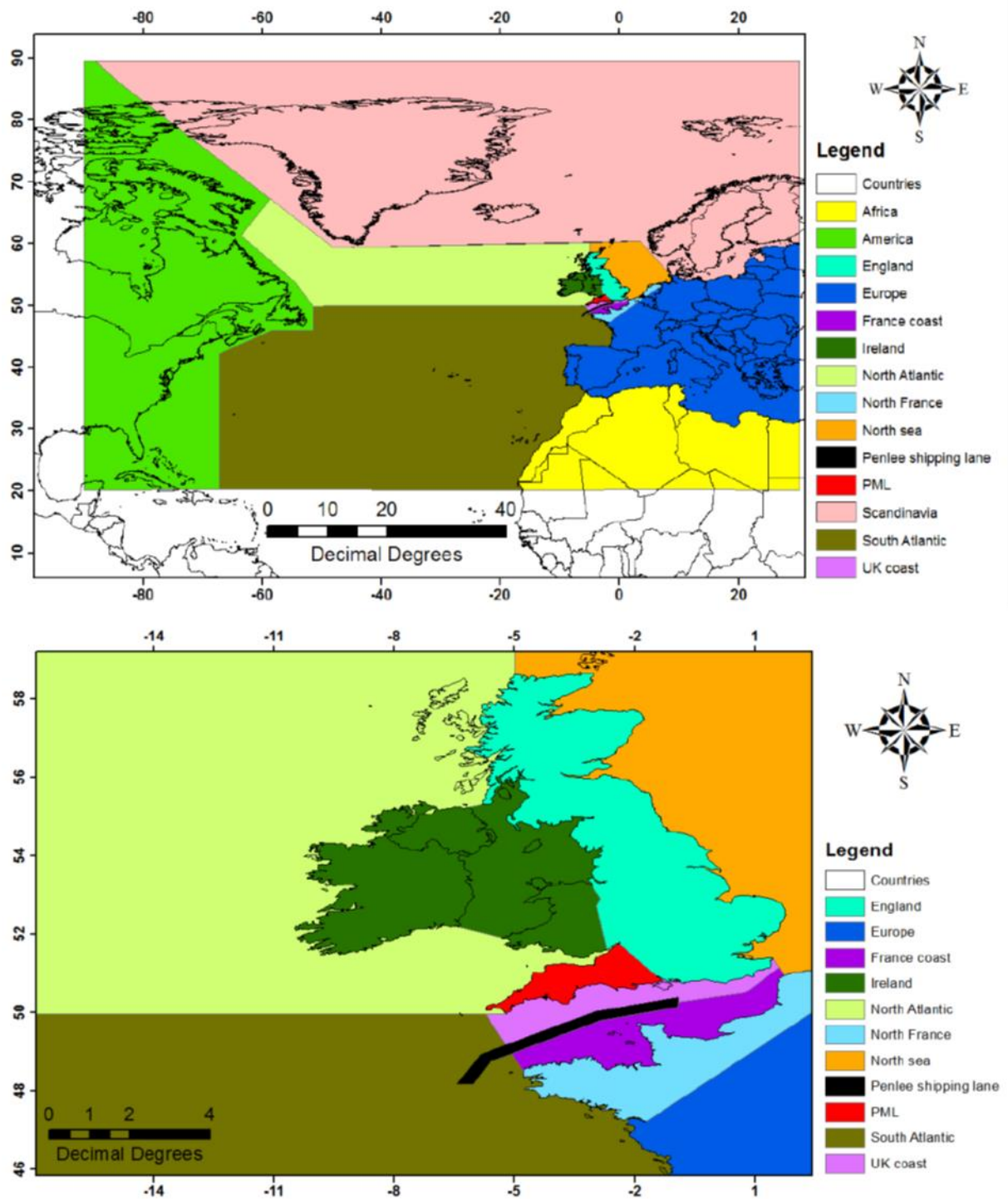


Figure 4.22 Map of air mass origin divisions for UoL campaigns (Fleming, 2017). Also used in similar analysis for Penlee Point campaign (see section 5.5)

An attempt was made to assess whether  $\text{ClNO}_2$  levels correlate with the proportion of influence from the land. The sum of several land-based zones' influences (Africa, America, England, Europe, Ireland, North France, PML) from

each night-time (00:00 and 03:00) footprint were therefore plotted against ClNO<sub>2</sub> concentration.

No significant correlations were apparent from these plots. The method was refined, this time combining only more local land areas (England, Ireland, North France, PML). Following this, the plots for each campaign tend to show marginally improved correlation between ClNO<sub>2</sub> concentration and percentage of air mass origin from local land areas, however this was still an insufficient basis upon which to draw any robust conclusions.

Only one such plot showed significant correlation (Figure 4.23 top), from the RAFT 2 campaign. This correlation combines the local land influence (as specified above) combined with the Scandinavia fraction plotted against ClNO<sub>2</sub> concentration and shows a high degree of correlation ( $r^2=0.94$ ). The four highest points in this plot correspond to the two nights in that campaign with the highest average ClNO<sub>2</sub> concentrations (146 ppt on the 13<sup>th</sup> and 169 ppt on the 14<sup>th</sup> December 2014). Both of these nights display a high degree of residence time over the UK (Figure 4.23 bottom).

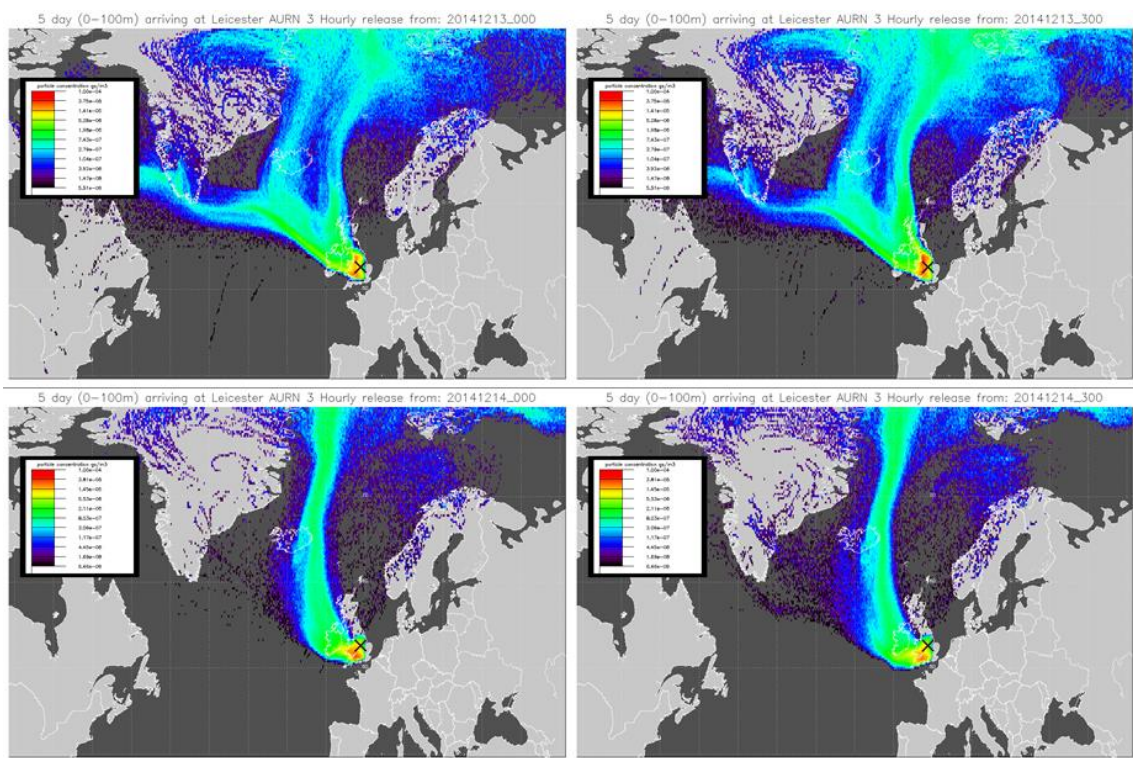
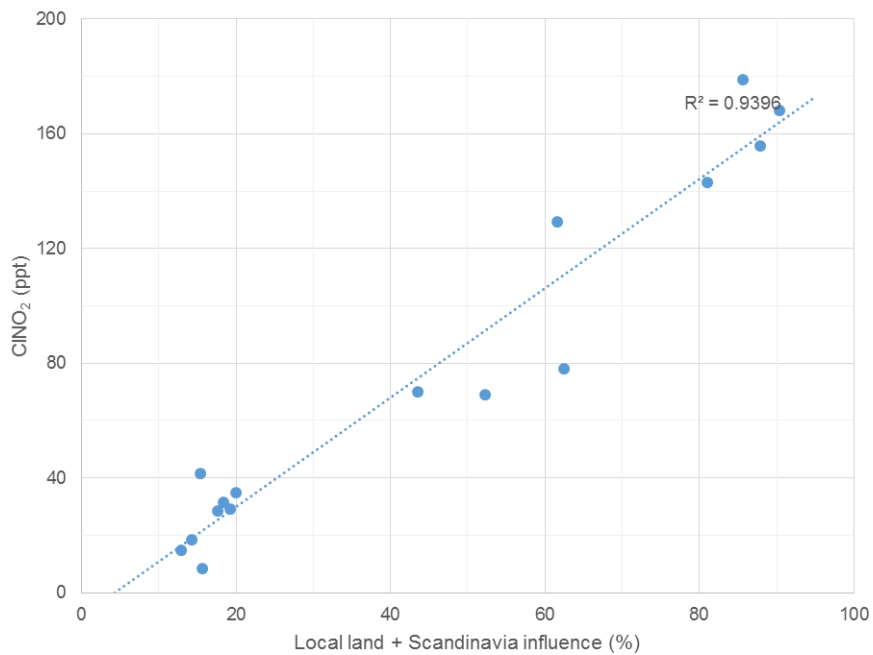


Figure 4.23 A correlation plot for the 8 days of the RAFT 2 campaign showing ClNO<sub>2</sub> concentration at 00:00 and 03:00 against percentage of air mass originating from local inland and Scandinavian sources (top; 3-hour averaged data), NAME particle dispersion footprints corresponding to the highest 4 points in the correlation plot (bottom; 5-day back).

It is possible that the air masses represented by these points denote an example of ozone-limited ClNO<sub>2</sub> formation, wherein ample NO<sub>x</sub> is present but insufficient

O<sub>3</sub> is available to oxidise generate NO<sub>3</sub> (and therefore N<sub>2</sub>O<sub>5</sub>), hampering ClNO<sub>2</sub> formation. The improvement in correlation due to the Scandinavian influence would therefore signify addition of O<sub>3</sub> from the Arctic Ocean to otherwise ozone-depleted air masses (as higher O<sub>3</sub> concentrations tend to be present in air masses that have marine origin - see section 4.6, low-ClNO<sub>2</sub> case). This hypothesis is supported by Figure 4.24, showing that ozone measured at the UoL AURN station remained low (*i.e.* relatively depleted) for most of this period (10 ppb or less until 13/12/2014 23:30). Limiting factors for ClNO<sub>2</sub> formation are discussed in more detail in section 5.7.

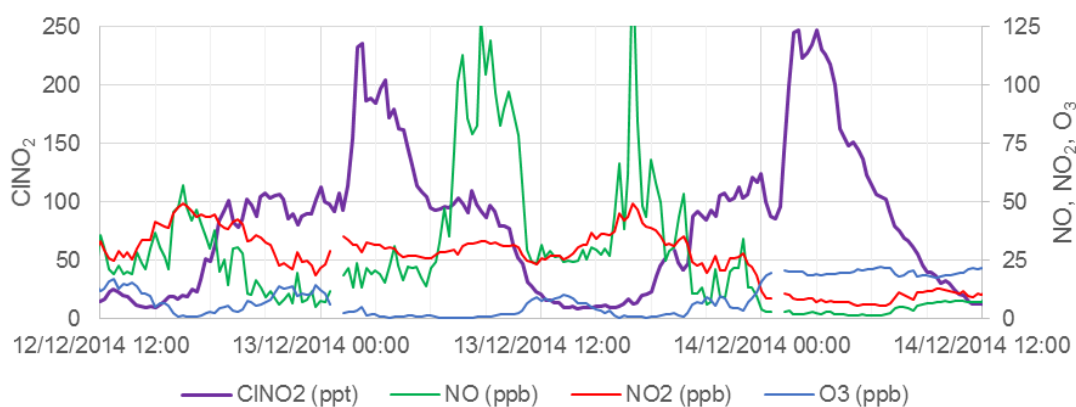


Figure 4.24 A time series of this 12-14 Dec 2014 (RAFT 2) showing concentrations of ClNO<sub>2</sub>, NO, NO<sub>2</sub> and O<sub>3</sub> (15 min averaged data).

#### 4.8 Model comparison: observations vs. GEOS-Chem model

Project collaborators (Dr. T. Sherwen and Dr. M. J. Evans; University of York) ran a regional model for ClNO<sub>2</sub> and its gas phase precursors using GEOS-Chem, modified to include halogen chemistry (see section 2.5). For UoL this was run at 2°x2.5° resolution for the project period (Mar 2014-Feb 2016) to allow for comparison of seasonal variations (geographical comparisons were also made - see section 5.8).

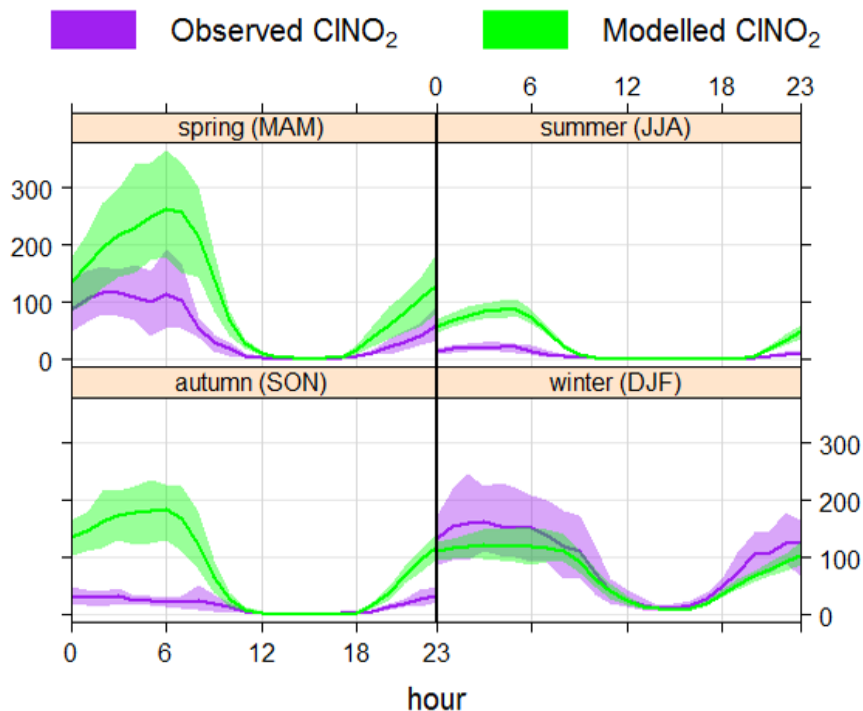


Figure 4.25 Comparison of observed and modelled  $\text{ClNO}_2$  (in ppt) average diel profiles during campaign periods for all UoL campaigns (60 min averaged data; mean and 95% confidence intervals; medium-resolution model).

Figure 4.25 shows diel profiles for  $\text{ClNO}_2$  made from observational and model data during the UoL campaigns. The model appears to agree well with winter observations in both the shape and magnitude of the average diel  $\text{ClNO}_2$  profile (though the model underestimates maximum  $\text{ClNO}_2$  by approx. 25 ppt). In the other seasons, the model consistently overestimates  $\text{ClNO}_2$ . The model predicts a factor of 5 greater than measured  $\text{ClNO}_2$  in summer and autumn. The model is closer in spring but still overestimates  $\text{ClNO}_2$  by a factor of 2.

Closer examination of the  $\text{ClNO}_2$  modelled results for the winter campaigns, however, reveals that the model is not as close to observed winter values as the averaged diel profile might indicate. Time series for UoL winter campaigns (Figure 4.26) show that the fit is good for the RAFT 2 campaign from 12-16 Dec, but begins to differ after this date. The AURN 2 campaign (note the different vertical axis scale) is a generally poor fit on most days, however, with the model tending to predict  $\text{ClNO}_2$  every night in a relatively narrow range of peak concentrations (maximum 40-420 ppt) where the observed values are more

variable (0-830 ppt) both in the occurrence or absence of ClNO<sub>2</sub> and in its peak concentration.

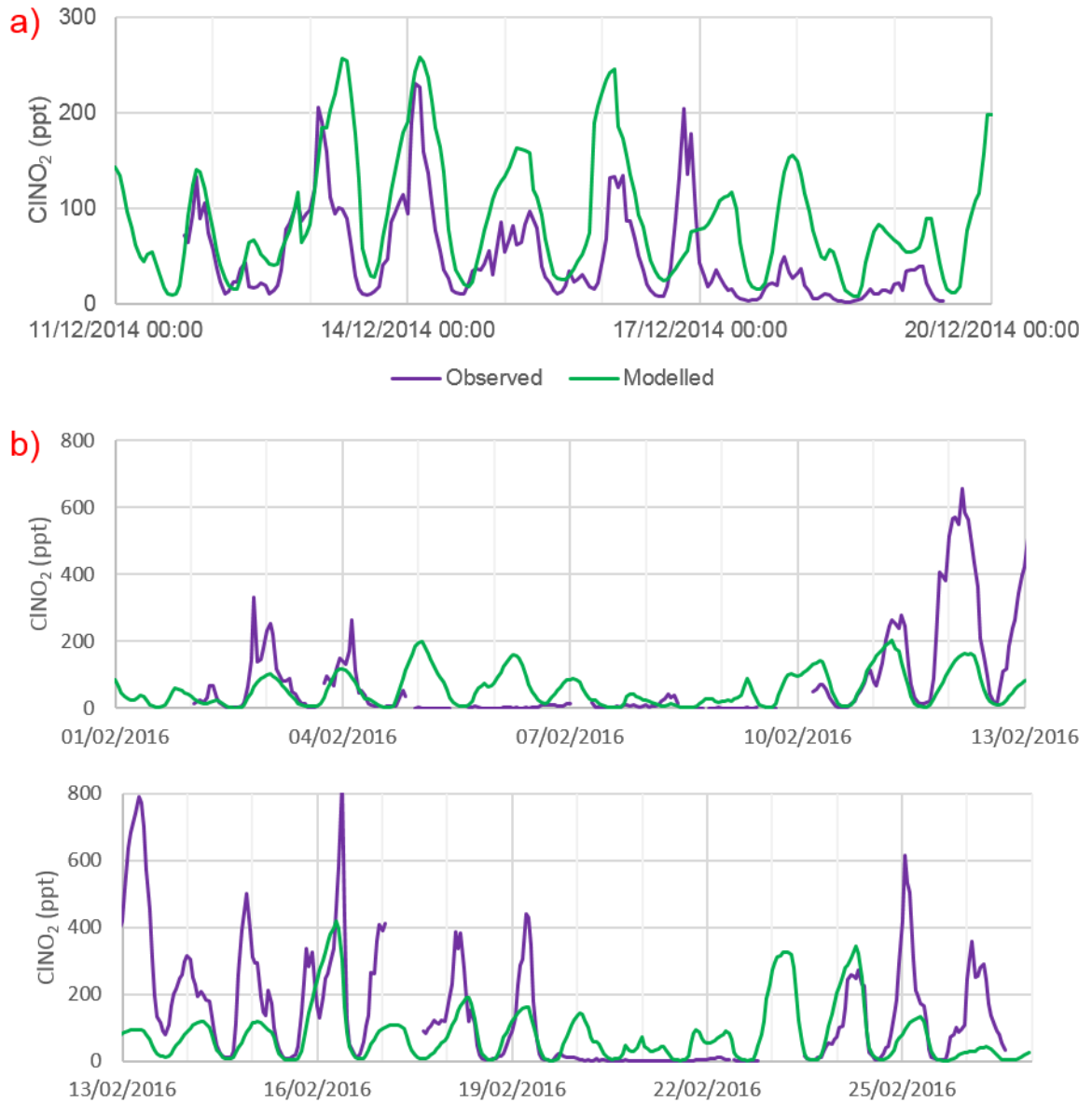


Figure 4.26 Time series comparing observed and modelled ClNO<sub>2</sub> concentrations for winter UoL campaigns (60 min averaged data; medium-resolution model).

- a) RAFT 2 campaign, December 2014.
- b) AURN 2 campaign, February 2016.

One possible explanation for the difference in the degree of agreement between observational and modelled ClNO<sub>2</sub> is shown by a weak correlation

between modelled mean nightly ClNO<sub>2</sub> and the chloride content measured for the aerosol (Figure 4.27a). This suggests that under some conditions chloride availability limits model ClNO<sub>2</sub> production at UoL. This chloride-limited ClNO<sub>2</sub> formation is not the case for actual ClNO<sub>2</sub> observed at UoL according to aerosol filter measurements (see section 5.7.1). This difference may be due to a non-sea salt source of chloride which is not accounted for in the model (Sommariva et al., 2018). Another slight correlation was visible between modelled ClNO<sub>2</sub> and NO<sub>2</sub> (Figure 4.27b) in both modelled and observed data. The correlation is weak for both, but marginally stronger for modelled ( $R^2 = 0.27$ ) than observed data ( $R^2 = 0.17$ , arguably non-existent) implying that the model predicts NO<sub>2</sub>-limited ClNO<sub>2</sub> production conditions at UoL more frequently than actually occurred during these campaigns (see section 5.7.2).

Interestingly, it can also be observed in Figure 4.26 that the model also predicts non-zero daytime ClNO<sub>2</sub> minima (see section 4.4) during the RAFT 2 campaign (in fact higher than was observed), however only barely for the AURN 2 campaign in which the highest such minimum was observed (12-13<sup>th</sup> February).

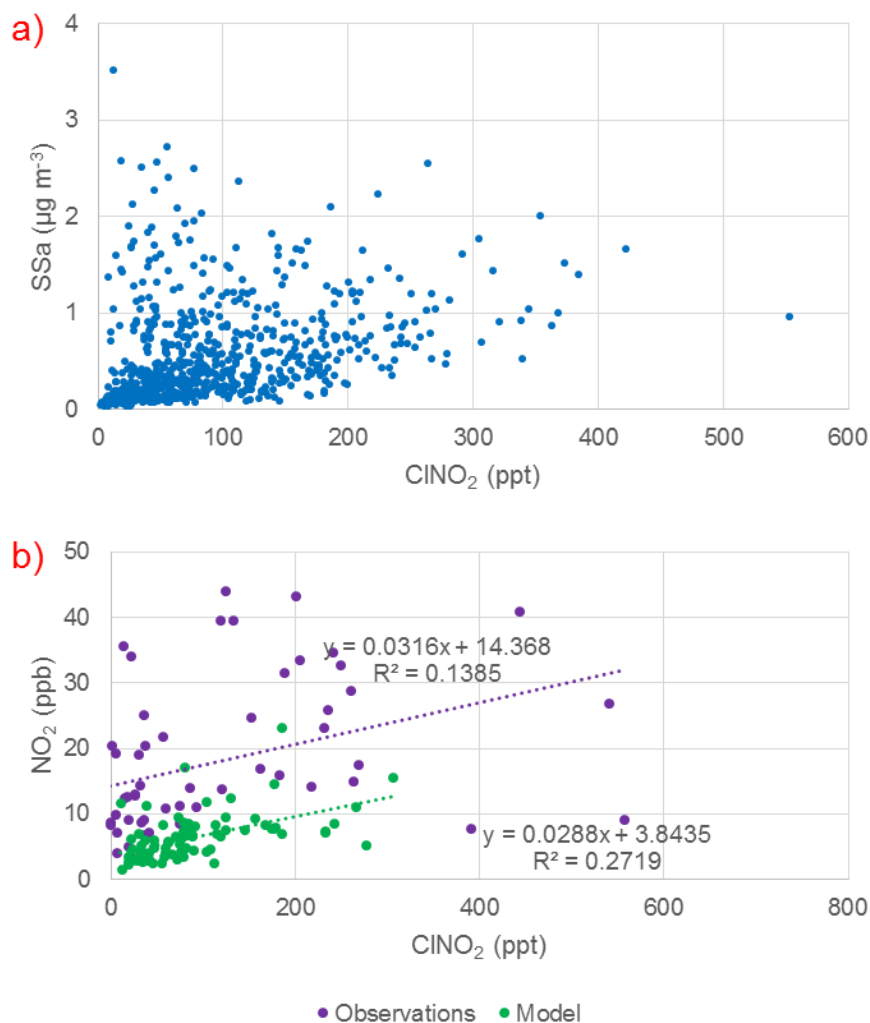


Figure 4.27 Correlations between nightly (23:00-04:59) mean ClNO<sub>2</sub> with modelled accumulation mode sea salt (a) or modelled and observed NO<sub>2</sub> concentrations (b) for all UoL campaigns (60 min averaged data; medium-resolution model).

#### 4.9 Detection of Cl<sub>2</sub> at UoL

CIMS using iodide as a reagent ion also allows for the detection of molecular chlorine, Cl<sub>2</sub>, for which the instrument was also calibrated. Cl<sub>2</sub> was observed above the detection limit (7.14 ppt) several times during both AURN station deployments, but generally remained below LoD during RAFT measurements.

One occasion where Cl<sub>2</sub> was observed arose during the AURN 2 campaign, as shown in Figure 4.28. In this case a possible diel pattern is visible whereby Cl<sub>2</sub> seems to peak around midday, however this is not the case for all such observations. As Cl<sub>2</sub> photolyses extremely rapidly, it should be expected that molecular chlorine concentrations are higher at night than during the day,

contrary to these time series. The presence of elevated  $\text{Cl}_2$  during the day suggests that the site is close to a source that is active only during the day, which is further supported by the “spiky” structure corresponding to slight changes in wind. The polar plots show that for the duration of the observations in Figure 4.28 all of the elevated  $\text{Cl}_2$  observations correspond to northeasterly wind (generally  $>2 \text{ ms}^{-1}$ ), which is the direction leading to the nearby sports centre exhaust vents (see Figure 4.2).

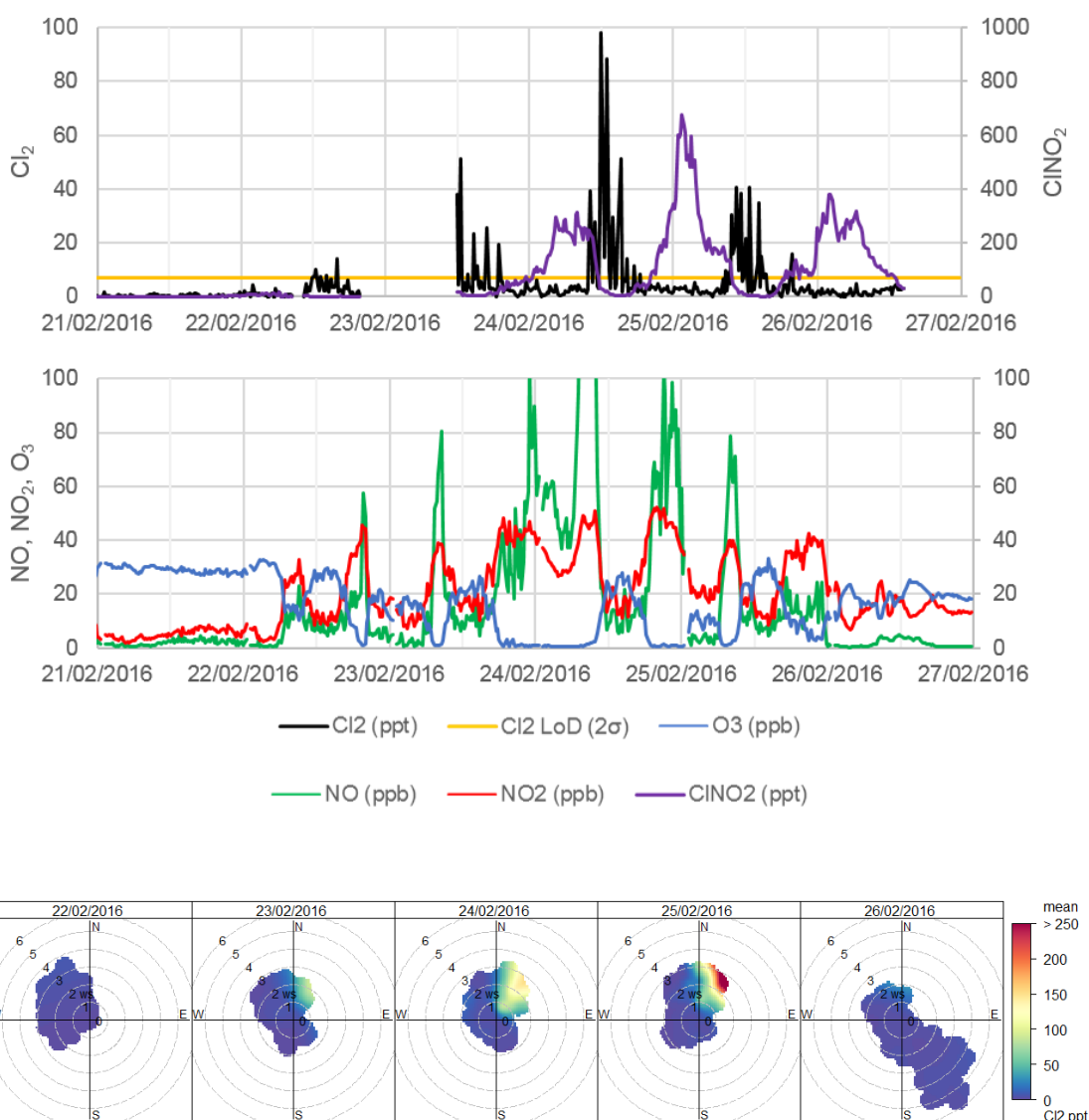


Figure 4.28 Time series of  $\text{Cl}_2$  (and LoD),  $\text{ClNO}_2$ ,  $\text{NO}$ ,  $\text{NO}_2$  and  $\text{O}_3$  during AURN 2 campaign (top; 15 min averaged data) and polar plots showing the wind conditions resulting in high detection of  $\text{Cl}_2$  (bottom; 1 min averaged data; days defined as 00:00 to 23:59 UTC on the labelled date).

Figure 4.29 shows a comparison of low  $\text{Cl}_2$  observations made during the RAFT 2 campaign, which also took place during winter.  $\text{Cl}_2$  concentrations remained well below the detection limit throughout this campaign. The activity of other species continued as before, however, such as  $\text{ClNO}_2$  forming at night and photolysing after dawn, and rush hour peaks of  $\text{NO}_x$  with corresponding  $\text{O}_3$  depletion.

The evidence from these two figures therefore implicates the sports centre as a source of molecular chlorine responsible for  $\text{Cl}_2$  observations above LoD at the AURN station, which are therefore likely to be a very localised phenomenon.

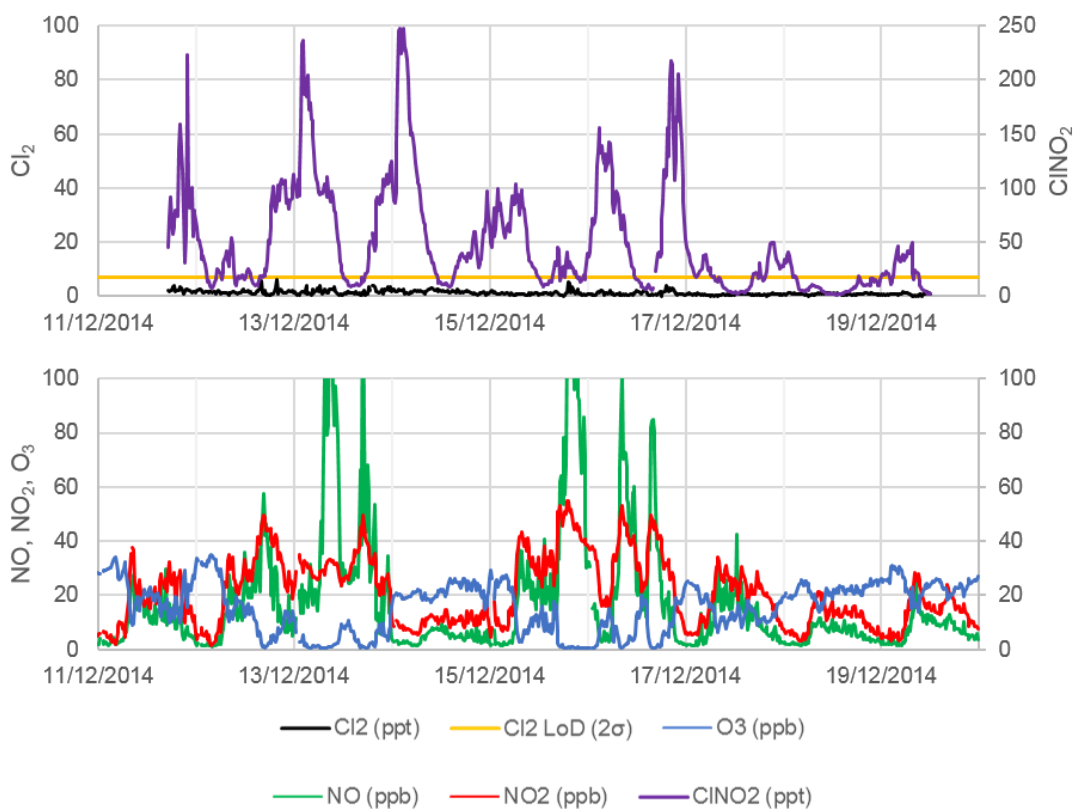


Figure 4.29 Time series of  $\text{Cl}_2$  (and LoD),  $\text{ClNO}_2$ ,  $\text{NO}$ ,  $\text{NO}_2$  and  $\text{O}_3$  during RAFT 2 campaign (15 min averaged data).

#### 4.10 Summary

The CIMS instrument was successfully deployed for 5 periods spanning all seasons across March 2014 to February 2016 at an urban inland location in the UK. Nitryl chloride was observed on most nights at this location in all 4 seasons,

suggesting that aerosol chloride is sufficiently abundant to enable ClNO<sub>2</sub> formation despite the significant distance of the Leicester site from sea salt sources of this precursor.

Diel profiles of ClNO<sub>2</sub> match the shape for a photolysable species with average maxima shortly before dawn and minima around midday, consistent with literature (e.g. Riedel et al., 2012; Mielke et al., 2013; Bannan et al., 2015).

Nitryl chloride observations were compared across the seasons. ClNO<sub>2</sub> precursors show some variability across the campaigns but did not differ significantly, unlike nitryl chloride itself which was highest in the winter (nightly average maximum ~150 ppt), almost an order of magnitude higher than summer (~20 ppt). Concentrations were also significant in spring (~120 ppt) and quite low during autumn (~40 ppt), but notably ClNO<sub>2</sub> was observed on most nights in all seasons. Wind roses show that prevailing wind is different during each season, which may be a factor in the different concentrations of measured species by conveying air from different areas to the site, however differences in temperature, aerosol and photolysis conditions during winter are still likely to be important.

In both winter campaigns ClNO<sub>2</sub> was several times observed persisting throughout daylight hours and into the next night. Even on days when this occurred, daytime ClNO<sub>2</sub> minima were generally quite small compared to night-time peak magnitudes, indicating that while ClNO<sub>2</sub> persistence through the day (owing to reduced photolysis) possibly contributes to elevated winter ClNO<sub>2</sub>, this effect is quite small compared to increased production.

A simple model was created showing instantaneous production rates of atomic chlorine and hydroxyl radicals. This model demonstrates very high Cl production in the winter daytime, but very little during the autumn.

The highest nightly average concentrations of ClNO<sub>2</sub> observed at the University of Leicester tended to occur when NO<sub>2</sub> concentrations (and ratio with respect to NO) were relatively high. Furthermore, air mass origins determined *via* NAME model usually indicated these air masses had resided over land for some time. Conversely, low ClNO<sub>2</sub> concentrations were observed in fresher air masses (as

indicated by higher ozone, lower  $\text{NO}_2/\text{NO}$  ratios and NAME footprints indicating more direct travel from the sea). These observations suggest that greater ageing of air masses supports  $\text{ClNO}_2$  production locally, likely in part due to elevated  $\text{NO}$  in fresher pollution reacting with  $\text{NO}_3$  to suppress  $\text{N}_2\text{O}_5$  formation. On some occasions,  $\text{ClNO}_2$  concentrations exhibited variations that could be attributed to changes in wind conditions (rather than formation or destruction), suggesting that much of the  $\text{ClNO}_2$  intercepted at Leicester is formed elsewhere and transported in. The highest  $\text{ClNO}_2$  measurement at UoL is an example of this, as the peak was observed after dawn (when  $\text{ClNO}_2$  production would be finished) and fell much more quickly than could be expected due to photolysis on similar days.

Diel profiles of  $\text{ClNO}_2$  made using the medium-resolution GEOS-Chem regional model for University of Leicester campaigns generally predicted the correct shape, but significantly overestimated  $\text{ClNO}_2$  concentrations for spring, summer and autumn. The winter profile appeared much closer to observed concentrations but closer examination of time series show a lesser degree of agreement than the average profile might suggest, possibly due to chloride availability limiting  $\text{ClNO}_2$  in the model but not in observations.

Molecular chlorine was measured *via* CIMS during all campaigns but rarely exceeded the limit of detection, except intermittently during AURN station deployments. On these occasions polar plots suggest the likely  $\text{Cl}_2$  source is the swimming pool exhaust vent.

## 5 Coastal measurements: Penlee Point and Weybourne Atmospheric Observatories (PPAO & WAO)

### 5.1 Site descriptions & data overview

Chapter 4 explored ClNO<sub>2</sub> formation across different seasons at a suburban inland site on the University of Leicester campus. This chapter details ClNO<sub>2</sub> measurements at two coastal sites - Penlee Point Atmospheric Observatory (PPAO) near Plymouth (Southwest England) and Weybourne Atmospheric Observatory (WAO) in Norfolk (East England) - each of which is compared with a UoL campaign set at the equivalent time of year. Dates for these campaigns are shown in Table 5.1 (section 5.1.3). The principal motivation for these campaigns was to investigate how ClNO<sub>2</sub> concentrations change with geographical location within the UK. The PPAO and WAO sites are both directly next to the sea (<200 m) therefore sea salt chloride should be plentiful.

PPAO is very close to Plymouth (<9 km) so this campaign, which lasted from 22<sup>nd</sup> April to 07<sup>th</sup> May 2015, allowed some comparison between urban inland and urban coastal settings. The location is, however, very close to the Atlantic Ocean therefore there is the possibility for clean air from the ocean to the southwest and urban outflow from Plymouth to the northeast, and potentially observable emission plumes from shipping traffic.

The Weybourne Atmospheric Observatory is positioned approx. 100 m from the sea and 20 m above mean sea level (Penkett et al., 1999). This campaign presented an opportunity to pool resources with the NERC-funded Integrated Chemistry of Ozone in the Atmosphere (ICOZA) field campaign (26<sup>th</sup> June to 31<sup>st</sup> July 2015) designed to understand formation and transport of ozone using a wide variety of measurements (especially the O<sub>3</sub> precursor species NO<sub>x</sub>, OH and RO<sub>2</sub>), with emphasis on comparing UK emissions with imported European pollution (University of Birmingham, 2015), therefore many supplementary measurements are available for the WAO campaign.

### 5.1.1 Penlee Point Atmospheric Observatory

The Penlee Point Atmospheric Observatory campaign was conducted in conjunction with Plymouth Marine Laboratory, who run the remote site (50°19'5"N, 4°11'21"W) adjacent to the Plymouth Sound bay on the Rame peninsula (Yang et al., 2016a).

The English Channel is a major shipping route, and the shipping lane lies approx. 60 km to the south of PPAO. Vessels entering the harbour (~4.5 km) must pass the Plymouth Breakwater, the most direct route for which passes approx. 2 km from the site. The hilly area directly around the site is rural with many trees. The nearby villages of Cawsand and Kingsand are likely too small to be influential. The most significant pollution source other than shipping in the Sound is the city of Plymouth itself, whose centre is only ~9 km northeast of the site (Figure 5.1). Despite the proximity to both city and harbour, air masses intercepted during the PPAO campaign were generally extremely clean as the prevailing wind originated from the Atlantic Ocean to the southwest (shown later in Figure 5.9). The wind at the PPAO site was generally strong - rarely much below 6 ms<sup>-1</sup>. This 6 ms<sup>-1</sup> threshold was conversely seldom exceeded during the springtime RAFT 1 campaign at UoL. Wind direction and speed observed during the PPAO campaign are consistent with existing literature (prevailing westerly/southwesterly winds mainly 4-12 ms<sup>-1</sup>; Yang et al., 2016b).

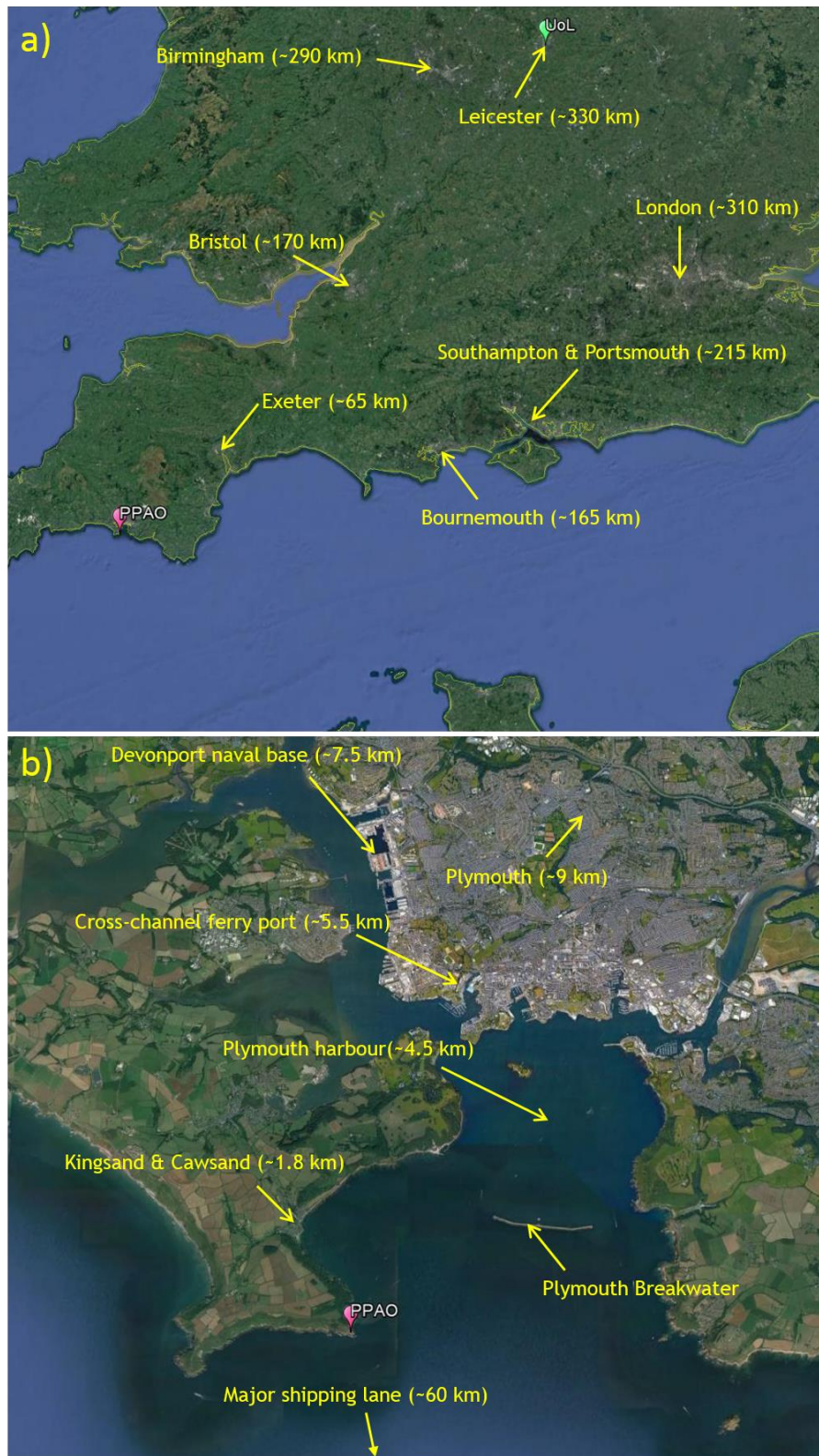


Figure 5.1 Maps & satellite images.

- a) PPAO location relative to nearest city, Plymouth (Google Earth, 2017c).
- b) PPAO closer image (Google Earth, 2017d).

For the PPAO campaign all instruments were housed in a small stone building (Figure 5.2) approx. 30 m away from the sea and 11 m above mean sea level (Yang et al., 2016b). The CIMS/BBCEAS inlets (PFA tubing ¼ inch OD, approx. 3 m length) were protected from rain using separate but adjacent upturned plastic funnels attached near the building roof (approx. 3 m from ground). The spectral radiometer was fastened to the building roof. The PPAO campaign took place in spring, from 22/04/2015 to 07/05/2015, therefore the RAFT 1 campaign (March 2014) was predominantly used as the UoL comparator campaign (see chapter 4). The building possessed some air conditioning but this was not always sufficient, resulting in significant temperature control issues. Most notable of these were high temperatures in the instrument room (often >40 °C) during the night when the door remained closed for many hours consecutively.



Figure 5.2 Housing for University of Leicester instruments during PPAO campaign.

### 5.1.2 Weybourne Atmospheric Observatory

The Weybourne site ( $52^{\circ}57'2''\text{N}$ ,  $1^{\circ}7'19''\text{E}$ ) is located on the Northern coast of rural Norfolk (Figure 5.3). Other than the sea ( $\sim 100$  m northeast), local features include an operational landing strip for light aircraft (starting  $\sim 400$  m away and ending almost adjacent to the site) and a demonstration ground for armoured vehicles ( $\sim 700$  m) associated with the nearby military museum which runs daily shows (approx. 14:00 BST). The nearest populated areas are Weybourne village ( $\sim 1.5$  km southeast), and the towns of Sheringham and Cromer are approx. 6 and 12 km east. The shipping lane lies approx. 25 km to the north. A number of cities could potentially influence the site, closest of which is Norwich ( $\sim 35$  km south). Prevailing wind during this campaign was again southwesterly therefore other potential sources of urban pollutants include Leicester (155 km) or possibly Nottingham (150 km) to the west, and Peterborough (100 km), Cambridge (105 km) and London (180 km) to the southwest. Air masses from these locations would likely be quite mature and well-processed, as all are fairly distant. The wind speeds observed at WAO (shown later in Figure 5.9) were mostly  $4\text{-}12\text{ ms}^{-1}$ , again higher than those during the equivalent UoL campaign (AURN 1) which was exceptionally calm, rarely exceeding  $4\text{ ms}^{-1}$ . All of the aforementioned cities are therefore within a reasonable range for pollution to be intercepted at WAO - for example, even  $6\text{ ms}^{-1}$  wind from London could reach the site in  $<8.5$  hours (assuming a direct path).

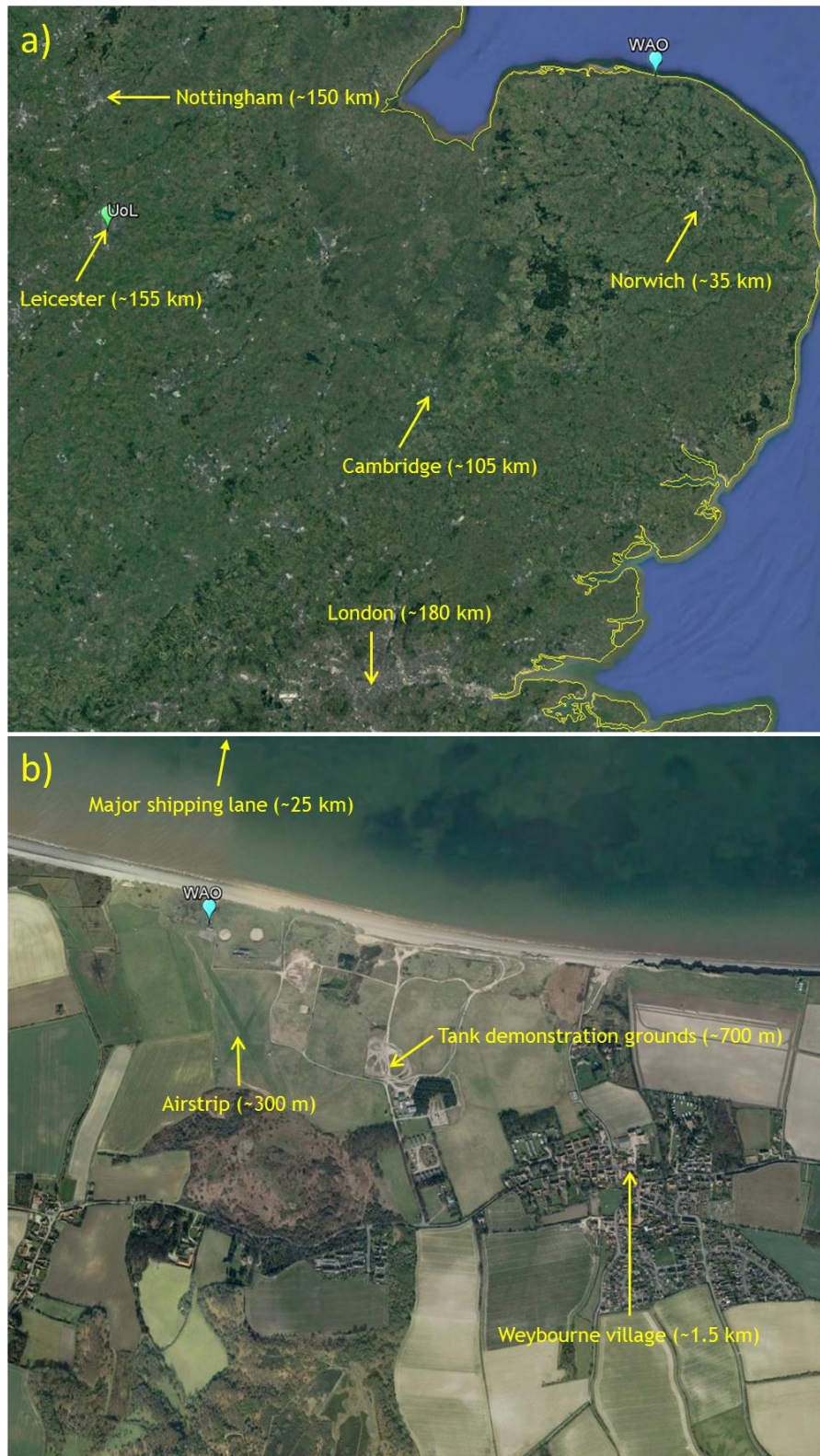


Figure 5.3 Maps & satellite images.

- a) WAO location relative to urban centres (Google Earth, 2017e).
- b) WAO closer image (Google Earth, 2017f).

Present at WAO during the ICOZA campaign were the universities of Birmingham (project lead), East Anglia (site management), Leeds, Leicester and York. WAO can intercept a diverse range of potential air masses. This site is more rural than the others, being much farther from the major urban centres, therefore a comparison with PPAO may potentially allow contrasting of coastal urban and coastal rural conditions. Weybourne is adjacent to the North Sea, and only arctic air masses travelling directly from the north will fully avoid urban centres from the UK (northeast, east, southwest, south) and Europe (south, southwest, west, northwest). The Leicester instruments were this time accommodated in an air conditioned converted shipping container (Figure 5.4). Both BBCEAS and the CIMS instruments had separate inlet tubes running parallel and attached adjacent to each other on the mast (PFA tubing ¼" OD, 4.5-5.5 m length; attached ~4 m above ground). The inlets were again protected from rainwater using upturned funnels. The spectral radiometer was attached at the top of the same mast (~5 m height). The Weybourne Atmospheric Observatory campaign took place during July 2015 so the AURN 1 campaign (August 2014) is mainly used to compare to UoL.



Figure 5.4 Housing for University of Leicester instruments during WAO campaign.

### 5.1.3 Data overview

Dates for each campaign are shown in Table 5.1 with mean, maximum and interquartile ranges for ClNO<sub>2</sub> observations. Corresponding data from RAFT 1 and AURN 1 campaigns at UoL are restated here, as these campaigns are extensively referenced for comparison throughout this chapter. Cl<sub>2</sub> was measured throughout both coastal campaigns. Like the UoL RAFT campaigns detailed in chapter 4, Cl<sub>2</sub> concentrations overwhelmingly remained below the limit of detection at PPAO and WAO therefore these data are not discussed further.

Table 5.1 Table summarising WAO and PPAO campaigns with comparison to UoL campaigns at similar time of year giving average, maximum and interquartile ranges (IQR) for ClNO<sub>2</sub>, NO, NO<sub>2</sub> and O<sub>3</sub> (15 min averaged night-time data, 23:00 to 04:59) in addition to aerosol chloride and nitrate (from 24-hour PM<sub>10</sub> filters (UoL) or multistage high-volume impactor (WAO)).

		PPAO 22 Apr-07 May 2015 (Spring)	RAFT 1 03-11 Mar 2014 (Spring)	WAO 28 Jun-31 Jul 2015 (Summer)	AURN 1 04-28 Aug 2014 (Summer)
ClNO <sub>2</sub> (ppt)	Mean	61	72	65	14
	IQR	0.4 - 7.3	4.7 - 130	8.7 - 59	1.3 - 23
	Max	922	274	1104	74
NO (ppb)	Mean	0.1	9.7	0.2	4.1
	IQR	-0.1 - 0.3	0.8 - 4.2	0.1 - 0.2	0.6 - 5.6
	Max	0.9	81	5.1	23
NO <sub>2</sub> (ppb)	Mean	1.3	14	3.0	10
	IQR	0.4 - 1.9	5.9 - 25	1.7 - 3.9	4.5 - 14
	Max	6.3	38	9.4	27
O <sub>3</sub> (ppb)	Mean	37	20	29	16
	IQR	33 - 43	13 - 28	22 - 33	11 - 22
	Max	50	36	98	30
Cl <sup>-</sup> (µg m <sup>-3</sup> )	Mean	-	4.6	3.7	3.1
	IQR	-	2.1 - 5.4	1.4 - 5.0	1.1 - 4.2
	Max	-	11	14	7.8
NO <sub>3</sub> <sup>-</sup> (µg m <sup>-3</sup> )	Mean	-	22	2.8	3.6
	IQR	-	8.8 - 33	1.4 - 2.8	2.5 - 3.8
	Max	-	50	11.3	10.0

The PPAO campaign took place in April/May 2015, and can be compared with several literature campaigns (detailed in section 1.3) in addition to RAFT 1 at UoL. The maximum ClNO<sub>2</sub> concentration observed at PPAO was 922 ppt, which significantly exceeds the highest concentration of 274 ppt observed during the RAFT 1 campaign and 250 ppt detected by Mielke et al., 2011 (continental Canada, April 2010). The PPAO maximum is, however, much lower than the 2150 ppt observed by Riedel et al., 2012 and 3600 ppt by Mielke et al., 2013, both in California (*i.e.* coastal USA) during May/June 2010.

The WAO campaign was carried out in July 2015, and in this campaign the ClNO<sub>2</sub> maximum concentration was 1104 ppt. This is a factor of 15 greater than the equivalent UoL measurement (74 ppt), exceeding the 724 ppt observed by Bannan et al., 2015 (London, July/August 2012) and 800 ppt by Phillips et al., 2012 (continental Germany, August/September 2011) and therefore represents

the highest ClNO<sub>2</sub> observation reported in Europe to date. This measurement is similar to the 1200 ppt observed by Osthoff et al., 2008 (coastal USA, August/September 2006) but lower than the previously mentioned 2150 and 3600 ppt measurements by Riedel et al., 2012 and Mielke et al., 2013, in addition to the 1997 and 2070 ppt measurements reported in Tham et al., 2013 (coastal China; August 2012) and Tham et al., 2016 (continental China; June to September 2014) respectively.

Figure 5.5 shows a complete time series for the PPAO campaign. ClNO<sub>2</sub> concentrations at generally remained quite low with one exceptionally high peak (Figure 5.6). Night-time CIMS data coverage from 24/04/15 onwards is very high with several daytime periods missing (for calibration and maintenance). Spectral radiometer data are also available, in addition to a variety of other supporting measurements including NO, NO<sub>2</sub> and O<sub>3</sub>.



Figure 5.5 Complete time series for PPAO campaign (April-May 2015) showing concentrations of ClNO<sub>2</sub>, NO, NO<sub>2</sub> and O<sub>3</sub> (15 min averaged data). The off-scale ClNO<sub>2</sub> peak is shown separately (Figure 5.6).

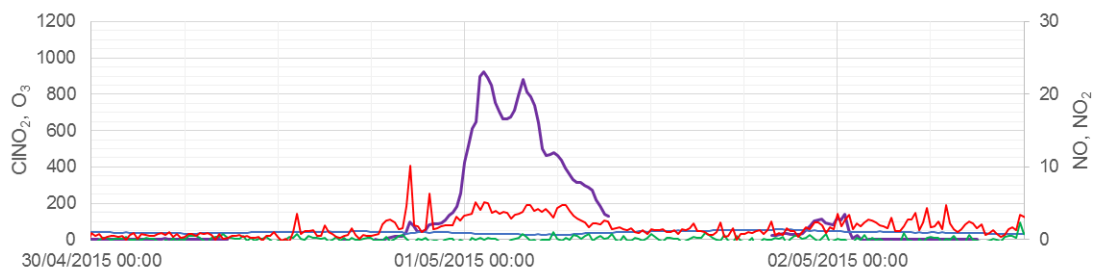
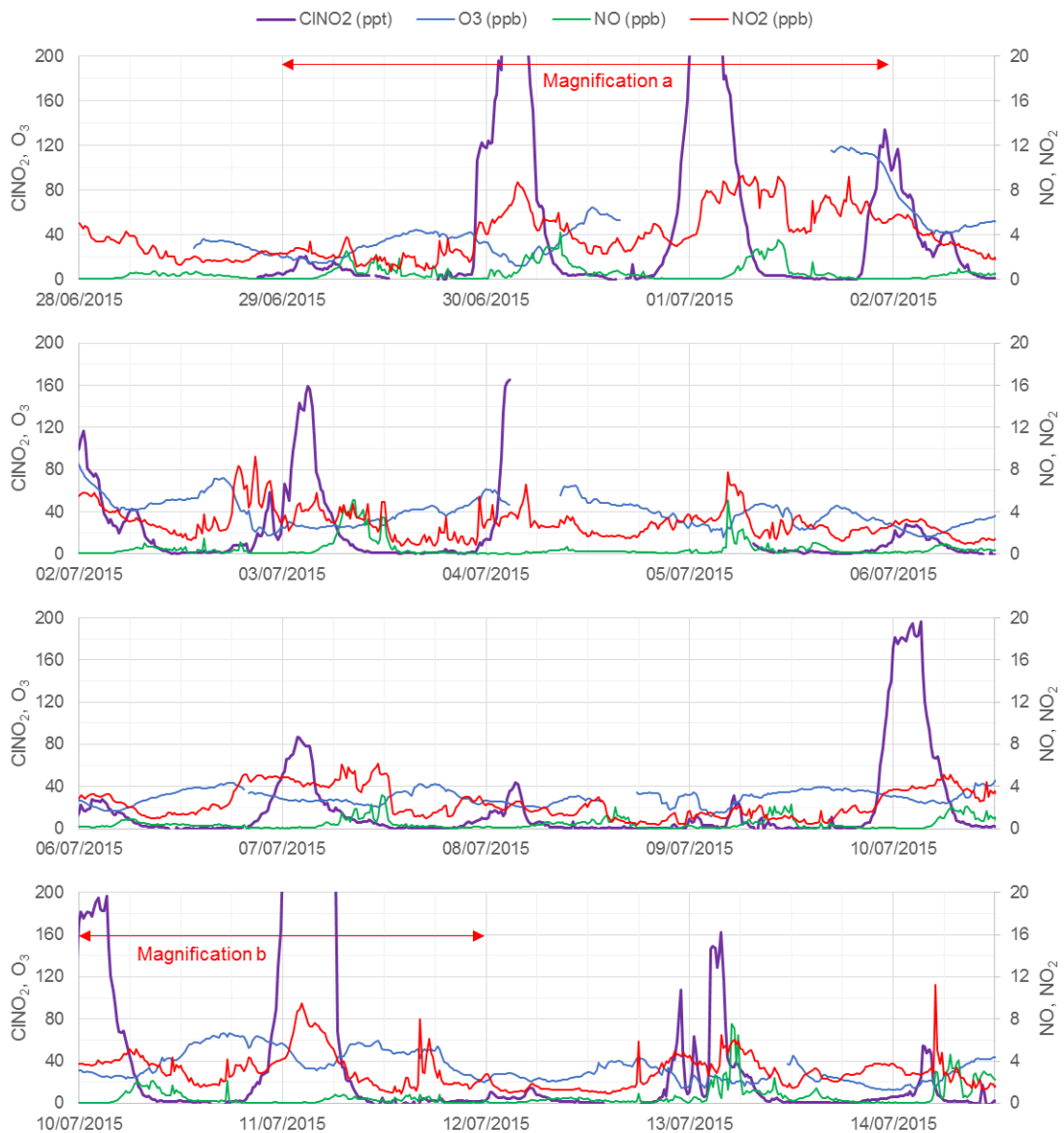


Figure 5.6 Magnified section PPAO time series showing the large ClNO<sub>2</sub> peak, 922 ppt at 01:15 (15 min averaged data).

In Figure 5.7 a complete time series for the WAO campaign is shown.  $\text{ClNO}_2$  concentrations were again generally low with one exceptionally high peak, however several middling peaks were also observed during this campaign (Figure 5.8). Night-time CIMS data coverage is similarly good at WAO, with several daytime periods missing (for calibration and maintenance) and on the night of 04-05 July due to a power cut.



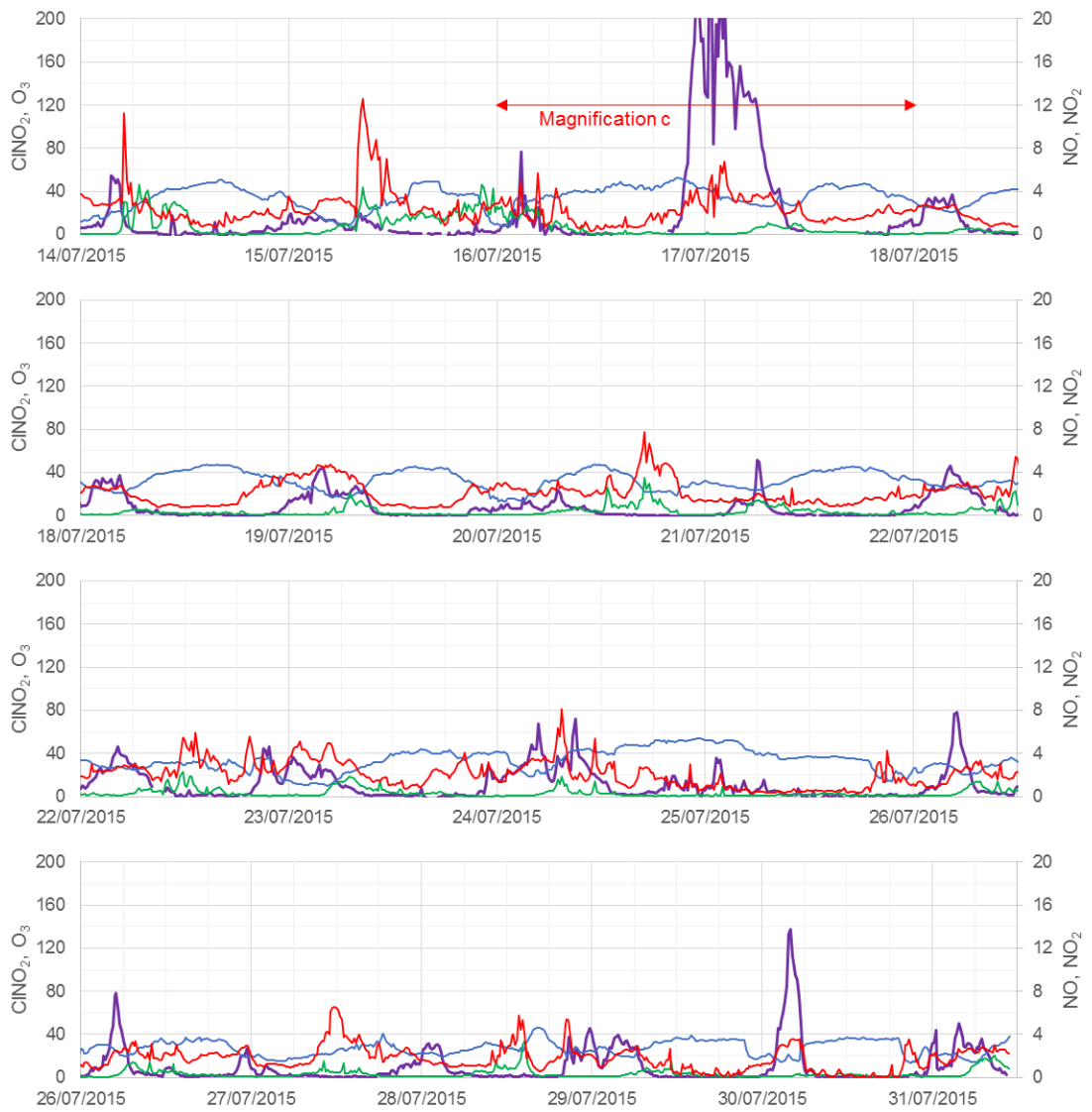


Figure 5.7 Complete time series for WAO campaign (July 2015) showing concentrations of ClNO<sub>2</sub>, NO, NO<sub>2</sub> and O<sub>3</sub> (15 min averaged data). Off-scale ClNO<sub>2</sub> peaks are shown separately (Figure 5.8).

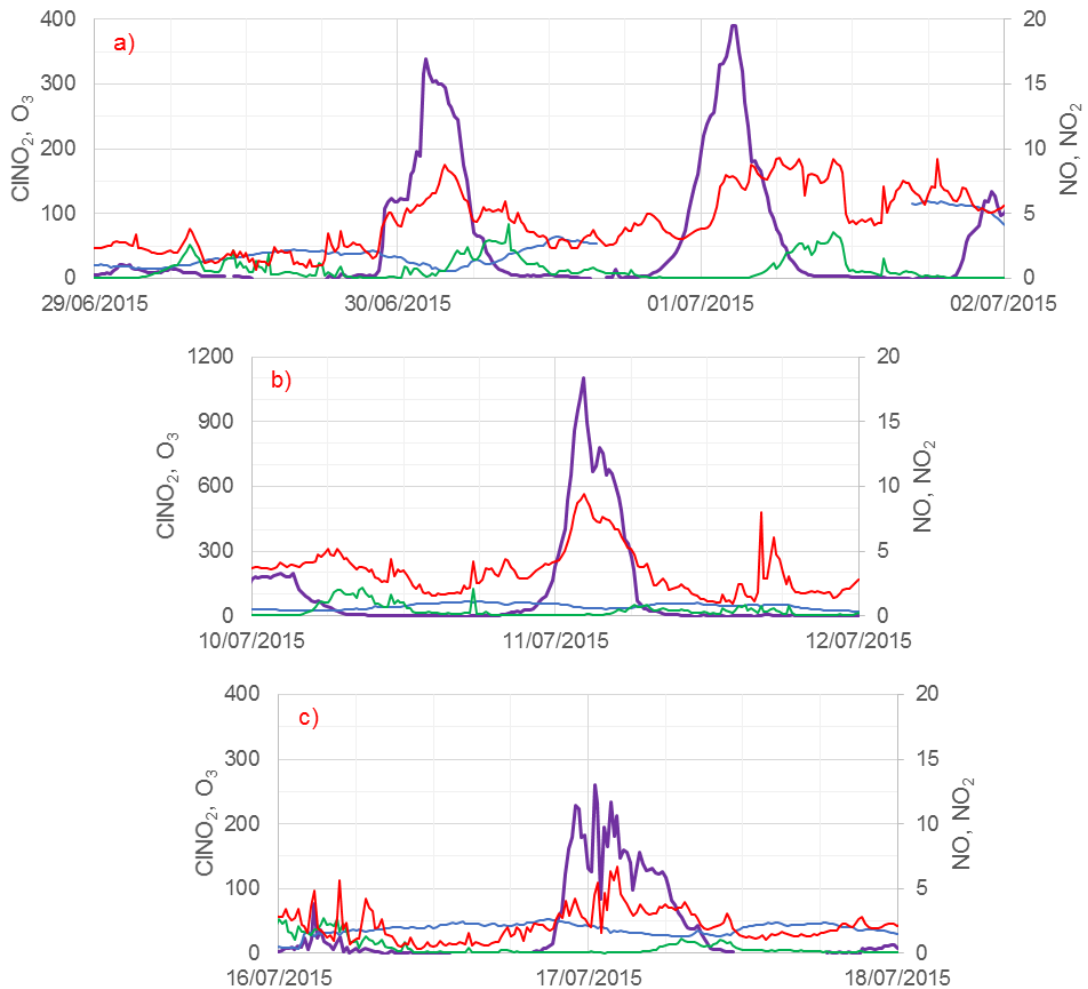


Figure 5.8 Magnified sections of the WAO time series showing large CINO<sub>2</sub> peaks (15 min averaged data; note the varying vertical axis scales).

- a) 339 ppt (30/06/15 02:15) and 390 ppt (01/07/15 02:45).
- b) The WAO highest CINO<sub>2</sub> observation, 1104 ppt (11/07/15 02:15).
- c) 260 ppt (17/07/15 00:30).

Figure 5.9 shows wind roses (a) and pollution roses (b) for PPAO, WAO and their respective paired UoL campaigns, giving data regarding wind direction combined with wind speed or observed CINO<sub>2</sub> concentrations respectively. These plots are given here to facilitate comparisons with the time series, but are mostly discussed elsewhere in sections 5.1.1 and 5.2.

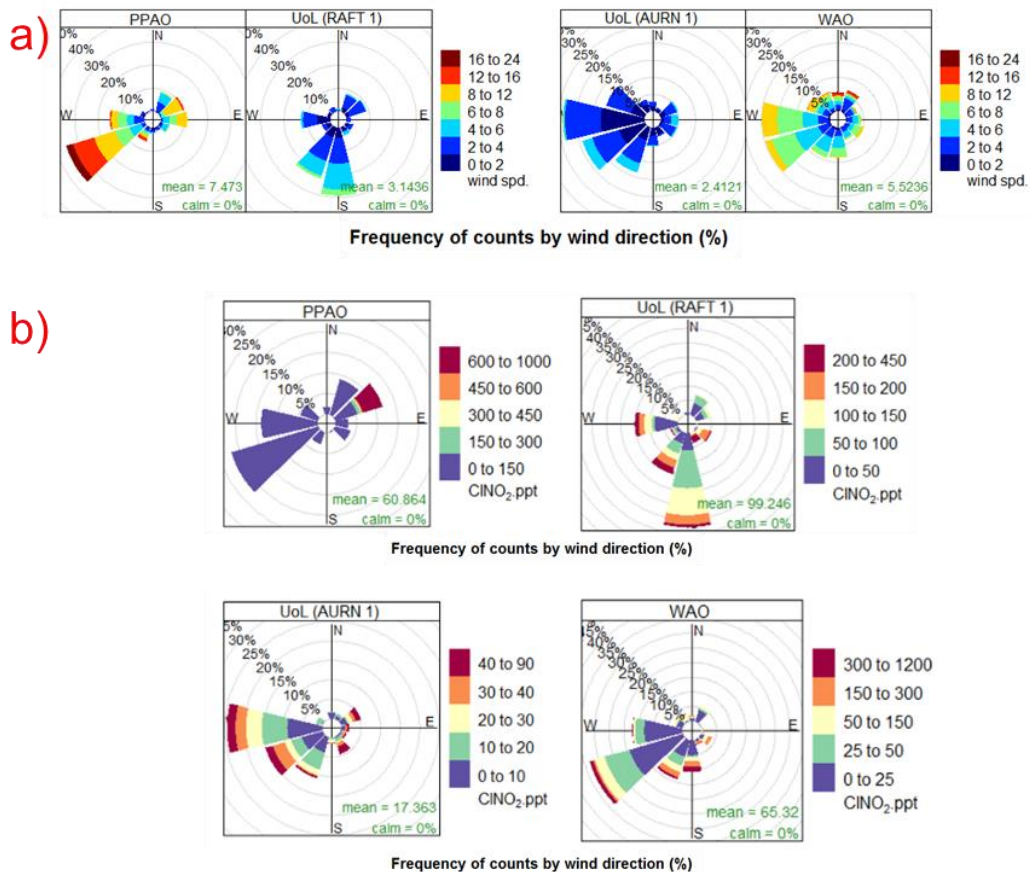


Figure 5.9 Plots relating to wind conditions for PPAO and WAO campaigns, each paired with the closest seasonally-equivalent UoL campaign (15 min averaged data).

- a) Wind roses (wind speed in  $\text{ms}^{-1}$ ).
- b)  $\text{ClNO}_2$  pollution roses (night-time data only, 23:00 to 04:59 UTC).

$\text{ClNO}_2$  concentrations at PPAO and WAO generally remained quite low with a few exceptionally high peaks, which are repeated at the bottom of each figure at a scale appropriate to each peak.  $\text{ClNO}_2$  diel patterns were unsurprisingly similar to UoL campaigns, but at both coastal sites  $\text{ClNO}_2$  peaks (observed almost every night at UoL) are much less reliably present, especially at PPAO where  $\text{ClNO}_2$  peaks significantly exceeded the detection limit on only a few nights. A more detailed comparison of data from PPAO and WAO campaigns with UoL is in section 5.2.

## 5.2 Site comparisons: locations & seasons

University of Leicester campaigns (see chapter 4) were picked from similar times of year in order to draw comparisons to the coastal campaigns. In spring, the PPAO campaign took place in April/May 2015 and was therefore paired with the UoL RAFT 1 campaign in March 2014. In the summer, the WAO campaign occurred in July 2015 and is compared with AURN 1 in August 2014. Wind speeds were briefly discussed earlier (section 5.1.1, Figure 5.9).

ClNO<sub>2</sub> concentrations initially appear quite similar between PPAO and RAFT 1 (Figure 5.10, top left), however the broad 95% confidence intervals (shaded area) show that both campaigns (but especially PPAO) are affected by widely variable concentrations. For PPAO this is due to the single night with exceptionally high ClNO<sub>2</sub> peaking at 922 ppt (discussed later in section 5.4.2) while most other nights of the campaign were near-zero, which is to say the “average” diel profile for ClNO<sub>2</sub> during PPAO is driven by this one night. The RAFT 1 campaign ClNO<sub>2</sub> peaks were much less divergent from each other - there was still one night of exceptionally high ClNO<sub>2</sub> (maximum 274 ppt) however ClNO<sub>2</sub> maxima still exceeded 50 ppt on all nights, therefore production of ClNO<sub>2</sub> at UoL is therefore generally higher (and more consistent) than at the PPAO site. The high ClNO<sub>2</sub> event during the PPAO campaign was attributed to pollution from the harbour (see section 5.4.2), suggesting that nitryl chloride production in this region may be substantial but is observed at this site only under certain wind conditions.

The Weybourne campaign also experienced one night with exceptionally high ClNO<sub>2</sub> (discussed later in section 5.4.4), however the 95% confidence intervals are narrower than for PPAO, suggesting the unusual peak at WAO (1104 ppt) is less anomalous for the site. The mean, maximum and interquartile range for WAO remain much higher than the summertime UoL equivalent.

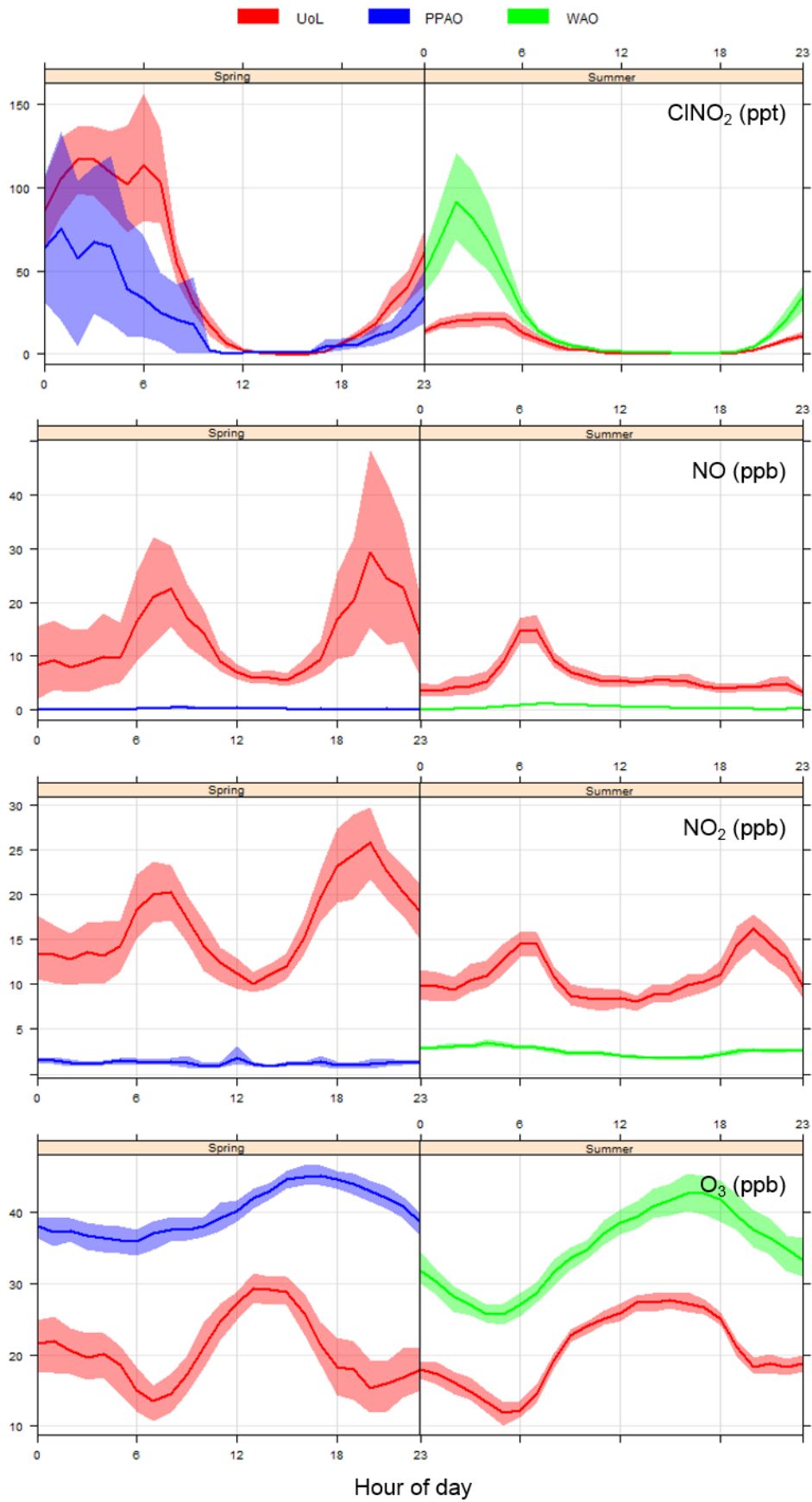


Figure 5.10 Average diel profiles of ClNO<sub>2</sub>, NO, NO<sub>2</sub> and O<sub>3</sub> at PPAO (left) and WAO (right) compared to UoL observations at equivalent time of year (15 min averaged data).

Campaign average O<sub>3</sub> concentrations for WAO were lower than at PPAO but are likely still comparable as both were approximately 1.8 times their UoL equivalent (PPAO 37 vs. 20 ppb, WAO 29 vs. 16 ppb). NO<sub>x</sub> concentrations are the greatest difference between locations, and like for O<sub>3</sub> the coastal campaigns are more similar to each other than to UoL. NO is not really observable in the diel plots for PPAO, and only barely for WAO, too small to confidently discern diel patterns. Campaign NO maxima were very small compared to UoL, 0.9 at PPAO vs. 80 ppb during RAFT 1 and 5.1 ppb at WAO vs. 23 ppb for AURN 1. NO<sub>2</sub> shows a similar pattern, with UoL dwarfing the coastal observations. PPAO average NO<sub>2</sub> is 1.3 ppb, approximately 10% of the 14 ppb for RAFT 1. Nitrogen dioxide at WAO is higher at 3 ppb, as compared to 10 ppb during AURN 1, and a diel profile is just about visible (which matches UoL). Notably, the 2-peak rush hour NO and NO<sub>2</sub> profile was not observable for either coastal campaign as they were at UoL (see section 4.2), suggesting these coastal sites are not usually influenced by fresh pollution sources (*e.g.* traffic).

The difference in ozone concentration between UoL and each coastal location, while considerable, is much less than the difference in NO<sub>x</sub> concentrations. The O<sub>3</sub> diel profile is similar at both coastal locations, showing depletion at night and growth during the day. Again, the signs of rush hour observed at UoL (*i.e.* additional depletion at rush hours, anticorrelated with NO<sub>x</sub>, from oxidation of NO to NO<sub>2</sub>) are missing from these profiles. Furthermore ozone is still present at significant levels throughout all campaigns so it is likely that the difference in ClNO<sub>2</sub> concentrations between sites is more controlled by availability of the nitrogen oxide precursors.

The higher average NO<sub>x</sub> shows that Weybourne intercepts much less clean air off the ocean than PPAO, which is unsurprising given the directions of prevailing wind observed during the campaigns - west and/or southwest in both cases, corresponding to the Atlantic Ocean for PPAO but inland for WAO (see Figure 5.9). Furthermore, air from the North Sea is more polluted than from the Atlantic Ocean as the former has more dense shipping traffic and is more surrounded by land. ClNO<sub>2</sub> pollution roses for PPAO, WAO and combined UoL data were superimposed upon a map of the UK (Figure 5.11). The pollution roses on this figure indicate that the highest ClNO<sub>2</sub> concentrations at all three sites

tended to come from southeast UK (and/or Europe), including the megacity London, suggesting that  $\text{NO}_x$ -bearing pollution is most often the determining factor for  $\text{ClNO}_2$  production in the UK.

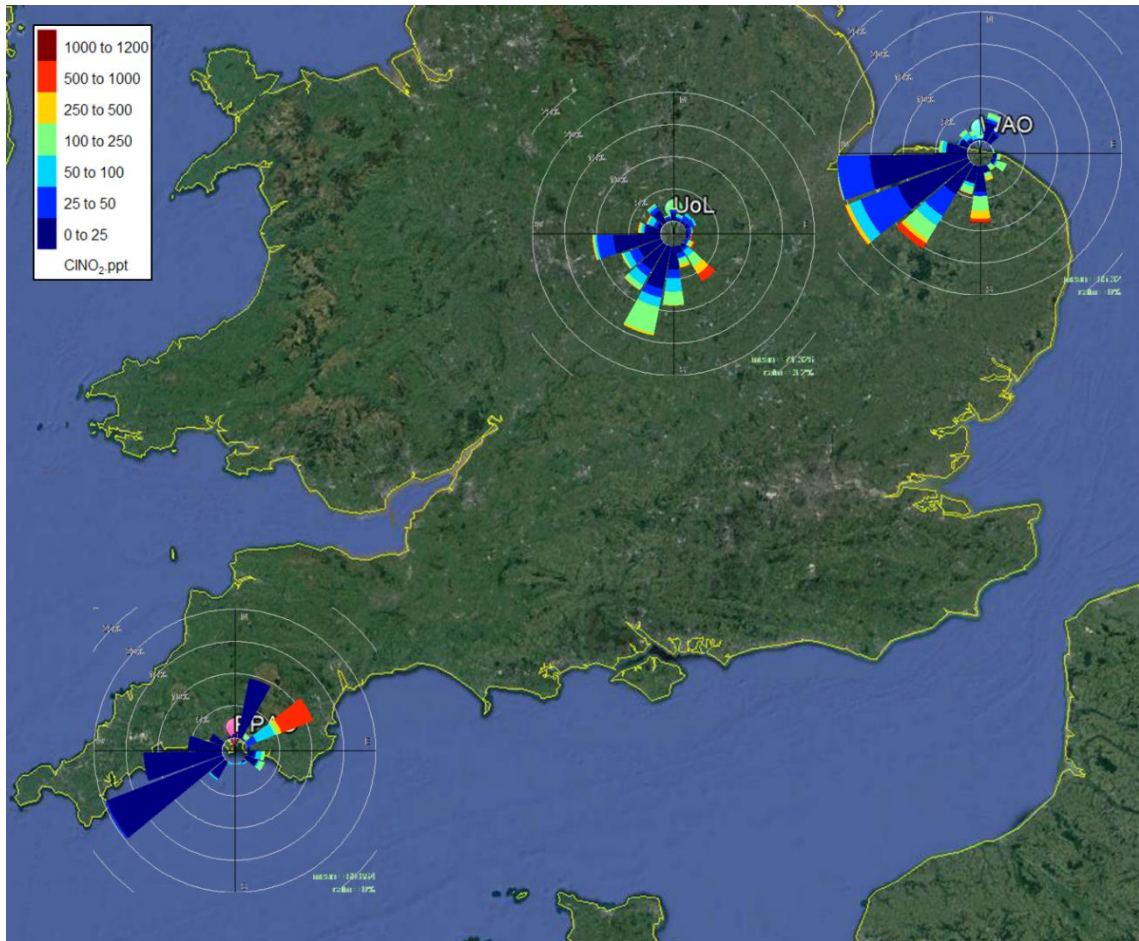


Figure 5.11 Satellite image of middle & southern UK with  $\text{ClNO}_2$  pollution rose for each measurement location (Google Earth, 2017g).

### 5.3 Radical production

The comparative rates of Cl and OH radical production were calculated using the same method as for UoL campaigns (see section 4.5) to enable comparison between the locations. Figure 5.12a shows a complete time series of the WAO campaign, with ClNO<sub>2</sub> concentration and instantaneous production rates of Cl and OH radicals. As this campaign took place in July, it was compared with the AURN 1 (September) campaign at UoL illustrated in Figure 4.17.

The section shown in Figure 5.12b is centred upon the night in which the highest ClNO<sub>2</sub> concentration was observed in the WAO campaign (1200 ppt on the night of 10-11 July). This section highlights the fact that Cl production was minimal compared to OH (similarly to the AURN 1 campaign) even on the day following the exceptionally high ClNO<sub>2</sub> peak.

In Figure 5.12c the Cl and OH production rates are shown on separate scales for easier comparison. The highest instantaneous Cl production value during this campaign predictably occurs in the morning following the 1200 ppt ClNO<sub>2</sub> peak, however even this is still an order of magnitude less than the OH production peak on the same day ( $9.6 \times 10^{-10}$  vs.  $9.3 \times 10^{-9}$  molecules cm<sup>-3</sup> s<sup>-1</sup>). The effect of Cl enhancing early morning initiation of oxidation chemistry may still be relevant at this time of year, however, as Cl production still begins and peaks significantly earlier than OH. This effect is small on most days (owing to low overall Cl production), but may be significant on days following unusually large ClNO<sub>2</sub> observations such as 11/07/15.

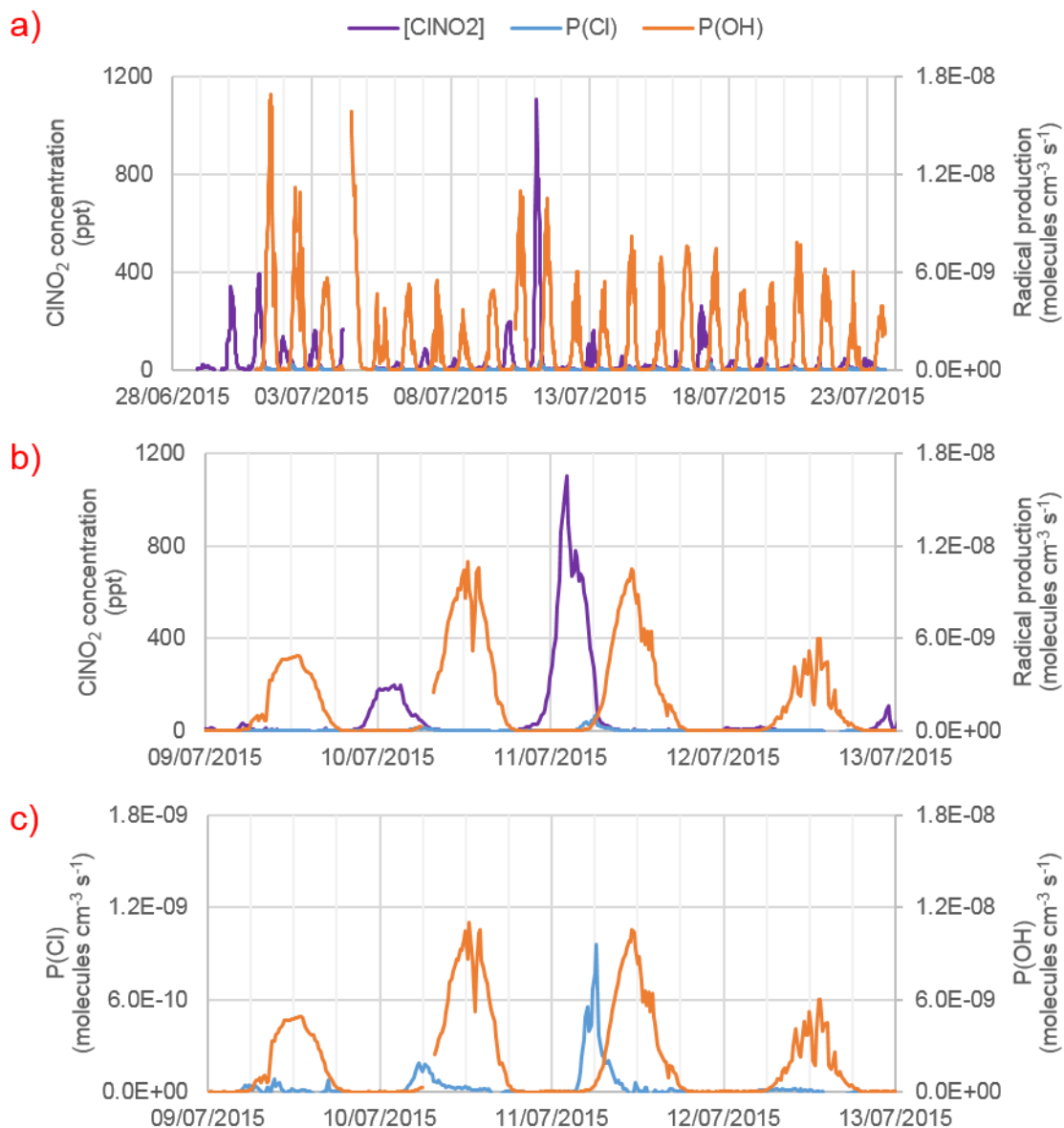


Figure 5.12 Time series showing comparative production rates of Cl and OH during the WAO campaign in July 2015 (15 min averaged data).

- a) Full campaign time series.
- b) Partial time series centred upon the night of 10-11 July, in which the highest ClNO<sub>2</sub> concentration was observed.
- c) Partial time series also centred upon the night of 10-11 July, with P(Cl) and P(OH) on separate scales.

Figure 5.13a shows a complete time series of the PPAO campaign, allowing some assessment of the relative importance of Cl derived from ClNO<sub>2</sub> photolysis in spring (*i.e.* April/May). The figure shows that Cl production is minimal on the majority of days during this campaign, even when ClNO<sub>2</sub> was observed during the prior night.

The section shown in Figure 5.13b shows the PPAO campaign's highest ClNO<sub>2</sub> peak (922 ppt on the night of April 30<sup>th</sup> to May 1<sup>st</sup>). The peak Cl production on this day is unusually high for the campaign ( $\sim 1 \times 10^{-9}$  molecules cm<sup>-3</sup> s<sup>-1</sup>), roughly half that of OH ( $\sim 2 \times 10^{-9}$  molecules cm<sup>-3</sup> s<sup>-1</sup>). Cl production on this day also rises much sooner than OH, in agreement with UoL (see section 4.5) and WAO (see Figure 5.12).

Figure 5.13c, combined with the previous plot, reveals that the unusually high Cl production on this day coincides with unusually low photolysis (peak  $j_{\text{ClNO}_2}$  on most days during this campaign is  $3 \times 10^{-4}$  to  $5 \times 10^{-4}$  s<sup>-1</sup>). Significant Cl/OH production ratios at this site in spring therefore depend on the combination of unusually high ClNO<sub>2</sub> concentrations during the night and low photolysis during the following day.

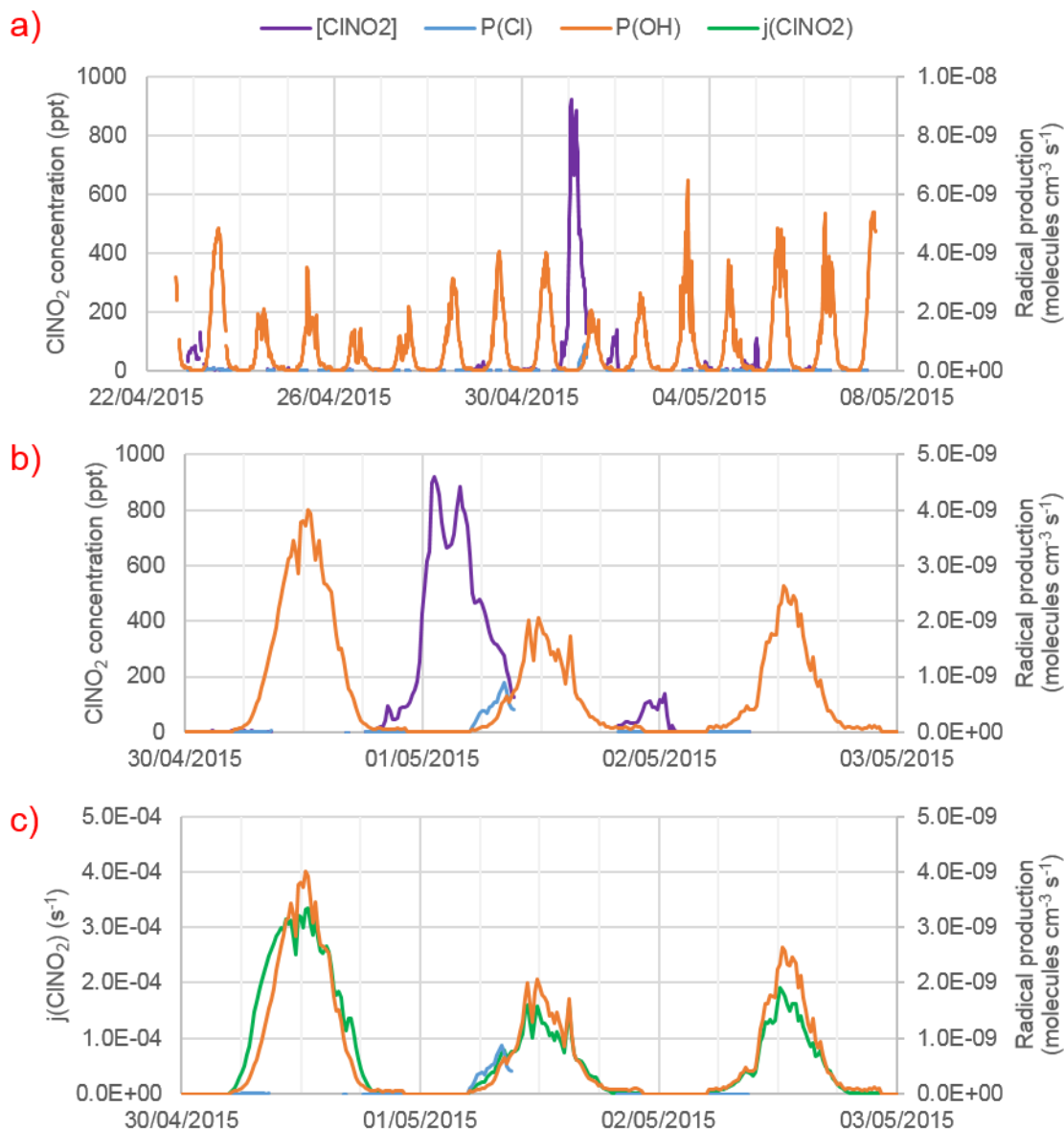


Figure 5.13 Time series showing comparative production rates of Cl and OH during the PPAO campaign in April/May 2015 (15 min averaged data).

- Full campaign time series.
- Selected partial time series showing 30 April to 03 May (note the different scale of the radical production axis).
- Partial time series also showing 30 April to 03 May, with ClNO<sub>2</sub> photolysis rate.

## 5.4 Case studies

### 5.4.1 PPAO: Low ClNO<sub>2</sub>

NAME dispersion models were used in conjunction with meteorological, NO<sub>x</sub> and O<sub>3</sub> data to ascertain conditions resulting in high and low ClNO<sub>2</sub> production at Penlee Point.

Remarkably clean air (with extremely low levels of anthropogenic pollutants, *e.g.* NO<sub>x</sub> rarely exceeding 5 ppb) was generally sampled during the PPAO campaign, and ClNO<sub>2</sub> usually remained close to or below the detection limit on most nights.

Most nights during the PPAO campaign are therefore similar to the one shown in Figure 5.14. During these nights relatively strong winds (in this case mostly >8 ms<sup>-1</sup>) are observed coming from the south and southwest, as is typical for the site (Yang et al., 2016b). Near-zero concentrations of NO, NO<sub>2</sub> and ClNO<sub>2</sub> are observed along with high O<sub>3</sub> (35-45 ppb). These concentrations of NO<sub>x</sub> and O<sub>3</sub>, along with the absence of rapid fluctuations, show no signs of fresh anthropogenic pollution (*e.g.* from shipping traffic) and represent very clean air coming from the northern Atlantic Ocean. The NAME footprints support this but add that the longer-term origins are similarly clean *via* the Arctic Ocean, avoiding large cities (*e.g.* London and continental Europe) and not dwelling in any location for long.

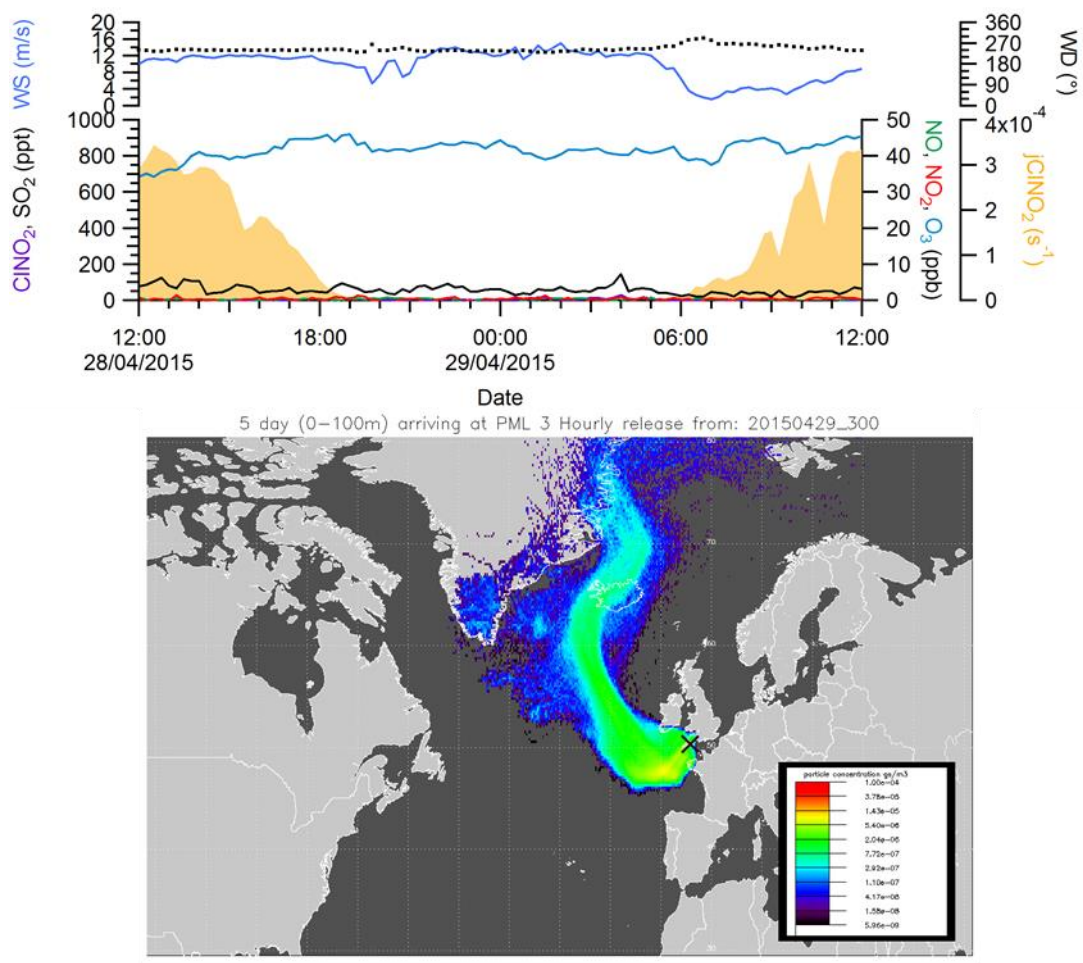


Figure 5.14 Plots for low ClNO<sub>2</sub> night, 28-29 Apr 2015 during the PPAO campaign. Top: time series showing wind speed/direction, ClNO<sub>2</sub> photolysis rate and concentrations of ClNO<sub>2</sub>, NO, NO<sub>2</sub>, O<sub>3</sub> and SO<sub>2</sub> (15 min averaged data). Bottom: NAME particle dispersion footprint at 03:00 (5-day back).

#### 5.4.2 PPAO: High ClNO<sub>2</sub>

The highest ClNO<sub>2</sub> concentration recorded during the PPAO campaign was 922 ppt at ~01:15 on 01/05/15, the night of which is shown in Figure 5.15. Other than this exceptional night only three other nightly peaks demonstrate significant concentrations (>50 ppt) of ClNO<sub>2</sub>, however even these are short-lived peaks with averages considerably lower than commonly observed during the springtime RAFT 1 campaign.

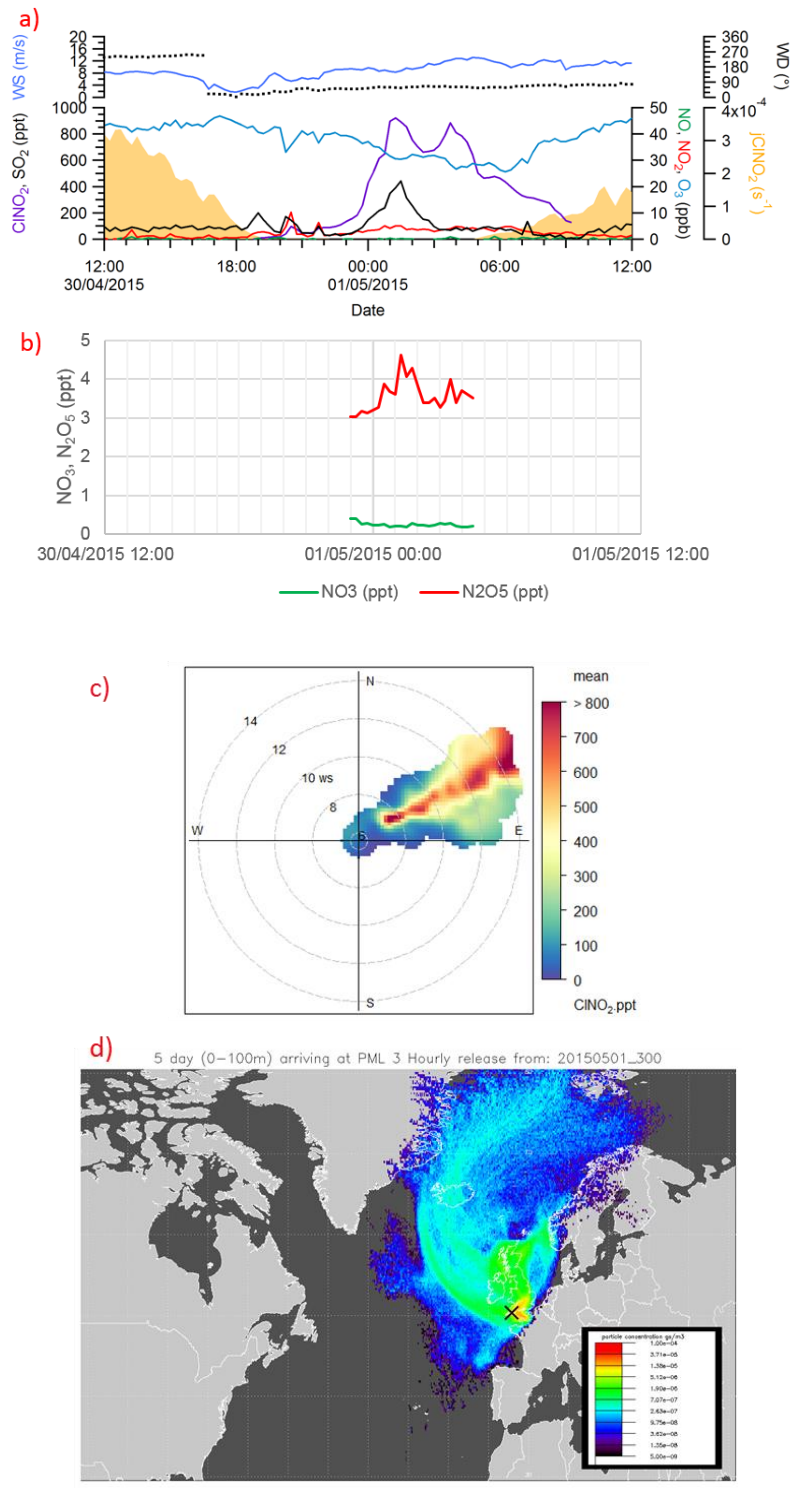


Figure 5.15 Plots for PPAO campaign highest ClNO<sub>2</sub> night, 30 Apr-01 May 2015.

- Time series showing wind speed/direction, ClNO<sub>2</sub> photolysis rate and concentrations of ClNO<sub>2</sub>, NO, NO<sub>2</sub>, O<sub>3</sub> and SO<sub>2</sub> (15 min averaged data).
- Time series showing NO<sub>3</sub> and N<sub>2</sub>O<sub>5</sub> (15 min averaged data, filtered).
- Polar plot for 30/04/15 21:00 to 01/05/15 09:59 (1 min averaged data; wind speed in ms<sup>-1</sup>).
- NAME particle dispersion footprint at 03:00 (5-day back).

In Figure 5.15a, NO<sub>2</sub> concentrations are shown to be slightly elevated and the O<sub>3</sub> slightly lowered for the period in which the very high ClNO<sub>2</sub> concentrations are observed. NO remains at approximately zero throughout, likely due to minimal emissions and rapid oxidation *via* the excess of O<sub>3</sub> present relative to NO<sub>x</sub>. Even for this high ClNO<sub>2</sub> event NO and NO<sub>2</sub> are very low and O<sub>3</sub> very high (generally ~0, <5 ppb and 25-45 ppb respectively) compared to UoL measurements, for example the AURN 2 high ClNO<sub>2</sub> event on 11-13 Feb 2016 (0-30, 10-50 and 5-30 ppb respectively - see Figure 4.18). There is also much less variability in these species' concentrations than at UoL (see section 4.6).

The available BBCEAS data for the relevant time period (Figure 5.15b) show detection of the ClNO<sub>2</sub> precursor N<sub>2</sub>O<sub>5</sub> concurrently with nitryl chloride, suggesting ideal conditions for ClNO<sub>2</sub> formation.

The polar plot (Figure 5.15c) indicates local wind directions bearing this ClNO<sub>2</sub> were 7-15 ms<sup>-1</sup> from the northeast (60°), along the English Channel and populated south coast of the UK, including the shipping lane and several cities (see Figure 5.1a in section 5.1.1).

The NAME particle dispersion model (Figure 5.15d) shows an orange patch where the air mass intercepted during the high ClNO<sub>2</sub> case resided for some time beforehand in two areas, one over the English Channel (including the shipping lane), and a second extending northeast towards Exeter (~60 km) and Bristol (170 km). London (315 km) is also on the border of this area. Relatively still air in the days prior to measurement like this on UoL campaign NAME footprints often resulted in high ClNO<sub>2</sub> concentrations, and is observed on several other days at PPAO but occurs mostly offshore preventing the accumulation and processing of urban pollution that would take place over land. The 7-15 ms<sup>-1</sup> wind speed corresponding to high ClNO<sub>2</sub> concentrations in the polar plot gives a range (assuming direct travel) of approx. 150-325 km in 6 hours, which would give ample time for pollution from any of the aforementioned cities (all of which lie in the approximate origin direction indicated by both local winds and the NAME model) to reach PPAO overnight, including by the beginning of the peak period (~01:00).

Two smaller, short-lived peaks were observed at approx. 20:45 and 22:00, in which  $\text{NO}_2$  rose and  $\text{O}_3$  dropped briefly (in the case of the 20:30 peak accompanied by a definite spike in  $\text{ClNO}_2$ ) without associated sudden changes in wind speed/direction, suggesting contributions from more local sources. In both small peaks and the initial rise in the main  $\text{ClNO}_2$  peak, an associated increase in sulphur dioxide,  $\text{SO}_2$ , was also observed.  $\text{SO}_2$  is often associated with dimethyl sulphide oxidation (most important over the remote ocean) or emissions from sulphur-rich heavy fuel oils often used by ships (Yang et al., 2016b). These smaller peaks shown in Figure 5.15a most likely correspond to aged pollution originating from shipping emissions coming in from the harbour, given the wind direction and associated  $\text{NO}_x/\text{O}_3$  observations. Associations between  $\text{ClNO}_2$  and shipping emissions are explored further in section 5.6.

$\text{NO}_2$  concentrations during the high (922 ppt)  $\text{ClNO}_2$  peak are relatively high and prolonged (>5 ppb throughout the peak) corresponding with an  $\text{O}_3$  depletion (minimum ~25 ppb, down from ~45 ppb daytime levels) indicative of prolonged chemical processing. In combination with a prolonged  $\text{SO}_2$  peak observed concurrently, it is likely that the high  $\text{ClNO}_2$  peak was derived from an amalgamation of local pollution from the harbour on top of aged pollution transported from other cities.

#### 5.4.3 WAO: Low $\text{ClNO}_2$

Weybourne observations were generally more similar to Leicester campaigns than Penlee Point.  $\text{ClNO}_2$  exceeded the limit of detection every night during the WAO campaign, with peak concentrations ranging from substantial (>100 ppt) on some nights to minimal (<10 ppt) on others. The increased concentration and variability of  $\text{NO}$  and  $\text{NO}_2$  at WAO compared to PPAO show that air masses sampled at the former were much less clean.

Unusually low (<20 ppt) nightly peak  $\text{ClNO}_2$  concentrations were observed on several nights at WAO including 24-25 July (Figure 5.16). In this case gentle ( $4 \text{ ms}^{-1}$ ) winds were generally incoming from the northeast at the start of the night and shifts slowly more north as the speed increases to  $>16 \text{ ms}^{-1}$ . Low concentrations were similarly observed for  $\text{NO}_x$  (<3 ppb) and  $\text{SO}_2$  (<20 ppt)

throughout the night, whereas  $O_3$  is relatively flat at 30-50 ppb and above the campaign nightly average (29 ppb). These observations are similar to the clean air mass (low  $NO_x$  &  $ClNO_2$ ) observations made at PPAO.

The NAME particle dispersion model shows an apparent period of stagnation for the 5 days prior to this night (24-25 July 2015) - as commonly happens on high- $ClNO_2$  nights - however this occurs offshore in the central/southwest section of the North Sea, preserving  $O_3$  while reducing acquisition of  $NO_x$  and related species.

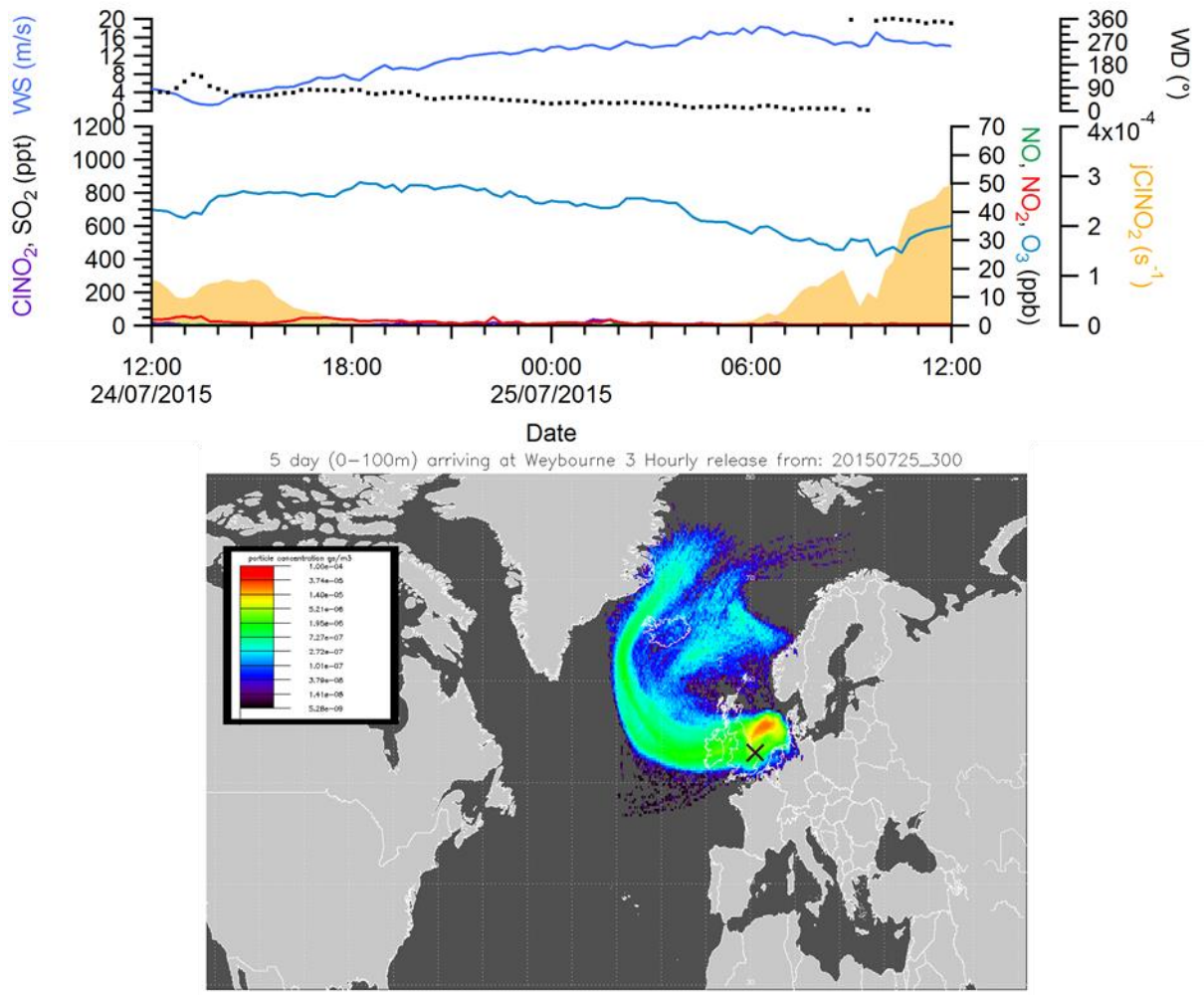


Figure 5.16 Plots for low  $ClNO_2$  night, 24-25 July 2015 during the WAO campaign. Top: time series showing wind speed/direction,  $ClNO_2$  photolysis rate and concentrations of  $ClNO_2$ ,  $NO$ ,  $NO_2$ ,  $O_3$  and  $SO_2$  (15 min averaged data). Bottom: NAME particle dispersion footprint at 03:00 (5-day back).

#### 5.4.4 WAO: High ClNO<sub>2</sub>

Similarly to PPAO, one unusually large peak of ClNO<sub>2</sub> stands out of the WAO dataset, in this case the night of 10-11 July 2015, reaching a maximum of 1104 ppt (15 min average). This was the highest concentration of ClNO<sub>2</sub> detected during all of the work in this thesis, well exceeding the 724 ppt observed during the ClearfLo campaign in London during summer 2012 (Bannan et al., 2015), although it not as high as some measurements made outside the UK, e.g. 3.6 ppb in Los Angeles during summer 2010 (Mielke et al., 2013) or the current highest recorded concentration of 4.7 ppb at a mountain site overlooking Hong Kong during winter 2012 (Wang et al., 2016).

Time series for the night of 10-11 July 2015 were generated (Figure 5.17a). This figure shows the highest ClNO<sub>2</sub> night for the Weybourne campaign. Similarly to the high ClNO<sub>2</sub> event during the PPAO campaign (see section 5.4.2), NO remains near-zero throughout and NO<sub>2</sub> rises during the night but remains <10 ppb. O<sub>3</sub> shows a smooth and typical diel profile, lower during the night and higher during the day (~35-65 ppb). These O<sub>3</sub> concentrations are extremely high (average during this 24-hour period is ~50 ppb, much greater than the campaign average 29 ppb), suggesting extensive photochemical production during the day of 10/07/15. SO<sub>2</sub> concentrations rise abruptly around 21:00 but stay level during the night, suggesting the site is intercepting a moderately polluted air mass throughout the night. SO<sub>2</sub> does not track with ClNO<sub>2</sub>, however, which is therefore unlikely to have any association with marine traffic in the same way as in PPAO (see section 5.4.2).

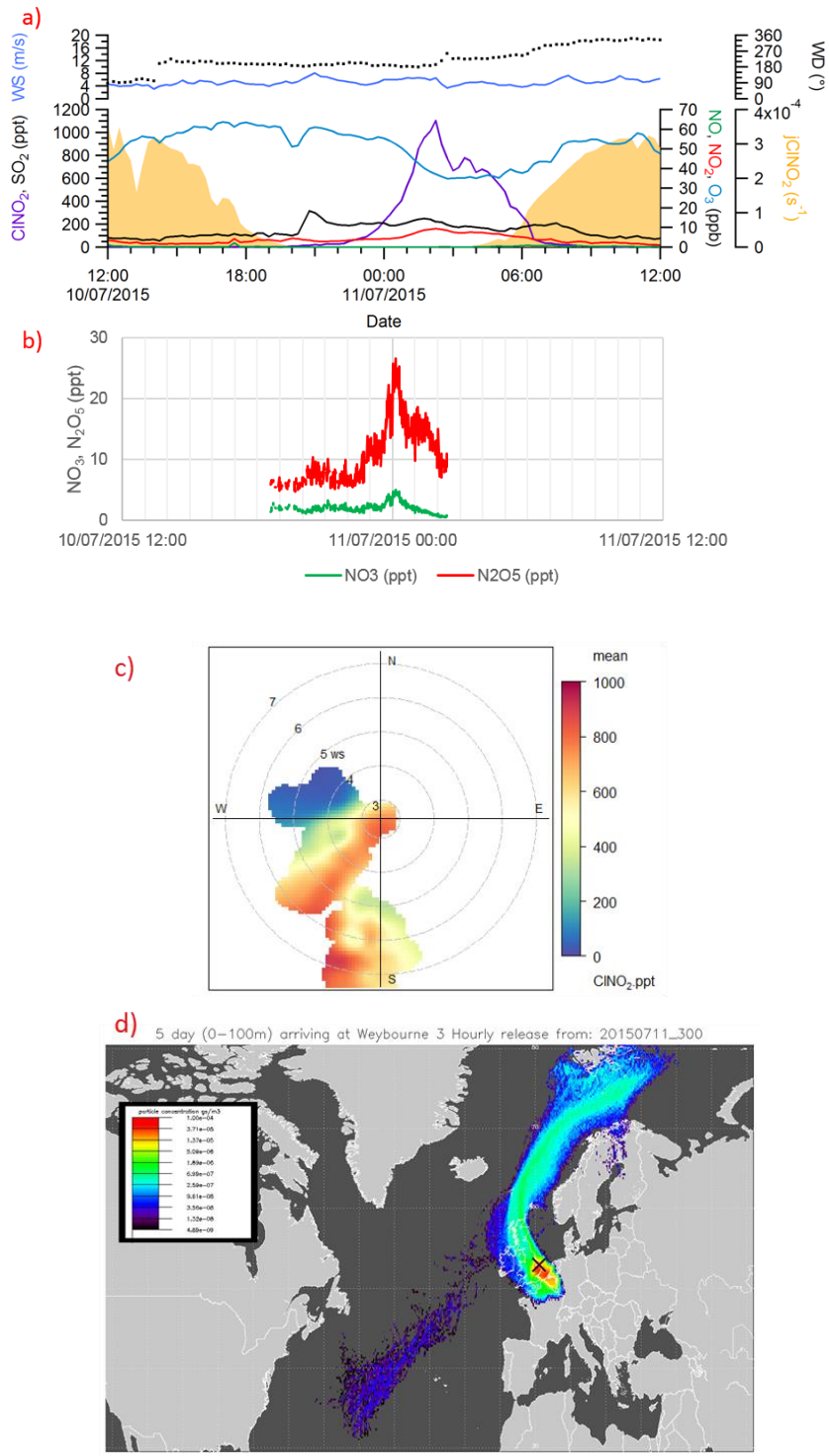


Figure 5.17 Plots for WAO campaign highest ClNO<sub>2</sub> night, 10-11 Jul 2015.

- Time series showing wind speed/direction, ClNO<sub>2</sub> photolysis rate and concentrations of ClNO<sub>2</sub>, NO, NO<sub>2</sub>, O<sub>3</sub> and SO<sub>2</sub> (15 min averaged data).
- Time series showing NO<sub>3</sub> and N<sub>2</sub>O<sub>5</sub> (15 min averaged data, filtered).
- Polar plot for 11/07/15 00:00 to 06:59 (1 min averaged data; wind speed in ms<sup>-1</sup>).
- NAME particle dispersion footprint at 03:00 (5-day back).

Figure 5.17b shows the available BBCEAS  $\text{NO}_3$  and  $\text{N}_2\text{O}_5$  data.  $\text{N}_2\text{O}_5$  concentrations are elevated during this night compared to others, peaking at ~31 ppt, but this  $\text{N}_2\text{O}_5$  peak occurs several hours before the  $\text{ClNO}_2$  maximum and actually declines as the latter rises.

The polar plot (Figure 5.17c) demonstrates that the  $\text{ClNO}_2$ -rich air arrived from the south and southwest, and  $\text{ClNO}_2$  was detected continuously as the wind speed varied from approx.  $3\text{-}8\text{ ms}^{-1}$ . The wind direction could feasibly correspond to an air mass arriving from London (180 km, approx. 6-16 hours) or Cambridge (105 km, 3-10 hours), therefore pollution produced from these cities during the day could be chemically ageing overnight to arrive at the site for the  $\text{ClNO}_2$  peak at ~02:30 (*i.e.* producing  $\text{ClNO}_2$  during the journey). The NAME footprint (Figure 5.17d) at 03:00 shows significant contribution from the area around these two cities but also offshore and towards Belgium, possibly indicating import of European pollution over several days. The time series shows  $\text{ClNO}_2$  beginning to fall well before daybreak, however this corresponds with a change in wind direction (shifting slowly northward), suggesting the pre-dawn reduction in  $\text{ClNO}_2$  is due to a difference in origins rather than a nocturnal loss process.

## 5.5 Air mass origins

The influence of several zones upon air masses for PPAO and WAO were analysed in the same way as for UoL campaigns described in section 4.7 (Dr. Z. L. Fleming; University of Leicester), enabling similar assessment of the origins of air masses arriving at PPAO and WAO. The same zones were used for PPAO as for UoL campaigns (Figure 4.22) but different zones (shown in Figure 5.18) were used for the WAO analysis.

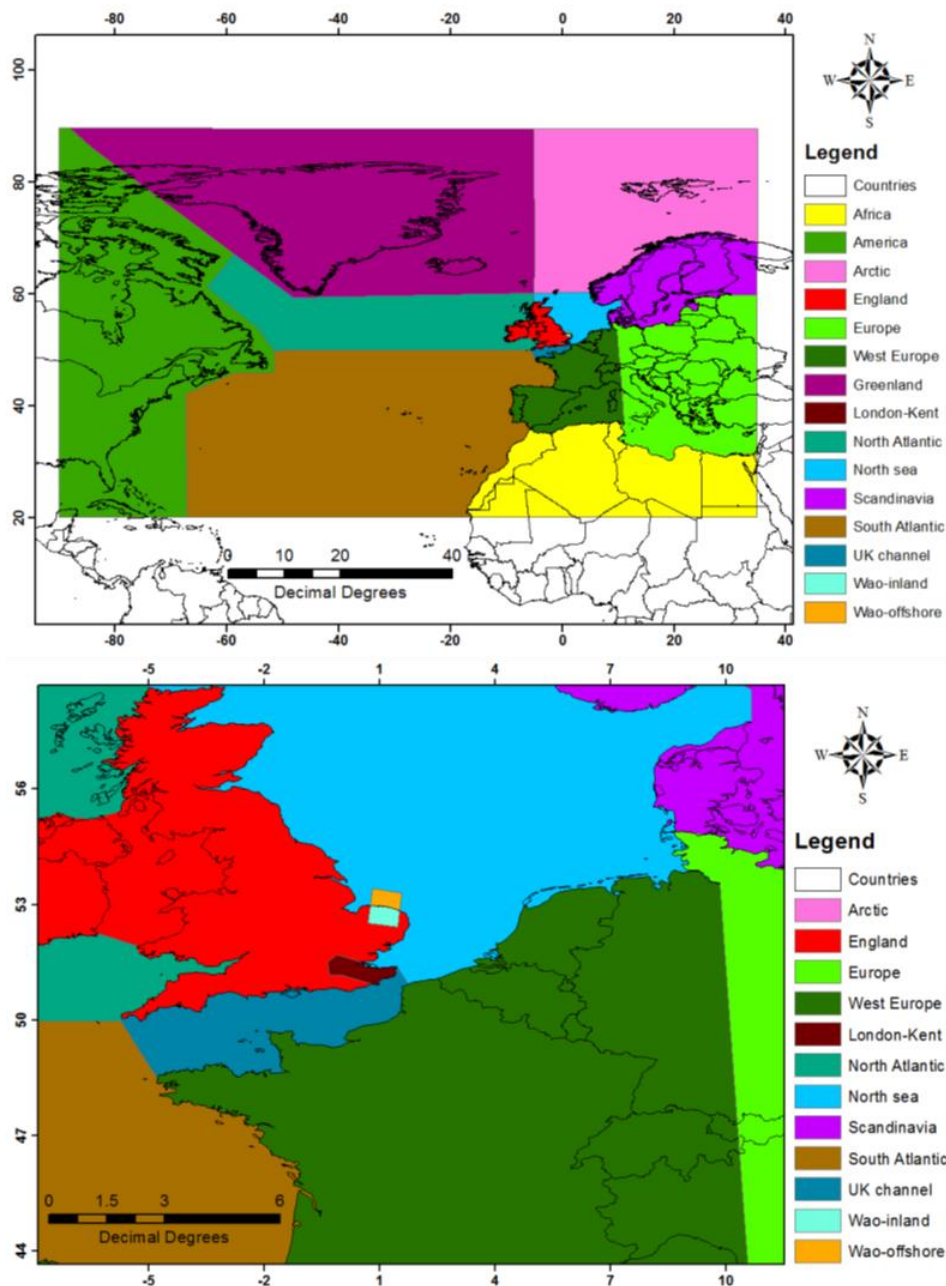


Figure 5.18 Map of air mass origin divisions for WAO campaign (Fleming, 2017). PPAO used the divisions shown in Figure 4.22.

ClNO<sub>2</sub> and NO<sub>2</sub> levels were plotted against the proportion of the air mass originating from each zone. Some of these zones showed a greater degree of correlation than others, which tended to be local areas. For PPAO, “local” areas were defined as England, France coast, Ireland, North France, Penlee shipping lane, PML and UK coast (see Figure 4.22), which were therefore combined in Figure 5.19 (top). The data points on the nitryl chloride plot (left) represent the high ClNO<sub>2</sub> event and correspond with the highest proportion of

local origin, indicating a possible correlation. The small number of data points make this a tentative connection, however. No correlation was observable in the PPAO NO<sub>2</sub> plot (right).

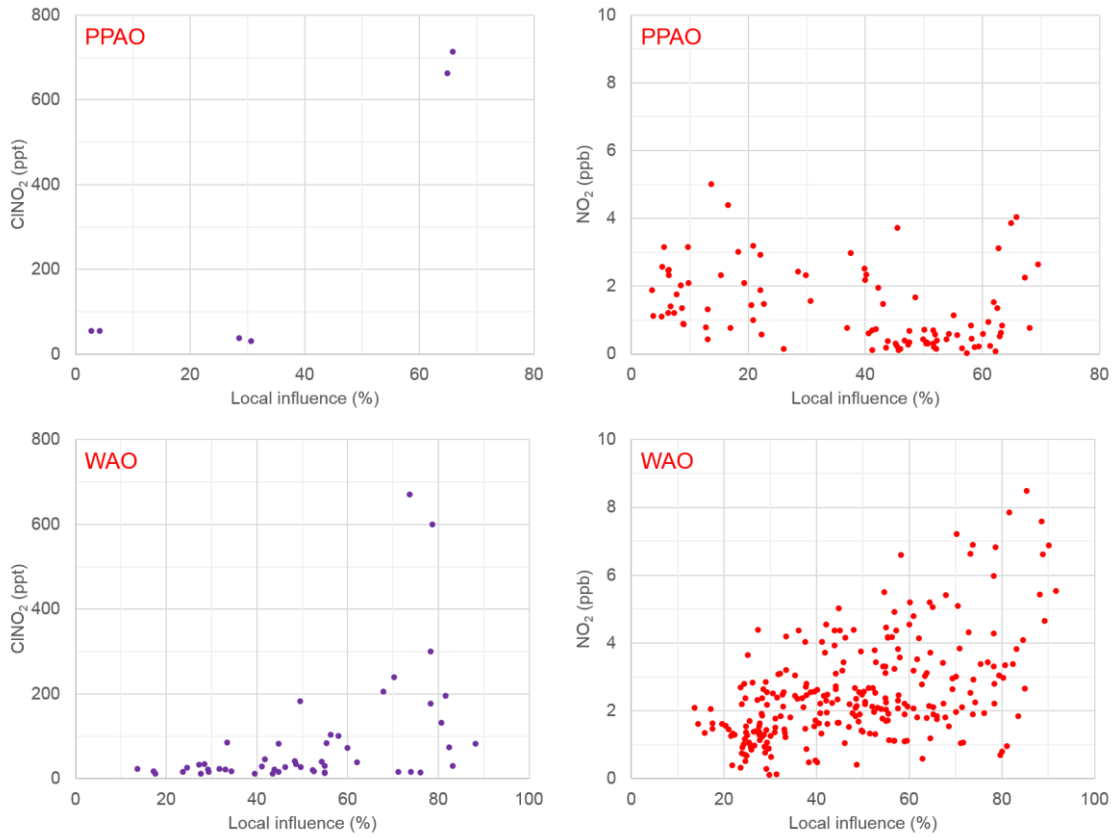


Figure 5.19 Correlation plots; top: PPAO campaign showing ClNO<sub>2</sub> and NO<sub>2</sub> concentrations against percentage of air mass originating from land-based sources; bottom: WAO campaign showing ClNO<sub>2</sub> concentration against percentage of air mass originating from local sources (3-hour averaged data, <10 ppt ClNO<sub>2</sub> filtered, 00:00-03:00 data only).

The local zones for Weybourne were England, Europe west, London & Kent, North Sea, UK channel, WAO inland and WAO offshore (see Figure 5.18). The correlations here are not simple lines - the campaign maximum ClNO<sub>2</sub> observations in the top right and an absence of points in the upper left of the WAO plots (Figure 5.19 (bottom)) suggests that the localness of air mass origins is correlated in that ClNO<sub>2</sub> and NO<sub>2</sub> tend to be observed less in air masses that have travelled long distances. The distribution of points in the bottom right, however, shows that other factors are involved. Owing to the smaller dataset, the PPAO ClNO<sub>2</sub> data resemble a less complete version of the WAO equivalent

so the factors affecting each site in this way may be the same, however the difference in correlation between “localness” and  $\text{NO}_2$  may suggest otherwise.

## 5.6 Emission plumes

### 5.6.1 PPAO

The location of Penlee Point atmospheric observatory close to shipping lanes has in the past enabled the study of shipping exhaust plumes (often characterised by a sharp spike in  $\text{SO}_2$ ,  $\text{CO}_2$  and/or  $\text{NO}_x$ , among others) originating both from cargo ships in the English Channel shipping lane and from naval vessels, passenger ferries and private vessels passing very close to the PPAO site as these vessels enter and leave the harbour in Plymouth (Yang et al., 2016b). The precursors of  $\text{ClNO}_2$  are, in theory, all available in a shipping plume. Sea spray provides abundant chloride, in addition to aerosol particles which are likely enhanced by particulates and  $\text{SO}_2$  (via  $\text{H}_2\text{SO}_4$ ) emitted in shipping plumes. Furthermore  $\text{NO}_x$ , generally the limiting factor for  $\text{ClNO}_2$  formation during the PPAO campaign (discussed later in section 5.7.2), is also a component of the emissions and  $\text{O}_3$ , which is likely to be depleted by oxidation of the fresh emissions (*i.e.*  $\text{NO}$  to  $\text{NO}_2$ ,  $\text{NO}_2$  to  $\text{NO}_3$ ), is generally quite plentiful over the sea. High-resolution (1-2 minute) time series were therefore examined for PPAO (Figure 5.20) to examine what, if any, exhaust plumes are observed and whether  $\text{ClNO}_2$  is appreciably enhanced within them.

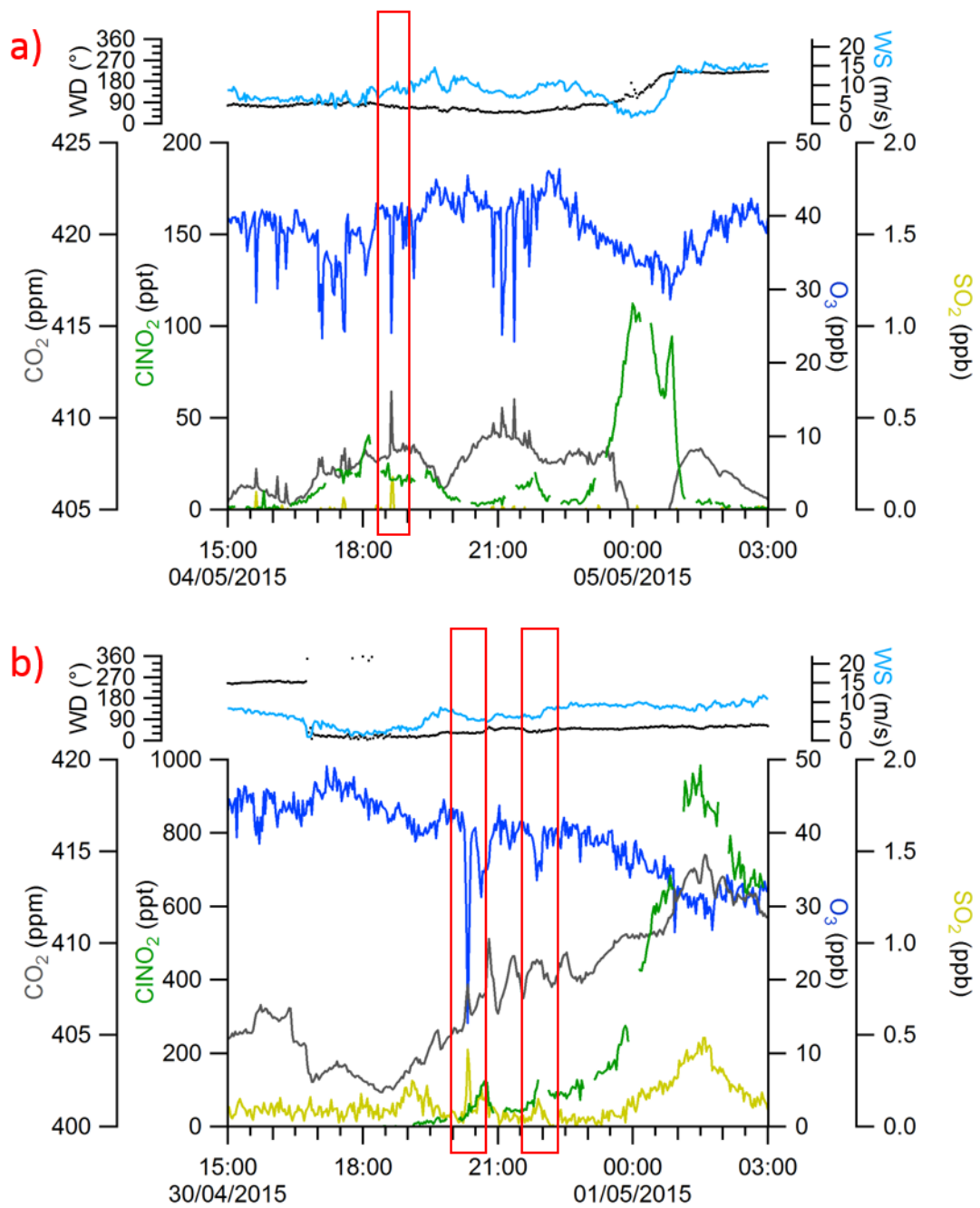


Figure 5.20 Time series for PPAO campaign showing concentrations of ClNO<sub>2</sub>, CO<sub>2</sub>, SO<sub>2</sub> and O<sub>3</sub> in addition to wind direction and speed (1 min averaged data). Note different vertical axis scales.

Several plumes are apparent during the PPAO campaign, represented by very narrow spikes of SO<sub>2</sub>, CO<sub>2</sub> and O<sub>3</sub> with durations of a few minutes or less indicative of vessels passing within 0-2 km of the site *via* Plymouth Sound rather than *via* the more distant English Channel shipping lane (Yang et al., 2016b). Only a few of these plumes occur at times when ClNO<sub>2</sub> was observed, partially

because of the remarkably clean air generally observed during the campaign (see section 5.4.1) but also because fewer vessels are active during the night when ClNO<sub>2</sub> is able to form.

Figure 5.20a shows a time series including an apparent shipping plume at ~18:45 on 04/05/15. At this time there is a sharp upward peak in SO<sub>2</sub> and CO<sub>2</sub>, and a corresponding sharp dip in O<sub>3</sub>, due to combustion of heavy fuel oil and partial titration of O<sub>3</sub> by co-emitted NO (Yang et al., 2016b). Even during the plume O<sub>3</sub> only dips to ~18 ppb. This concentration of ozone matches or exceeds typical levels observed at UoL (in which ClNO<sub>2</sub> was forming), and suggests these levels are sufficient for oxidation of NO to generate NO<sub>3</sub> (and prevent titration thereof) required for N<sub>2</sub>O<sub>5</sub> formation, however ClNO<sub>2</sub> does not seem to be affected by this plume. The hypothesis of the plumes coming from nearby ships is strengthened by the wind direction being from the east/northeast (corresponding to the Plymouth Sound). In Figure 5.20b the plume at ~20:15 on 30/04/15 shows these fresh plumes are distinct from both broader harbour pollution peaks (e.g. 22:00) discussed in section 5.4.2 and the aged plumes discussed in section 5.6.2 below.

### 5.6.2 WAO

Emission plumes are also visible in the data from Weybourne, but these are dissimilar to the ones observed at PPAO. Examples of plumes from two different nights are shown in Figure 5.21. On both nights, spikes in NO<sub>2</sub> are observed coinciding with ozone depletion, on 09/07/15 just before and just after 00:00 (Figure 5.21a) and on 22/07/15 ~21:15 (Figure 5.21b). On neither night do these plumes have an accompanying feature in SO<sub>2</sub> or, on 09/07/15, in CO<sub>2</sub> either (the 22/07/15 peak occurs during a gap in CO<sub>2</sub> data). Despite the lack of CO<sub>2</sub> and SO<sub>2</sub> features, the abrupt rise and fall of NO<sub>2</sub> despite steady wind conditions suggest that these features are due to emission plumes. The wind from northerly directions indicates that the plumes approach from the sea and may well correspond to vessels passing *via* the shipping lane, which at ~5 ms<sup>-1</sup> wind speed would take ~85 minutes to reach the site.

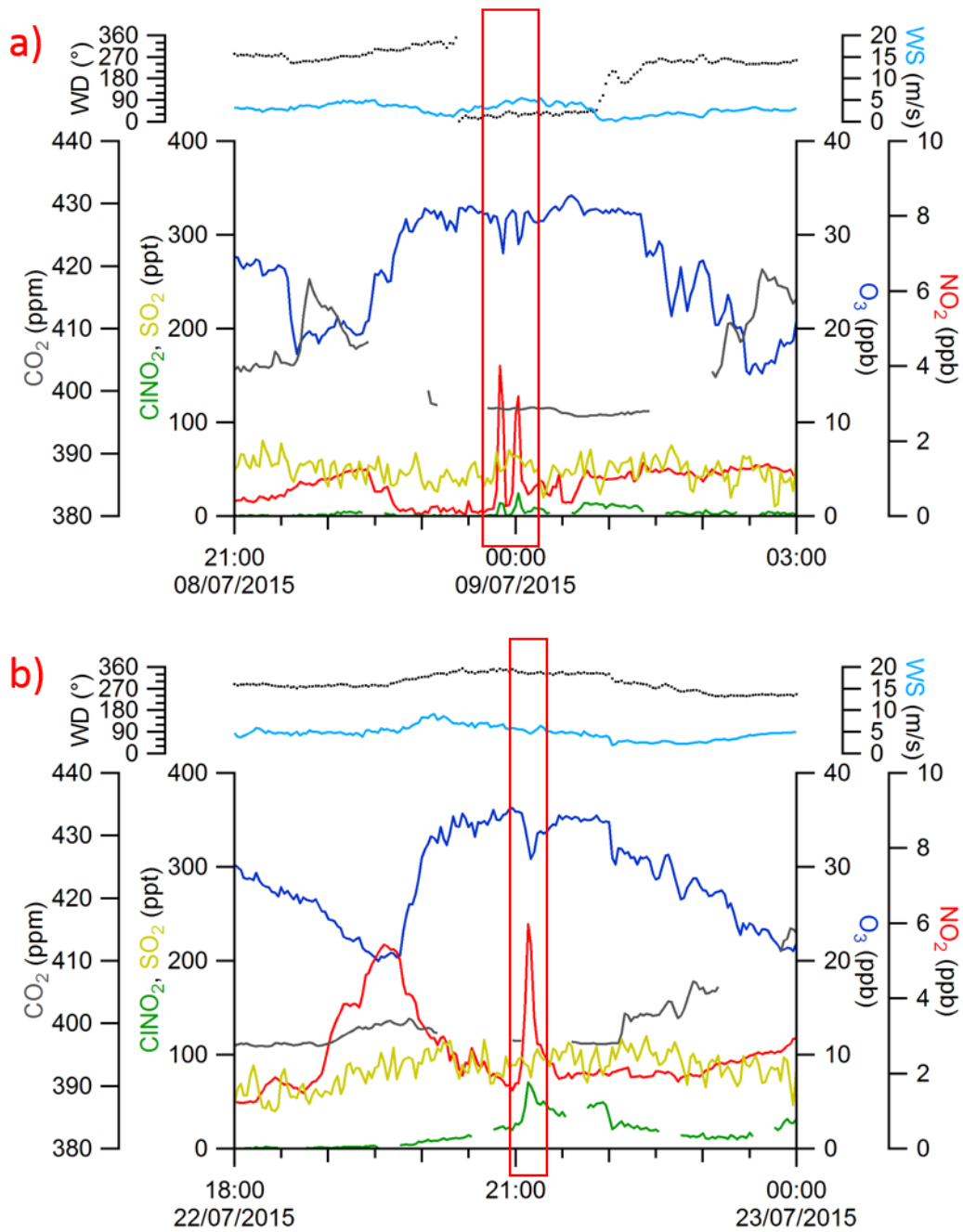


Figure 5.21 Time series for WAO campaign showing concentrations of CINO<sub>2</sub>, SO<sub>2</sub>, CO<sub>2</sub>, NO<sub>2</sub> and O<sub>3</sub> in addition to wind direction and speed (2 min averaged data).

Interestingly, CINO<sub>2</sub> also rises noticeably during the plumes observed at WAO. The peaks are broader than those observed at PPAO, and the ozone depletion seems to be less pronounced, suggesting that these may be aged plumes that have been diluted during travel (Yang et al., 2016b). The lack of response in CINO<sub>2</sub> concentrations in the fresh plumes and presence thereof in more aged

emissions suggests that ClNO<sub>2</sub> formation occurs relatively slowly, longer than it took for the 04/05/15 plume to reach PPAO (<10 minutes from centre of Plymouth Sound) however ClNO<sub>2</sub> may be present in emissions still distinguishable as plumes if more time is permitted such as the 09/07/15 plumes (~85 minutes from shipping lane to WAO), possibly due to N<sub>2</sub>O<sub>5</sub> formation being suppressed *via* titration of NO<sub>3</sub> by freshly issued NO, in addition to NO<sub>3</sub> formation from NO<sub>2</sub> and O<sub>3</sub> being fairly slow (Daniels, 2012).

## 5.7 Limiting factors for ClNO<sub>2</sub> formation

### 5.7.1 Aerosol data and aerosol chloride availability

Data regarding aerosol composition were measured using PM<sub>10</sub> (particulate matter, 10 µm and larger) filters during the 2014 UoL campaigns and multistage high-volume impactor during the WAO campaign (see section 2.4.3).

Figure 5.22a shows a correlation plot of 24-hour concentrations of particulate sodium vs. chloride with the average seawater ratio shown by the red line. Aerosol Na and Cl data correlate well, with R<sup>2</sup> of 0.81 (UoL) and 0.99 (WAO), suggesting that sea salt is the aerosol chloride source for both sites (Sommariva et al., 2018). The gradient in this plot (*i.e.* Cl/Na mass ratios) for WAO (1.88) is very close to the expected seawater mass ratio, 1.8 (Stumm and Morgan, 1995) whereas the UoL ratio was lower (1.32) due to dechlorination as air masses age during transport from the ocean source.

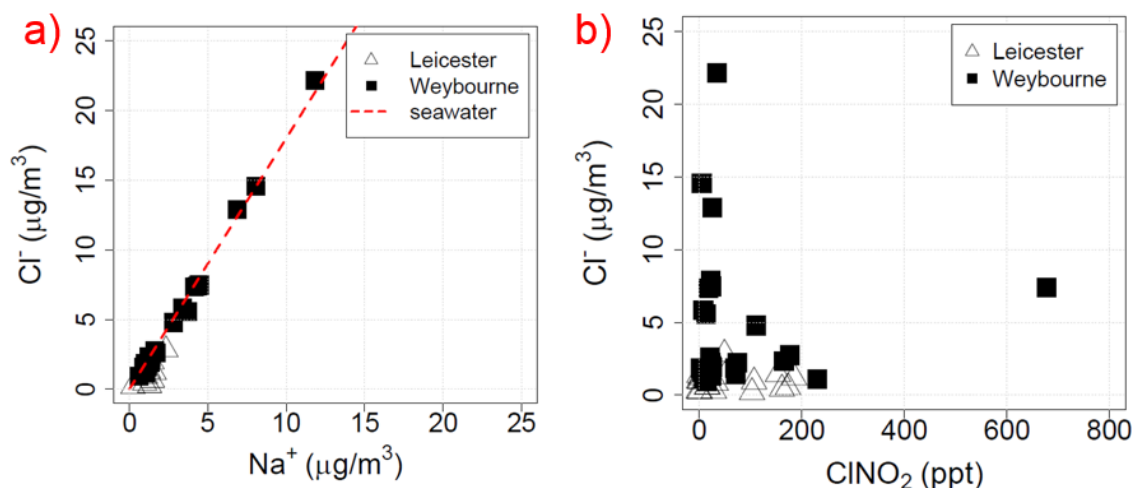


Figure 5.22 Particulate chloride and sodium data for UoL and WAO campaigns (24 hour averaged data;  $\text{ClNO}_2$  data 00:00-04:00 GMT only). Figure reprinted from Sommariva et al., 2018.

- Median nightly particulate  $\text{Cl}^-$  and  $\text{Na}^+$ , with mean seawater ratio (red line).
- Correlation plot of nightly maximum  $\text{ClNO}_2$  vs. aerosol chloride concentration.

Nightly aerosol chloride data were also correlated with  $\text{ClNO}_2$  concentration maxima (Figure 5.22b) to examine whether chloride was the controlling factor in nitryl chloride production. No correlation was visible for either site, indicating that  $\text{ClNO}_2$  production was not limited by aerosol chloride abundance at either of these sites.

The lack of chloride limitation of  $\text{ClNO}_2$  production suggests that sea salt chloride is likely to be fairly ubiquitous in the UK, as the UoL site is roughly in the centre of the country (approx. ~200 km from the sea; see section 4.1.2). This is perhaps unsurprising given the findings of Vester et al., 2007, in which aerosol chloride attributed to aged sea salt was observed >350 km from the sea in Germany, but still warrants further study to confirm.

### 5.7.2 Gas phase precursors

The aerosol measurements taken in Leicester and Weybourne (see section 5.7.1) suggest that aerosol chloride is available at most locations throughout the UK in sufficient quantities that it does not restrict ClNO<sub>2</sub> formation even for inland locations. The gas-phase precursors (ozone and NO<sub>x</sub>) must therefore be the limiting factor(s), which was investigated using correlations between these two species for spring and summer data from the PPAO and WAO coastal campaigns and the UoL comparators RAFT 1 and AURN 1. In Figure 5.23a, the data points are coloured by location/season, and in Figure 5.23b by measured ClNO<sub>2</sub> concentration.

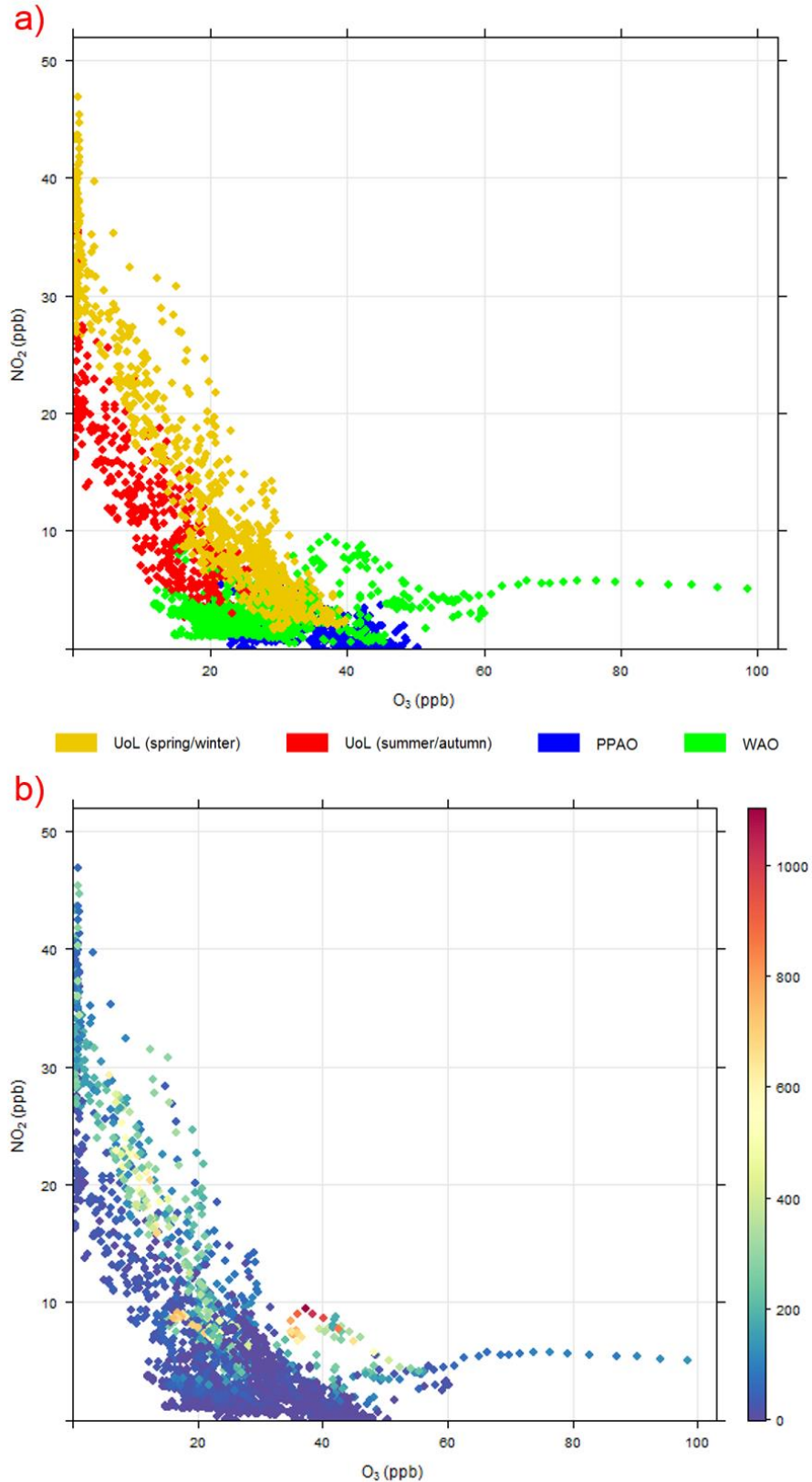


Figure 5.23 Scatter plots showing concentrations of nitrogen dioxide against ozone (15 min averaged data, 23:00 to 04:59 only). Figures adapted from Sommariva et al., 2018.

- a) Data points coloured by campaign.
- b) Data points coloured by ClNO<sub>2</sub> concentration.

Figure 5.23a shows that the majority of points corresponding to the coastal campaigns are clustered at the lower end of the NO<sub>2</sub> scale (0-5 ppb) but vary from approx. 15-50 ppb O<sub>3</sub>, whereas much of the UoL data are distributed along the y axis with low O<sub>3</sub> (0-5 ppb) but approx. 15-50 ppb NO<sub>2</sub>.

Most of the higher ClNO<sub>2</sub> observations can be seen in the more central areas of in Figure 5.23b, for example the highest observation (WAO 10-11 July 2015, ~1.1 ppb; dark red point) is considerably distant from both axes at approx. 38 ppb O<sub>3</sub> and 10 ppb NO<sub>2</sub>. Also, some of the higher ClNO<sub>2</sub> measurements from the spring and winter UoL campaigns (400-600 ppt) are clustered around 20 ppb NO<sub>2</sub> and 15 ppb O<sub>3</sub>. These data show two distinct cases of ClNO<sub>2</sub> limitation in the UK based on restricted formation of its N<sub>2</sub>O<sub>5</sub> precursor (see section 1.2.4).

In one case formation is limited by ozone (*e.g.* at UoL), represented in the upper left of the plots in Figure 5.23, with NO<sub>x</sub> available but mostly remaining in the form of NO and NO<sub>2</sub> formation as insufficient O<sub>3</sub> is available to consistently oxidise NO to NO<sub>2</sub> and then NO<sub>3</sub> (see section 1.2.2). Furthermore NO<sub>3</sub> will be titrated back to NO<sub>2</sub> in the presence of NO. The scarcity of NO<sub>3</sub> resulting from low-ozone conditions therefore diminishes formation of N<sub>2</sub>O<sub>5</sub> (and, therefore, ClNO<sub>2</sub>).

In the other case ClNO<sub>2</sub> formation is limited by NO<sub>x</sub> (*e.g.* during the Penlee Point and Weybourne campaigns), represented in the lower right of the plots in Figure 5.23. Under these conditions oxidation is easily achieved *via* plentiful O<sub>3</sub> but there is not much NO<sub>x</sub> oxidise, similarly preventing N<sub>2</sub>O<sub>5</sub> formation.

ClNO<sub>2</sub> therefore forms preferentially in the zone near the centre of the plots in Figure 5.23, representing situations in which both NO<sub>2</sub> and O<sub>3</sub> are readily available. These regimes limiting ClNO<sub>2</sub> concentration arise owing to the restriction of NO<sub>3</sub> (and thus N<sub>2</sub>O<sub>5</sub>) formation, as this is the rate limiting step (Sommariva et al., 2018), requiring both NO<sub>2</sub> and O<sub>3</sub>.

## 5.8 Model comparison: observations vs. GEOS-Chem model

For comparison of the different measurement sites, project collaborators (Dr. T. Sherwen and Dr. M. J. Evans; University of York) ran a modified GEOS-Chem model similar to the medium-resolution model discussed in section 4.8 (see also section 2.5) at the higher resolution of  $0.25^{\circ} \times 0.3125^{\circ}$  for the RAFT 1, AURN 1, PPAO and WAO campaigns.

Average observed and high-resolution modelled diel profiles shown in Figure 5.24 demonstrate significantly improved agreement than the medium-resolution equivalent. The shape of the profile matches fairly accurately in all cases, however the model prominently overestimates  $\text{ClNO}_2$  for both UoL campaigns (peak  $\text{ClNO}_2$  approx. 200 vs. 125 ppt for RAFT 1, 50 vs. 20 ppt for AURN 1) similarly to the medium-resolution UoL model (section 4.8) but to a lesser degree.

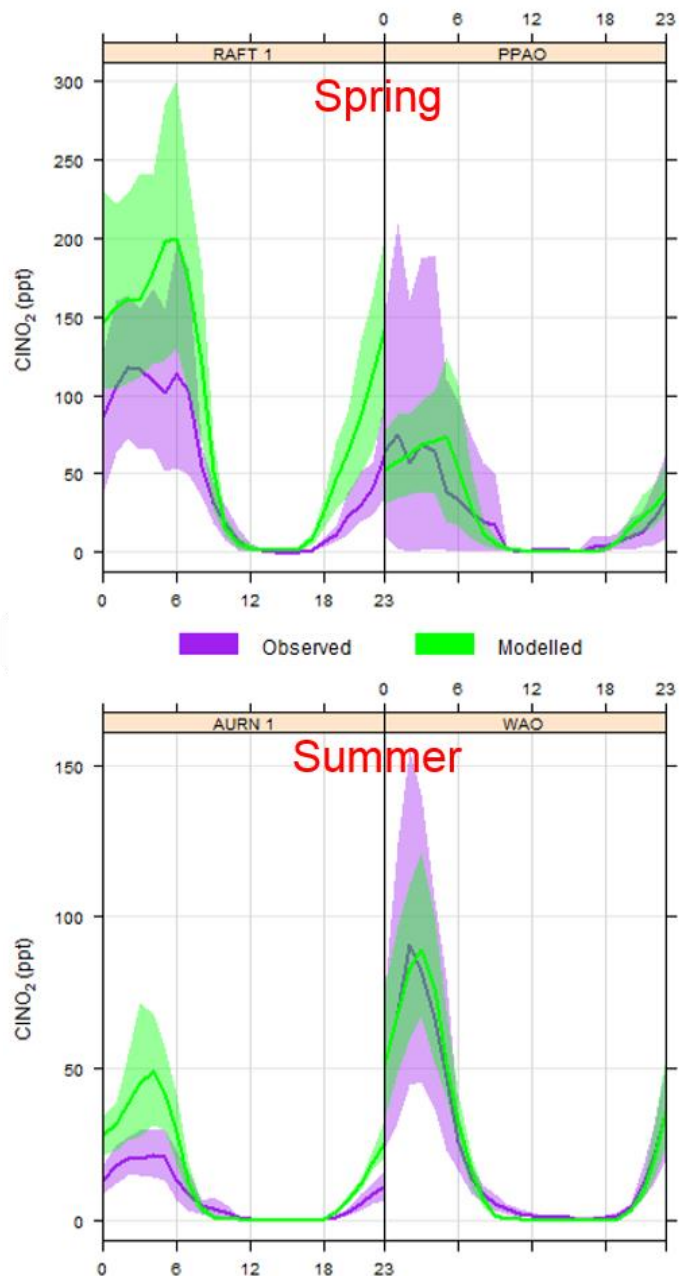


Figure 5.24 Comparison of observed and modelled  $\text{ClNO}_2$  average diel profiles during campaign periods for PPAO, WAO and seasonally equivalent UoL campaigns (60 min averaged data; mean and 95% confidence intervals; high-resolution model).

Figure 5.25 shows the model agreeing very well with observations in that  $\text{ClNO}_2$  was present on most nights at UoL and WAO and absent on many nights at PPAO, strengthening the suggestion that the model is greatly improved at this higher resolution. For the RAFT 1 campaign the  $\text{ClNO}_2$  maxima are broadly in agreement, with some of the disagreement being where the observed  $\text{ClNO}_2$  plateaus early. For example a simple smooth peak is predicted on the night of

03-04 Mar 2014 but the observed ClNO<sub>2</sub> has a more complex shape, rising and falling slightly over the course of the night suggesting that the observed peak may have been higher (*i.e.* agreeing better with the model) if not for changes in air mass sampled due to variable wind conditions. The AURN 1 high-res model output is a less dramatic improvement over the medium-res model, with ClNO<sub>2</sub> occasionally predicted accurately but more often noticeably over- or under-reported. The medium-resolution model over-reported by a factor of 2 or more on most nights for this campaign but the high-resolution model under-reports as often as over-reports, and generally does either by a much smaller margin.

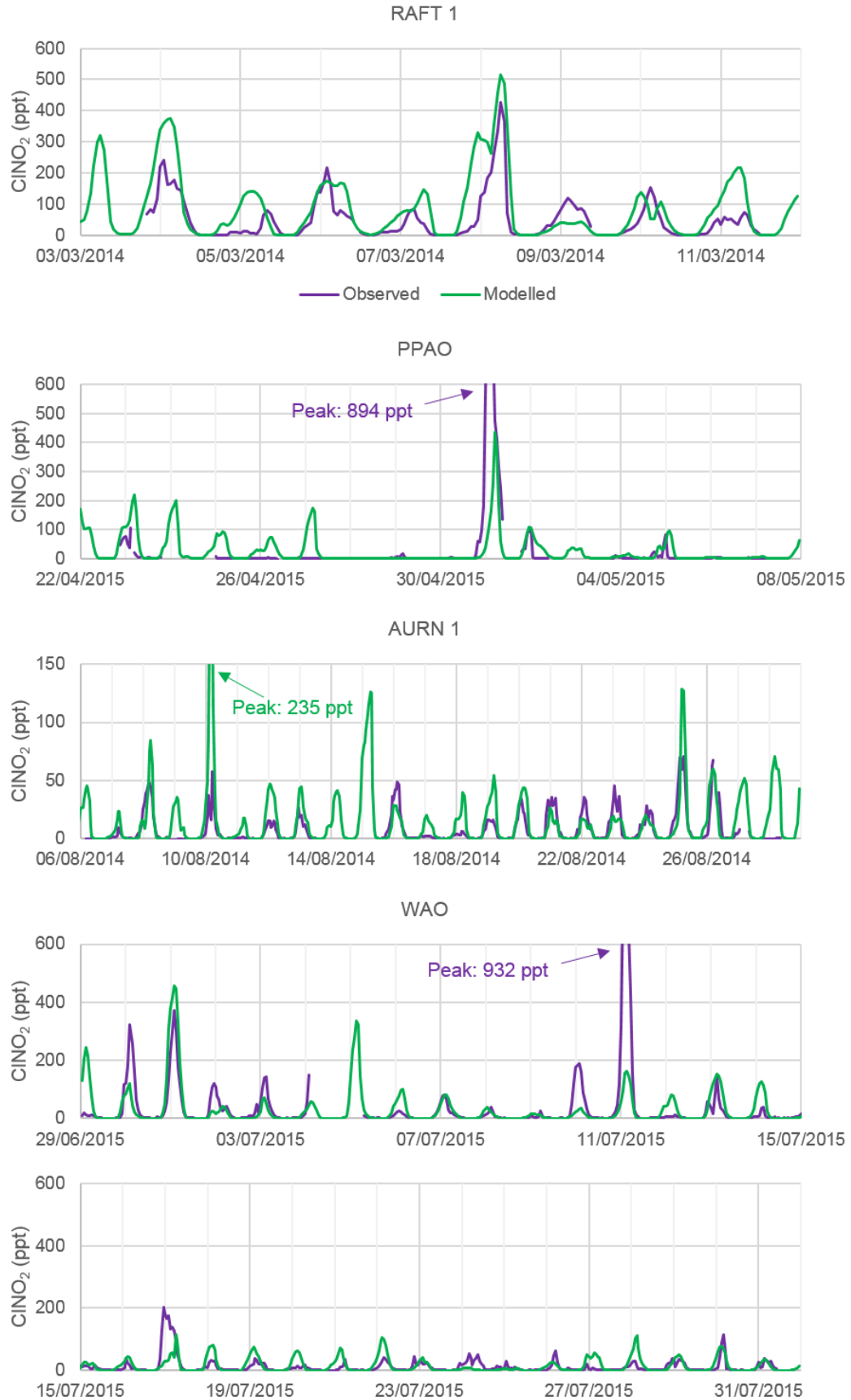


Figure 5.25 Time series comparing observed and modelled  $\text{ClNO}_2$  concentrations for PPAO, WAO and seasonally equivalent UoL campaigns (60 min averaged data; high-resolution model).

The model for PPAO campaign correctly predicts that the campaign maximum ClNO<sub>2</sub> concentration occurs on 30 Apr-01 May 2015, but under-reports the peak ClNO<sub>2</sub> amount by a factor of 2. At other times ClNO<sub>2</sub> was predicted at PPAO on nights where none was observed. The end effect is an average diel profile that “coincidentally” matches one made from observed values, as happened with the winter UoL campaigns in the medium-resolution model (see section 4.8). The model PPAO high-res model is, however, much closer overall in the shape and magnitude of ClNO<sub>2</sub> peaks.

The WAO model generally predicts with reasonable accuracy nights when ClNO<sub>2</sub> is present but quite low (20-200 ppt peaks), for example 15-31 July 2015. The first half of the campaign also matches quite well in places, for example 01-02 and 13-14 July, but the campaign maximum is even more dramatically under-reported by the model (120 vs. 922 ppt).

Factors limiting ClNO<sub>2</sub> formation were examined to investigate the differences between modelled and observed nitryl chloride using correlations between mean nightly ClNO<sub>2</sub> and NO<sub>2</sub> concentrations, and between ClNO<sub>2</sub> and accumulation-mode sea salt aerosol (where data are available for the latter) for the PPAO, WAO and from their seasonal comparator UoL campaigns (RAFT 1 and AURN 1 respectively).

It is not expected for sea salt (*i.e.* chloride) availability to be limiting ClNO<sub>2</sub> production at UoL, PPAO or WAO (see section 5.7.1). Figure 5.26a shows the correlation plot between high-resolution modelled sea salt aerosol and ClNO<sub>2</sub> concentration for the UoL RAFT 1 and AURN 1 campaigns. The model correctly shows no correlation for AURN 1 campaign, and likewise for both PPAO and WAO in Figure 5.26b ( $R^2 < 0.16$ ). The model does, however, show a correlation for the RAFT 1 campaign suggesting sea salt sometimes limits model ClNO<sub>2</sub>. This correlation is weak ( $R^2 = 0.27$ ), therefore sea salt limitation is unlikely to be the only cause for the difference in modelled and observed ClNO<sub>2</sub>, especially given the lack of similar correlation for the AURN 1 campaign.

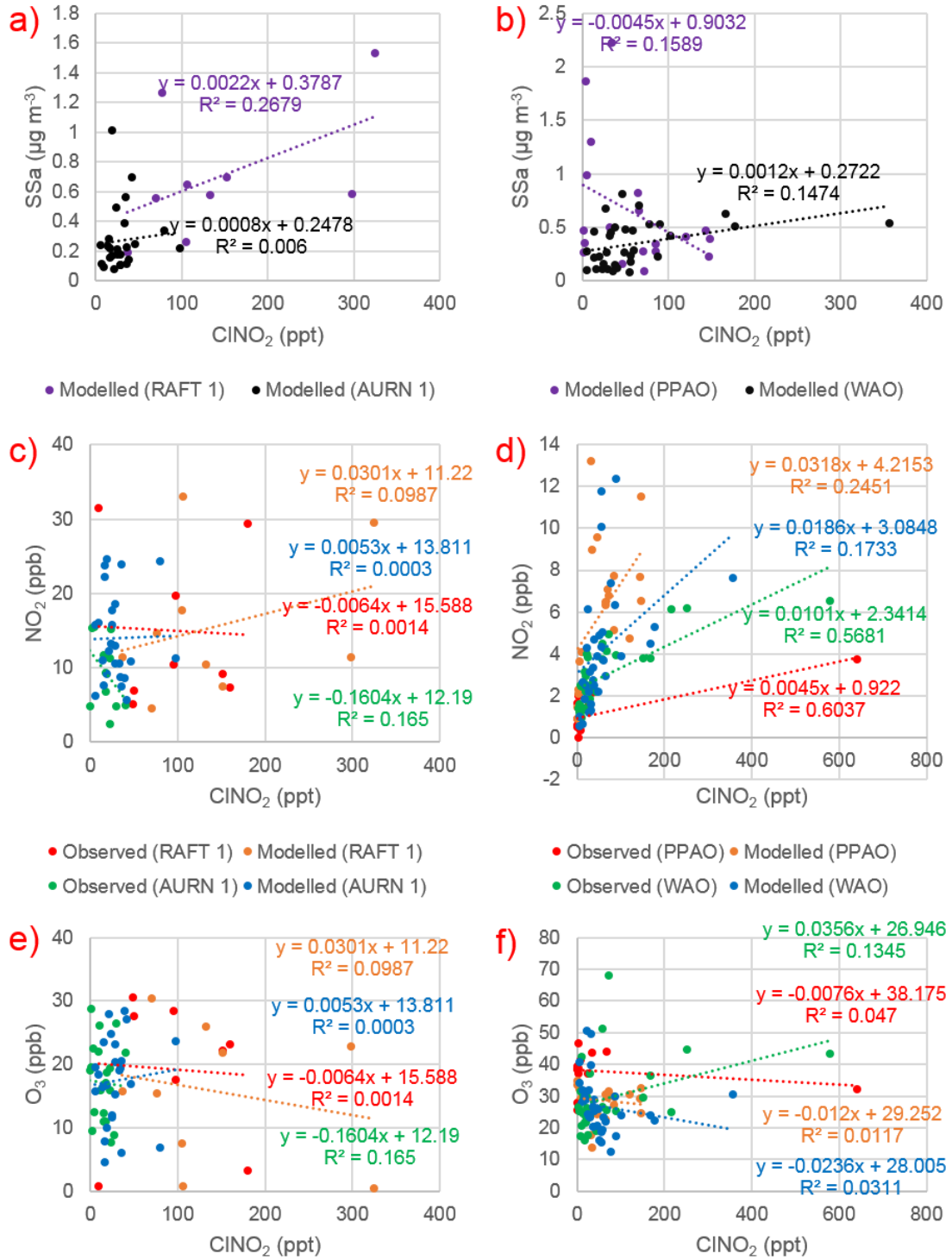


Figure 5.26 Correlations of nightly (23:00-04:59) mean CINO<sub>2</sub> concentrations with observed and high-resolution modelled accumulation mode sea salt aerosol and NO<sub>2</sub>.

- Sea salt aerosol vs. CINO<sub>2</sub> for UoL (a) and coastal (b) campaigns.
- NO<sub>2</sub> vs. CINO<sub>2</sub> for UoL (c) and coastal (d) campaigns.
- O<sub>3</sub> vs. CINO<sub>2</sub> for UoL (e) and coastal (f) campaigns.

Figure 5.26c shows correlation plots between ClNO<sub>2</sub> and NO<sub>2</sub> for both observed and model data during the UoL RAFT 1 and AURN 1 campaigns. No significant correlations are present ( $R^2 < 0.17$ ) for modelled and observational data alike, indicating the model correctly predicts that NO<sub>2</sub> does not limit ClNO<sub>2</sub> production at UoL.

Contrariwise, observational data showed that NO<sub>x</sub> availability was often the controlling factor for the PPAO and WAO campaigns, as is reflected by the correlation between observed ClNO<sub>2</sub> and NO<sub>2</sub> in Figure 5.26d ( $R^2 = 0.60$  for PPAO and  $0.57$  for WAO). The modelled data shows a weak correlation for PPAO ( $R^2 = 0.25$ ) and none for WAO ( $R^2 = 0.17$ ), indicating that the model fails to adequately predict the NO<sub>x</sub>-limitation of ClNO<sub>2</sub> production at these coastal sites. Similar correlation plots between ClNO<sub>2</sub> and O<sub>3</sub> (Figure 5.26e and Figure 5.26f) are inconclusive, however, as these show no significant correlation at any site using modelled or observed data ( $R^2 < 0.17$ ).

Figure 5.27a is similar to the NO<sub>2</sub>/O<sub>3</sub> scatter plots (Figure 5.23) in section 5.7.2, this time using 60-minute data and compared with model data. Note that the UoL summer/autumn campaigns (red) show significantly more ozone in the model compared to observed data. This overprediction of O<sub>3</sub> would explain the concomitant overprediction of ClNO<sub>2</sub>, given the prior conclusion of O<sub>3</sub>-limitation of nitryl chloride production at UoL. Note also in this figure the distribution of NO<sub>2</sub> points at PPAO (*i.e.* NO<sub>x</sub>-limited regime) at 0-20 ppb in the model but generally 0-5 ppb in observed data, which explains the prediction of ClNO<sub>2</sub> more frequently than was actually observed (a similar effect is visible for WAO, albeit less pronounced).

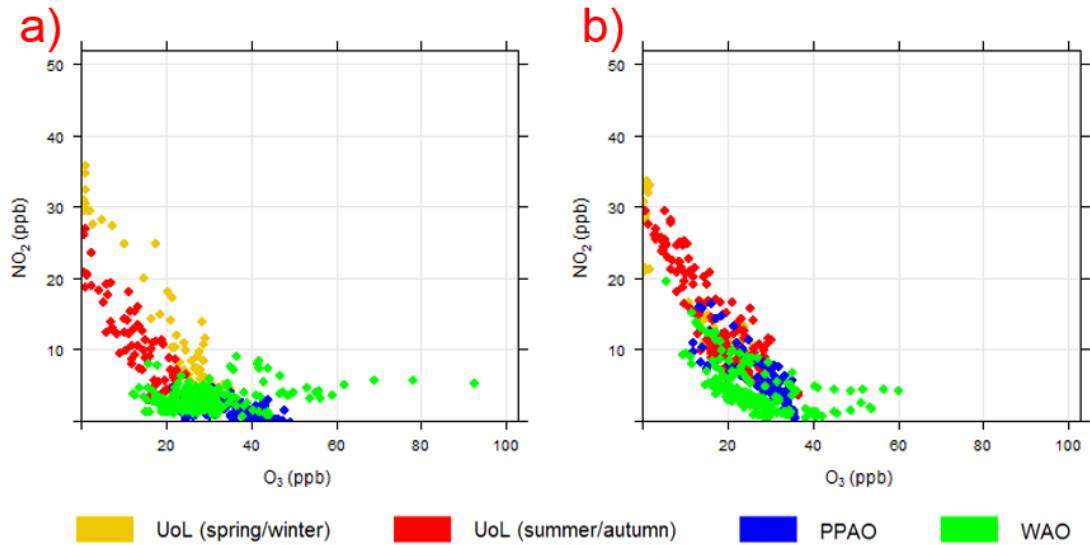


Figure 5.27 Scatter plots showing a) observed and b) modelled concentrations of nitrogen dioxide against ozone (60 min averaged data, 23:00 to 04:59 only).

### 5.9 NO<sub>2</sub> measurements and intercomparison

Among the instruments operated by the University of Leicester team at Weybourne was a BBCEAS operating in blue wavelengths (430-485 nm) to detect NO<sub>2</sub> (see section 2.3.5). A complete time series of the WAO NO<sub>2</sub> measurements is shown in Figure 5.28. The blue BBCEAS instrument ran from 01-31 July, with gaps of approx. 1 hour each morning for calibrations. Several other gaps exist in this data set - firstly some data were excluded from 01-02 and 06-07 July because of instrument issues; secondly on 04-05 July due to power loss; and thirdly the afternoons of 16 and 17 July as the instrument was in use for CIMS calibrations.

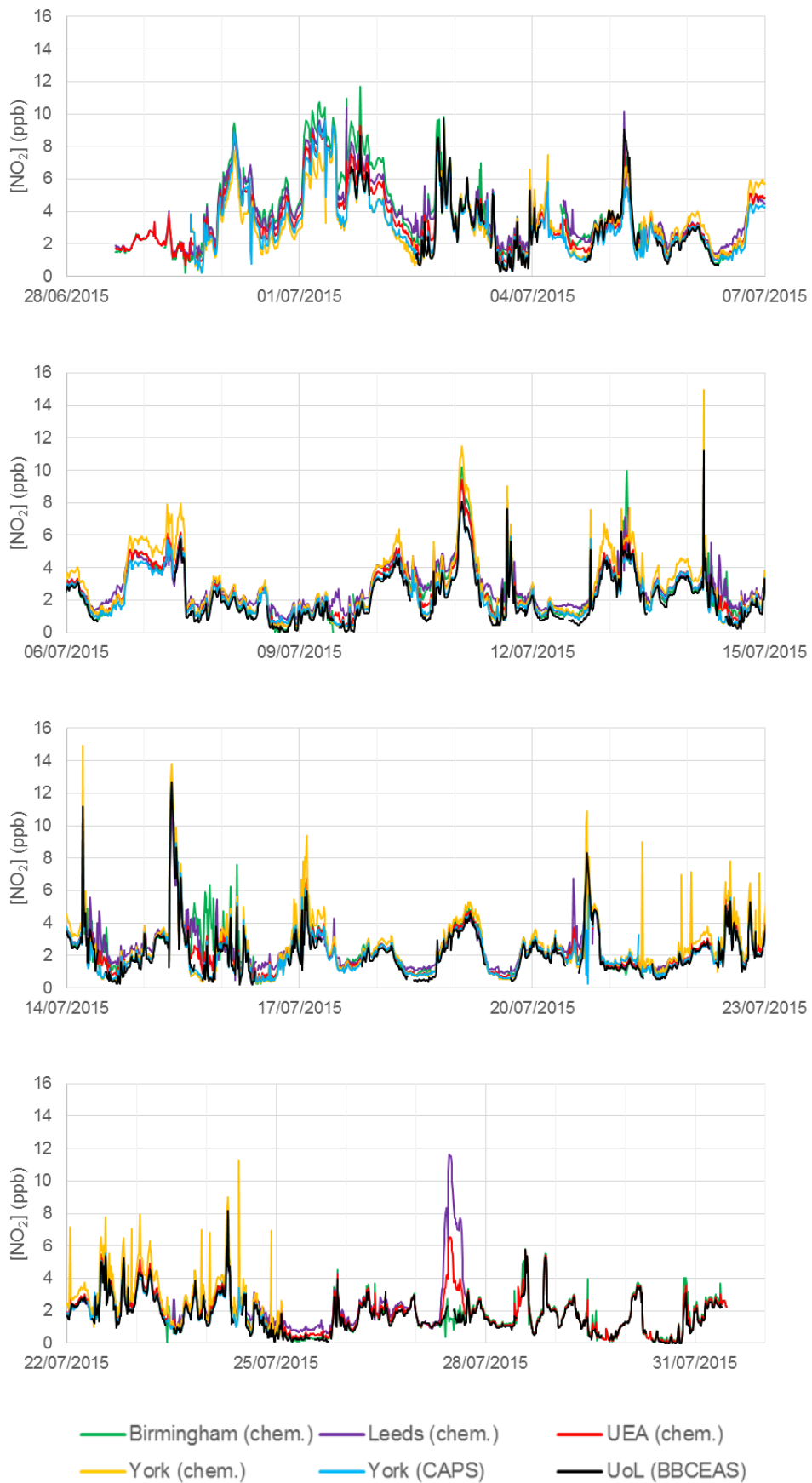
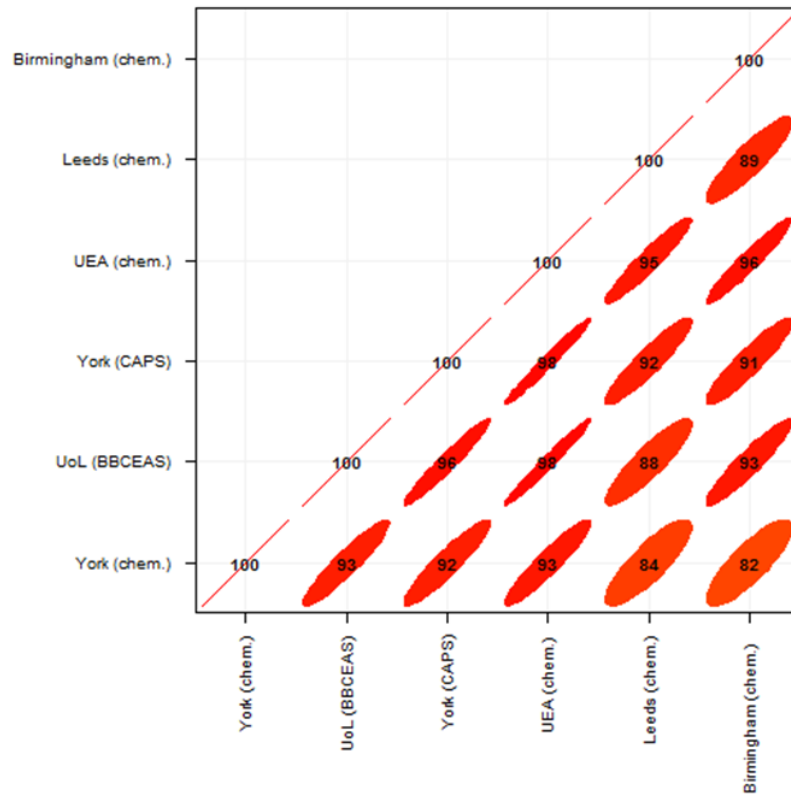


Figure 5.28 Complete time series of all NO<sub>2</sub> measurements for WAO campaign (15 min average data).

Other institutions similarly conducted NO<sub>2</sub> measurements with a variety of instruments, therefore several NO<sub>2</sub> datasets are available for this campaign. The various instruments had inlets at several different heights and locations, but all were within ~50 m of each other. Teams from the Universities of Birmingham, East Anglia and Leeds used commercial *Thermo Scientific 42i-TL* chemiluminescence analysers. York University's team operated an *Air Quality Design NOxy* chemiluminescence instrument and a *Teledyne T500U* Cavity Attenuated Phase Shift (CAPS) device. Notably the York NO<sub>xy</sub> instrument uses a photolytic converter (UV-LED light source) to convert NO<sub>2</sub> to NO prior to chemiluminescence detection (Air Quality Design Inc., 2008) rather than a molybdenum catalyst (see section 2.4.1), and is ostensibly not susceptible to the interference from non-NO<sub>2</sub> NO<sub>y</sub> discussed later in this subchapter. Data from these instruments are also shown in Figure 5.28. Most of these datasets also have some downtime, for example both York instruments ceased measurements on 24-25 July following a storm during which water entered the instruments' inlets. Figure 5.28 also shows where some measurements differ from others, for example on 01 July all instruments follow the same basic shape but the peak at ~06:15 is variously recorded at 7.5-11 ppb, and the peak on 27 July (~12:00) at 1.5, 6.5 and 11.5 ppb.

A more efficient way of comparing NO<sub>2</sub> datasets is *via* correlation plots. Figure 5.29a is a correlation matrix allowing quick comparison between all WAO NO<sub>2</sub> datasets. This figure shows that of all the NO<sub>2</sub> measurements the UoL BBCEAS, York CAPS and UEA chemiluminescence instruments demonstrated the closest correlations, despite the BBCEAS inlet being mounted on the UoL container mast slightly apart from the other two on the observatory station mast (distance approx. 30 m). Correlation plots were then generated to more closely compare the UoL BBCEAS dataset with the York CAPS and UEA chemiluminescence instruments (5.28b). The gradient of the correlation between UoL BBCEAS and UEA chemiluminescence NO<sub>2</sub> measurements (0.977) is close to 1.0, indicating close agreement in addition to the close the correlation demonstrated by the R<sup>2</sup> (0.955) being close to 1.0.

a)



b)

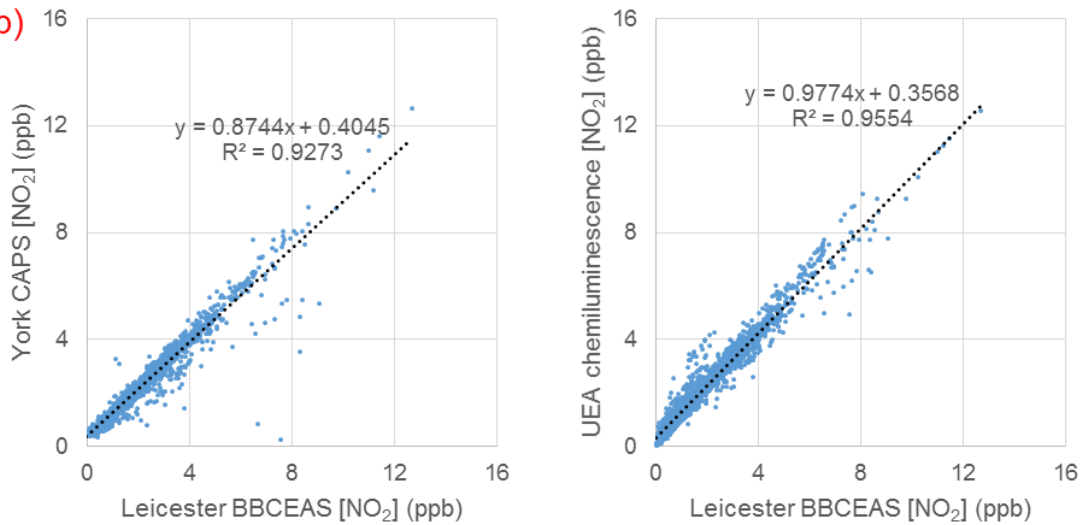


Figure 5.29 Correlations between NO<sub>2</sub> datasets at WAO.

- Correlation matrix for WAO NO<sub>2</sub> datasets (15 min averaged data) showing correlation coefficients between all datasets. Colour and shape also indicate correlation - circle/yellow = low, line/red = high.
- UoL BBCEAS NO<sub>2</sub> dataset correlated to York CAPS (left) and UEA chemiluminescence instruments (right).

A possible explanation for reduced correlation for most of the chemiluminescence instruments to the cavity-based techniques is that chemiluminescence instruments tend to over-report  $\text{NO}_2$ . This is because other  $\text{NO}_y$  species (e.g. HONO) are similarly decomposed by the molybdenum catalyst intended to decompose  $\text{NO}_2$  to  $\text{NO}$ , which the instrument then interprets as  $\text{NO}_2$  (Dunlea et al., 2007). Section 2.4.1 describes chemiluminescence  $\text{NO}_x$  detection principles in more detail. The positive bias in  $\text{NO}_2$  is likely greater in low- $\text{NO}_x$  environments (Reed et al., 2016) such as WAO due to greater proportion of  $\text{NO}_y$  relative to  $\text{NO}_x$ . This explanation fits with the observations in Figure 5.28, as the BBCEAS and CAPS for the most part report lower  $\text{NO}_2$  than the other instruments. Nitryl chloride is potentially one such interferent.

Figure 5.30a shows a time series of  $\text{ClNO}_2$  and all  $\text{NO}_2$  instruments' measurements for the highest  $\text{ClNO}_2$  night of the WAO campaign. During this  $\text{ClNO}_2$  peak, the CAPS and BBCEAS remain in near-perfect agreement, whereas the chemiluminescence instruments spread above them. The difference between cavity and chemiluminescence instruments is greater during this peak than when  $\text{ClNO}_2$  is low.

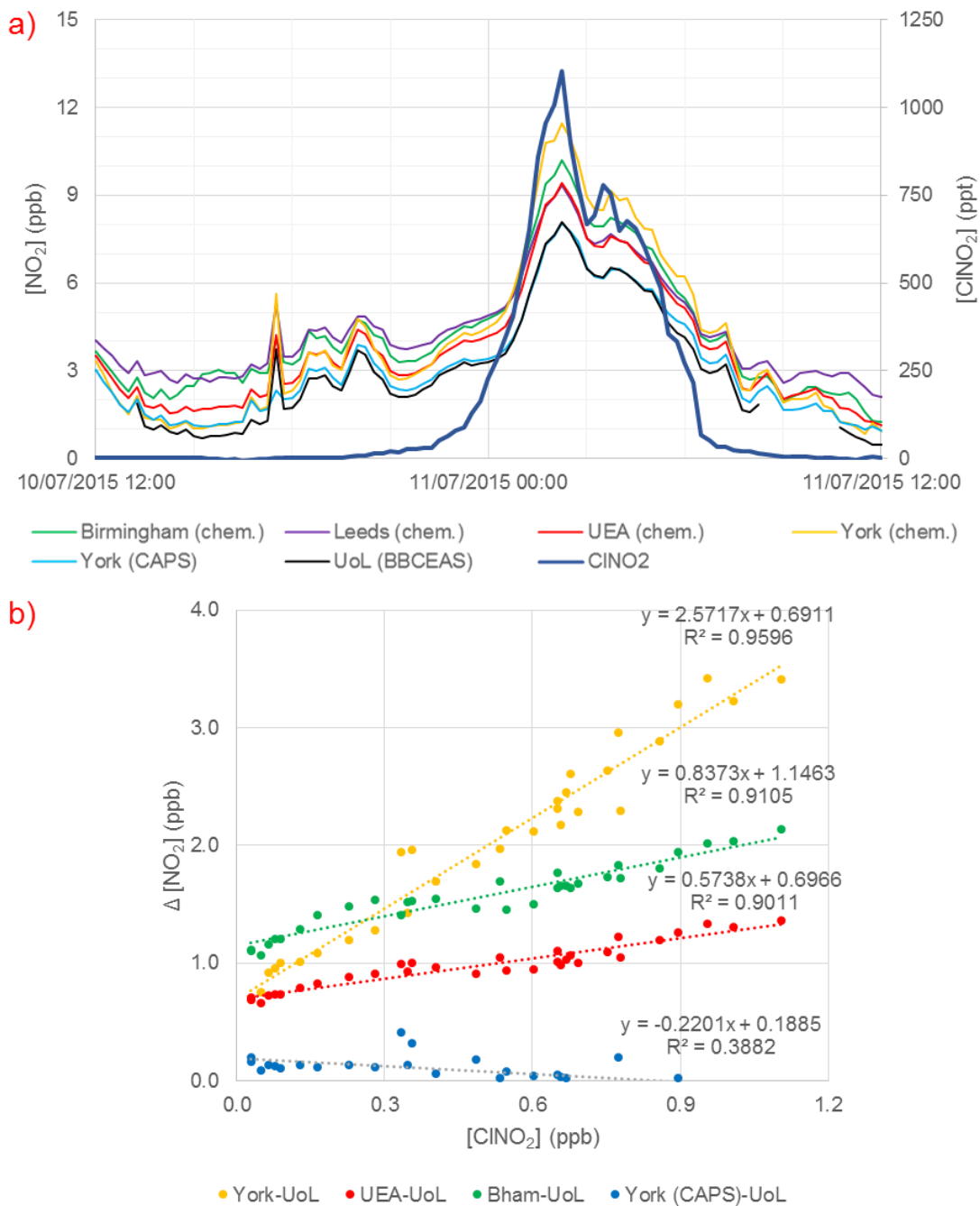


Figure 5.30 WAO  $\text{NO}_2$  and  $\text{ClNO}_2$  measurements for the night of 10-11 July.

- a) Time series comparing all  $\text{NO}_2$  measurements with  $\text{ClNO}_2$  (bold line).
- b) Selected  $\text{NO}_2$  measurements with UoL BBCEAS  $\text{NO}_2$  subtracted, correlated with  $\text{ClNO}_2$ .

Figure 5.30b shows selected instruments'  $\text{NO}_2$  measurements with the UoL BBCEAS measurement subtracted. The UoL BBCEAS was selected as the reference dataset, as this instrument is not susceptible to the non- $\text{NO}_2$   $\text{NO}_y$  interference and has a mostly complete dataset. The figure shows the selected

chemiluminescence instruments' differential NO<sub>2</sub> measurements scaling with ClNO<sub>2</sub> concentration ( $R^2 > 0.9$ ) in Figure 5.30b, whereas the equivalent CAPS-BBCEAS line does not ( $R^2 = 0.38$ ), suggesting that ClNO<sub>2</sub> was the major interferent for chemiluminescence instruments in this case. The scaling is not 1:1, however, indicating that other NO<sub>y</sub> are probably also involved. This correlation was only observed on this specific night of the WAO campaign, suggesting that ClNO<sub>2</sub> is a significant interferent in Molybdenum-converter chemiluminescence instruments only when concentrations are exceptionally high (at least >400 ppt, which was the next highest ClNO<sub>2</sub> peak observed at WAO).

While all instruments other than the UoL BBCEAS and York CAPS seemed to show some degree of NO<sub>2</sub> over-reporting during the WAO campaign, the UEA chemiluminescence instrument dataset was chosen for use in the analyses shown earlier this chapter. This was because the UEA chemiluminescence instrument showed very good agreement with the UoL BBCEAS but had almost no downtime (*i.e.* the dataset was more complete). The UEA instrument furthermore seemed to show the least amount of NO<sub>2</sub> over-reporting of the molybdenum-catalyst chemiluminescence instruments.

## 5.10 Summary

CIMS and BBCEAS instruments were deployed at two coastal locations in April/May and again in July 2015. Several challenges with respect to instrument operation were encountered. The structure housing instruments at PPAO was small and contained many instruments resulting in significant accumulation of heat, largely due to the numerous pumps on the CIMS and heaters on the BBCEAS. Elevated temperatures are not believed to have affected CIMS measurements but lead to increased noise on the BBCEAS spectrometer (which was later housed in a modified refrigerator) and frequently exceeded recommended operating conditions for the CO monitor. Heat buildup was not an issue during the WAO campaign (despite taking place in summer), as UoL instruments were housed in a much less crowded environment, a modified shipping container with powerful air conditioning. Furthermore, the BBCEAS

required frequent maintenance at Penlee Point due to accumulation of dust and salt on the mirrors. In the subsequent WAO campaign BBCEAS instruments were run with a flow of nitrogen purging the mirrors, which vastly diminished the required frequency of such maintenance.

Comparison of observations between the different sites showed that both coastal locations experience much more variability in ClNO<sub>2</sub> concentrations and consistently stronger winds than UoL at the same time of year. ClNO<sub>2</sub> was observed on only a few nights at PPAO but on most nights at WAO and UoL. At equivalent times of year, average diel peak ClNO<sub>2</sub> was greater at WAO than UoL, and greater at UoL than PPAO. Ozone is consistently present but at much lower concentrations at UoL than either coastal site, however NO<sub>x</sub> levels are consistently minimal at WAO and PPAO. In cases of high ClNO<sub>2</sub> at either coastal site, wind directions point towards major sources of NO<sub>x</sub>.

A simple model showing instantaneous production rates of atomic chlorine and hydroxyl radicals similar to the one used in UoL campaigns (see section 4.5) was also created for the PPAO and WAO campaigns. This model demonstrates that total Cl production in the summer (WAO) is small compared to OH, even on the day following the highest ClNO<sub>2</sub> concentration observed in this work. Cl production relative to OH was generally small for the PPAO campaign except for one day, on which the peak Cl production was only a factor of 2 smaller than the OH peak. In both campaigns Cl production begins much earlier than OH, in agreement with UoL campaigns.

Similarly to UoL, “fresher” air masses arriving at either coastal site with little time spent over land in the 5 days prior (according to NAME footprints) displayed very little ClNO<sub>2</sub> (typically none at PPAO). NAME footprints also indicate air masses with periods of stillness over the sea arriving at the site on several days with little or no ClNO<sub>2</sub> observed, indicating that stagnant air on its own does not result in ClNO<sub>2</sub> formation (therefore, significant ClNO<sub>2</sub> production depends on residence time occurring over land, presumably to pick up NO<sub>x</sub>-based pollution). ClNO<sub>2</sub> concentrations were generally low at PPAO, but large concentrations are occasionally observable - for example >900 ppt on the night of 30 Apr - 01 May. In general, air masses intercepted at WAO bear more NO<sub>x</sub>

than PPAO (further reflected in the presence of ClNO<sub>2</sub> on almost every night) but less than UoL. A notable exception to this is manifest in the highest ClNO<sub>2</sub> concentration observed in this project (1109 ppt, 15 min average), observed at WAO - on this night local winds suggest an origin in the direction of London, and NAME footprints indicated the air mass having dwelled over southeast England, the English Channel and Belgium.

Emission plumes from nearby shipping were visible at Penlee Point, however ClNO<sub>2</sub> concentrations were not visibly elevated in these. Emission plumes were also detected at WAO, however these were slightly different and less conclusively linked to shipping traffic. The Weybourne plumes showed enhanced ClNO<sub>2</sub> concentrations but were much more aged and likely somewhat diluted in comparison to those observed at PPAO.

Aerosol composition data were available for WAO and the 2014 UoL campaigns, which showed *via* Na<sup>+</sup>/Cl<sup>-</sup> ratios close to the mean value for seawater, suggesting that the majority of aerosol chloride present at both sites originated from seawater. Furthermore no correlation was apparent between ClNO<sub>2</sub> and chloride concentrations, suggesting that aerosol chloride content was not the limiting factor for ClNO<sub>2</sub> production even inland at UoL. Of the gas phase precursors, two different regimes are noticeable - at UoL, NO<sub>x</sub> is generally available but O<sub>3</sub> limits ClNO<sub>2</sub> production, and at the coastal sites O<sub>3</sub> is much more abundant but ClNO<sub>2</sub> is limited by the low NO<sub>x</sub> levels present.

A GEOS-Chem model modified to include ClNO<sub>2</sub> chemistry was run again for the coastal campaigns and their most comparable UoL equivalents, but at higher resolution than those discussed in chapter 4. Modelled and observed average diel profiles match more closely than the medium-resolution model for UoL campaigns, and even closer to observed values for the coastal campaigns. The model incorrectly predicted ClNO<sub>2</sub> production to be somewhat dependent on chloride for UoL. The model correctly predicted some ClNO<sub>2</sub> production dependency upon NO<sub>2</sub> for coastal campaigns, however not as strongly as did observed data. Over-prediction of ClNO<sub>2</sub> for the UoL campaigns seems to be a result of O<sub>3</sub> overestimation.

There were many more instruments present during the coastal campaigns than at the University of Leicester, for example six measurements of NO<sub>2</sub> via several different principles at Weybourne. The chemiluminescence instruments experienced interference from NO<sub>y</sub> species, likely including ClNO<sub>2</sub>. Three instruments, including the UoL BBCEAS (*i.e.* a non-chemiluminescence instrument), had particularly close agreement with each other despite slightly different inlet heights/positions. Of these, the instrument with fewest data gaps was chosen as a primary measurement for use in analysis.

## 6 Conclusions

### 6.1 Overview

The work presented in this thesis describes the measurement of nitryl chloride (and several related species) in the atmosphere to assess its ubiquity and impact in a UK context. A new I<sup>-</sup> CIMS instrument was successfully calibrated to quantify ClNO<sub>2</sub>. The instrument was then deployed with supporting measurements 7 times - five at the University of Leicester over various times of year to assess seasonal variations, and a further two times at Penlee Point (PPAO) and Weybourne Atmospheric Observatories (WAO) to evaluate geographical variations of ClNO<sub>2</sub>.

Nitryl chloride was successfully measured *via* CIMS during all campaigns, with very little instrument downtime. ClNO<sub>2</sub> was observed in significant quantities on most nights at WAO and UoL sites. At PPAO nitryl chloride was observed in significant concentrations on only a few nights, with very low observations generally corresponding to extremely clean air masses intercepted directly off the ocean. This indicates that ClNO<sub>2</sub> is indeed ubiquitous in the UK at both coastal and inland locations, typically wherever pollution is present.

### 6.2 CIMS calibration

A new I<sup>-</sup> CIMS instrument was used by the University of Leicester team to measure ambient ClNO<sub>2</sub> during work described in this thesis. Several experiments were carried out to successfully commission the instrument, which was subsequently optimised for simultaneous detection of both ClNO<sub>2</sub> and Cl<sub>2</sub>.

Raw data from the CIMS are output as counts per second, which required conversion to an absolute concentration *via* correlation to an independent measure of the relevant species, for which experiments were successfully developed. Calibration of ClNO<sub>2</sub> was achieved *via* quantitative dissociation to NO<sub>2</sub>, which was then measured using a BBCEAS instrument running in parallel. Cl<sub>2</sub> was instead quantified by calculating the dilution from a source cylinder of certified concentration.

The techniques used to calibrate ClNO<sub>2</sub> and Cl<sub>2</sub> were largely the same, allowing the same equipment to be used for both. The apparatus were developed to fit into a portable case to facilitate transport and use during fieldwork.

For each calibration experiment the instrument sensitivity was determined. There was significant variation in sensitivity over time, therefore several sensitivities were grouped together to determine a calibration factor for each field campaign. The precision of each sensitivity and the accuracy of each calibration factor were also calculated. These precision and accuracy values generally compared favourably with the literature.

### 6.3 Seasonal & geographical variability of ClNO<sub>2</sub>

While average diel profiles of NO, NO<sub>2</sub> and O<sub>3</sub> showed broad similarity across all the UoL campaigns, ClNO<sub>2</sub> varied significantly (section 4.3). ClNO<sub>2</sub> average diel maxima varied by a factor of 15, being largest in winter and smallest in summer.

A significant proportion of the air during each of the UoL campaigns originated from the southwest. Pollution roses indicate that many of the larger ClNO<sub>2</sub> concentrations in each campaign (except RAFT 3) corresponded to these southwesterly air masses. The difference in ClNO<sub>2</sub> concentrations corresponding to the same wind direction at different times of year strengthens the hypothesis that the observed seasonality of ClNO<sub>2</sub> correlates mainly with a difference in production, rather than entirely a difference in sources. The higher ClNO<sub>2</sub> concentrations were observed in winter, likely due to an increase in aerosol surfaces and N<sub>2</sub>O<sub>5</sub> availability resulting from meteorological conditions.

Observed ClNO<sub>2</sub> concentrations were slightly different between the two winter-time UoL campaigns, RAFT 2 and AURN 2. The ClNO<sub>2</sub> concentrations observed during each campaign from the southwest were similar, however during AURN 2 a significant amount of air was also intercepted from the southeast. These southeasterly air masses contained the highest ClNO<sub>2</sub> concentrations observed at UoL and are responsible for the higher ClNO<sub>2</sub> observations for this campaign, indicating that the higher winter-time ClNO<sub>2</sub> concentrations were also partially attributable to a difference in sources.

Geographical variations in observed ClNO<sub>2</sub> concentrations were also assessed (section 5.2) by comparing average diel profiles with UoL campaigns at the equivalent time of year. The UoL average diel maxima were higher than PPAO but lower than WAO. Notably, the UoL observations were more uniform (*i.e.* demonstrated less night to night variability) than both coastal campaigns. Comparison of average diel profiles for ClNO<sub>2</sub> precursors showed that O<sub>3</sub> was available at all times at all sites (but more abundant at the coastal sites) whereas NO<sub>x</sub> was mostly depleted at both coastal sites but relatively abundant at all hours at UoL. This indicates that air masses at the coastal sites are generally much cleaner, and ClNO<sub>2</sub> production is likely limited by the availability of N<sub>2</sub>O<sub>5</sub>.

#### 6.4 Radical production via ClNO<sub>2</sub> photolysis

A model showing production rates of atomic chlorine and hydroxyl radicals demonstrated that ClNO<sub>2</sub> has the potential to contribute significantly to tropospheric oxidising capacity *via* photolysis yielding atomic chlorine.

The model for UoL winter campaigns (section 4.5) demonstrates very high Cl production in the daytime (due to elevated ClNO<sub>2</sub> on the preceding nights). The maximum production of OH (which initiates HO<sub>x</sub> cycling described in section 1.2.1) is also reduced which, since O<sub>3</sub> concentrations are relatively similar throughout the year (see section 4.3.2), is presumably due to the lower light intensity. Peak Cl production frequently exceeded peak primary OH production following nights in which more than approx. 100 ppt ClNO<sub>2</sub> was observed. This threshold is below the average diel maximum for the AURN 2 (~190 ppt) campaign (February 2016), and similar to the average diel maximum for the RAFT 2 (~90 ppt) campaign (December 2014).

In the AURN 1 (September 2014) campaign, observed ClNO<sub>2</sub> concentrations were relatively low (average diel maximum ~40 ppt), dramatically reducing Cl production. Atomic chlorine from ClNO<sub>2</sub> photolysis is therefore less likely to be a major factor with respect to oxidising capacity during the warmer months at UoL.

The average diel maximum  $\text{ClNO}_2$  for the springtime RAFT 1 campaign (~120 ppt) is also similar to the aforementioned 100 ppt threshold, however data regarding photolysis, which seems to be the major factor for OH production at UoL, were unavailable for this campaign therefore similar comparison of relative Cl and OH production rates was not possible.

One day during the PPAO campaign observed elevated Cl production, resulting from a combination of factors relatively uncommon at this site as intercepted air masses are generally quite clean. This observation does, however, suggest that  $\text{ClNO}_2$ -derived atomic chlorine production may have increased significance during the spring (though not as high as during winter) in more polluted areas, especially on days with inclement weather.

During all campaigns at all sites where photolysis data were obtained Cl production was shown to begin as soon as sunlight is available, whereas there was often a significant time lag before OH production caught up.  $\text{ClNO}_2$ -derived atomic chlorine may therefore have significant impact on overall daytime oxidation chemistry, even when total Cl production is significantly less than OH, by enhancing the initiation of VOC oxidation in the early morning.

Photolysis of molecular chlorine,  $\text{Cl}_2$ , also releases atomic chlorine.  $\text{Cl}_2$  concentrations observed during the work presented in this thesis tended to be minimal and, where they frequently exceeded the CIMS detection limit, were attributed to a swimming pool exhaust vent (section 4.9). Effects of  $\text{Cl}_2$  upon oxidising capacity are therefore likely to be highly localised and very small compared to the more ubiquitous  $\text{ClNO}_2$ . For this work the effects of  $\text{Cl}_2$  were therefore neglected, but may become more relevant in the presence of other, larger  $\text{Cl}_2$  sources.

## 6.5 Daytime persistence of $\text{ClNO}_2$

A novel observation was made during the winter campaigns at UoL (RAFT 2 and AURN 2), whereby  $\text{ClNO}_2$  persisted throughout the day (see section 4.4). This phenomenon, which was not observed outside of winter, was attributed to reduced photolysis rate during the day combined with significant

concentrations of ClNO<sub>2</sub> on the nights prior. This phenomenon was shown in numerous examples, and the ClNO<sub>2</sub> average diel profile for both winter campaigns showed a minimum well above zero, demonstrating that it is not an unusual occurrence. On such days overall OH production tended to be lower than usual, likely indicating an even larger role of Cl production in oxidation chemistry. ClNO<sub>2</sub> from one night can therefore contribute to the concentration present the following night, however this is typically a small amount.

## 6.6 Conditions leading to ClNO<sub>2</sub> formation

Several case studies were selected in which ClNO<sub>2</sub> was observed at unusually high or low concentrations (sections 4.6 and 5.4). From these it was possible to make an assessment of the conditions that facilitate nitryl chloride formation.

As the UK is an island, 5 day back NAME footprints show air masses almost always having originated from or passed over the ocean, however some of these will have spent more time over land than others. The air masses that have spent very little time over land in those 5 days are typically “cleaner”, having had less time to pick up pollution. The lowest concentrations of ClNO<sub>2</sub> tend to correspond with these clean air masses. Observations of higher ClNO<sub>2</sub> concentrations correspondingly occur mostly when the NAME footprint shows that the air mass has resided over the land for a significant amount of time prior to interception at the site. This finding is consistent across all the sites at which ClNO<sub>2</sub> was observed for this thesis.

Analysis of emission plumes (section 5.6) at PPAO has shown that exceptionally fresh pollution (aged <10 minutes) does not typically contain ClNO<sub>2</sub>. A similar analysis with regards to WAO data, on the other hand, demonstrated the presence of nitryl chloride in slightly more aged (<90 minutes) but still distinguishable emission plumes. This result indicates that ClNO<sub>2</sub> formation is a relatively slow process.

In summary, nitryl chloride formation is driven by the presence of pollution but takes time to form. The air masses richest in ClNO<sub>2</sub> are therefore those which have spent time over a large urban/industrial area to pick up significant

amounts of  $\text{NO}_x$ , but have also aged several hours allowing an advanced degree of chemical processing.

### 6.7 Factors limiting $\text{ClNO}_2$ production

The availability of aerosol chloride was investigated (section 5.7.1). The Na/Cl ratio measured by aerosol filters at UoL matched well with literature values for seawater, indicating that sea salt chloride sources were available this far inland. This is in keeping with the findings of Vester et al., 2007 and Phillips et al., 2012 (see section 1.3). Furthermore, nitryl chloride concentration did not correlate with measurements of aerosol chloride at either UoL or WAO, indicating  $\text{ClNO}_2$  formation is not limited by chloride availability at either site.

Correlation plots of  $\text{NO}_2$  vs.  $\text{O}_3$  ( $\text{ClNO}_2$  precursors) were created using observational data from several campaigns (section 5.7.2), in which data points nearer the centre of the plots had the greatest abundance of both precursors. As mentioned in section 6.3,  $\text{O}_3$  tended to be abundant but  $\text{NO}_x$  was extremely low at the coastal sites, whereas during UoL campaigns  $\text{O}_3$  was comparatively depleted but  $\text{NO}_x$  was abundant.

Data points on the  $\text{NO}_2/\text{O}_3$  correlation plots that corresponded to high  $\text{ClNO}_2$  concentrations during the coastal campaigns occurred when  $\text{NO}_2$  concentrations were relatively high (>8 ppb) but the location of these points on the  $\text{O}_3$  scale was variable (18-45 ppb), implying that  $\text{NO}_2$  was correlated to (and therefore limited) the high  $\text{ClNO}_2$  concentration whereas  $\text{O}_3$  was not.

The UoL measurements showed a different pattern. High  $\text{ClNO}_2$  measurements occurred variably along the  $\text{NO}_2$  axis (15-30 ppb), however the highest  $\text{ClNO}_2$  observations for these campaigns corresponded to the higher values of  $\text{O}_3$  (>10 ppb). While the highest (>400 ppt)  $\text{ClNO}_2$  measurements are observed under these conditions, some elevated (200-400 ppt) observations occur at approx. 0 ppb ozone, which indicates that this pattern is not as strong as the one for coastal sites.

These results suggest that the factor limiting  $\text{ClNO}_2$  production for coastal sites is availability of  $\text{NO}_x$ , whereas  $\text{O}_3$  availability seems to be the limiting factor at

UoL. As sea salt chloride was available in Leicester (which is approximately as far from the sea as one can be within the UK) and did not seem to limit ClNO<sub>2</sub> production, there are therefore two identifiable regimes for ClNO<sub>2</sub> formation observed in this thesis: O<sub>3</sub>-limited and NO<sub>x</sub>-limited. Ozone is ubiquitous and NO<sub>x</sub> is abundant wherever pollution reaches, therefore it is possible to conclude that nitryl chloride is ubiquitous within the UK. The significant concentrations of ClNO<sub>2</sub> observed at both urban (UoL) and rural (WAO) sites further supports this conclusion.

## 6.8 Observations vs. model

The GEOS-Chem medium-resolution (regional) model ClNO<sub>2</sub> did not reproduce the UoL data (section 4.8). The average diel profiles for ClNO<sub>2</sub> in spring, summer and autumn are overestimated (dramatically so for the latter two).

The model data for winter are significantly closer to observed values. The RAFT 2 campaign has a close match on more than half of the days. For the AURN 2 campaign, the model estimates the correct order of magnitude for ClNO<sub>2</sub> but tends to err towards a relatively consistent peak every night, whereas the observed data show a wide variety of peak heights. The average diel profiles, however, are a surprisingly close match. Some of the difference between observed and modelled ClNO<sub>2</sub> may be due to the model predicting chloride-limitation of ClNO<sub>2</sub> production, which was not borne out by observations (see section 6.7).

A higher resolution GEOS-Chem model was available for PPAO, WAO and the two UoL campaigns set at similar times of year, RAFT 1 and AURN 1 respectively (section 5.8). This model predicted ClNO<sub>2</sub> concentrations much more closely, for example the average diel maxima were the correct order of magnitude for all campaigns. For all of these campaigns there are often differences between observed and modelled data (significant on some days) but the two datasets broadly agree in terms of averages and overall magnitudes. The major difference between modelled and observed ClNO<sub>2</sub> here is general overestimation for the UoL campaigns (but by a smaller margin than the medium-resolution model).

Overall, GEOS-Chem shows promise for ClNO<sub>2</sub> modelling, but in its current state needs to be treated with caution. Predicted ClNO<sub>2</sub> concentrations are rarely accurate in a night-to-night context but campaign average diel profiles produced from the high-resolution model data were reasonable (the average diel profile for the medium-resolution UoL winter model data was also sensible). This worked best for coastal locations, but not as well for inland locations where O<sub>3</sub> estimations were less accurate. Inaccuracies in predicted ClNO<sub>2</sub> for inland locations were more pronounced during summer and autumn due to greater overestimation of O<sub>3</sub> in these seasons compared to winter and spring. There was also evidence of NO<sub>x</sub> overestimation for the coastal sites and chloride underestimation for the inland site, however these factors seemed to be less inaccurate and therefore had less impact on ClNO<sub>2</sub> predictions.

## 6.9 Future directions

The maximum concentrations of ClNO<sub>2</sub> observed in the work presented here tended to be quite small compared to many literature sources at similar times of year. It was noted that the highest literature observations tended to be close to megacities, which presumably affects the pollution levels and, therefore, available N<sub>2</sub>O<sub>5</sub>. One avenue of investigation would therefore be a comparison of ClNO<sub>2</sub> detected at urban background sites within numerous cities of varying size. Such a study would be complicated, however, both by the fact that ClNO<sub>2</sub> tends to be most abundant in mature air masses, and the need to make observations at the same time of year. The latter issue may be resolved by simply coordinating simultaneous observations with several institutions.

Future observations of ClNO<sub>2</sub> should preferably include photolysis measurements. Atomic chlorine produced from nitryl chloride photolysis was noted to be high in winter and low in summer relative to OH primary production, however there is still room to explore the seasonality of Cl production *via* ClNO<sub>2</sub> photolysis especially during spring, as the RAFT 1 campaign was missing photolysis measurements and mostly clean air masses were intercepted during the PPAO campaign.

Full mass spectra (30-300 amu) were gathered periodically during field campaigns detailed in this thesis. Some preliminary work was done to investigate other molecules that are potentially detectable *via* I<sup>-</sup> CIMS. This work could be continued by conclusively identifying some of the species observed in these mass spectra, for which the instrument could potentially be calibrated.

One of the apparent targets for future ClNO<sub>2</sub> research is quantification and identification of chloride sources. This may not necessarily be a priority with respect to ClNO<sub>2</sub> formation in the UK (or other island/coastal regions), as the research in this thesis has shown that chloride availability is not the limiting factor, however many literature sources have identified this as a major gap in knowledge including calls for “develop[ment of] a more accurate emissions inventory for particulate chloride” (Sarwar et al., 2014) which will surely improve estimates of ClNO<sub>2</sub> prevalence and, therefore, impact in continental locations and in a global context. A particular target specified in Sarwar et al., 2014 was determination of whether ClNO<sub>2</sub> can form on the surface of particles produced *via* biomass burning, which have been identified as a potential chloride source (*e.g.* Tham et al., 2016).

Another avenue of research involves the branching ratio between [ICl]<sup>-</sup> and [I(ClNO<sub>2</sub>)]<sup>-</sup> ionisation products of ClNO<sub>2</sub> with respect to I<sup>-</sup> CIMS techniques. Pressure, CDC field strength and humidity all affect this branching ratio, establishing the nature of which would allow greater flexibility in these operating parameters (Kercher et al., 2009).

Modelling studies to assess the impacts of nitryl chloride have been developed in the past (*e.g.* Sarwar et al., 2014 and Simon et al., 2009), however models studied in this thesis have had mixed success in predicting ClNO<sub>2</sub> concentrations. While the high-resolution model examined in this thesis showed some skill in reproducing the observed ClNO<sub>2</sub> concentrations (section 5.8), the medium-resolution regional model was significantly flawed (section 4.8). The development of large-scale models to accurately predict concentrations of ClNO<sub>2</sub> is likely the most important part of fully establishing the importance of nitryl chloride with respect to tropospheric oxidation capacity, as this will

similarly enable the production rates of its atomic chlorine photolysis product to be accurately modelled for comparison with other tropospheric oxidants.

## Publications

HOLLIS, L. D. J., SOMMARIVA R., BALL S. M. & MONKS, P. S. 2014. Atmospheric impact & detection of nitryl chloride [oral presentation]. *Midlands Universities Group Symposium*, Warwick, UK, September 04 2014.

SOMMARIVA, R., HOLLIS, L. D. J., ADAMS, T. J., BALL, S. M. & MONKS, P. S. 2014. Observations of chlorine species in the UK [poster]. *IGAC Science Conference on Atmospheric Chemistry*, Natal, Brazil, September 22-26 2014.

SOMMARIVA R., HOLLIS, L. D. J., BAKER, A. R., BALL S. M., BELL, T. G., CORDELL R. L., FLEMING Z. L., GAGET, M., YANG, M. & MONKS, P. S. 2015. Spatial and temporal variability of inorganic chlorine in Northwestern Europe [oral presentation]. *AGU Fall Meeting*, San Francisco, USA, December 14-18 2015.

SOMMARIVA, R., HOLLIS, L. D. J., BALL, S. M., BROWN, T. C., CORDELL, R. L., EVANS, M. J., FLEMING, Z. L. & MONKS, P. S. 2014. Inorganic chlorine in an urban environment: measurements and seasonal patterns [poster]. *Chemistry in the Urban Atmosphere: Faraday Discussion*, London, UK, April 06-08 2016.

SOMMARIVA, R., HOLLIS, L. D. J., BALL, S. M., BAKER, A. R., BELL, T. G., BROWN, T. C., CORDELL, R. L., EVANS, M. J., FLEMING, Z. L., SHERWEN, T., YANG, M. & MONKS, P. S. 2014. Seasonal and geographical patterns of chlorine species in Northern Europe [poster]. *IGAC Science Conference*, Breckenridge, USA, September 26-30 2016.

SHERWEN, T., EVANS, M. J., SOMMARIVA, R., HOLLIS, L. D. J., BALL, S. M., MONKS, P. S., REED, C., CARPENTER, L. J., LEE, J. D., FORSTER, G., BANDY, B., REEVES, C. E. & BLOSS, W. J. 2017. Effects of halogens on European air-quality. *Faraday Discussions*, 200, 75-100.

HOLLIS, L. D. J., SOMMARIVA, R., CORDELL, R. L., FLEMING, Z. L., BALL, S. M. & MONKS, P. S. 2017. Impact of nitryl chloride on urban atmospheric oxidation chemistry [poster]. *The international conference on Atmospheric Sciences and Application to Air Quality (ASAAQ)*, Strasbourg, France, May 29-31 2017.

SOMMARIVA, R., HOLLIS, L. D. J., BAKER, A. R., BALL, S. M., BANDY, B. J., BELL, T. G., CORDELL, R. L., EVANS, M. J., LEE, J. D., REED, C., REEVES, C. E., SHERWEN, T., YANG, M. & MONKS, P. S. 2018. Seasonal and geographical variability of nitryl chloride and its precursors in Northern Europe [in preparation]. *Geophysical Research Letters*.

## Bibliography

- ADAMS, T. J. 2015. *Atmospheric Measurements of Biogenic and Anthropogenic Emissions by Broadband Cavity Enhanced Absorption Spectroscopy*. PhD thesis, University of Leicester, UK.
- AIR QUALITY DESIGN INC. 2008. AQD NO<sub>2</sub> Converter Manual.
- ALICKE, B., GEYER, A., HOFZUMAHAUS, A., HOLLAND, F., KONRAD, S., PATZ, H. W., SCHAFFER, J., STUTZ, J., VOLZ-THOMAS, A. & PLATT, U. 2003. OH formation by HONO photolysis during the BERLIOZ experiment. *Journal of Geophysical Research-Atmospheres*, 108, 17.
- ATKINSON, R., BAULCH, D. L., COX, R. A., CROWLEY, J. N., HAMPSON, R. F., HYNES, R. G., JENKIN, M. E., ROSSI, M. J. & TROE, J. 2004. Evaluated kinetic and photochemical data for atmospheric chemistry: Volume I - gas phase reactions of O<sub>x</sub>, HO<sub>x</sub>, NO<sub>x</sub> and SO<sub>x</sub> species. *Atmos. Chem. Phys.*, 4, 1461-1738.
- BAKER, A. R., WESTON, K., KELLY, S. D., VOSS, M., STREU, P. & CAPE, J. N. 2007. Dry and wet deposition of nutrients from the tropical Atlantic atmosphere: Links to primary productivity and nitrogen fixation. *Deep Sea Research Part I: Oceanographic Research Papers*, 54, 1704-1720.
- BALL, S. M. 2017. Personal communication.
- BALL, S. M., HOLLINGSWORTH, A. M., HUMBLE, J., LEBLANC, C., POTIN, P. & MCFIGGANS, G. 2010. Spectroscopic studies of molecular iodine emitted into the gas phase by seaweed. *Atmos. Chem. Phys.*, 10, 6237-6254.
- BALL, S. M. & JONES, R. L. 2003. Broad-band cavity ring-down spectroscopy. *Chemical Reviews*, 103, 5239-5262.
- BANNAN, T. J., BOOTH, A. M., BACAK, A., MULLER, J. B. A., LEATHER, K. E., LE BRETON, M., JONES, B., YOUNG, D., COE, H., ALLAN, J., VISSER, S., SLOWIK, J. G., FURGER, M., PREVOT, A. S. H., LEE, J., DUNMORE, R. E., HOPKINS, J. R., HAMILTON, J. F., LEWIS, A. C., WHALLEY, L. K., SHARP, T., STONE, D., HEARD, D. E., FLEMING, Z. L., LEIGH, R., SHALLCROSS, D. E. & PERCIVAL, C. J. 2015. The first UK measurements of nitryl chloride using a chemical ionization mass spectrometer in central London in the summer of 2012, and an investigation of the role of Cl atom oxidation. *Journal of Geophysical Research-Atmospheres*, 120, 5638-5657.
- BEHNKE, W., GEORGE, C., SCHEER, V. & ZETZSCH, C. 1997. Production and decay of ClNO<sub>2</sub>, from the reaction of gaseous N<sub>2</sub>O<sub>5</sub> with NaCl solution: Bulk and aerosol experiments. *Journal of Geophysical Research-Atmospheres*, 102, 3795-3804.
- BENTON, A. K., LANGRIDGE, J. M., BALL, S. M., BLOSS, W. J., DALL'OSTO, M., NEMITZ, E., HARRISON, R. M. & JONES, R. L. 2010. Night-time chemistry above London: measurements of NO<sub>3</sub> and N<sub>2</sub>O<sub>5</sub> from the BT Tower. *Atmospheric Chemistry and Physics*, 10, 9781-9795.
- BERDEN, G., PEETERS, R. & MEIJER, G. 2000. Cavity ring-down spectroscopy: Experimental schemes and applications. *International Reviews in Physical Chemistry*, 19, 565-607.
- BROWN, S. S. 2003. Absorption spectroscopy in high-finesse cavities for atmospheric studies. *Chemical Reviews*, 103, 5219-5238.
- BROWN, S. S., STARK, H. & RAVISHANKARA, A. R. 2003. Applicability of the steady state approximation to the interpretation of atmospheric observations of NO<sub>3</sub> and N<sub>2</sub>O<sub>5</sub>. *Journal of Geophysical Research*, 108.
- BROWN, S. S. & STUTZ, J. 2012. Nighttime radical observations and chemistry. *Chem Soc Rev*, 41, 6405-47.
- BROWN, T. C. 2016. *Assessment of Nitryl Chloride as a Missing Oxidant in the UK Atmosphere*. MChem dissertation, University of Leicester.

- BURNS, S. J., MATTHEWS, J. M. & MCFADDEN, D. L. 1996. Rate Coefficients for Dissociative Electron Attachment by Halomethane Compounds between 300 and 800 K. *The Journal of Physical Chemistry*, 100, 19436-19440.
- CANTRELL, C. A. 2008. Technical Note: Review of methods for linear least-squares fitting of data and application to atmospheric chemistry problems. *Atmospheric Chemistry and Physics*, 8, 5477-5487.
- CARSLAW, D. C. & ROPKINS, K. 2012. Openair – An R package for air quality data analysis. *Environmental Modelling & Software*, 27, 52-61.
- CHAPMAN, S. 1930. *A Theory of Upper-atmospheric Ozone*, Edward Stanford.
- CORDELL, R. L. 14 June 2017. RE: Personal communication.
- DANIELS, M. J. S. 2012. *Measurements of Atmospheric Trace Gases by Broadband Cavity Enhanced Absorption Spectroscopy*. PhD thesis, University of Leicester, UK.
- DAVIDSON, J. A., VIGGIANO, A. A., HOWARD, C. J., DOTAN, I., FEHSENFELD, F. C., ALBRITTON, D. L. & FERGUSON, E. E. 1978. Rate constants for reactions of  $O_2^+$ ,  $NO_2^+$ ,  $NO^+$ ,  $H_3O^+$ ,  $CO_3^+$ ,  $NO_2^+$ , and halide ions with  $N_2O_5$  at 300 K. *Journal of Chemical Physics*, 68, 2085-2087.
- DE HOFFMANN, E. & STROOBANT, V. 2007. *Mass Spectrometry: Principles and Applications*, Wiley.
- DEFRA. 2011a. *Brief history [of monitoring networks]* [Online]. Available: <https://uk-air.defra.gov.uk/networks/brief-history> [Accessed September 14 2017].
- DEFRA. 2011b. *Site environment types* [Online]. Available: <https://uk-air.defra.gov.uk/networks/site-types> [Accessed 08 May 2017].
- DIEC, D. 2015. *Mass Spectrometry Measurements of Nitryl Chloride in the Atmosphere*. MChem dissertation, University of Leicester.
- DUBÉ, W. P., BROWN, S. S., OSTHOFF, H. D., NUNLEY, M. R., CICIORA, S. J., PARIS, M. W., MCLAUGHLIN, R. J. & RAVISHANKARA, A. R. 2006. Aircraft instrument for simultaneous, *in situ* measurement of  $NO_3$  and  $N_2O_5$  via pulsed cavity ring-down spectroscopy. *Review of Scientific Instruments*, 77, 034101.
- DUNLEA, E. J., HERNDON, S. C., NELSON, D. D., VOLKAMER, R. M., SAN MARTINI, F., SHEEHY, P. M., ZAHNISER, M. S., SHORTER, J. H., WORMHOUDT, J. C., LAMB, B. K., ALLWINE, E. J., GAFFNEY, J. S., MARLEY, N. A., GRUTTER, M., MARQUEZ, C., BLANCO, S., CARDENAS, B., RETAMA, A., RAMOS VILLEGAS, C. R., KOLB, C. E., MOLINA, L. T. & MOLINA, M. J. 2007. Evaluation of nitrogen dioxide chemiluminescence monitors in a polluted urban environment. *Atmos. Chem. Phys.*, 7, 2691-2704.
- EDWARDS, G. D. & MONKS, P. S. 2003. Performance of a single-monochromator diode array spectroradiometer for the determination of actinic flux and atmospheric photolysis frequencies. *Journal of Geophysical Research-Atmospheres*, 108, 13.
- ELLIS, A. M. & MAYHEW, C. M. 2014. *Proton Transfer Reaction Mass Spectrometry: Principles and Applications*, John Wiley & Sons.
- ENGELN, R., BERDEN, G., PEETERS, R. & MEIJER, G. 1998. Cavity enhanced absorption and cavity enhanced magnetic rotation spectroscopy. *Review of Scientific Instruments*, 69, 3763-3769.
- ERICKSON, D. J., SEUZARET, C., KEENE, W. C. & GONG, S. L. 1999. A general circulation model based calculation of HCl and ClNO<sub>2</sub> production from sea salt dechlorination: Reactive Chlorine Emissions Inventory. *Journal of Geophysical Research: Atmospheres*, 104, 8347-8372.
- EVANS, C. D., MONTEITH, D. T., FOWLER, D., CAPE, J. N. & BRAYSHAW, S. 2011. Hydrochloric Acid: An Overlooked Driver of Environmental Change. *Environmental Science & Technology*, 45, 1887-1894.
- FAXON, C., BEAN, J. & RUIZ, L. 2015. Inland Concentrations of Cl<sub>2</sub> and ClNO<sub>2</sub> in Southeast Texas Suggest Chlorine Chemistry Significantly Contributes to Atmospheric Reactivity. *Atmosphere*, 6, 1487-1506.

- FINLAYSON-PITTS, B. J. 2003. The tropospheric chemistry of sea salt: A molecular-level view of the chemistry of NaCl and NaBr. *Chemical Reviews*, 103, 4801-4822.
- FINLAYSON-PITTS, B. J., EZELL, M. J. & PITTS, J. N. 1989. Formation of chemically active chlorine compounds by reactions of atmospheric NaCl particles with gaseous N<sub>2</sub>O<sub>5</sub> and ClONO<sub>2</sub>. *Nature*, 337, 241-244.
- FINLAYSON-PITTS, B. J. & PITTS JR, J. N. 2000. *Chemistry of the Upper and Lower Atmosphere*, Academic Press.
- FINLEY, B. D. & SALTZMAN, E. S. 2006. Measurement of Cl<sub>2</sub> in coastal urban air. *Geophysical Research Letters*, 33.
- FLEMING, Z. L. 2017. Personal communication.
- GOOGLE EARTH 2017a. Satellite image of the UK, with ClONO<sub>2</sub> measurement sites marked (copyright 2016 Google, 2009 Geobasis-DE/BKG). Map data: SIO, NOAA, U.S. Navy, NGA, GEBCO. Images: Landsat/Copernicus.
- GOOGLE EARTH 2017b. Satellite image of Leicester city, with University of Leicester marked. Images (copyright 2016): Google.
- GOOGLE EARTH 2017c. Satellite image of the UK, with Penlee Point Atmospheric Observatory and University of Leicester marked. Map data: SIO, U.S. Navy, NGA, GEBCO. Images: Landsat/Copernicus.
- GOOGLE EARTH 2017d. Satellite image of Penlee Point Atmospheric Observatory and surroundings. Map data: SIO, NOAA, U.S. Navy, NGA, GEBCO. Images (copyright 2017): TerraMetrics, Getmapping plc.
- GOOGLE EARTH 2017e. Satellite image of the UK, with Weybourne Atmospheric Observatory and University of Leicester marked (copyright 2017 Google). Map data: SIO, NOAA, U.S. Navy, NGA, GEBCO.
- GOOGLE EARTH 2017f. Satellite image of Weybourne Atmospheric Observatory (copyright 2017 Infoterra Ltd & Bluesky). Map data: SIO, NOAA, U.S. Navy, NGA, GEBCO. Images: Landsat/Copernicus, (copyright 2017) Infoterra Ltd & Bluesky.
- GOOGLE EARTH 2017g. Satellite image of the UK with Weybourne Atmospheric Observatory, Penlee Point Atmospheric Observatory and University of Leicester marked. Map data: SIO, NOAA, U.S. Navy, NGA, GEBCO.
- HALONEN, J. I., LANKI, T., TIITTANEN, P., NIEMI, J. V., LOH, M. & PEKKANEN, J. 2010. Ozone and cause-specific cardiorespiratory morbidity and mortality. *J Epidemiol Community Health*, 64, 814-20.
- HEARN, J. D. & SMITH, G. D. 2004. A chemical ionization mass spectrometry method for the online analysis of organic aerosols. *Analytical Chemistry*, 76, 2820-2826.
- HEINRITZI, M., SIMON, M., STEINER, G., WAGNER, A. C., KURTEN, A., HANSEL, A. & CURTIUS, J. 2016. Characterization of the mass-dependent transmission efficiency of a CIMS. *Atmospheric Measurement Techniques*, 9, 1449-1460.
- HOLLINGSWORTH, A. 2010. *Quantitative detection of trace gas species in the atmosphere using LED Broadband Cavity Enhanced Absorption Spectroscopy*. PhD thesis, University of Leicester, UK.
- HOLLOWAY, A. M. & WAYNE, R. P. 2010. *Atmospheric chemistry*.
- HUEY, L. G. 2007. Measurement of trace atmospheric species by chemical ionization mass spectrometry: speciation of reactive nitrogen and future directions. *Mass Spectrom Rev*, 26, 166-84.
- HUEY, L. G., DUNLEA, E. J., LOVEJOY, E. R., HANSON, D. R., NORTON, R. B., FEHSENFELD, F. C. & HOWARD, C. J. 1998. Fast time response measurements of HNO<sub>3</sub> in air with a chemical ionization mass spectrometer. *Journal of Geophysical Research: Atmospheres*, 103, 3355-3360.
- HUEY, L. G., HANSON, D. R. & HOWARD, C. J. 1995. Reactions of SF<sub>6</sub><sup>-</sup> and I<sup>-</sup> with atmospheric trace gases. *Journal of Physical Chemistry*, 99, 5001-5008.
- JACK, A. S. & ALOIS, S. 2004. Using helium as a standard of refractive index: correcting errors in a gas refractometer. *Metrologia*, 41, 189.

- JENKIN, M. E. & CLEMITSHAW, K. C. 2000. Ozone and other secondary photochemical pollutants: chemical processes governing their formation in the planetary boundary layer. *Atmospheric Environment*, 34, 2499-2527.
- JONES, A., THOMSON, D., HORT, M. & DEVENISH, B. 2007. The U.K. Met Office's Next-Generation Atmospheric Dispersion Model, NAME III. In: BORREGO, C. & NORMAN, A.-L. (eds.) *Air Pollution Modeling and Its Application XVII*. Boston, MA: Springer US.
- KEENE, W. C., KHALIL, M. A. K., ERICKSON, D. J., MCCULLOCH, A., GRAEDEL, T. E., LOBERT, J. M., AUCOTT, M. L., GONG, S. L., HARPER, D. B., KLEIMAN, G., MIDGLEY, P., MOORE, R. M., SEUZARET, C., STURGES, W. T., BENKOVITZ, C. M., KOROPALOV, V., BARRIE, L. A. & LI, Y. F. 1999. Composite global emissions of reactive chlorine from anthropogenic and natural sources: Reactive Chlorine Emissions Inventory. *Journal of Geophysical Research: Atmospheres*, 104, 8429-8440.
- KELLER-RUDEK, H., MOORTGAT, G. K., SANDER, R. & SÖRENSEN, R. 2013. The MPI-Mainz UV/VIS Spectral Atlas of Gaseous Molecules of Atmospheric Interest. *Earth Syst. Sci. Data*, 5, 365-373.
- KENNEDY, O. J., OUYANG, B., LANGRIDGE, J. M., DANIELS, M. J. S., BAUGUITTE, S., FRESHWATER, R., MCLEOD, M. W., IRONMONGER, C., SENDALL, J., NORRIS, O., NIGHTINGALE, R., BALL, S. M. & JONES, R. L. 2011. An aircraft based three channel broadband cavity enhanced absorption spectrometer for simultaneous measurements of NO<sub>3</sub>, N<sub>2</sub>O<sub>5</sub> and NO<sub>2</sub>. *Atmospheric Measurement Techniques*, 4, 1759-1776.
- KERCHER, J. P., RIEDEL, T. P. & THORNTON, J. A. 2009. Chlorine activation by N<sub>2</sub>O<sub>5</sub>: simultaneous, in situ detection of ClNO<sub>2</sub> and N<sub>2</sub>O<sub>5</sub> by chemical ionization mass spectrometry. *Atmospheric Measurement Techniques*, 2, 193-204.
- KRAMIDA, A., RALCHENKO, Y. & READER, J. 2016. NIST Atomic Spectra Database (version 5.4).
- KRUPA, S. V., NOSAL, M. & LEGGE, A. H. 1998. A numerical analysis of the combined open-top chamber data from the USA and Europe on ambient ozone and negative crop responses. *Environmental Pollution*, 101, 157-160.
- KURTEN, A., RONDO, L., EHRHART, S. & CURTIUS, J. 2011. Performance of a corona ion source for measurement of sulfuric acid by chemical ionization mass spectrometry. *Atmospheric Measurement Techniques*, 4, 437-443.
- LEE, B. H., LOPEZ-HILFIKER, F. D., MOHR, C., KURTEN, T., WORSNOP, D. R. & THORNTON, J. A. 2014. An Iodide-Adduct High-Resolution Time-of-Flight Chemical-Ionization Mass Spectrometer: Application to Atmospheric Inorganic and Organic Compounds. *Environmental Science & Technology*, 48, 6309-6317.
- LEE, J., KIM, K.-H., KIM, Y. J. & LEE, J. 2008. Application of a long-path differential optical absorption spectrometer (LP-DOAS) on the measurements of NO<sub>2</sub>, SO<sub>2</sub>, O<sub>3</sub>, and HNO<sub>2</sub> in Gwangju, Korea. *Journal of Environmental Management*, 86, 750-759.
- LEE, J. D., WHALLEY, L. K., HEARD, D. E., STONE, D., DUNMORE, R. E., HAMILTON, J. F., YOUNG, D. E., ALLAN, J. D., LAUFS, S. & KLEFFMANN, J. 2016. Detailed budget analysis of HONO in central London reveals a missing daytime source. *Atmospheric Chemistry and Physics*, 16, 2747-2764.
- LIAO, J., HUEY, L. G., LIU, Z., TANNER, D. J., CANTRELL, C. A., ORLANDO, J. J., FLOCKE, F. M., SHEPSON, P. B., WEINHEIMER, A. J., HALL, S. R., ULLMANN, K., BEINE, H. J., WANG, Y. H., INGALL, E. D., STEPHENS, C. R., HORN BROOK, R. S., APEL, E. C., RIEMER, D., FRIED, A., MAULDIN, R. L., SMITH, J. N., STAEBLER, R. M., NEUMAN, J. A. & NOWAK, J. B. 2014. High levels of molecular chlorine in the Arctic atmosphere. *Nature Geoscience*, 7, 91-94.
- LIAO, J., SIHLER, H., HUEY, L. G., NEUMAN, J. A., TANNER, D. J., FRIESS, U., PLATT, U., FLOCKE, F. M., ORLANDO, J. J., SHEPSON, P. B., BEINE, H. J., WEINHEIMER,

- A. J., SJOSTEDT, S. J., NOWAK, J. B., KNAPP, D. J., STAEBLER, R. M., ZHENG, W., SANDER, R., HALL, S. R. & ULLMANN, K. 2011. A comparison of Arctic BrO measurements by chemical ionization mass spectrometry and long path-differential optical absorption spectroscopy. *Journal of Geophysical Research*, 116.
- MA, X., VON SALZEN, K. & LI, J. 2008. Modelling sea salt aerosol and its direct and indirect effects on climate. *Atmos. Chem. Phys.*, 8, 1311-1327.
- MCNEILL, V. F., PATTERSON, J., WOLFE, G. M. & THORNTON, J. A. 2006. The effect of varying levels of surfactant on the reactive uptake of N<sub>2</sub>O<sub>5</sub> to aqueous aerosol. *Atmospheric Chemistry and Physics*, 6, 1635-1644.
- MIELKE, L. H., FURGESON, A. & OSTHOFF, H. D. 2011. Observation of ClNO<sub>2</sub> in a mid-continental urban environment. *Environ Sci Technol*, 45, 8889-96.
- MIELKE, L. H., STUTZ, J., TSAI, C., HURLOCK, S. C., ROBERTS, J. M., VERES, P. R., FROYD, K. D., HAYES, P. L., CUBISON, M. J., JIMENEZ, J. L., WASHENFELDER, R. A., YOUNG, C. J., GILMAN, J. B., DE GOUW, J. A., FLYNN, J. H., GROSSBERG, N., LEFER, B. L., LIU, J., WEBER, R. J. & OSTHOFF, H. D. 2013. Heterogeneous formation of nitryl chloride and its role as a nocturnal NO<sub>x</sub> reservoir species during CalNex-LA 2010. *Journal of Geophysical Research: Atmospheres*, 118, 10,638-10,652.
- MIN, K. E., WASHENFELDER, R. A., DUBÉ, W. P., LANGFORD, A. O., EDWARDS, P. M., ZARZANA, K. J., STUTZ, J., LU, K., ROHRER, F., ZHANG, Y. & BROWN, S. S. 2016. A broadband cavity enhanced absorption spectrometer for aircraft measurements of glyoxal, methylglyoxal, nitrous acid, nitrogen dioxide, and water vapor. *Atmos. Meas. Tech.*, 9, 423-440.
- MONKS, P. S. 2005. Gas-phase radical chemistry in the troposphere. *Chem Soc Rev*, 34, 376-95.
- MONKS, P. S. 2007a. Chapter 2 Chemistry of the Atmosphere. *Principles of Environmental Chemistry*. The Royal Society of Chemistry.
- MONKS, P. S. 2007b. Tropospheric Photochemistry. *Handbook of Atmospheric Science*. Blackwell Science Ltd.
- MONKS, P. S., ARCHIBALD, A. T., COLETTE, A., COOPER, O., COYLE, M., DERWENT, R., FOWLER, D., GRANIER, C., LAW, K. S., MILLS, G. E., STEVENSON, D. S., TARASOVA, O., THOURET, V., VON SCHNEIDEMESSER, E., SOMMARIVA, R., WILD, O. & WILLIAMS, M. L. 2015. Tropospheric ozone and its precursors from the urban to the global scale from air quality to short-lived climate forcer. *Atmos. Chem. Phys.*, 15, 8889-8973.
- MONKS, P. S., GRANIER, C., FUZZI, S., STOHL, A., WILLIAMS, M. L., AKIMOTO, H., AMANN, M., BAKLANOV, A., BALTENSBERGER, U., BEY, I., BLAKE, N., BLAKE, R. S., CARSLAW, K., COOPER, O. R., DENTENER, F., FOWLER, D., FRAGKOU, E., FROST, G. J., GENEROSO, S., GINOUX, P., GREWE, V., GUENTHER, A., HANSSON, H. C., HENNE, S., HJORTH, J., HOFZUMAHAUS, A., HUNTRIESER, H., ISAKSEN, I. S. A., JENKIN, M. E., KAISER, J., KANAKIDOU, M., KLIMONT, Z., KULMALA, M., LAJ, P., LAWRENCE, M. G., LEE, J. D., LIOUSSE, C., MAIONE, M., MCFIGGANS, G., METZGER, A., MIEVILLE, A., MOUSSIOPOULOS, N., ORLANDO, J. J., O'DOWD, C. D., PALMER, P. I., PARRISH, D. D., PETZOLD, A., PLATT, U., PÖSCHL, U., PRÉVÔT, A. S. H., REEVES, C. E., REIMANN, S., RUDICH, Y., SELLEGRI, K., STEINBRECHER, R., SIMPSON, D., TEN BRINK, H., THELOKE, J., VAN DER WERF, G. R., VAUTARD, R., VESTRENG, V., VLACHOKOSTAS, C. & VON GLASOW, R. 2009. Atmospheric composition change - global and regional air quality. *Atmospheric Environment*, 43, 5268-5350.
- MOOIBROEK, D., STAELENS, J., CORDELL, R., PANTELIADIS, P., DELAUNAY, T., WEIJERS, E., VERCAUTEREN, J., HOOGERBRUGGE, R., DIJKEMA, M., MONKS, P. S. & ROEKENS, E. 2016. PM<sub>10</sub> Source Apportionment in Five North Western

- European Cities-Outcome of the Joaquin Project. *Airborne Particulate Matter: Sources, Atmospheric Processes and Health*. The Royal Society of Chemistry.
- MYHRE, G., SHINDELL, D., BRÉON, F.-M., COLLINS, W., FUGLESTVEDT, J., HUANG, J., KOCH, D., LAMARQUE, J.-F., LEE, D., MENDOZA, B., NAKAJIMA, T., ROBOCK, A., STEPHENS, G., TAKEMURA, T. & ZHAN, H. 2014. Anthropogenic and Natural Radiative Forcing. *In: INTERGOVERNMENTAL PANEL ON CLIMATE, C. (ed.) Climate Change 2013 - The Physical Science Basis: Working Group I Contribution to the Fifth Assessment Report of the Intergovernmental Panel on Climate Change*. Cambridge: Cambridge University Press.
- MYKROLIS CORPORATION MKS Type M100B Mass-Flo® Controller and Type M10MB Mass-Flo Meter manual.
- OFFICE FOR NATIONAL STATISTICS. 2017. Available: <https://www.ons.gov.uk/peoplepopulationandcommunity/populationandmigration/populationestimates/bulletins/annualmidyearpopulationestimates/latest> [Accessed 13 July 2017].
- OSTHOFF, H. D., ROBERTS, J. M., RAVISHANKARA, A. R., WILLIAMS, E. J., LERNER, B. M., SOMMARIVA, R., BATES, T. S., COFFMAN, D., QUINN, P. K., DIBB, J. E., STARK, H., BURKHOLDER, J. B., TALUKDAR, R. K., MEAGHER, J., FEHSENFELD, F. C. & BROWN, S. S. 2008. High levels of nitryl chloride in the polluted subtropical marine boundary layer. *Nature Geoscience*, 1, 324-328.
- PANCHAL, R. 2016. *Determination of OH reactivity in the atmosphere by way of the Comparative Reactivity Method*. PhD thesis, University of Leicester, UK.
- PENKETT, S. A., PLANE, J. M. C., COMES, F. J., CLEMITSHAW, K. C. & COE, H. 1999. The Weybourne Atmospheric Observatory. *Journal of Atmospheric Chemistry*, 33, 107-110.
- PHILLIPS, G. J., TANG, M. J., THIESER, J., BRICKWEDDE, B., SCHUSTER, G., BOHN, B., LELIEVELD, J. & CROWLEY, J. N. 2012. Significant concentrations of nitryl chloride observed in rural continental Europe associated with the influence of sea salt chloride and anthropogenic emissions. *Geophysical Research Letters*, 39, n/a-n/a.
- PLATT, U. & STUTZ, J. 2008. *Differential Optical Absorption Spectroscopy: Principles and Applications*, Springer.
- PRINN, R. G. 2003. The cleansing capacity of the atmosphere. *Annual Review of Environment and Resources*, 28, 29-57.
- PRINN, R. G. 2014. 5.1 - Ozone, Hydroxyl Radical, and Oxidative Capacity A2 - Holland, Heinrich D. *In: TUREKIAN, K. K. (ed.) Treatise on Geochemistry (Second Edition)*. Oxford: Elsevier.
- REED, C., EVANS, M. J., DI CARLO, P., LEE, J. D. & CARPENTER, L. J. 2016. Interferences in photolytic NO<sub>2</sub> measurements: explanation for an apparent missing oxidant? *Atmospheric Chemistry and Physics*, 16, 4707-4724.
- RIEDEL, T. P., BERTRAM, T. H., CRISP, T. A., WILLIAMS, E. J., LERNER, B. M., VLASENKO, A., LI, S. M., GILMAN, J., DE GOUW, J., BON, D. M., WAGNER, N. L., BROWN, S. S. & THORNTON, J. A. 2012. Nitryl chloride and molecular chlorine in the coastal marine boundary layer. *Environ Sci Technol*, 46, 10463-70.
- RIEDEL, T. P., WAGNER, N. L., DUBÉ, W. P., MIDDLEBROOK, A. M., YOUNG, C. J., ÖZTÜRK, F., BAHREINI, R., VANDENBOER, T. C., WOLFE, D. E., WILLIAMS, E. J., ROBERTS, J. M., BROWN, S. S. & THORNTON, J. A. 2013. Chlorine activation within urban or power plant plumes: Vertically resolved ClNO<sub>2</sub> and Cl<sub>2</sub> measurements from a tall tower in a polluted continental setting. *Journal of Geophysical Research: Atmospheres*, 118, 8702-8715.
- ROBERTS, J. M., OSTHOFF, H. D., BROWN, S. S. & RAVISHANKARA, A. R. 2008. N<sub>2</sub>O<sub>5</sub> oxidizes chloride to Cl<sub>2</sub> in acidic atmospheric aerosol. *Science*, 321, 1059.

- ROBERTS, J. M., OSTHOFF, H. D., BROWN, S. S., RAVISHANKARA, A. R., COFFMAN, D., QUINN, P. & BATES, T. 2009. Laboratory studies of products of N<sub>2</sub>O<sub>5</sub> uptake on Cl<sup>-</sup>containing substrates. *Geophysical Research Letters*, 36.
- ROSSI, M. J. 2003. Heterogeneous reactions on salts. *Chemical Reviews*, 103, 4823-4882.
- ROTHMAN, L. S., GORDON, I. E., BARBE, A., BENNER, D. C., BERNATH, P. F., BIRK, M., BOUDON, V., BROWN, L. R., CAMPARGUE, A., CHAMPION, J. P., CHANCE, K., COUDERT, L. H., DANA, V., DEVI, V. M., FALLY, S., FLAUD, J. M., GAMACHE, R. R., GOLDMAN, A., JACQUEMART, D., KLEINER, I., LACOME, N., LAFFERTY, W. J., MANDIN, J. Y., MASSIE, S. T., MIKHAILENKO, S. N., MILLER, C. E., MOAZZEN-AHMADI, N., NAUMENKO, O. V., NIKITIN, A. V., ORPHAL, J., PEREVALOV, V. I., PERRIN, A., PREDOI-CROSS, A., RINSLAND, C. P., ROTGER, M., ŠIMEČKOVÁ, M., SMITH, M. A. H., SUNG, K., TASHKUN, S. A., TENNYSON, J., TOTH, R. A., VANDAELE, A. C. & VANDER AUWERA, J. 2009. The HITRAN 2008 molecular spectroscopic database. *Journal of Quantitative Spectroscopy and Radiative Transfer*, 110, 533-572.
- SAIZ-LOPEZ, A. & VON GLASOW, R. 2012. Reactive halogen chemistry in the troposphere. *Chem Soc Rev*, 41, 6448-72.
- SARWAR, G., SIMON, H., XING, J. & MATHUR, R. 2014. Importance of tropospheric ClNO<sub>2</sub> chemistry across the Northern Hemisphere. *Geophysical Research Letters*, 41, 4050-4058.
- SHERWEN, T., EVANS, M. J., SOMMARIVA, R., HOLLIS, L. D. J., BALL, S. M., MONKS, P. S., REED, C., CARPENTER, L. J., LEE, J. D., FORSTER, G., BANDY, B., REEVES, C. E. & BLOSS, W. J. 2017. Effects of halogens on European air-quality. *Faraday Discussions*, 200, 75-100.
- SHERWEN, T., SCHMIDT, J. A., EVANS, M. J., CARPENTER, L. J., GROSSMANN, K., EASTHAM, S. D., JACOB, D. J., DIX, B., KOENIG, T. K., SINREICH, R., ORTEGA, I., VOLKAMER, R., SAIZ-LOPEZ, A., PRADOS-ROMAN, C., MAHAJAN, A. S. & ORDONEZ, C. 2016. Global impacts of tropospheric halogens (Cl, Br, I) on oxidants and composition in GEOS-Chem. *Atmospheric Chemistry and Physics*, 16, 12239-12271.
- SIMON, H., KIMURA, Y., MCGAUGHEY, G., ALLEN, D. T., BROWN, S. S., OSTHOFF, H. D., ROBERTS, J. M., BYUN, D. & LEE, D. 2009. Modeling the impact of ClNO<sub>2</sub> on ozone formation in the Houston area. *Journal of Geophysical Research*, 114.
- SIMPSON, W. R., BROWN, S. S., SAIZ-LOPEZ, A., THORNTON, J. A. & GLASOW, R. 2015. Tropospheric halogen chemistry: sources, cycling, and impacts. *Chem Rev*, 115, 4035-62.
- SIMPSON, W. R., VON GLASOW, R., RIEDEL, K., ANDERSON, P., ARIYA, P., BOTTENHEIM, J., BURROWS, J., CARPENTER, L. J., FRIESS, U., GOODSITE, M. E., HEARD, D., HUTTERLI, M., JACOBI, H. W., KALESCHKE, L., NEFF, B., PLANE, J., PLATT, U., RICHTER, A., ROSCOE, H., SANDER, R., SHEPSON, P., SODEAU, J., STEFFEN, A., WAGNER, T. & WOLFF, E. 2007. Halogens and their role in polar boundary-layer ozone depletion. *Atmospheric Chemistry and Physics*, 7, 4375-4418.
- SKOOG, D. A., WEST, D. M., HOLLER, F. J. & CROUCH, S. R. 2013. *Fundamentals of Analytical Chemistry*, Cengage Learning.
- SLUSHER, D. L., HUEY, L. G. & TANNER, D. J. 2004. A thermal dissociation-chemical ionization mass spectrometry (TD-CIMS) technique for the simultaneous measurement of peroxyacyl nitrates and dinitrogen pentoxide. *Journal of Geophysical Research*, 109.
- SLUSHER, D. L., PITTERI, S. J., HAMAN, B. J., TANNER, D. J. & HUEY, L. G. 2001. A chemical ionization technique for measurement of pernitric acid in the upper troposphere and the polar boundary layer. *Geophysical Research Letters*, 28, 3875-3878.

- SNEEP, M. & UBACHS, W. 2005. Direct measurement of the Rayleigh scattering cross section in various gases. *Journal of Quantitative Spectroscopy and Radiative Transfer*, 92, 293-310.
- SOLOMON, S. 1999. Stratospheric ozone depletion: A review of concepts and history. *Reviews of Geophysics*, 37, 275-316.
- SOMMARIVA, R., HOLLIS, L. D. J., BAKER, A. R., BALL, S. M., BANDY, B. J., BELL, T. G., CORDELL, R. L., EVANS, M. J., LEE, J. D., REED, C., REEVES, C. E., SHERWEN, T., YANG, M. & MONKS, P. S. 2018. Seasonal and geographical variability of nitryl chloride and its precursors in Northern Europe [in preparation]. *Geophysical Research Letters*.
- SPICER, C. W., CHAPMAN, E. G., FINLAYSON-PITTS, B. J., PLASTRIDGE, R. A., HUBBE, J. M., FAST, J. D. & BERKOWITZ, C. M. 1998. Unexpectedly high concentrations of molecular chlorine in coastal air. *Nature*, 394, 353-356.
- STONE, D., EVANS, M. J., WALKER, H., INGHAM, T., VAUGHAN, S., OUYANG, B., KENNEDY, O. J., MCLEOD, M. W., JONES, R. L., HOPKINS, J., PUNJABI, S., LIDSTER, R., HAMILTON, J. F., LEE, J. D., LEWIS, A. C., CARPENTER, L. J., FORSTER, G., ORAM, D. E., REEVES, C. E., BAUGUITTE, S., MORGAN, W., COE, H., ARUFFO, E., DARI-SALISBURGO, C., GIAMMARIA, F., DI CARLO, P. & HEARD, D. E. 2014. Radical chemistry at night: comparisons between observed and modelled HO<sub>x</sub>, NO<sub>3</sub> and N<sub>2</sub>O<sub>5</sub> during the RONOCO project. *Atmospheric Chemistry and Physics*, 14, 1299-1321.
- STUMM, W. & MORGAN, J. J. 1995. *Aquatic chemistry: chemical equilibria and rates in natural waters*, Wiley.
- TANNER, D. J. & EISELE, F. L. 1995. Present OH measurement limits and associated uncertainties. *Journal of Geophysical Research-Atmospheres*, 100, 2883-2892.
- TANNER, D. J., JEFFERSON, A. & EISELE, F. L. 1997. Selected ion chemical ionization mass spectrometric measurement of OH. *Journal of Geophysical Research: Atmospheres*, 102, 6415-6425.
- TELEDYNE INC. 2012. Operation Manual: Model T300/T300M Carbon Monoxide Analyzer.
- TELEDYNE INC. 2014. Operation Manual: Model T400 Photometric Ozone Analyzer.
- TELEDYNE INC. 2015. Operation Manual: Model T200 NO/NO<sub>2</sub>/NO<sub>x</sub> Analyzer.
- THALER, R. D., MIELKE, L. H. & OSTHOFF, H. D. 2011. Quantification of nitryl chloride at part per trillion mixing ratios by thermal dissociation cavity ring-down spectroscopy. *Anal Chem*, 83, 2761-6.
- THALMAN, R., BAEZA-ROMERO, M. T., BALL, S. M., BORRÁS, E., DANIELS, M. J. S., GOODALL, I. C. A., HENRY, S. B., KARL, T., KEUTSCH, F. N., KIM, S., MAK, J., MONKS, P. S., MUÑOZ, A., ORLANDO, J., PEPPE, S., RICKARD, A. R., RÓDENAS, M., SÁNCHEZ, P., SECO, R., SU, L., TYNDALL, G., VÁZQUEZ, M., VERA, T., WAXMAN, E. & VOLKAMER, R. 2015. Instrument intercomparison of glyoxal, methyl glyoxal and NO<sub>2</sub> under simulated atmospheric conditions. *Atmospheric Measurement Techniques*, 8, 1835-1862.
- THAM, Y. J., WANG, Z., LI, Q., YUN, H., WANG, W., WANG, X., XUE, L., LU, K., MA, N., BOHN, B., LI, X., KECORIUS, S., GRÖB, J., SHAO, M., WIEDENSOHLER, A., ZHANG, Y. & WANG, T. 2016. Significant concentrations of nitryl chloride sustained in the morning: investigations of the causes and impacts on ozone production in a polluted region of northern China. *Atmospheric Chemistry and Physics*, 16, 14959-14977.
- THAM, Y. J., YAN, C., XUE, L., ZHA, Q., WANG, X. & WANG, T. 2013. Presence of high nitryl chloride in Asian coastal environment and its impact on atmospheric photochemistry. *Chinese Science Bulletin*, 59, 356-359.
- THORNTON, J. A., BRABAN, C. F. & ABBATT, J. P. D. 2003. N<sub>2</sub>O<sub>5</sub> hydrolysis on sub-micron organic aerosols: the effect of relative humidity, particle phase, and particle size. *Physical Chemistry Chemical Physics*, 5, 4593-4603.

- THORNTON, J. A., KERCHER, J. P., RIEDEL, T. P., WAGNER, N. L., COZIC, J., HOLLOWAY, J. S., DUBE, W. P., WOLFE, G. M., QUINN, P. K., MIDDLEBROOK, A. M., ALEXANDER, B. & BROWN, S. S. 2010. A large atomic chlorine source inferred from mid-continental reactive nitrogen chemistry. *Nature*, 464, 271-4.
- UNIVERSITY OF BIRMINGHAM. 2015. *ICOZA campaign updates* [Online]. Available: <http://www.atmos.bham.ac.uk/icoza.htm> [Accessed 28 Jun 2017].
- VANDAELE, A. C., HERMANS, C., FALLY, S., CARLEER, M., COLIN, R., MÉRIENNE, M. F., JENOUVRIER, A. & COQUART, B. 2002. High-resolution Fourier transform measurement of the NO<sub>2</sub> visible and near-infrared absorption cross sections: Temperature and pressure effects. *Journal of Geophysical Research: Atmospheres*, 107, ACH 3-1-ACH 3-12.
- VESTER, B. P., EBERT, M., BARNERT, E. B., SCHNEIDER, J., KANDLER, K., SCHÜTZ, L. & WEINBRUCH, S. 2007. Composition and mixing state of the urban background aerosol in the Rhein-Main area (Germany). *Atmospheric Environment*, 41, 6102-6115.
- VOLKAMER, R., SPIETZ, P., BURROWS, J. & PLATT, U. 2005. High-resolution absorption cross-section of glyoxal in the UV-vis and IR spectral ranges. *Journal of Photochemistry and Photobiology a-Chemistry*, 172, 35-46.
- VON GLASOW, R. 2008. Atmospheric chemistry - Pollution meets sea salt. *Nature Geoscience*, 1, 292-293.
- WANG, T., THAM, Y. J., XUE, L., LI, Q., ZHA, Q., WANG, Z., POON, S. C. N., DUBÉ, W. P., BLAKE, D. R., LOUIE, P. K. K., LUK, C. W. Y., TSUI, W. & BROWN, S. S. 2016. Observations of nitryl chloride and modeling its source and effect on ozone in the planetary boundary layer of southern China. *Journal of Geophysical Research: Atmospheres*, 121, 2476-2489.
- WARNECK, P. & WILLIAMS, J. 2012. *The Atmospheric Chemist's Companion*, Springer Netherlands.
- WASHENFELDER, R. A., LANGFORD, A. O., FUCHS, H. & BROWN, S. S. 2008. Measurement of glyoxal using an incoherent broadband cavity enhanced absorption spectrometer. *Atmos. Chem. Phys.*, 8, 7779-7793.
- WORLD HEALTH ORGANIZATION. 2014. *Ambient (outdoor) air quality and health fact sheet* [Online]. Available: <http://www.who.int/mediacentre/factsheets/fs313/en/> [Accessed 07 Feb 2018].
- YANG, M., BELL, T. G., HOPKINS, F. E., KITIDIS, V., CAZENAVE, P. W., NIGHTINGALE, P. D., YELLAND, M. J., PASCAL, R. W., PRYTHERCH, J., BROOKS, I. M. & SMYTH, T. J. 2016a. Air-Sea Fluxes of CO<sub>2</sub> and CH<sub>4</sub> from the Penlee Point Atmospheric Observatory on the South West Coast of the UK. *Atmospheric Chemistry and Physics Discussions*, 1-30.
- YANG, M., BELL, T. G., HOPKINS, F. E. & SMYTH, T. J. 2016b. Attribution of Atmospheric Sulfur Dioxide over the English Channel to Dimethylsulfide and Changing Ship Emissions. *Atmospheric Chemistry and Physics Discussions*, 1-19.
- YOKELSON, R. J., BURKHOLDER, J. B., FOX, R. W., TALUKDAR, R. K. & RAVISHANKARA, A. R. 1994. Temperature Dependence of the NO<sub>3</sub> Absorption Spectrum. *The Journal of Physical Chemistry*, 98, 13144-13150.
- YOUNG, C. J., WASHENFELDER, R. A., ROBERTS, J. M., MIELKE, L. H., OSTHOFF, H. D., TSAI, C., PIKELNAYA, O., STUTZ, J., VERES, P. R., COCHRAN, A. K., VANDENBOER, T. C., FLYNN, J., GROSSBERG, N., HAMAN, C. L., LEFER, B., STARK, H., GRAUS, M., DE GOUW, J., GILMAN, J. B., KUSTER, W. C. & BROWN, S. S. 2012. Vertically resolved measurements of nighttime radical reservoirs in Los Angeles and their contribution to the urban radical budget. *Environ Sci Technol*, 46, 10965-73.

ZHU, R. S. & LIN, M. C. 2004. Ab initio studies of ClO<sub>x</sub> reactions: Prediction of the rate constants of ClO+NO for the forward and reverse processes. *Chemphyschem*, 5, 1864-1870.